ANALYSIS OF THERMOELECTRICAL MODULES FOR ENERGY HARVESTING SYSTEMS

Teză destinată obţinerii
titlului ştiinţific de doctor inginer
la
Universitatea "Politehnica" din Timişoara
în domeniul INGINERIE ELECTRONICĂ
ȘI TELECOMUNICAȚII
de către

Ing. Mihail Octavian Cernăianu

Conducător ştiinţific: prof.univ.dr.ing. Aurel Gontean
Referenţi ştiinţifici: prof.univ.dr.ing. Paul Svasta
prof.univ.dr.ing. Dan Pitică
prof.univ.dr.ing. Dan Lascu

Ziua susţinerii tezei: 17.01.2013

Seriile Teze de doctorat ale UPT sunt:

1. Automatică
2. Chimie
3. Energetică
4. Ingineria Chimică
5. Inginerie Civilă
6. Inginerie Electrică
7. Inginerie Electronică şi Telecomunicaţii
8. Inginerie Industrială
9. Inginerie Mecanică
10. Ştiinţa Calculatoarelor
11. Ştiinţa şi Ingineria Materialelor
12. Ingineria sistemelor
13. Inginerie energetică
14. Calculatoare şi tehnologia informaţiei

Universitatea „Politehnica” din Timişoara a iniţiat seriile de mai sus în scopul diseminării expertizei, cunoştinţelor şi rezultatelor cercetărilor întreprinse în cadrul şcolii doctorale a universităţii. Seriile conţin, potrivit H.B.Ex.S Nr. 14 / 14.07.2006, tezele de doctorat susţinute în universitate începând cu 1 octombrie 2006.

România, 300159 Timişoara, Bd. Republicii 9,
tel. 0256 403823, fax. 0256 403221
e-mail: editura@edipol.upt.ro

Acknowledgements

This work was partially supported by the strategic grant POSDRU/88/1.5/S/50783, Project ID50783 (2009), co-financed by the European Social Fund – Investing in People, within the Sectoral Operational Programme Human Resources Development 2007-2013.

This paper primary addresses to those interested in the waste heat energy recovery process using thermoelectrical modules.

The work could not be completed without the plentiful discussions carried with my father concerning the mechanical setup and without his active participation at its implementation.

I would like to address my sincere thanks to Prof. PhD. Aurel Gontean for his implication, support and ideas that led to the completion of this work.

I am grateful to proffesors Dan Lascu and Aurel Filip for their sugesstions and the support they provided me during this research.

I also address special thanks to Mr. Vasile Danaila for the technical support he offered and to my friend and colleague eng. Cosmin Cirstea for his advices and hastily help.

Many thanks go to all my friends and also to Monica Chiosa for the help undertaken during her undergraduate summer practice programme.

Timişoara, January 2013 Mihail Octavian Cernaianu

To my parents,

Cernaianu, Mihail Octavian

Analysis of Thermoelectrical Modules for Energy Harvesting Systems

Teze de doctorat ale UPT, Seria 7, Nr. 60, Editura Politehnica, 2013, 168 pagini, 147 figuri, 12 tabele.

ISSN: 1842-7014

ISBN: 978-606-554-598-4

Cuvinte cheie: thermoelectrical module, SPICE model, energy harvesting system, energy storage, DC-DC converter.

Abstract,

This work presents the analysis of thermoelectric modules (TEMs) and the implementation of an improved SPICE model for these devices. Accurate TEM models are required by electrical engineers when designing energy harvesting systems, in order to determine the precise output power delivered by the design and to implement intelligent power management algorithms. All these aspects are discussed in the current work, where the author also implements an original energy recovery system that uses TEMs to harvest the unused waste heat. A complete setup is simulated in SPICE and the results are compared to the experimental data.

The thesis encompasses an interdisciplinary study that was required to implement the neccesary mechanical parts, electronics, SPICE models and deals with important aspects that are encounted when designing and evaluating efficient energy harvesting systems based on TEMs.

Contents

Index of figures

Index of tables

Formula symbols

A	Material surface area [m^2]
a	Thermal diffusion coefficient [m^2/2]
c_p	Specific heat capacity [J/kgK]
C_{mol}	Molar heat capacity [J/molK]
$C_{<material>}$	Heat capacity of <material> [J/K]
C_{th}	Thermal capacitance or heat capacity in general [J/K]
g	Free fall acceleration [m/s^2]
j	Electric current density [A/m^2]
k	Thermal conductivity in general [W/mK]
k_S	Specific thermal conductivity or thermal conductance of a TEM module [W/K]
σ_s	Electrical conductance of a TEM module
l	Characteristic length of the heat exchange surface [m]
L_f	Distance between heatsink fins [m]
m	Material mass [kg]
p	Pressure [N/m^2]
$\vec{q}$	Thermal flux density [W/m^2]
w	Fluid speed [m/s]
S_{AB}	Thermoelectric force that appear at the contact of A material with B material [V/K]
C,n	Constants for *Nu* number
T	Temperature [K]
T_H	Hot side temperature [K]
T_C	Cold side temperature [K]
M	Molar mass [g/mol]
Nu	Nusselt number
Gr	Grashof number
Pr	Prandtl number
I	Electric current [A]
P	Electric power [W]
R	Electrical resistance in general [Ω]
R_m	Electrical resistance of the TEM module [Ω]
R_{th}	Thermal resistance in general[K/W]
R_{thTEM}	Thermal resistance of the TEM module [K/W]
$\dot{Q}$	Heat flow [W]
Q	Heat [J]
S	Seebeck coefficient for a TEM module [V/K]
τ	Thomson coefficient [V/K]
ρ_E	Electrical resistivity [Ωm]
Π_{AB}	Peltier coefficient [J/C]
Π_i	Similitude criteria
G	Thermoelectric pellet geometry factor
Z	Thermoelement figure of merit [1/K]
ZT	Dimensionless figure of merit

COP	Coefficient of performance for thermoelectric materials
ν	Kinematic viscosity coefficient [m^2/s]
β	Volumetric thermal expansion coefficient [1/K]
σ	Electrical conductivity [S/m]
δ	Material width or thickness [m]
α	Heat transfer coefficient [W/m^{2}K]
ρ	Material density [kg/m^3]
V	Material volume [m^3]
H_{AE}	Error amplifier transfer function
$\overline{T}$	Mean temperature between the hot and cold sides of a TEM
N	Number of thermocouples
ΔT	Temperature difference
∇	Gradient operator
∇^2	Laplace operator
ε_f	Heat sink fin efficacy
$\Phi_{w,f}$	Heat flows through wall and fin, in a heat sink [W]

Acronyms

TEM	Thermoelectric module
TEG	Thermoelectric generator
TEC	Thermoelectric cooler
LDO	Linear dropout regulator
TEM	Thermoelectric module
TEG	Thermoelectric generator
TEC	Thermoelectric cooler
Dc	Duty cycle
DUT	Device under test
MPPT	Maximum power point tracking
MPPC	Maximum power point control
NTC	Negative temperature coefficient
PWM	Pulse Width Modulation
PCS	Power Control Switch
RTEG	Radioisotope TEG
PV	Photovoltaic
MMRTEG	Multi-mission RTEG
HTC	Heat transfer coefficient
FPGA	Field Programmable Gate Array
OA	Operational amplifier
ACC	Average current control
FE	Finite element
CAD	Computer Aided Design
CFD	Computational Fluid Dynamics
PI	Proportional Integrator

Chapter 1

Renewable energy and thermoelectric materials

In this chapter, a short introduction is made concerning the renewable energy facts that also point the increasing interest in this type of energy source. A review of the classical physical background of the thermoelectric material is presented and the drawbacks of the existent SPICE models are highlighted, in order to motivate the current work and its applications. This chapter describes the state of the art in the research area and usage of the TEMs, the modelling techniques, previous models and the author's new ideas of usage.

1.1 Goals of the work

The objectives of this work is the accurate SPICE modelling of thermoelectrical modules, including the internal parameters extraction, the implementation of the SPICE thermoelectrical model of an energy harvesting device and developing a practical application for generating and storing electrical energy from low temperature (< 90℃) heat sources.

1.2 Renewable energy facts

The need for renewable energy sources, other than fossil fuels, has become one of the most critical current issues that led to a significant research into alternative energy sources and energy conversion techniques [1].

The Renewable Energy Policy Network for the 21st century (REN21) convenes international multi-stakeholder leaders to enable a rapid global transition to renewable energy [2] and is formed of a numerous steering committees from various countries around the world (US, Japan, Germany, Austria, UK, China, etc). Into their 2012 report [3], REN21 states that the total renewable power capacity, not including hydropower rose from 315 GW in 2010 to 390 GW in 2011, showing an important growth of 23%. This demonstrates the importance paid to this subject by countries all around the world and that efforts are being made to find alternative solutions to natural resources (e.g. petroleum and coal) that are getting depleted.

World primary energy consumption grew by 2.5% in 2011, as presented in Fig 1.1 by the BP Statistical review of world energy report 2012 [4].

The prediction made by the "Science of sustainability" 2006 summary report (Fig. 1.2), that the global energy consumption will reach 12 billion toe (tons of oil equivalent) proved to be correct (as represented in Fig. 1.1) and is expected to increase by 60% until 2030, compared to the value from 1971 (Fig. 1.2). From this high amount of energy, a large portion is dissipated into ambient air as unused heat which leads to the necessity of techniques capable to recover the wasted heat [5].

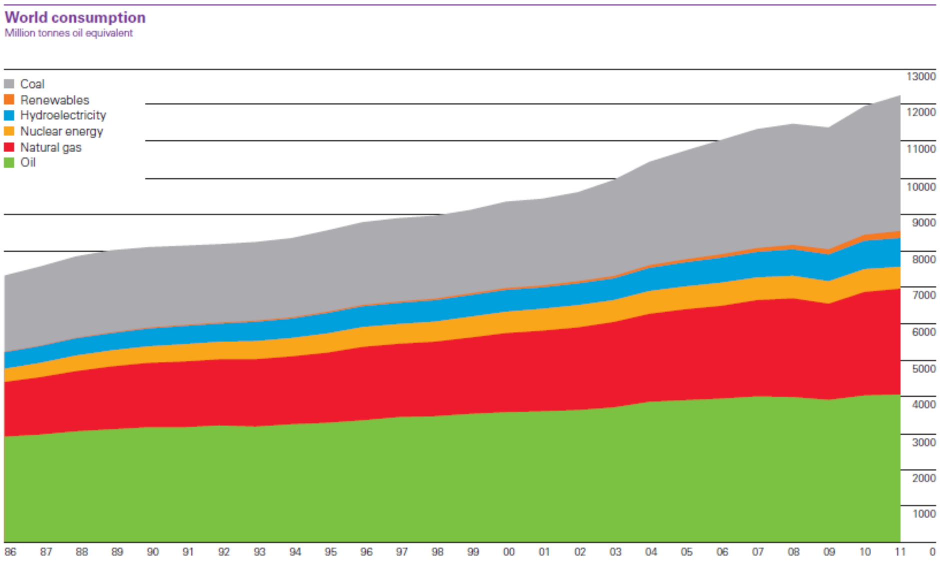

Figure 1.1 World energy consumption in million tones oil equivalent, from ’86 – 2011. Source [4]

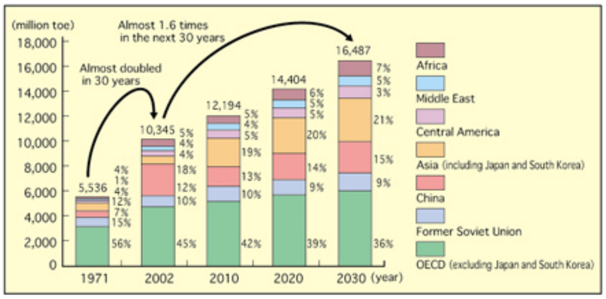

Figure 1.2 Global primary energy consumption until 2030. Source [6]

The REN 21 status report states that thermoelectric generators (TEGs), devices that convert heat to electricity, are becoming cost effective and allow wood burning stoves to generate both heat and electricity enabling them to operate fans for improved combustion or provide electricity for other applications. In most applications (energy transportation, factories, thermal engines, electric generators, etc) enormous amounts of heat are wasted. This type of energy is difficult to use due to its low temperature although the amount is very large [7].

The TEGs employ direct thermal to electrical energy conversion, without the intermediate step of kinetic energy. With no moving parts, this technology offers an alternative of high potential, as stated in [7], where the author claims that the improvements in material sciences and the progress of nanotechnology bring thermoelectric materials and therefore thermoelectric converters to renewed significance. The drawback of using TEG solutions in energy harvesting devices is the need for cooling systems to create the necessary temperature gradient that is proportional to the output power of the TEG. However, in practical situations a real thermoelectric generator combines thermoelectric modules with the specific heat exchangers in very large scale installations [8].

A TEG generates electricity due to the later called Seebeck effect that was first discovered in 1821 by the German physicist Thomas Johann Seebeck. Given a uniform temperature in a closed circuit that is formed by metals, the electromotive contact forces compensate each other and their algebraic sum is zero. Seebeck discovered that this compensation does not persist and that an electromotive force appears if one of the contact points between two metals has another temperature than the others [9]. Conversely, the Peltier effect is the presence of heat at the contact region of two metals when they are electrified [9].

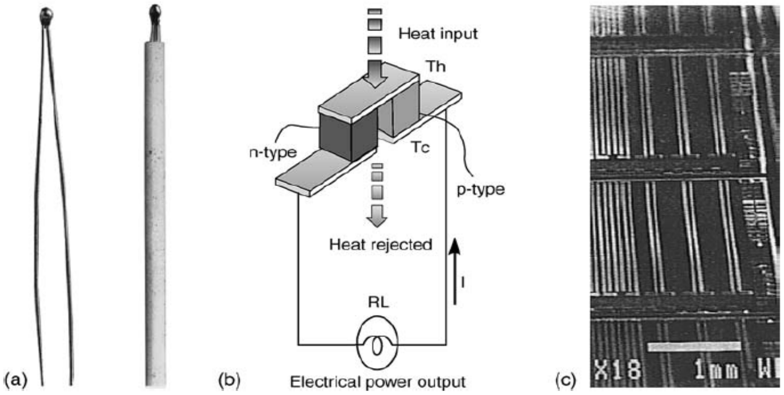

Figure 1.3 Different thermoelectric devices: a) Conventional metal alloy thermocouple b) Bulk semiconductor c) Miniature thin film. Source [9]

Conventional metallic thermocouples (Fig. 1.3a) are made from metal or metal alloys. They generate small voltages, typically tens of micro volts per degree temperature difference when its junction is located in a hot or cold environment compared to the ambient, and generate small amounts of electrical power when connected to a resistive load. They are used extensively as sensors, in the measurement of temperature. The thermocouple also operates as a heat pump by the Peltier effect when a voltage source is connected across the open ends so that an electric current is driven through the couple. Modern thermocouples benefit from the advances made in semiconductors materials. The material properties and geometry have been tailored specifically to meet the intended application requirements and possess Seebeck coefficients of hundreds of micro volts per degree [9].

In bulk devices for electricity generation or cooling applications, thermocouples have a typical geometry that consists of two ingot-shaped pellets (thermo-elements) of semiconducting material having dimensions in the order of millimeters connected at one end with an electrically conducting metal strap [9].

1.3 Thermoelectric physical background

The electromotive voltage that appears at the circuit's ends is proportional to the temperature difference of the contacts with the proportional coefficient S_{AB} called thermoelectric force that is material dependent [10]. The electromotive voltage can be written as:

$$dV_{AB} = S_{AB} dT \tag{1.1}$$

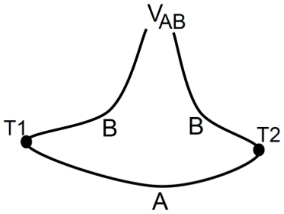

Figure 1.4 Circuit explaining the Seebeck effect. Source [reproduced as in 10]

Because S_{AB} depends on temperature, the electromotive voltage results from integrating Eq. 1.1.

$$V_{AB} = \int_{T1}^{T2} S_{AB} dT = \int_{T1}^{T2} (S_A - S_B) dT \tag{1.2}$$

where S_A and S_B are the differential thermoelectric forces for A and B materials.
The appearance of the V_{AB} voltage between the two points that reside at different temperatures $T_1 > T_2$ can be explained in a semiconductor by the charge carriers diffusion. In the hot side, the charge carriers' concentration is high which determines their diffusion into the colder region that charges positive or negative, depending on the charge carriers sign. The electric field that appears opposes to the infinite rise of the charge on the cold side of the probe which determines a stationary regime. We call the stationary electromotive voltage as thermoelectric force, defined as volts per Kelvin [V/K].

The thermoelectric force is much smaller in metals than in semiconductors (because the charge concentration does not vary with temperature), where it reaches tens of mV/K. The electromotive force is generated similar in the thermoelements presented in Fig. 1.3b that are formed of two different semiconductors, type n and p which are in contact with a conducting metal strap. Other two thermoelectric effects appear in such a device – the Peltier effect and the Thomson effect.

The Peltier effect, as briefly described above consists of heat generation or absorption at the contact point of two materials that are passed by a current flow, even in the absence of a temperature gradient [10]. The absorbed or released heat

Q in a time unit depends on the intensity and direction of the current flow I. The $\dot{Q}$ heat flow [W] will be expressed as:

$$\dot{Q} = \Pi_{AB} I \tag{1.3}$$

where Π_{AB} is the Peltier coefficient defined as [J/C].

If we have a similar circuit to the one in Fig. 1.4, in the stationary regime, but we use an energy source to generate a current flow, the two contacts absorb and release the same amount of heat. If the current flow is reversed, the phenomenon takes place in reverse (the contact that absorbed heat now releases heat) [11].

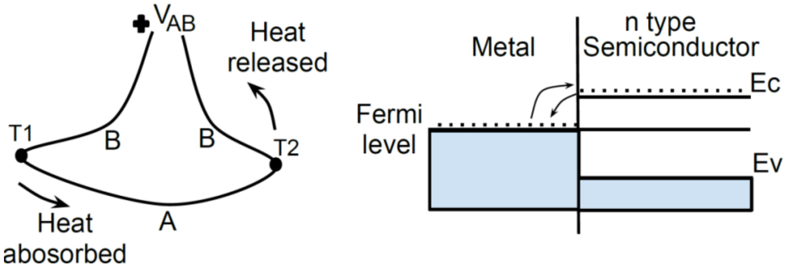

Figure 1.5 The Peltier effect. Source [reproduced as in 10]

Regarding the representation from Fig. 1.5, the electrons that pass from metal to semiconductor under the action of the current flow have to gain energy in order to jump the energy potential barrier so that they absorb energy and the contact is cooled. Reversely, if they have to pass from semiconductor to metal they release energy and the contact is heated [10].

The Thomson effect consists in the absorption or releasing of heat in a metallic conductor that resides at a temperature gradient and is passed by an electric current. The released or absorbed heat is independent of the Joule heating and depends on the current flow intensity and temperature gradient [11]. The effect is not restricted to metals and appears also in semiconductors. Depending on the direction of the electric flow, if this corresponds with the thermoelectric current determined by the temperature gradient, the electrons are carried to colder regions where they release energy and the crystal is heated. If the electric flow carries the electrons to the hotter region, they will absorb energy and the crystal will get colder [10].

The Thomson heat flux $\dot{Q}_T$ in one unit of volume is proportional to the temperature gradient and the electric current density:

$$\dot{Q}_T = -\tau \nabla T \cdot j \tag{1.4}$$

where $\boldsymbol{\tau}$ is the Thomson coefficient.

The four effects that appear in the thermoelectric device – the Seebeck effect, the Peltier effect, the Thomson effect and Joule effect must all be considered and

studied if a correct and real analysis is to be made although the Thomson effect for example is in most cases neglected due to its low influence.
In order to study the thermoelectric effects and their connection it is necessary to compute the total energy flux through a thermoelectric element.

Under steady state conditions, the contribution of the four phenomena to energy flow, through a unit volume of a TEG is expressed as follows [12]:

$$Tj\frac{dS}{dx} + \tau j\frac{dT}{dx} - \rho_E j^2 - \frac{d}{dx}\left(k\frac{dT}{dx}\right) = 0 \tag{1.5}$$

where ***T*** is the temperature, ***j*** is the electrical current density, ***S*** is the Seebeck coefficient, ***τ*** is the Thomson coefficient, ***ρ_E*** is the electrical resistivity and ***κ*** the thermal conductivity of the material.

Writing the energy equilibrium at the hot and cold side of a TEM that operates in the mode of thermoelectric cooler (TEC) and neglecting the Thomson effect one obtains:

$$\dot{Q}_a = ST_C I - \frac{1}{2}I^2 R_m - k_S(T_H - T_C) \tag{1.6}$$

$$\dot{Q}_e = ST_H I + \frac{1}{2}I^2 R_m - k_S(T_H - T_C) \tag{1.7}$$

$$\dot{Q}_e = \dot{Q}_a + P_{electrical} \tag{1.8}$$

$$P_{electrical} = S\cdot(T_H - T_C)\cdot I + R_m I^2 \tag{1.9}$$

$\dot{Q}_a$ and $\dot{Q}_e$ represent the heat flows at the absorbing (cold side) and emitting (hot side), respectively, ***T_H*** and ***T_C*** refers to the hot side and cold side temperatures, respectively, ***R_m*** is the internal resistance of the module, ***S*** is the Seebeck coefficient, ***k_S*** is the thermal conductance or specific thermal conductivity and ***$P_{electrical}$*** is the electrical power consumed for the TEM to operate as a cooler. The k_S, R_m and S parameters represent the total values of the N couples that form the module [12]:

$$k_S = (k_p + k_n)\cdot N\cdot G \tag{1.10}$$

$$S = (S_p + S_n)\cdot N \tag{1.11}$$

$$R_m = \frac{(\rho_n + \rho_p)\cdot N}{G} \tag{1.12}$$

where $G = \frac{area}{length}$ represents the geometry factor of one pellet.

Eq. 1.6-1.9 are similar if written for a thermoelectrical generator (TEG):

$$\dot{Q}_e = ST_C I + \frac{1}{2}I^2 R_m - k_S(T_H - T_C) \tag{1.13}$$

$$\dot{Q}_a = ST_H I - \frac{1}{2}I^2 R_m - k_S(T_H - T_C) \tag{1.14}$$

The electrical power produced by the module becomes:

$$P_{electrical} = S\cdot(T_H - T_C)\cdot I - R_m I^2 = V_{TEG}\cdot I \tag{1.15}$$

While in practice the two arms of the junction have similar material constants and similar doped alloys are adopted to make p and n type semiconductor legs [9, 13,

32], we obtain $k_p=k_n=k$, $\sigma_p= \sigma_n= \sigma$, $S_p= S_n$. Some manufacturers (e.g. Melcor) provide in their datasheet these parameters values that together with Eq. 1.10-1.12 lead to the total k, R and S values of the module.
In [9] the figure of merit of one couple is defined as:

$$Z_c = \frac{S_{pn}^2}{R \cdot k_{pn}} \tag{1.16}$$

where $\boldsymbol{S_{pn}}$ is the Seebeck coefficient of one couple , $\boldsymbol{k_{pn}}$ is the thermal conductance of the couple and $\boldsymbol{R}$ is the electrical resistance of the TEM.

In practice, as a TEM comprises of $\boldsymbol{N}$ couples the figure of merit of the material is used:

$Z_c = \frac{\sigma_S S^2}{k_S}$ where $\boldsymbol{\sigma_S}$ is the total electrical conductance, $\boldsymbol{S}$ is the Seebeck coefficient of the module and $\boldsymbol{k_S}$ the module thermal conductance.

More often, the ZT dimensionless parameter is used:

$ZT = \frac{\sigma_S S^2}{k_S}\overline{T}$ where $\overline{T}$ is the average temperature between the hot and cold side. For a material to be thermoelectric efficient, we want ZT as high as possible, meaning we desire materials with a high Seebeck coefficient, a high electrical conductivity but low thermal conductivity at the same moment [1].

In Fig. 1.6 the Carnot and conversion efficiency versus temperature and material figure of merit is presented, showing that a TEM with Z = $3\text{x}10^{-3}$/K would have 20% efficiency when operated over a temperature difference of 500K [9].

When the TEM performs as a cooler, its performance is generally expressed by the COP – coefficient of performance representing the cooling power produced divided by the rate at which electrical energy is supplied [9].
The COP is defined as:

$$COP = \frac{absorbed\ heat}{input\ electrical\ power} = \frac{ST_C I - \frac{1}{2}I^2 R_m - k_S(T_H - T_C)}{S \cdot (T_H - T_C) \cdot I + R_m I^2} \tag{1.17}$$

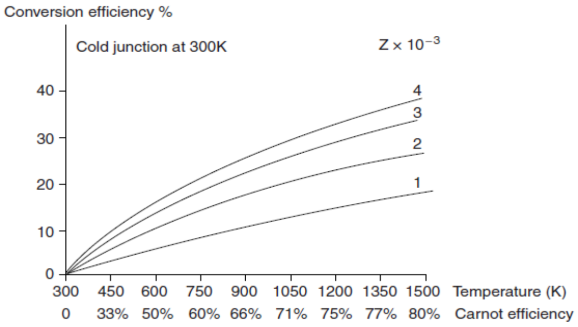

Figure 1.6 Thermoelectric generator efficiency function of temperature. Source [9]

The general construction for a TEM is very similar for both TEG and TEC and ideally the geometry of the thermoelements should be wire-long (long and thin) for generation and squat (short and fat) for refrigeration, as presented in [9].

Figure 1.7 presents a high performance multi segmented TEG. The segmentation technique permits that two materials that are segmented together to have each its optimized figure of merit for a different temperature range. In the figure below this technique is used to generate a TEG that can withstand a temperature difference *ΔT* of approximately 700K with 15% efficiency.

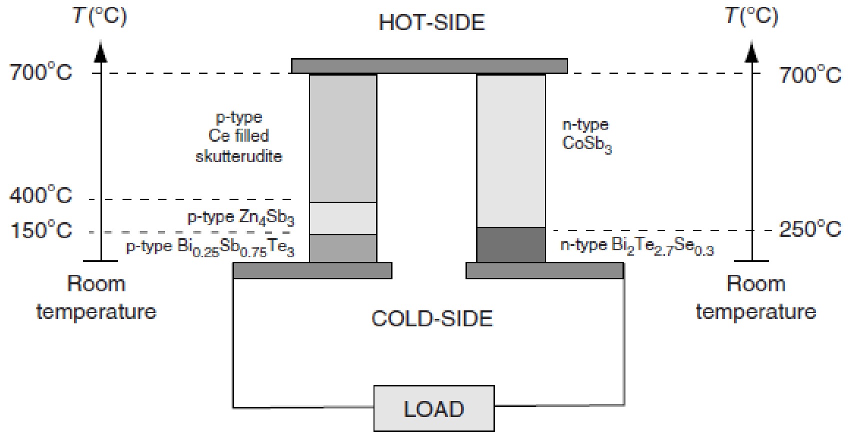

Figure 1.7 Multisegmented thermoelectric generator. Source [9]

1.4 Thermoelectric materials

In the beginning, the thermoelectric materials were made of two joined metal components e.g. copper – constantan that has a Seebeck coefficient of approximately 41μV/K [14]. Later on, the semiconductors became the choice for further development of thermoelectric materials. The reason can be explained by the help of Fig. 1.8.

In order to obtain high ZT thermoelectric materials all the three parameters that comprise the ZT figure of merit must be improved in certain ways. The electrical conductivity σ is given as the product of the concentration and mobility of charge carriers [7]. This parameter is high with metals, very low with insulators and has intermediate values in semiconductors. The $S^2\sigma$ factor, called "electrical power factor" has been introduced to facilitate the optimization of the thermoelectrical material. It can be seen that in semiconductors the Seebeck coefficient falls with carrier concentration while the electrical conductivity rises. The best values are indicated to be found when the carrier concentration reaches $10^{19}/cm^3$. Regarding the thermal conductivity, in semiconductors the electronic thermal conductivity is increasing with the carrier concentration while in insulators it has the lowest value. High efficient thermoelectric materials must have high electrical conductivity and low thermal conductivity. Therefore, semiconductor materials must be used. Rowe [9] reports that the researcher's efforts are focused on reducing the lattice thermal conductivity by using crystal structures that conduct heat as glass and electricity like a crystal "phonon glass-electronic crystals".

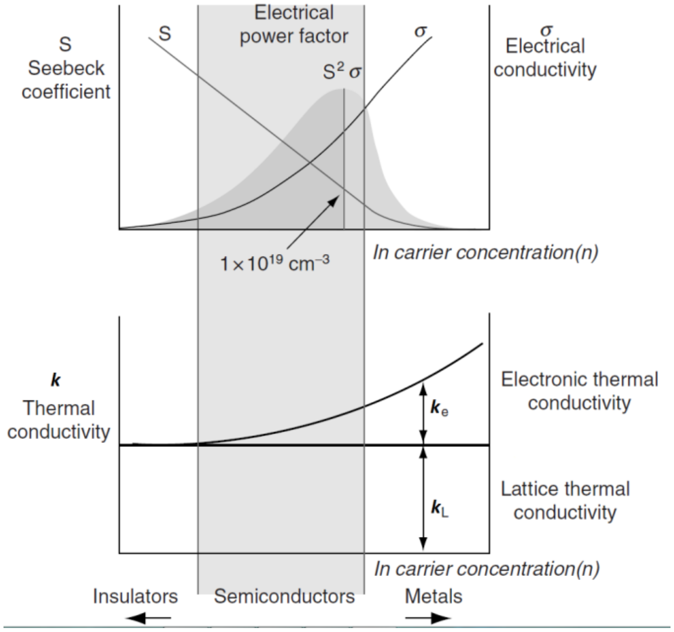

Figure 1.8 Dependence of Seebeck coefficient, electrical conductivity and thermal conductivity on concentration of free carriers. Source [9]

In 2012, the company Hi-Z Technology presented a report showing the ZT figure of merit for the best known thermoelectric materials function of temperature (Fig. 1.9). It can be observed that high temperature modules have been obtained that also exhibit high ZT.

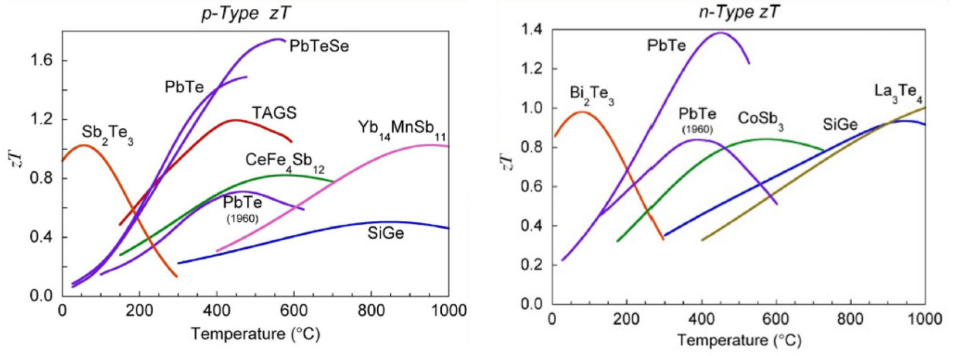

Figure 1.9 Different alloys figure of merit function of temperature. Source [14]

In order to decrease the lattice thermal conductivity, other researchers are using nanocomposite structures [1] and although high ZT materials have been achieved, they are not ready to be commercialized due to the high fabrication costs.

1.5 Advances in general usage

Thermoelectric technology has been used since 1930's as an alternative to batteries in devices such as gas operated radios and home generating stations [14]. Later on, radio receivers were powered by TEGs that were heated from kerosene lamps. As technology evolved, different implementations were made where TEGs were used to recover the heat generated by the exhaust pipes of trucks and cars [14], [15] and [16].

A few watch companies (Citizen, Seiko) implemented in their products in the late 90's TEGs for harvesting the body heat and due to the difference between ambient air and body to generate the necessary energy to power the watch. The watches, however, were not appreciated very much, their usage being limited to colder regions of the world. The Seiko Thermic wristwatch design is presented in [23] where microfabricated thermoelectric devices are discussed. The waste heat energy recovery from the human body is now again into attention, as presented in the 2011 Engineering and Physical Sciences Research Council 2011 report.

BMW received an award in 2008 for the development of a prototype TEG system [14] that was able to recover 300W electric power from the engine exhaust system. With the advances made in material technology the power has been raised in 2011 to more than 600W as reported in [17] and [18]. Amerigon, now Gentherm, a well known thermoelectric manufacturer introduced the climate control seat technology based on TEMs that equipped the high end class of 2009 Jaguar XF mid-size sport cars [14]. The company is also delivering working prototypes for BMW and Ford to improve the waste heat recovery [19]. The concept of seat climate control based on TECs is also presented in [25].

A commercial usage of TEMs can be found in portable refrigeration boxes where numerous manufacturers are using thermoelectric coolers in their designs.
Also, different research directions are presented in [20], [21], [22] and [24] where wireless TEG powered sensor nodes and TEC based cooling solutions for electronic packaging are investigated.

TEGs are also used in devices called radioisotope thermoelectric generators (RTEGs) that obtain their power by converting the heat released by the radioactive decay into electricity through the Seebeck effect. These devices have been used to power satellites and space probes over time (Apollo, Voyager I&II). One of the latest applications is powering the "Curiosity" Mars rover that was launched in 2011[14]. The particular one used in this rover is a special case of RTEG developed by NASA and the DOE and is called a Multi-Mission Radioisotope Thermoelectric Generator (MMRTG). The heat from the natural radioactive decay of the inside plutonium 238 dioxide power source is applied to the hot thermocouple junction, while the cold junction is connected to a radiator that stands in the cold of outer space [26].

1.6 Advances in Research

Since the discovery of the Seebeck effect in 1821, scientists have been continuously trying to improve and discover new materials in order to increase the efficiency of the thermoelectric modules.

In 2006, Jovanovic et al. [20] presented an energy harvesting device prototype based on TEGs with the purpose of temperature, vibrations and other measurements of Navy shipboard machinery. An innovative technology called Quantum Well that uses a design of less than one cubic inch is used to provide increased conversion efficiency. The novel manufacturing technique was successfully demonstrated.

A study from 2009 conducted by Zhang et al [27] presents the implementation of a new thermoelectric-photovoltaic hybrid energy source for hybrid electrical vehicles. Their results validate the proposed system and its ability to track the maximum power point. Kraemer et al presents in [28] a methodology to optimize the partitioning of the solar spectrum in order to yield the maximum conversion efficiency of a photovoltaic (PV) – thermoelectric (TE) hybrid system that was first presented in 2006[29]. In the latter, the author states that the efficiency of the hybrid system with the TEG is around 30%, a higher value compared to the efficiency of today’s PV panels.

Other works investigate the efficiency of TEGs taking into consideration the dimensions and structure of the heat-sinks. In 2010, Rosendahl et al propose a micro-channel heat sink [30] in order to increase the efficiency of the TEG. Their results are compared to a sink with the same dimensions as the micro-channel one but in macro-scale. Their conclusions are that the removed heat is significantly higher in the micro-channel comparison to the macro-channel heatsink.

In a recent work from 2012 [31], the authors show through a numerical investigation that the scaling down of the thermoelectric cooling elements (meaning miniaturizing the TEC size and increasing the number of elements) enhances the cooling capacity of the TEC.

Numerical analysis and experimental investigations that takes into account the Thomson effect have been carried out in current researches from 2011 [32], [33].

In a research presented in 2012, Apertet et al. [34] study how the maximum power output can be obtained from a thermoelectric generator with non ideal heat-exchangers by taking into account the working conditions of the TEG and in this way the thermal impedance matching. The authors expressed the thermal impedance matching in a simple fashion: the equality of the thermal contact conductance and the equivalent thermal conductance which comprises of the conductive and convective heat transports of the generator. Their conclusion is that one should search for modules with ZT values that allow both thermal and electrical impedance matching.

A 2006 report from the Sandia National Laboratories [35], US, presents a new miniaturized thermoelectric power source that was built and tested which has a power density higher than any system of that size previously reported. The authors demonstrate the significant progress that has been made in the miniaturization process of TEMs.

In [36], the authors present the usage of thermo-generators in combination with medical devices that are powered using the heat from the human skin.

Taking into consideration all the above reported researches it can be seen the interest in increasing the thermoelectric modules efficiency and that improvements can be achieved by taking into account all the aspects starting from the materials used up to the modelling part.

1.7 Modelling thermoelectric devices and previous models

The modelling of thermoelectric devices can be made in several ways.

One approach would be using finite element (FE) analysis which is a comprehensive modelling and is realized with the help of powerful software. This would be necessary if one needs to know the heat and electric flow in the entire volume of a thermoelectrical element or module.

Another possibility is the investigation of the concurrent physical phenomena that takes place inside a TEM by using quantum mechanics.

The third approach uses the classical physics and models the physical phenomena through thermodynamic equations. The author will refer further on to this technique, as it is the only one that can be combined with electrical circuits models in a SPICE simulator. In order to design and simulate energy systems that employ TEMs, accurate models for these devices must be developed. Regardless we refer to low or high power harvesting, the TEM models should replicate as accurate as possible the real behavior of the device. This is useful when we need to know the precise generated power of an energy harvesting device that uses TEMs and when implementing efficient algorithms that use the harvested energy in accomplishing different tasks, like Mateu et al. presented in [21]. The authors paper is focused on harvesting energy from human power as it continuously radiates heat. While the electrical energy is not constant over the operating time, the authors find necessary to use DC-DC converters and capacitors or batteries to store the energy and ensure continuous power. Their proposed device powers a temperature sensor and an efficient wireless communication module to transmit the sensor data. The authors characterized the TEGs to be used and represented the voltage versus current and the internal resistance for different temperature difference (ΔT) values. Further on, the authors are researching an optimized, energy-aware operation of the communication module. The dynamic power management along with an optimized wireless communication protocol was investigated and the results demonstrated the correct operation of the system. In the presented paper, the designed system was intended to work on a low temperature gradient (<10℃), between the human body and environment. Even at such low temperature gradients the internal parameters of the TEMs are varying as also presented in the paper.

This proves the usefulness and the need of a high accuracy SPICE TEM model that takes into account all the internal parameters variations.

Some authors [37], [38] and [39] have already implemented thermoelectric models, but they used only the manufacturer's datasheet constant parameters when building their models. In their paper, Lineykin et al [37] propose an equivalent circuit of a thermoelectric module based on the Eq. 1.5 - 1.8 presented in Section 1.1.

Other authors proposed improved models, for example in [40] a TEM SPICE model is presented that takes into account the variable internal resistance with temperature, while in [41] the model accounts for all temperature-dependent characteristics of the thermoelectric material. In the latter research the thermoelectric processes of Seebeck, Peltier, and Thomson effects are integrated with transient and Joule source terms through a combined finite-difference method (FDM) and Newton–Raphson numerical scheme. In [40], the authors have implemented the temperature dependence of the internal resistance in an improved SPICE model. Their results prove that the error resulting from assuming that the internal resistance is constant is greater than 12%. In [42], the authors investigated the transient thermal and electrical behavior of a TEG.

In the present thesis, the simulations errors when considering the internal parameters constant over temperature proved to reach 12% in some cases. The errors have been lowered down to 2% after implementing the temperature variation of the parameters, as it will be presented in the following chapters.

In the following chapters the author will describe the steps made to fully describe the TEM and the results obtained with the improved TEM SPICE model along with the analysis details, conclusions and a complete energy harvesting system design.

1.8 Scope of the work

This work is focused on the development of a high accuracy thermoelectrical model for TEMs. The model is based on the governing thermodynamic equations. The internal parameters of the TEM (electrical resistance, thermal conductivity and Seebeck coefficient) are extracted using a proposed test rig and autonomous applications are designed and built in LabVIEW programming language [43]. The internal parasitic components of the TEMs used in the work are also investigated. The simulation and the experimental data are compared and a discussion over the obtained results is performed.

Using the thermal to electrical analogy, a SPICE model that simulates the conductive heat transfer through the proposed test rig is implemented and a discussion on the obtained results is carried out. The author proposes a complete energy harvesting system based on TEGs. The energy harvesting system is simulated in SPICE and the results are compared to the experiments.

Further on, a SPICE implementation of the convective heat transfer mechanism that appears in normal operation in the proposed energy harvesting system is proposed and implemented. The differences between the simulation results and the experimental data are afterwards discussed.

The proposed TEM SPICE model is compared to other implementations and the performance is analyzed. A step down DC-DC converter is implemented and an average current control loop is proposed and implemented in a digital system. The converter aims to charge a Li-Ion battery while fulfilling the charging process – constant current constant voltage.

A customized DC-DC converter that is intended to be used with multiple TEM devices is proposed and developed. The converter employs an indirect current control loop and precise dead time control for increased efficiency.

1.9 Proposed new harvesting system

The author proposes an original self-sustainable wireless monitoring system that is powered from an energy harvesting device based on TEGs. The energy harvesting device purpose is to gather unused heat, convert it to electrical energy and store it into rechargeable batteries. The condition monitoring system (CMS) is to be used for the monitoring of heat dissipation equipment such as:

- Medium to high power electric generators,
- Wind turbine generators,
- Water turbines,
- Gas turbines,
- Boilers, exhaust pipes,

or any other equipment that needs to be monitored and can dissipate energy through heat.

The device can be used for monitoring various parameters such as vibrations, temperatures, pressures, pollution, gases etc. with the purpose of minimizing the repair costs and preventing equipment damage. The energy stored into rechargeable batteries is intended to be used for:

- Extending the autonomy of the wireless sensor network while no heat is present.
- Increasing the transmission power of the wireless transceiver.

The energy harvesting device is comprised of two major subsystems. The main subsystem is the mechanical device that considers also the TEGs and is intended to be placed where waste heat exists and is desired to be harvested. The second subsystem contains all the electronics necessary to harvest the maximum power available from the TEGs, store it into rechargeable batteries and use it accordingly.

The general system is presented in Fig. 1.10. The output voltage generated by the LTC 3105 converter [44] is used to charge a Ni-Mh rechargeable battery pack with low current in trickle charge regime. Depending on the output current, the battery will be fully charged in a period starting from a couple of days up to two weeks. From the experiments, assuming a charging current of 5mA, that corresponds to a heat source with a temperature of 50℃, a 2.4V 1000mAh battery would charge in 9 days. The charging period of the Ni-Mh battery pack is lower than the discharging time of the Li-Ion battery. The Li-Ion energy will be mainly used to power the high gain wireless amplifier in order to increase the distance the system can transmit the measured data. The SST12CP11 high gain power amplifier is intended to be used. It provides 34dB gain with a maximum power consumption of 2.5W (5V and a maximum of 470mA). Assuming a case with a maximum transfer period of 10ms at maximum power – 2.5W, once every 1 min, we obtain a consumed energy of

1.5Ws. Taking into account that the Li-Ion battery will have a capacity of 1000mAh and provides a voltage of minimum 3.7V this functioning rate will deplete the battery in more than 300 days.

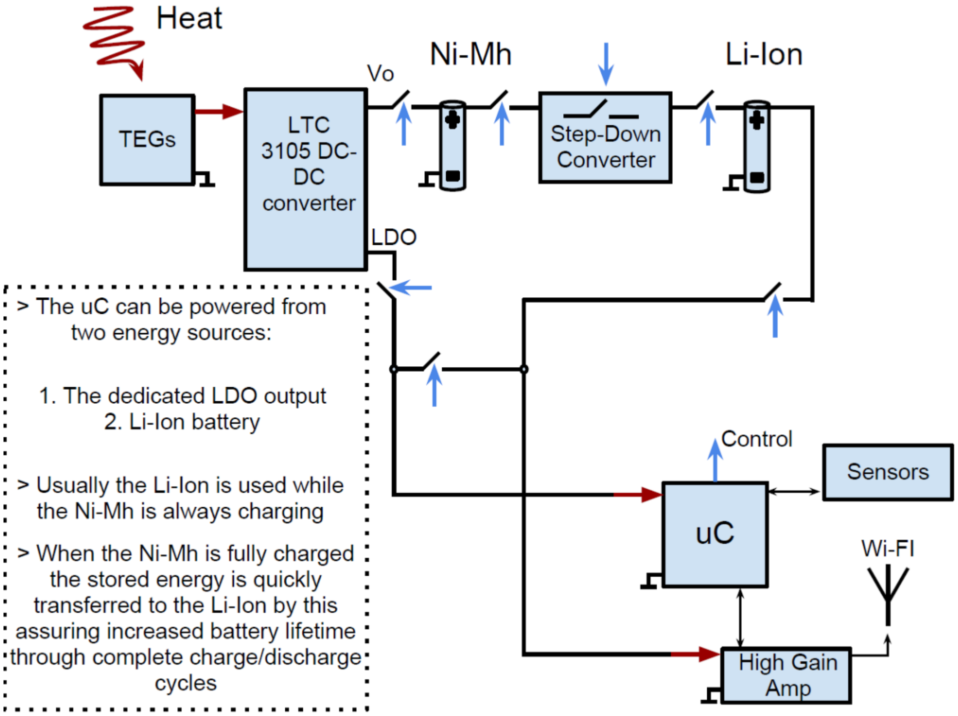

Figure 1.10 Proposed energy harvesting system, employing energy storage for high power Wi-Fi. Source [original]

The energy consumption calculation proves that the proposed system will successfully achieve its purpose and the ratio between the available energy and consumption is excellent.

The microcontroller power management will be implemented in such way that the power consumption will be monitored by computation of the functioning and activity time. The design of the energy harvesting system is presented in detail in Chapter 5.

1.10 Conclusions

The analysis made in this chapter over the advances made in the research and industry area of thermoelectric devices, with numerous and state of the art bibliographic references (2010-2012), demonstrates that due to the improvements made in material science, the TEMs are being used in different systems for voltage generation or cooling purpose. Their usage is also preferred because of being robust and having no moving parts. As different materials with an increased figure of merit are being researched, the TEM promise to be a solution for waste heat recovery energy devices, fact that led to the goal of this research.

Besides the research for new materials that are necessary to create more performing TEM devices, an accurate SPICE model must be available for electrical engineers. This is necessary because:

- The electronics behind the DC-DC converters that extract the energy generated by the TEMs, together with the software control techniques must be simulated and tweaked before practical implementation.
- An efficient management of the harvested energy must take into account the precise energy a TEM can generate under normal operating conditions.

Prior work demonstrates that large errors appear when considering the TEM parameters as constant over temperature (12% reported when considering the internal resistance constant).

Up to the moment the current research was developed, no prior work was found to investigate the internal parasitic components of a TEM.

1.11 Contributions:

1. **The drawbacks of the previous SPICE models** that are of interest in the current topic **were discussed and a new model** that takes into account the internal parameters variation with temperature is proposed.
    - The model aims to help electrical engineers design and simulate energy harvesting devices employing DC-DC converters, energy storage and predict the amount of energy the TEM generates in a real system.
2. A complete **self-sustainable wireless device for waste heat recover**y **is proposed**.
    - The device aims to recover the waste heat produced by industrial machinery to power a conditional monitoring system that communicates with a base system via a high power Wi-Fi transceiver.
    - The proposed device is completely autonomous and employs a **two stage energy storage system**.
    - Based on the improved TEM SPICE model proposed, the waste heat recovery device output power can be accurately predicted and the control algorithm follows to be optimized for **optimum power consumption.**

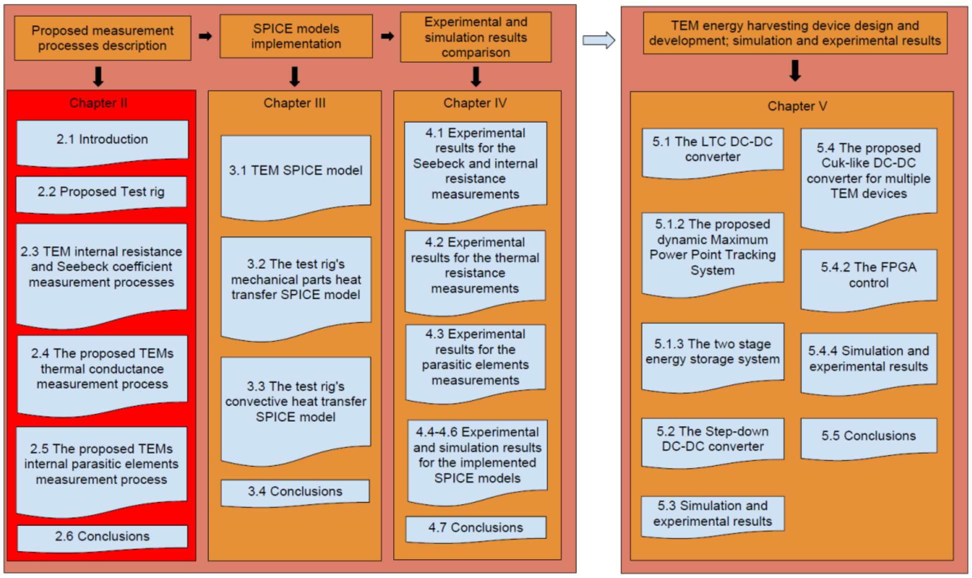

Chapter 2

TEM Parameters Analysis and Extraction

In the following, the proposed test rig is presented, together with the implemented measurement processes and the necessary equipment to extract the TEM's parameters (internal resistance, thermal conductance, Seebeck coefficient and parasitic components).

2.1 Introduction

In [7] the author summarizes a couple of analytical and numerical models and aims to link the best known TEM models and define the optimal generator assembly, running conditions and system integration. The case when the TEM is used along with different types of heat exchangers is also brought into discussion. The analysis of the heat transfer mechanism through various heat exchangers, especially with the ones that use liquid as cooling agent is a difficult thermodynamic problem. The analysis of circulating or turbulent fluids is a problem that has not been mathematically solved, as Feynman also explains in [45]. Numerical analysis proves to offer much more detailed information than analytical ones, as stated in [7]. The 3D finite element analysis simulation the author proposes proves a good agreement

with a large scale TEG model up to 110℃. The author uses afterwards the finite element (FE) model to evaluate and optimize different TEM modules.
The current work is intended to improve the design and evaluation of different TEM based electronic systems by developing an accurate TEM model. While most electric circuit simulations are made in a SPICE based application and a certain type of thermoelectrical module is supposed to be used, a precise thermoelectrical model is necessary. Although the FE analysis can provide a more accurate and detailed model than an analytical approach this solution cannot be easily integrated with electrical SPICE simulators. Moreover, the very detailed approximation a FE model can offer may prove to be of little use in an electrical simulation where the macroscopic effects of the TEM are of concern (output voltage, thermal and electrical resistivity), not the heat and electrical flow or distribution inside of the thermoelectric material.

As presented in Chapter 1, SPICE TEM models have already been proposed, but these do not take into account neither the modules temperature varying parameters nor the Thomson effect that lead to errors up to 12% in simulations as proved by the tests conducted in this work.

In the present chapter the author will describe the experimental setup that will be used to extract the TEMs internal parameters. These will be later used to build the thermoelectrical model and the results will be compared to the experiment for validation. The heat transfer system, a heat exchanger based on heatsinks and liquid cooling pipes will also be described and simulated in SPICE using the thermoelectrical analogy.

2.2 Proposed test rig

The author proposes a modular test rig comprising of two thermoelectrical generators sandwiched between an aluminum radiator and a copper plate that is connected to an electrical heater. The heater is made of serial connected power resistors that are controlled by a programmable power supply unit which provides a serial interface for communication. Two NTC thermistors are located each at the contact point of the TEG with the hot side and cold side, respectively (Fig. 2.1, 2.2).
The radiant brick along with the heater support are intended to force and direct the heat from the resistive heater through the copper plate. The copper plate is in direct contact with the two duralumin blocks that in turn are in contact with the two TEGs. One duralumin block contains a duct where a thermistor which provides the hot side’s temperature of the TEGs is located. The cold sides of the two TEGs are in contact with a duralumin chamber that incorporates cooling pipes. The duralumin chamber also has a thermistor that will provide the cold side temperature of the TEGs. Four additional heatsinks are used to provide extra cooling. A third thermistor is located in the heating element (necessary when measuring the thermal conductance). Each thermistor employs a second order active low pass filter in order to remove the noise generated by the long wires and other interferences. The hot side is separated by the cold side through a 10mm thermal insulator board and an additional 3mm air layer (Fig. 2.1 and 2.2). The thermal insulation board is manufactured by Selitherm [46] and has a thermal resistance of 0.25m^{2}K/W. The insulation board is used to prevent the heat touching the cold side of the TEMs and it also permits the test rig to be used in parameters extraction or in an energy harvesting device as it will be detailed later.

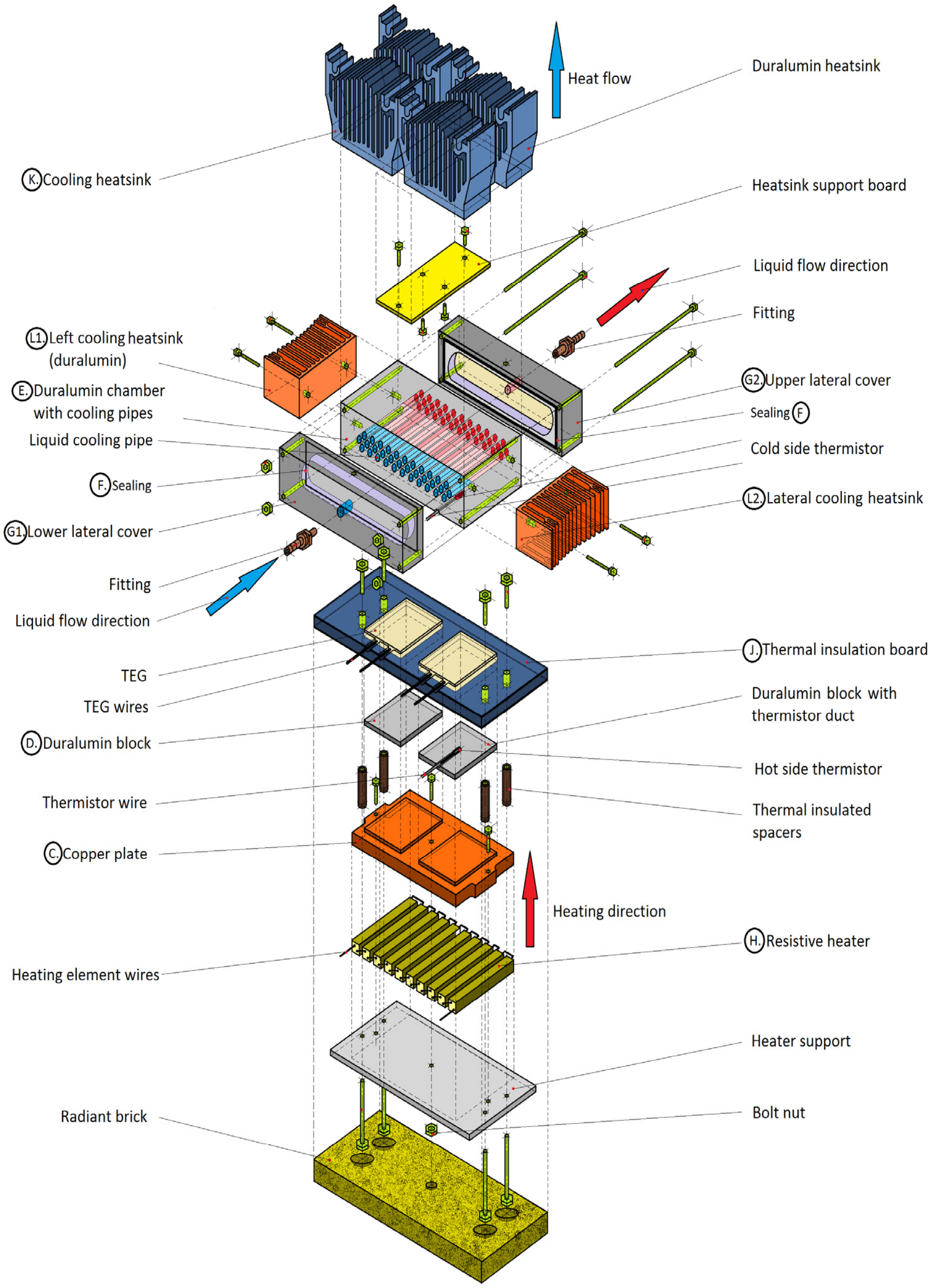

Figure 2.1 Proposed test rig exploded view. Source [original]

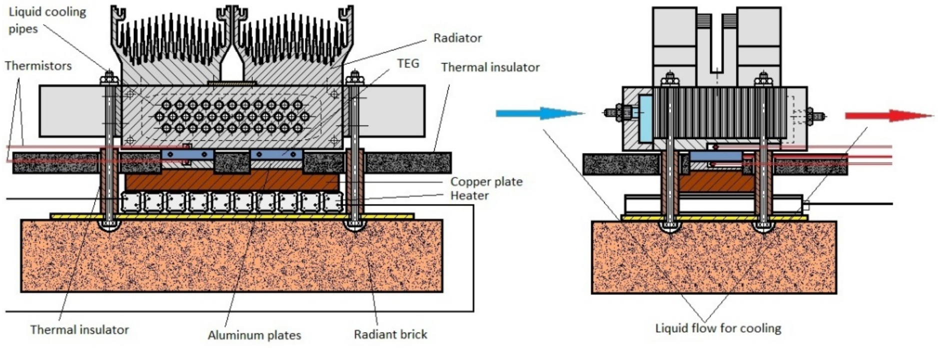

Figure 2.2 Proposed test rig section view. Source [original]

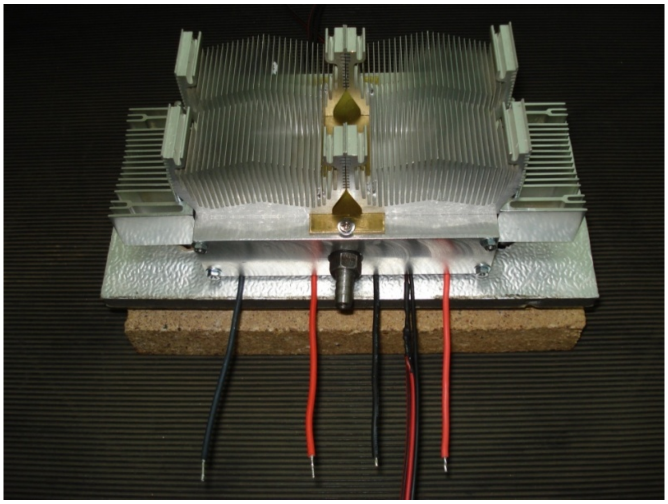

Figure 2.3 Proposed test rig main unit. Source [original]

Four spacers with low thermal conductivity, connected through bolts, are used to fasten all the elements and provide the necessary pressure to create a good physical contact between parts. Silver based, high thermal conductivity paste (higher than 4W/mK) is used between each contact point to ensure an increased thermal conductivity. The liquid pipes inside the duralumin chamber are used to cool the cold side of the TEMs when extracting the internal parameters or when the system is used as an energy harvesting device. The input and output fittings are connected to a heat exchanger through plastic pipes. When used as an energy harvesting system, the test rig is connected in thermosyphon setup, with distilled water as cooling agent. The complete mechanical description of the test rig is presented in Fig. 2.1, 2.2 and 2.3 and the heat exchanger is further detailed in Appendix A.

The experiments were conducted using two different TEM manufacturers. One of them (Everredtronics [47]) provides little detailed specifications about the TEMs, only the Seebeck coefficient, thermal conductivity and pellet geometry. The variation of these parameters with temperature is not available. For the selected model (127 thermocouples – TEG127-40A) the Seebeck coefficient value found on the manufacturers website is S = 0.04236 V/K. The Everredtronics module works as a TEG.

The other manufacturer, Melcor, provides very detailed specifications for its products. For the selected modules: CP1.4-127-06L-RTV the datasheet [48] gives the variation law for the Seebeck coefficient, thermal conductivity and electrical resistivity. However, the Melcor TEM is designed to be used as a heat pump or TEC.

The three measurable parameters – internal resistance, thermal conductivity and Seebeck coefficient were measured with the setup presented above and with the help of additional hardware and software presented in the following.

2.3 Internal resistance and Seebeck coefficient measurement process

The measurement setup configuration is presented in Fig. 2.4. It uses:

- Laboratory programmable power source P6100 [49];
- NI DAQ 6221 acquisition board;
- 25.5Ω resistor as load;
- Control relay;
- PC with NI LabVIEW software;

The PC controls through an application implemented in LabVIEW the DAQ board (NI 6221) and the P6100 power supply unit. The relay controlled by the DAQ board connects or disconnects the resistive load to the TEMs. The DAQ board also measures the hot and cold side temperatures and the TEMs output voltage. Active second order low pass filters and software implemented moving average filters were designed to minimize noise.

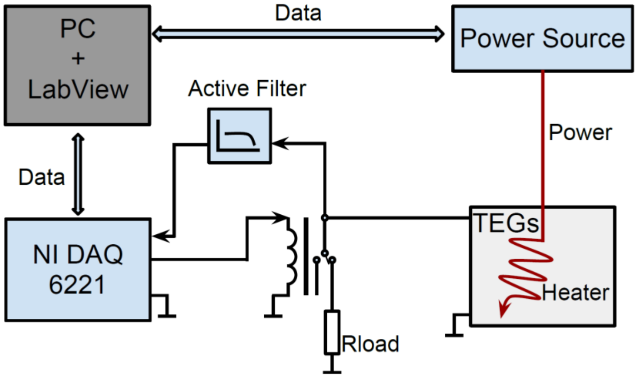

Figure 2.4 Schematic of the experimental measurement setup. Source[original]

A PC application was developed in LabVIEW for automatic measurement of the open loop voltage (without load) and load voltage with gradually increasing temperature at the hot side. Values are automatically written in a .csv file format. The logic diagram associated with the measurement application is presented in Fig. 2.5. At startup the power resistors are heated until the desired temperature of the hot side is reached; the default start temperature is 29℃. This is because at the time the measurements were made the room temperature reached 27℃. In this way, a minimum temperature gradient was necessary to achieve a measurable output from the TEMs. A settle time of 3600 seconds proved necessary for the equilibrium state to be reached for every temperature setpoint. The measurement process stops when the temperature setpoint reaches 85℃. This value was assumed to be the maximum waste heat available to be harvested.

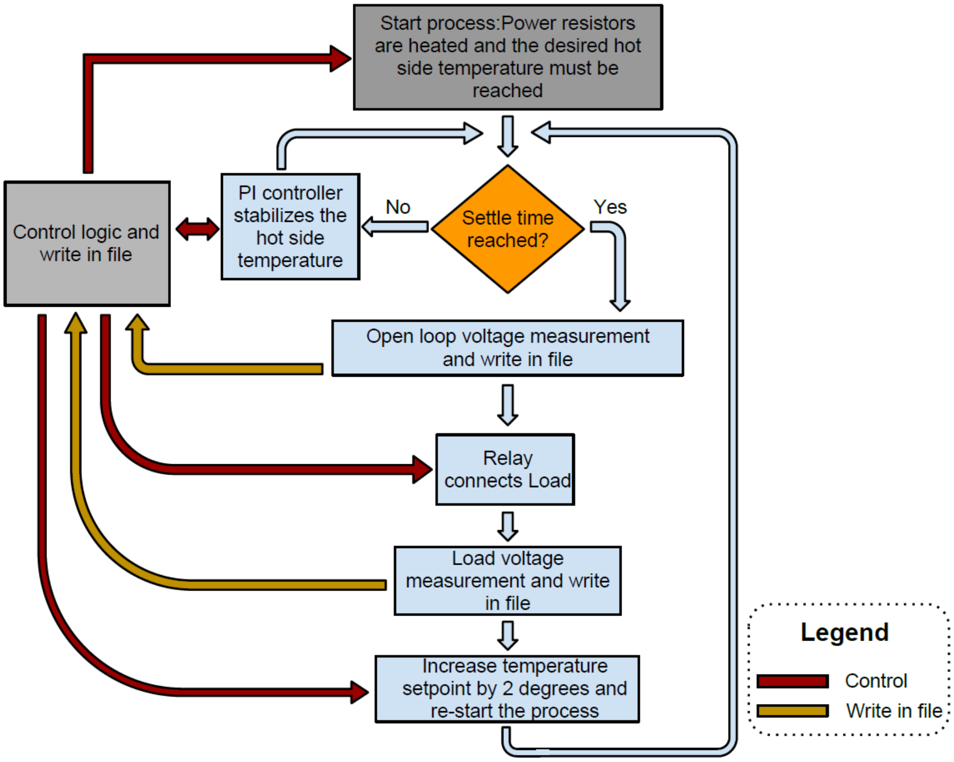

Figure 2.5 Logic diagram of the internal resistance and Seebeck coefficient measurement process. Source [original]

The Seebeck coefficient [V/K] is extracted from the open loop voltage value and the actual temperature. The output voltage under load, together with the open loop voltage is used to compute the internal resistance of the module.

Although the Thomson coefficient is not measured, its effect is indirect visible in the electrical resistance value. When the relay connects the load to the TEMs a current flow starts to pass through the load. Due to the temperature gradient on the TEMs sides, the Thomson effect appears and its presence will be reflected in the equivalent electrical resistance.

2.4 Thermal conductance measurement process

The measurement of the thermal conductance of a material can be a complicated process because the system must be brought to equilibrium and thermally isolated, so that it cannot exchange heat with the exterior. An experimental method for determining the thermal conductance is presented in [52]. Based on this, a similar approach is proposed. A thermally insulated chamber was built where the test rig from Fig. 2.1-2.3 can be inserted to create an isolated system.

The thermally insulated chamber is made of two layers of low thermal conductivity material separated by an air gap. The upper part of the box acts as a cover (Fig. 2.6).

Figure 2.6 Thermal insulated chamber (only inner layer presented) top-view with TEM test rig. Source [original]

In order to verify the thermal insulation, the chamber was tested with a thermo vision camera (FLIR ThermaCAM E2) [50]. Three different voltages were supplied consecutively, each for 30-40 min to the power resistors and the chamber was inspected with the thermal camera. The cover joining and the holes used for connecting the wires were the ones investigated as they represent the only regions where the heat can escape. For this experiment, the test rig was inserted without the plastic pipes that connects it to the heat exchanger, as in Fig. 2.6. However, when the thermal conductance measurements are performed, the plastic pipes and the heat exchanger are compulsory in order to implement the required cooling.

The results are presented in Fig. 2.7 – 2.10, at different time moments during the heating process, covering a period of 120min. In Table 2.1 the input power and the power resistors temperature are presented.

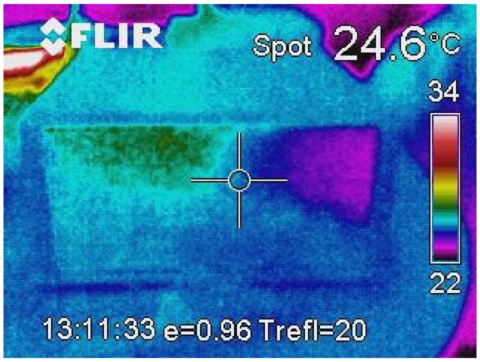

Figure 2.7 Thermo-vision of the isolated chamber for 10W heat power. [experiment]

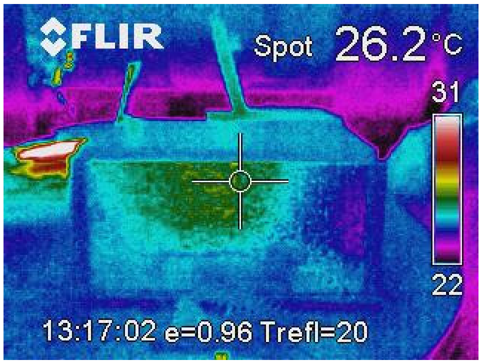

Figure 2.7b Thermo-vision of the isolated chamber for 10W heat power (2).

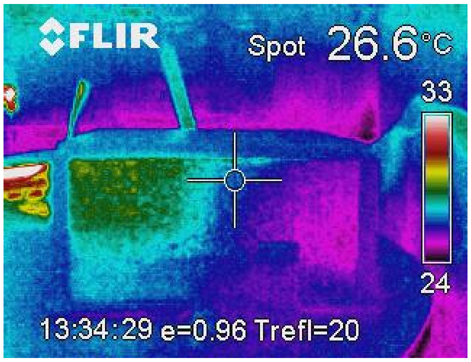

Figure 2.7c Thermo-vision of the isolated chamber for 10W heat power (3).

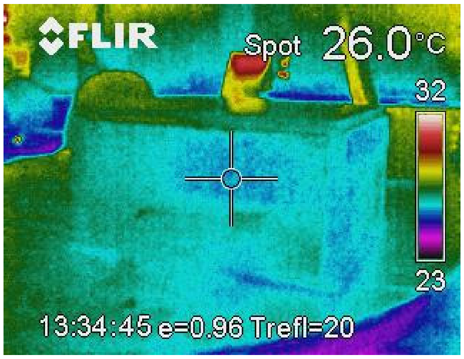

Figure 2.7d Thermo-vision of the isolated chamber for 10W heat power (4).

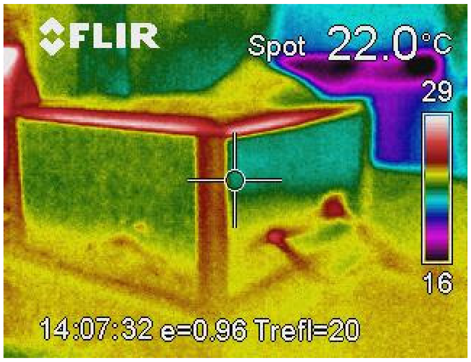

Figure 2.8 Thermo-vision of the isolated chamber for 40W heat power.

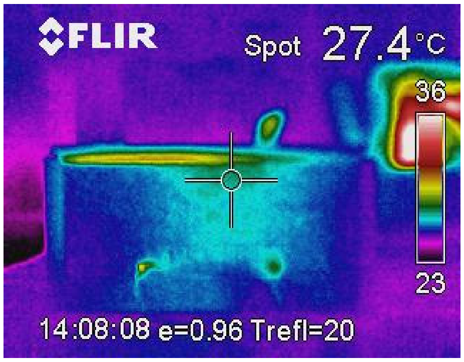

Figure 2.8b. Thermo-vision of the isolated chamber for 40W heat power (2).

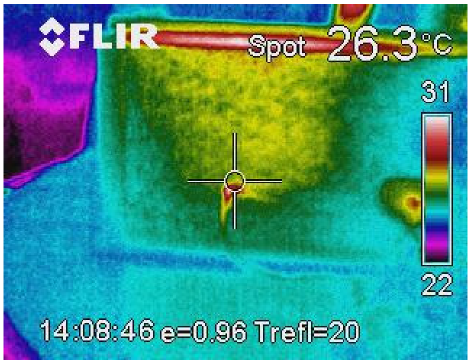

Figure 2.8c Thermo-vision of the isolated chamber for 40W heat power (3)

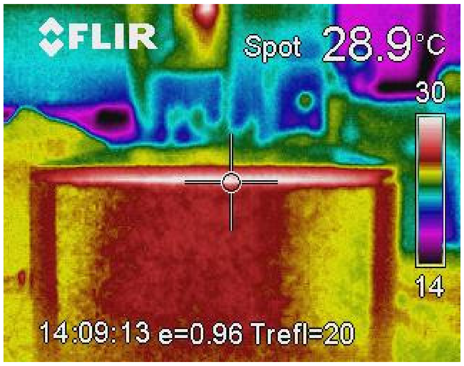

Figure 2.8d Thermo-vision of the isolated chamber for 40W heat power (4)

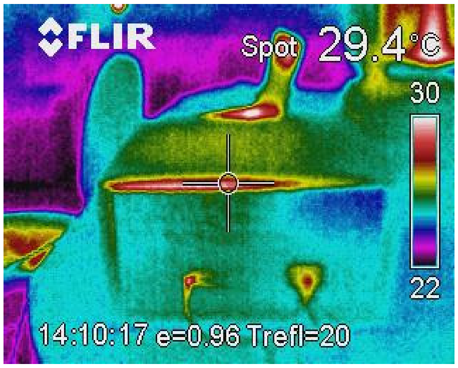

Figure 2.9 Thermo-vision of the isolated chamber for 90W heat power

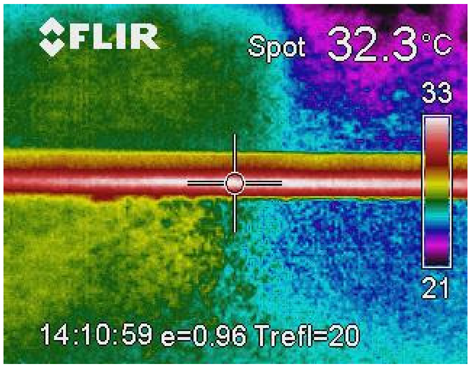

Figure 2.9b Thermo-vision of the isolated chamber for 90W heat power (2)

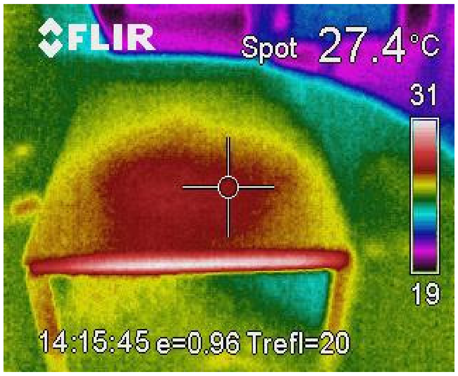

Figure 2.9c Thermo-vision of the isolated chamber for 90W heat power (3)

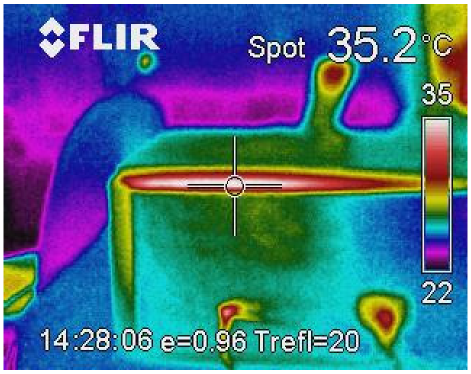

Figure 2.9d Thermo-vision of the isolated chamber for 90W heat power (4)

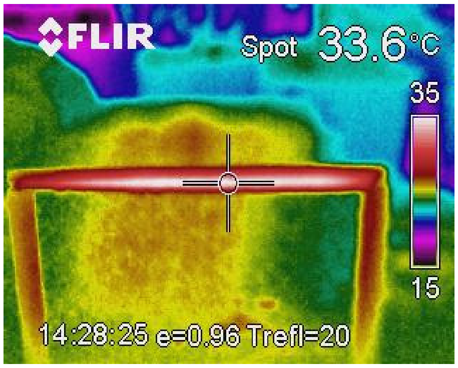

Figure 2.9e Thermo-vision of the isolated chamber for 90W heat power (5)

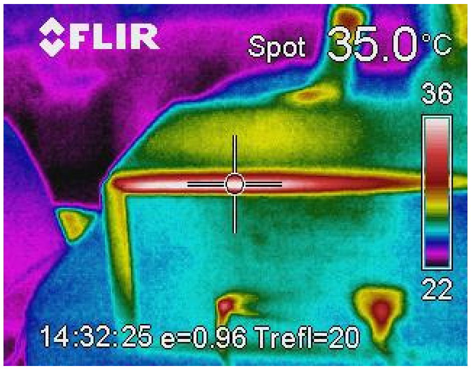

Figure 2.9f Thermo-vision of the isolated chamber for 90W heat power (6)

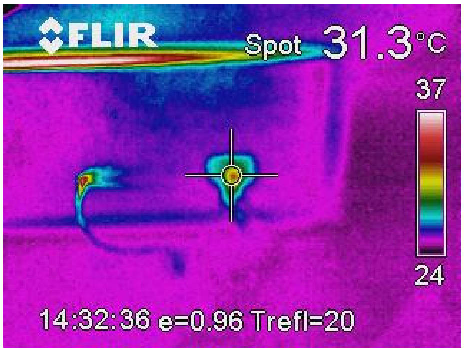

Figure 2.9g Thermo-vision of the isolated chamber for 90W input power (7)

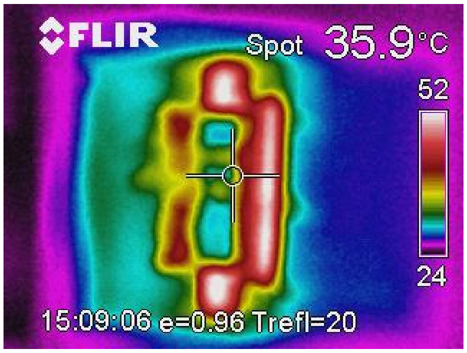

Figure 2.10 Thermo-vision of the test rig after heating and 20 minutes cool down

Table 2.1 Power resistor temperature vs. input power

Input power	**Power resistors temperature**
10W	42℃
40W	93℃
90W	160℃

One can see that when the internal resistor reaches 160℃, the chamber starts loosing heat through the cover joining. The amount of lost energy is lower than 0.05%, on a surface that represents less than 0.2% of the entire chamber's surface. Considering the scope of the test stand, the reachable temperature ranges and the secondary goal to use the system for energy harvesting applications (where such high temperatures are not common), it was concluded that the chamber fits the needs of the current work and the system can be considered thermally insulated.

In the stationary regime of temperatures the thermal conductivity of materials is determined by using the Fourier law described in Eq. 2.1 [51], according to which the thermal flux density is proportional to the temperature gradient.

$$\vec{q} = -k \cdot \nabla T \qquad (2.1)$$

where ***k*** is the thermal conductivity [W/m·K].
Equation 2.1 becomes:

$$\vec{q} = \frac{k}{\delta}(T_0 - T_1) \text{ [W/m}^2\text{]} \qquad (2.2)$$

where ***δ*** represents the width of the material, $\boldsymbol{T_0}$ the temperature at ***x=0*** and $\boldsymbol{T_1}$ the temperature at ***x=δ*** [51].
The heat flow transmitted through the whole surface of a homogenous material is:

$$\dot{Q} = kA\frac{T_0 - T_1}{\delta} \text{ [W]} \qquad (2.3)$$

where ***A*** is the section area of the material, ***δ*** its width, $\boldsymbol{T_0}$ the highest temperature of the material and $\boldsymbol{T_1}$ the temperature at the other end of the material.

The ratio between *k* and *δ* is called heat transfer coefficient (HTC) and is used when calculating the heat transfer by convection between a solid and a fluid [52].

$$\alpha = \frac{k}{\delta} \text{ [W/m}^2\text{K]} \qquad (2.4)$$

When measuring the thermal conduction the necessity is that after reaching the stationary regime, the heat flux transmitted through the material under test must be kept at a constant value; also the surface temperatures of the probe must be kept constant.

$$\dot{Q} = \alpha A(T_p - T_f) \text{ [W]} \qquad (2.5)$$

where: ***α*** is the heat transfer coefficient, ***A*** - surface area, $\boldsymbol{T_p}$ and $\boldsymbol{T_f}$ –the two sides temperatures.

The method proposed in [52] for determining the thermal conductivity of a material with a parallelepiped shape of known surface ***A*** and thickness ***δ***, crossed by a heat flow $\dot{Q}$ that resides at temperature difference of $\Delta T = T_1 - T_2$, is expressed by Eq. 2.6.

$$k = \frac{\dot{Q}\delta}{A(T_1 - T_2)} \text{ [W/m·K]} \qquad (2.6)$$

The device presented in [52] and intended to determine the thermal conductivity for plane, parallel materials consists of a thermal isolated chamber in which the probe is inserted to be measured. The test rig presented in Fig. 2.1-2.3 is based on the same principle the difference being that between the probe under test (the TEM) and the heat source exists two additional blocks – the cooper plate ***C*** and the duralumin block ***D***.

In the current work, taking into account that the ***C*** and ***D*** blocks material properties are known, their thermal conductivities will be subtracted from the measurement results, the residual value representing the probe's thermal conductivity.

The heat flow is generated by the power resistors and the thermistors placed on the heater and on the cold side of the TEMs will record the temperature. In order to improve the accuracy of the results, the thermal conductivity variation with temperature of the ***C*** and ***D*** plates is also taken into account. The cold side TEMs surface temperature can be controlled with the help of the *E* chamber (Fig. 2.1) that is connected through pipes to a cooled heat exchanger. A controllable liquid pump regulates the flow (in this case water) from the ***E*** chamber and the heat exchanger and consequently the temperature. The setup's general overview is presented in Fig. 2.11.

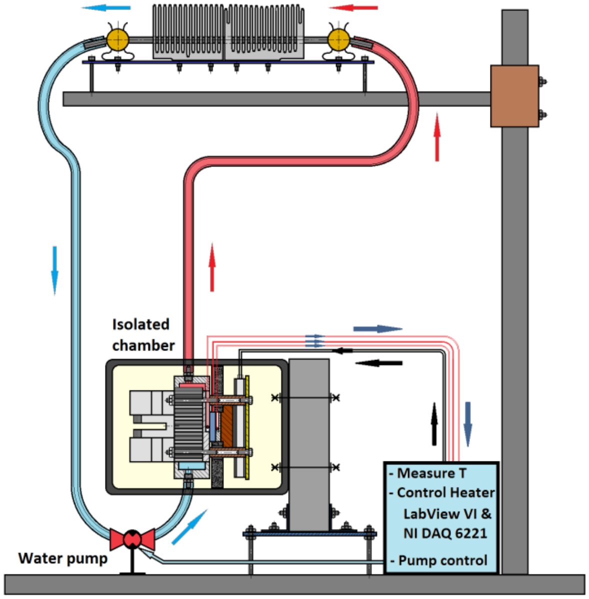

Figure 2.11 Overview of the thermal conductivity measurement setup. Source [original]

In the present work, the ensemble heater – copper plate ***C*** – duralumin block ***D*** – TEM is presented in Fig. 2.1 and detailed in Fig. 2.12 (left side) as a non-homogenous wall comprised of layers perpendicular to the heat flux. The study of the thermal heat flux passing through non-homogenous walls is made in [52]. In the following, the general equations presented in [52] were specifically written for the current case of the test rig presented in Fig. 2.1.

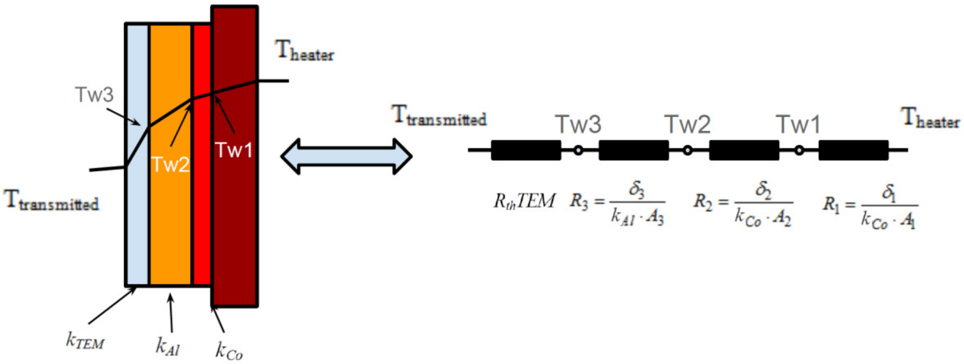

Figure 2.12 Thermal flux passing from heater to TEM. Source [original]

The thermal flux has the same value in any layer of the wall. The equivalent thermal circuit can be expressed as in Fig. 2.12 (right side) where R_1, R_2 and R_3 represent the thermal resistances of each layer. The first layer that is in contact with the heater (the copper plate ***C***) is characterized by its thermal conductivity (k_{Co}) and by its physical dimensions. Because of this reason, the ***C*** block has been split into two parts with the same conductivity, but with different dimensions (Fig. 2.12, right side).
The thermal flux density transmitted through one fluid to the other (considering the ***C, D*** and TEM ensemble from Fig. 2.1 resides in air) can be written as:

$$\vec{q} = \frac{T_{heater} - T_{transmitted}}{\frac{1}{\alpha_h} + \frac{\delta_1}{k_{Co}} + \frac{\delta_2}{k_{Co}} + \frac{\delta_3}{k_{Al}} + \frac{\delta_{TEM}}{k_{TEM}} + \frac{1}{\alpha_t}} \tag{2.7}$$

where $\boldsymbol{\alpha_h}$ and $\boldsymbol{\alpha_t}$ represent the heat transfer coefficients on the heater and transmitted side, respectively and $\boldsymbol{\delta_1}$, $\boldsymbol{\delta_2}$, $\boldsymbol{\delta_3}$ the thicknesses of each layer. In the current case, the ensemble is "sandwiched" between the heater and the ***E*** cooling block which gives an equation similar to Eq. 2.7 but without the heat transfer coefficients on the heater and transmitted sides.

The thermal conductance and resistance of a material represent the specific thermal conductivity and resistivity of that material.

From Eq. 2.6 and 2.7, the thermal resistance of the TEM can be written as:

$$R_{thTEM} = \frac{T_h - T_t}{\dot{Q}} - R_1 - R_2 - R_3 \ \text{[K/W]} \tag{2.8}$$

The heat flux $\dot{Q}$ from the heater is considered to be entirely transmitted to the ***C*** copper plate and it is continuously measured ($P=V \cdot I$ [W]) to reduce the errors caused by resistance variations with temperature.

The measurement process is started from the highest temperature difference (ΔT). In this way the hot side plates ***C*** and ***D*** stores the thermal energy. The voltage is lowered and the fluid pump is controlled to stabilize the hot side's temperature for a period long enough to consider the process in a steady state. The temperatures and input power are measured and the thermal conductance is computed taking into consideration equation 2.8. In order to improve the measurement process, the thermal conductivity (***k***) variation with temperature was taken into account in the computation process and the correct value was determined based on an a priori built lookup table. The voltage is decremented and the process of thermal stabilization starts again (Fig. 2.13). The value of 4V for the voltage value to be decremented was chosen experimentally, as it proved to generate a 16% decreasing value of the temperature difference (ΔT) and thermal flux, respectively. This decreasing rate was considered satisfactory in plotting the variation of the thermal conductance versus temperature. The temperature and pump flow regulation processes are implemented by the help of PI regulators where the required tuning parameters were experimentally determined. The electronics for the liquid pump that is driven by a DC motor is built around the L6203 integrated circuit and the control algorithm is implemented in LabVIEW and the interface with the real world is performed with the NI DAQ 6221 board. For this measurement, the heat exchanger presented in Fig. 2.11 and in Appendix A was additionally cooled by the help of DC fans.

In order to achieve higher resolutions and determine the thermal conductance variation with respect to a higher temperature, an improved cooling solution should be used (e.g. a vapor compression cycle system). In the current work, because of the low temperature ranges where the TEMs are expected to operate (<90℃), the proposed setup provided satisfactory results.

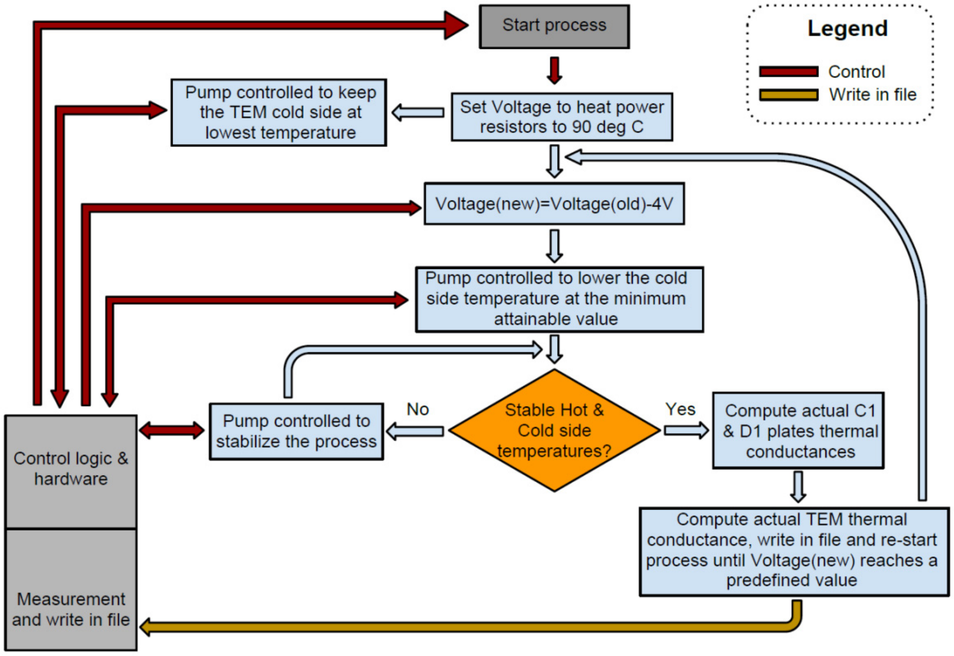

Figure 2.13 Logic diagram explaining the thermal conductance measurement as a function of temperature difference ΔT. Source [original]

2.5 Parasitic elements measurement process

Due to the fact that in bulk devices the semiconductor pellets of a TEM are connected with electrically conducting metal straps and taking into consideration the difference between the *p* and *n* type semiconductor materials, parasitic components appear like in any semiconductor based device.

In the current topic, the author introduces a method for determining the parasitic inductance and capacitance and then a SPICE model of a TEM that employs these elements. The parasitic components values can represent an indicator of the manufacturing process and materials used, a method for comparing similar or different products and present importance in the dynamic functioning regime.

The heat and electrical flow in a TEM can be represented as in Fig. 2.14 with the associated equivalent resistance network as in Fig. 2.15. ***A*** and ***B*** points represent the terminals of the TEM that can have *N* thermocouples.

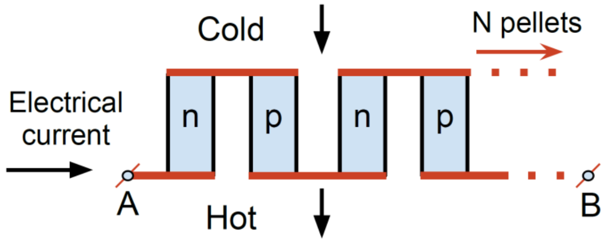

Figure 2.14 Heat passing through a bulk semiconductor thermoelectric device. Source [original]

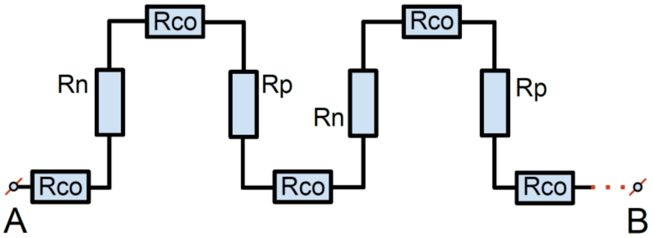

Figure 2.15 TEM's internal resistances of the semiconductor pellets and metal interconnections. Source [Reproduced as in 32]

As also presented in [32], the electrical resistance of the N and P type legs is represented through R_n and R_p while R_{co} represents the metal interconnection resistance between the semiconductors. In practice, similar dopped alloys, similar geometries of the pellets and similar material constants are adopted to make the *p* and *n* type semiconductor legs, as stated in [9, 32]. In this case, $R_p = R_n$.

Equation 2.9 represents the TEMs equivalent resistance as the sum of the conducting strips resistance and the P and N type legs resistances.

$$R_m = (R_n + R_p) \cdot N + (2 \cdot N + 1) \cdot R_{co} \tag{2.9}$$

where *N* is the number of thermocouples.

The author proposes in Fig. 2.16 the equivalent electrical network that takes into account the presence of parasitic inductances and capacitances. The parasitic inductance L_p appears due to the geometry of the pellet and at the soldering points between the semiconductor and the metallic strap. The parasitic capacitance C_p appears in parallel with the metallic strap and across the pellets as it does in any semiconductor based device.

Finally, the overall equivalent circuit proposed by the author for a bulk thermoelectric module device is represented in Fig. 2.17, where R_m, L_{peq} and C_{peq} represent the overall equivalent elements. Because of the Seebeck effect that appears only under a temperature gradient, the equivalent circuit also has an intrinsic power source, in series with the internal resistance and dependent on the Seebeck coefficient and the temperature difference.

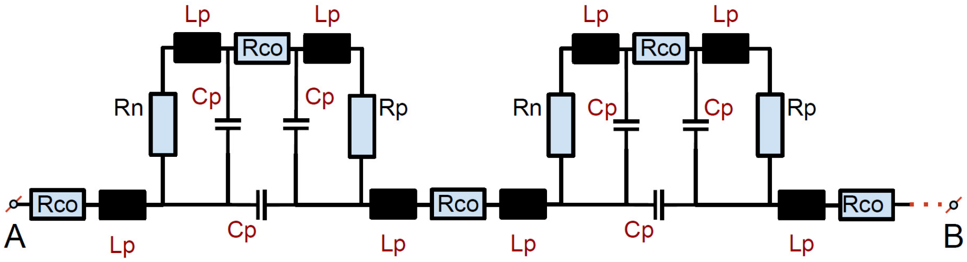

Figure 2.16 Schematic of the electrical network containing parasitic components. Source [original]

Equation (2.10) offers the generated voltage through the Seebeck effect:

$$V_g = S \cdot (T_H - T_C) \tag{2.10}$$

where: ***S*** represents the Seebeck coefficient in [V/K], $\boldsymbol{T_H}$ and $\boldsymbol{T_C}$ the hot side and cold side temperatures respectively. However, if the two sides of the TEM are kept at the same temperature difference, the Seebeck generator will give no output voltage.

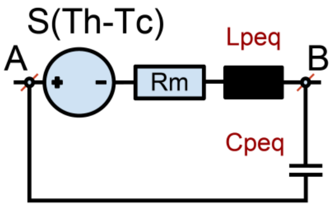

Figure 2.17 Equivalent electrical circuit of an internal TEM. Source [original]

The circuit presented in Fig. 2.17 refers only to the electrical part of a TEM, because only the electrical parasitic components are investigated in the current topic. The thermal part, dependent on the TEM's sides temperature difference is not represented, as further explained. The proposed method for measuring the internal parasitic $\boldsymbol{L_{peq}}$ and $\boldsymbol{C_{peq}}$ involves keeping the device's sides at the same temperature. The reason is that the measurement is based on the experimental measured internal resistance at room temperature. If the device faces would have a temperature gradient, then also the internal resistance would have a different value than the standard room temperature one and the internal parasitic components computation would give erroneous results.

Several ways exist in order to determine the resistance, inductance and capacitance in a standard RLC circuit. One can easily use an LCR meter that automatically displays these values.

A second solution would require measuring the phase shift between the voltage and current fed to the DUT (device under test) and depending on the internal equivalent circuit to compute the values for resistance, inductance and capacitance.
In the following, both methods are presented.

A. LCR/ESR Meter method

In the tests, the BK Precision 889B Bench LCR/ESR Meter is used [53]. Supposing the dominant component of the TEM is the internal resistance, this method tries to determine if the TEM behaves like a real resistance. The method provided no results; the L and C values could not be computed by the LCR meter.

B. The phase measurement method

For this method, the Tektronix DPO4104B Digital Phosphor Oscilloscope [54] was used together with:

1) *TPP1000 voltage probe.*
2) *TCP0030 current clamp probe with 1mA resolution.*
3) *An electronic power amplifier*

This method is based on measuring the voltage-current phase shift when a high power sine wave is fed to the TEM. This is performed with the help of the oscilloscope with a voltage probe and a current clamp probe. Because of the low internal resistance of the TEM (range of ohms) and the fact that the signal generator exhibits relative high output impedance (50Ω), a power amplifier is also needed.

The amplifier must have small crossover distortions (that would make the phase angle measurement difficult). The output signal must have 0V DC bias component in order to avoid the TEM having a DC voltage applied to it (that would make it function as a heat pump or TEC). As already explained above, this would increase the internal resistance of the TEM which would generate an erroneous result for the parasitic $\boldsymbol{L_{peq}}$ and $\boldsymbol{C_{peq}}$ computation.

Because in a TEM, four concurrent physical phenomena take place of which three are dependent on the module's sides temperature (Thomson, Seebeck, Fourier), it is necessary to measure the parasitic electrical components by first involving as few phenomena as possible. Afterwards, after drawing the conclusions involving the obtained values, a more in depth analysis, temperature dependent can be driven. In the current work, the parasitic components were determined only in conditions of no temperature gradient on the TEMs sides. The temperature dependent parasitic components could not be investigated with the available instruments.

A high current sine wave generator is needed for amplifying the output of a signal generator that will ultimately be fed to the TEM. The author concluded that a maximum frequency of 200 kHz is enough to determine the parasitic components. At the frequency of 200 kHz, a purely resistive load of the same value as a TEM (1-3Ω) would have a very small phase shift (<5°) which in turn means a very small parasitic inductance (< 150nH). The author considered that a similar result for a TEM would lead to the assumption that the internal parasitic components are too small to be taken into account or measured with the proposed method.

First, a standard AB class amplifier with operational amplifier was tested. This should be able to provide at least 1.5W as the internal resistance of a TEM is in the range of ohms.

The topology is represented in Fig. 2.18. A TI TL072 was used because of the high slew rate of 13V/µs and 3MHz unity gain bandwidth.

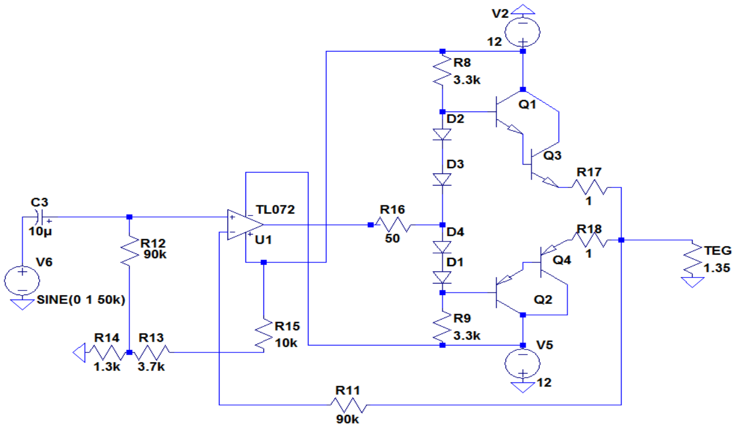

Figure 2.18 AB class power amplifier. Source [classical topology]

The amplifier reproduced correctly the sine waveform from the input up to 100 kHz but starting from 150 kHz, with the TEM as load, distortions appeared in the output. This made the phase angle calculation difficult, also leading to errors.

An improved solution based on MOSFET power transistors is presented in Fig. 2.19. The circuit is inspired from Elektor [55] where the idea is to connect the MOSFET transistors in complementary drain follower [55].

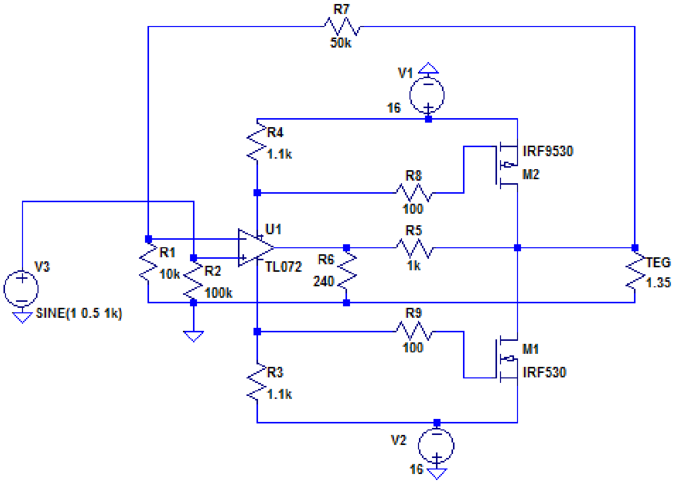

Figure 2.19 MOSFET power amplifier. Source [55]

The output current generated by the MOSFET transistors is limited by the level of the supply voltage and the saturation voltage of M_1 and M_2. Resistors R_5 and R_6 provide feedback for the transistors and the operational amplifier. The closed loop amplification is $1+R_7/R_1$. In the current setup, the amplification is set to 6.

The original schematic employs two extra bipolar transistors in current source configuration to set the quiescent current of M_1 and M_2 at 50mA. This arrangement was not used in the modified circuit from Fig. 2.19 in order to simplify the schematic as much as possible. Different values than the one from the original setup must be chosen for resistors R_3 and R_4 in order to make the circuit working. The values decide the voltages drop across the resistors R_3 and R_4 that are needed to open M_1 and M_2.

The experimental circuit, the voltage probe, current clamp probe and TEM are presented in Fig. 2.20.

To be sure that the power amplifier will not affect the TEM under test and that the voltage-current phase angle is correctly measured, the power amplifier was first tested with a carbon resistive load within the same range value with the TEM (2 Ω). At the maximum frequency of 200 kHz, the phase measurement was 7°. This leads to a value of approximately 180nH for the internal parasitic inductor. The measurements made with the LCR meter on the same 2Ω resistor gave a value of 120nH for the parasitic inductor.

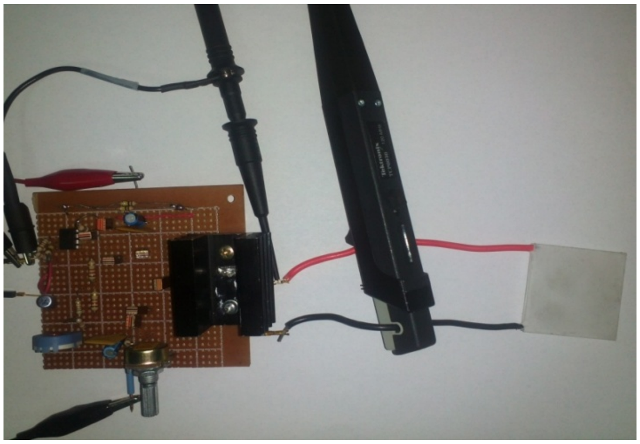

Figure 2.20 MOSFET power amplifier with current, voltage probe and TEM. Source [original]

Because of the two different results obtained through different methods, a third solution was also investigated and a high performance 650W power amplifier EV Q44 [56] was used. The phase offset result, when using a carbon resistive load of 2 Ω is presented in Fig. 2.21. The measured value gave the same result to the one when using the LCR meter, the phase measurement method being validated in this way with the EV Q44 amplifier. This led to the conclusion that the proposed amplifier circuit (Fig. 2.19) may need improvements because other error sources exist, although these were not visibly reflected in the shape of the output wave.

The test conducted with the custom built MOSFET amplifier and the TEMs as load showed that the results matched the ones with the EV Q44 amplifier in 70% of cases. In conclusion, the final experimental data was obtained when using the EV Q44 power amplifier.

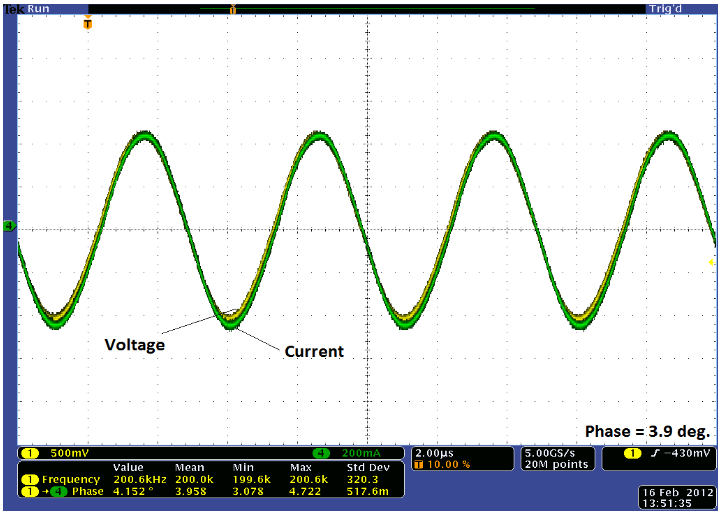

	Value	Mean	Min	Max	Std Dev
1 Frequency	200.6kHz	200.0k	199.6k	200.6k	320.3
1 → 4 Phase	4.152 °	3.958	3.078	4.722	517.6m

Figure 2.21 Phase angle measurement using the EV Q44 power amplifier. Source [experiment]

During the experiments where an AC signal was fed to the TEM, it was observed that the module's hot and cold side temperatures were able to follow the applied voltage up to approximately 1Hz, each side either absorbing or releasing heat during one period of the applied signal. While the frequency was increased, the amplitude of the temperature variation decreased, due to the internal heat capacity of module that will be calculated in Chapter 3. At higher frequencies, the module's sides will not be able to alternatively absorb and release heat during one period, but only release heat through the Joule effect.

Referring to Eq. 1.6-1.9, when an AC signal is applied to the TEM, the equations can be rewritten by replacing the current with $I_m \sin\omega t$.

$$\dot{Q}_a = ST_C\left(I_m \sin\omega t\right) - \frac{1}{2}\left(I_m \sin\omega t\right)^2 R_m - k_S(T_H - T_C) \tag{2.10}$$

$$\dot{Q}_e = ST_H\left(I_m \sin\omega t\right) + \frac{1}{2}\left(I_m \sin\omega t\right)^2 R_m - k_S(T_H - T_C) \tag{2.11}$$

Integrating the power on the absorbing and emitting side for the first half period, one obtains:

$$\int_0^{T/2} \dot{Q}_a dt = ST_C \int_0^{T/2} \left(I \sin\omega t\right) dt - \frac{1}{2}\int_0^{T/2} \left(I_m \sin\omega t\right)^2 R_m dt - \int_0^{T/2} k_S(T_H - T_C) dt = $$

$$= 2ST_C I_m - \frac{T}{8} I_m^2 R_m \tag{2.12}$$

$$\int_0^{T/2} \dot{Q}_e dt = ST_H \int_0^{T/2} \left(I_m \sin\omega t\right) dt + \frac{1}{2}\int_0^{T/2} \left(I_m \sin\omega t\right)^2 R_m dt - \int_0^{T/2} k_S(T_H - T_C) dt = $$

$$= 2ST_H I_m + \frac{T}{8} I_m^2 R_m \tag{2.13}$$

Integrating for the second half period, one obtains:

$$\int_{T/2}^{T} \dot{Q}_a dt = ST_C \int_{T/2}^{T} \left(I_m \sin\omega t\right) dt - \frac{1}{2}\int_{T/2}^{T} \left(I_m \sin\omega t\right)^2 R_m dt - \int_{T/2}^{T} k_S (T_H - T_C) dt =$$

$$= -2ST_C I_m - \frac{T}{8} I_m^2 R_m \tag{2.14}$$

$$\int_{T/2}^{T} \dot{Q}_e dt = ST_H \int_{T/2}^{T} \left(I_m \sin\omega t\right) dt + \frac{1}{2}\int_{T/2}^{T} \left(I_m \sin\omega t\right)^2 R_m dt - \int_{T/2}^{T} k_S (T_H - T_C) dt =$$

$$= -2ST_H I_m + \frac{T}{8} I_m^2 R_m \tag{2.15}$$

By writing the power integral over each half period, one obtains:

$$\int_{0}^{T/2} Pdt = 2S\left(T_H - T_C\right) I_m + \frac{T}{4} I_m^2 R_m \tag{2.16}$$

$$\int_{T/2}^{T} Pdt = -2S\left(T_H - T_C\right) I_m + \frac{T}{4} I_m^2 R_m \tag{2.17}$$

It can be observed that the energy over one period is:

$$\int_{0}^{T/2} Pdt + \int_{T/2}^{T} Pdt = \frac{T}{2} I_m^2 R_m \tag{2.18}$$

where $\boldsymbol{I_m}$ represents the peak current and $\boldsymbol{T}$ represents the period over which we integrate. When a DC current is applied to the TEM, the energy over one period equals:

$$\int_{0}^{T} Pdt = S\left(T_H - T_C\right) I \cdot T + T \cdot I^2 R_m \tag{2.19}$$

This demonstrates that when looking at the behavior over one period, the module behaves like a resistor when an AC signal is applied to its input; the total energy dissipates through Joule effect. If the frequency is small enough (<1Hz in the experiments), each side of the module will be able to “follow” the applied voltage, and each side will alternatively absorb and release heat. When the frequency increases, due to the internal heat capacity, the module will only release heat through the Joule effect. The calculation of the internal heat capacity and the experimental results that demonstrates this behavior is presented in Chapters III and IV.

2.6 Conclusions

In order to implement a SPICE TEM model that takes into account all the parameters variation with temperature, the parameters had to be measured with the help of a test rig that was designed and built for the current work. The test rig presented in Fig. 2.1 is an improved version of a first setup presented in [Appendix B] that was used as a guide for developing the current setup. All the building blocks were explained in details and a special care was taken to select the materials with high and low thermal conductivity as required and design the mechanical parts to optimize the heat transfer. The thermosyphon has been manufactured for this purpose while the heat pipe is designed for cooling a Technics audio amplifier and was recovered from such a device.

The author found necessary to implement autonomous measurement systems, either due to the long time processes involving the achievement of temperature steady states or because the measurement processes required closed loop feedback control.

The author made a study of the thermodynamic heat transfer process and starting from a method and setup described in [52] designed a similar device for measuring the thermal conductance adapted to the current setup.

2.7 Contributions:

1. **Design and development of a modular test rig** used for parameters extraction and also for the energy harvesting system (thermal to electrical conversion and cooling).
2. **Proposal of two cooling solutions**, one using a thermosyphon and the other a heat pipe.
3. **Designing and building of a two layer thermally isolated chamber** to be used in the thermal conductance measurement process.
    - Thermo-vision analysis of the built isolated chamber for heat leakage, used for validation of the enclosure isolation ability.
4. **Designing and development of an autonomous measurement application for measuring the internal resistance and Seebeck coefficient of a TEM,** employing PI feedback loop and serial power source control.
5. **Designing and development of an automatic measurement application for measuring the thermal conductance of a TEM** employing two PI control loops, serial power source control and DC H bridge motor control using the NI DAQ 6221, one PWM output and the onboard FPGA for signal routing in order to change the pump's flow direction. The PI controllers were used for water pump flow control and temperature setpoint regulation and the tuning parameters have been experimentally determined.
    - Implementation of an H bridge motor controller**.**
    - Implementation of second order active filters for measured signals noise reduction and additional software moving average filters.
    - LabVIEW software implementations of the measurement and control applications using the NI DAQ 6221 board.
    - LabVIEW VI implementation for the P6100 power source serial communication**.**
6. **Proposal and implementation of a phase offset measurement method for determining the parasitic inductance and capacitance that appear inside a TEM**.
7. **Proposal of an equivalent SPICE electrical model employing the internal parasitic components of a TEM.**
    - Integration of the thermodynamic governing equations in order to highlight the TEM's resistor-like behavior, when high frequency AC signals (50-200 kHz) are fed to its input.

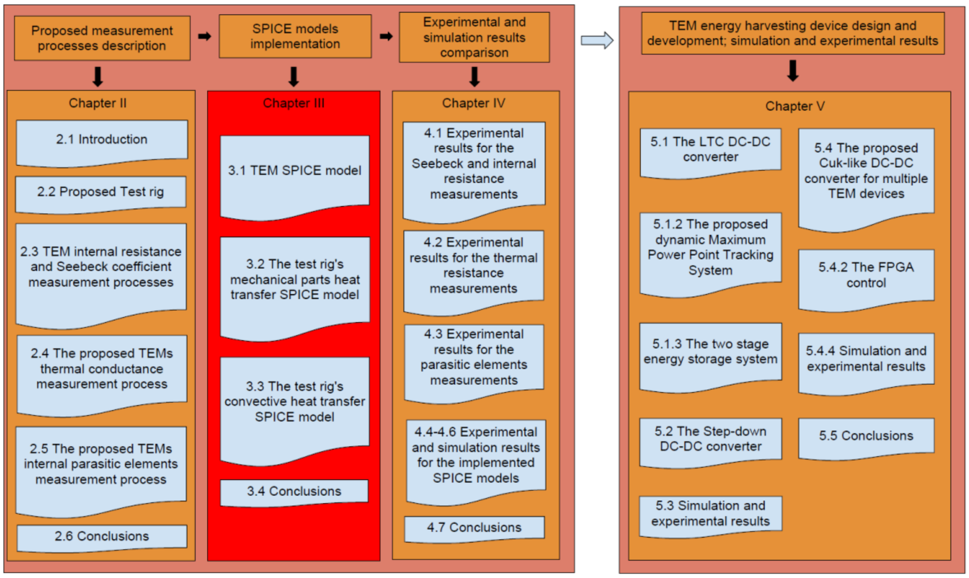

Chapter 3

TEM and Test Rig SPICE Thermoelectrical Modelling

In this chapter, the SPICE models for the TEG and the mechanical test rig are being developed. For the TEG model, the parameters variation with temperature is taken into account. The convective heat transfer that appears when the TEGs test rig functions in natural environment is implemented in SPICE using the thermodynamics similitude criteria.

3.1 TEM SPICE Model

The study of Lineykin et al. [37] presents a SPICE model for a TEM starting from Eq. 1.6 – 1.9. Considering the heat transfer through the TEM in one dimension the equivalency of thermal to electrical components is made.

The thermal resistance is expressed as an electrical resistance, the temperature as a voltage and the electrical current represents the heat flow. The thermal analogy between the thermal field and the electrical field is explained in [52] and presented in [Appendix C].

The physical analogy between the electrical and thermal components is used by Lineykin [37] to build the TEM model. Writing Eq. 1.6, 1.7 and 1.9 for a TEC and substituting in Eq. 1.8 one obtains the circuit as presented in Fig. 3.1.

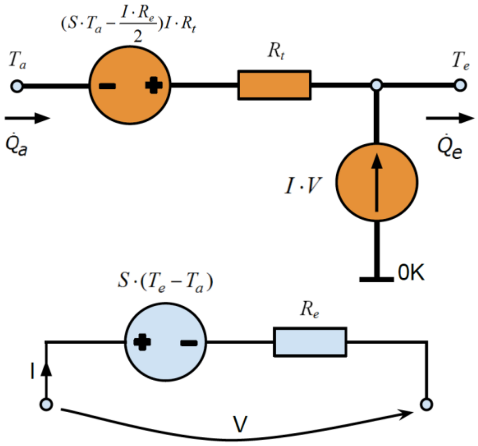

Figure 3.1 TEM SPICE model. Source [reproduced]

R_t represents the thermal resistance of the TEM, $\dot{Q}_a$ and $\dot{Q}_e$ refers to the absorbed and emitted heat flows. The upper circuit elements from Fig. 3.1 represent the thermal part of the module. On the lower side are the voltage generator and the internal resistance. The link between the two parts is made by the ***I*** current. This circuit does not take into account the Thomson effect that is considered small, the heat capacity of the TEM element and the fact that all the internal parameters (***S***, ***R_t*** and ***R_e***) vary with temperature. In the model proposed by Lineykin the internal parameters are taken from the datasheet of the product. However, the experiments conducted with the Everredtronics product proved that the datasheet parameters vary from the real values.

In the present work, the model presented by Lineykin [37] was reproduced in the Linear Technology LTspice simulator [57]. The TEM's electrical resistance, Seebeck coefficient and thermal conductance were first implemented as constant, like in Fig. 3.1 and the results were similar to the one presented in [37].

When taking into account the variation with temperature, the ***S***, ***R_t*** and ***R_e*** parameters are implemented by using arbitrary behavioral voltage sources (ABVS). The experimentally determined values (presented in Chapter 4) will be implemented in ABVS as functions dependent on temperature (voltage). The use of interpolation functions has the benefit that simulations can also be done based on the extrapolated data offered by the fitting functions. However, high order interpolation functions can slow the simulation time and even create convergence problems. In this way, a lookup table can be used with the restriction that the simulations can only be performed up to the maximum values determined in the experiment.

Chakib et al [39] present an improved TEM model that takes into account the heat capacity of the ceramic plates and pellets of the TEMs. However, the research gives no details about the numerical values or how the heat capacity was obtained.

The current work presents a method for obtaining the TEMs heat capacity using the experimental results presented in [60]. One way of obtaining the heat capacity of a material is by knowing its mass, molar heat capacity and molar mass of the constructing elements (ceramics and semiconductor pellets in the current case).
The mass of the tested modules (Everredtronics and Melcor) was measured with an electronic balance. Both manufacturers specify that the material used in the semiconductor pellets is Bi_2Te_3, a usual material for this kind of devices.

The specific heat capacity of a material can be calculated using $c_p = \frac{C_{mol}}{M}$ [J/KgK], where $\boldsymbol{C_{mol}}$ is the molar heat capacity [J/molK] and $\boldsymbol{M}$ is the molar mass [g/mol]. The molar heat capacity for the thermoelectric material Bi_2Te_3 has been studied in [60] and the results showed a value of 126.19 [J/molK] at 298.15 K. The molar mass of Bi_2Te_3 has been taken from [61], [62].

The approximate value for the TEM's heat capacity is computed using the molar heat capacity of the Bi_2Te_3 material, the geometry of the ceramic plates and the total mass of the TEM module using Eq. 3.1 and 3.2, as presented in Fig. 3.2.

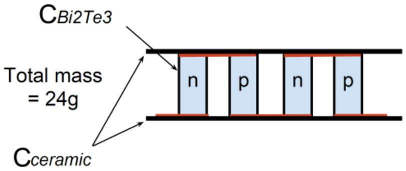

Figure 3.2 TEMs heat capacity computation method. Source [original]

$$C_{Bi_2Te_3} = \frac{C_{mol}}{molarMass} \cdot m_{Bi_2Te_3} = \frac{126.6}{800} \cdot 17 \text{ [J/K]} \tag{3.1}$$

$$C_{ceramic} = \rho \cdot c_p \cdot V_{total} = \\ = 2300 \cdot 800 \cdot (0.04 \cdot 0.04 \cdot 0.002) \text{ [J/K]} \tag{3.2}$$

The semiconductor's mass - $m_{Bi_2Te_3}$ was determined by subtracting the ceramic layer's mass ($m_{ceramic} = \rho \cdot V_{total}$) from the total mass of 24 grams.

The total computed heat capacity of the Everredtronics module is ≅ 10 J/K. The ceramic plate's density value was taken from [63].

The computed heat capacity of the TEM must be equally distributed along the TEM's sides in order to correctly model the device. The internal heat capacity has been distributed into two equal parts that appear at the hot and cold sides of the module (Fig. 3.3). The distributed parameters method is also presented in [39], [42] and [58] where the distributed internal thermal resistance is implemented.

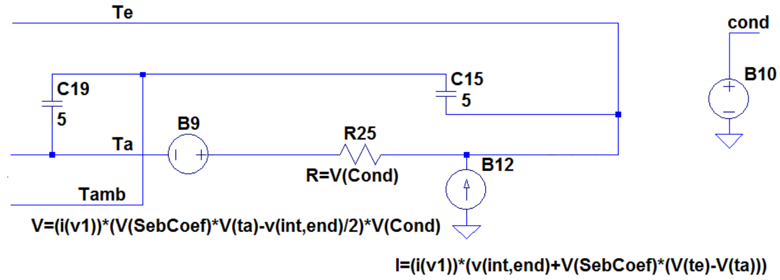

Figure 3.3 SPICE implementation of the TEM’s thermal part using ABVS. Source [original]

Each part of the circuit from Fig. 3.3 is explained in Table 3.1.

Table 3.1 Thermal part circuit components and their designation

Circuit component	Designation
T_e	Hot side temperature.
T_a	Cold side temperature.
C_{19}, C_{15}	Distributed thermal capacitance of the module.
B_{12}	Implementation of the $I \cdot (I \cdot R + I \cdot S \cdot (T_H - T_C))$ [W] that represents the connection between the thermal and electrical parts.
B_9	Implementation of the $I \cdot (S \cdot T_C - I \cdot \frac{R_{electric}}{2}) \cdot R_{thermal}$ [K] from Eq. 1.6-1.9.
R_{25}	Thermal resistance of the module.
B_{10}	Implementation of the variable thermal resistance function of temperature with the help of an ABVS voltage. Current value is $((-0.01151) \cdot \ln(0.008 + V_{(te)} - V_{(ta)}) + 0.45)$ - experimentally determined.
T_{amb}	Ambient temperature [K] expressed as a voltage source of 300V.
$V_{(int,end)}$	Represents the voltage across the electrical resistance of the TEM.

The model presented in Fig. 3.3 employs only the heat capacity as distributed parameter. The simulations conducted in the current work showed no difference in the TEM’s behavior compared to the situation when the internal thermal resistance was modelled as a distributed parameter. However, the model is presented in Figure 3.4 because it was used in simulations as an alternative to the equivalent circuit from Fig. 3.3. This alternative was adopted because if proved to solve different convergence problems that appeared in various simulations with a large number of voltage dependent sources. The nodes ***Sebcoef***, ***int*** and ***end*** are presented in Fig. 3.5.

The distributed current source thermal model also allows the correct implementation of the distributed thermal capacity that appears in a TEM that was computed in Eq. 3.2. The thermal capacity must be equally distributed on each side of the TEM because it appears mainly due to the ceramic plates.

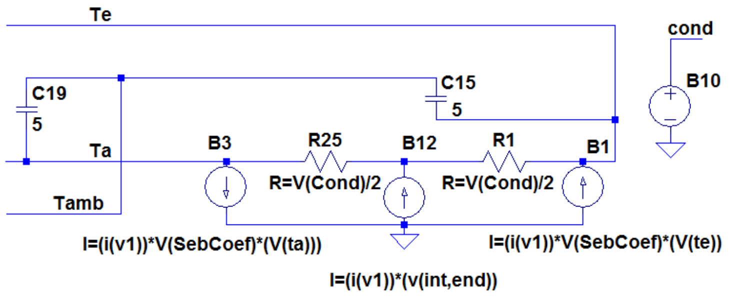

Figure 3.4 TEM equivalent circuit represented with current sources and distributed thermal resistance and heat capacity. Source [original]

The improved model presented in this topic includes also the experimental determined parasitic inductance and capacitance discussed in Chapter 2.
Figure 3.5 presents the electrical part model of the Everredtronics TEG.

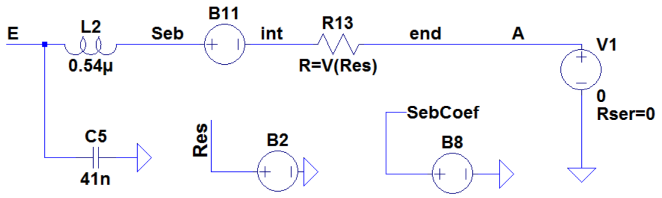

Figure 3.5 SPICE implementation of the TEG's electrical part. Source [original]

The connection between the thermal part of the TEM SPICE circuit and the electrical part is made through the current that passes through the $\boldsymbol{V_1}$ source. The ***E*** potential in the circuit from Fig. 3.5 represents the positive voltage of the TEM module if $\boldsymbol{T_a}$ is the cold temperature and $\boldsymbol{T_e}$ the hot temperature of the TEM.

Table 3.2 TEM's electrical part circuit components and their designation

Circuit component	**Designation**
L_2	Parasitic inductance.
C_5	Parasitic capacitance.
B_2	Implementation of the internal resistance function of temperature difference with an ABVS. Current value is $\left(0.015\cdot(V_{(te)}-V_{(ta)})+1.37\right)$ as experimentally determined.
B_8	Implementation of the Seebeck coefficient variation function of temperature difference with an ABVS. Current value is $\left(0.00484\cdot\ln(1+V_{(te)}-V_{(ta)})+0.040\right)$
R_{13}	Internal electrical resistance.
B_{11}	Seebeck voltage generator. Current value is $\boldsymbol{V_{(SebCoef)}}$.
V_1	Voltage source used for current reading.
E,A	Positive and negative terminals of the TEM.

3.2 Test Rig Heat Transfer SPICE Model

The mechanical parts of the test rig presented in Fig. 2.1 must also be modelled in the SPICE simulator. This is necessary in order to test the validity of the TEM model and to have a simulation model of the complete environment where the TEM will normally operate.

The experiments showed incorrect and erroneous results when considering the mechanical parts as homogenous blocks, each modelled through an equivalent thermal resistance and heat capacity. The way the Biot number indicates if it is sufficient to use the so called lumped capacitance method to represent the system is explained in [64], [65]. For the Newton's law to be applied and the region of interest to be considered a "lump" that acts like a RC circuit (thermal resistance and heat capacity), the temperature at all points inside the region of interest must be approximately the same at each time moment. The lumped RC elements are also used in modelling the power MOSFETs electro-thermal characteristics [59].

In the current work, due to the geometry of the mechanical parts, the spatial effect must be considered and a discretization must be made. This is explained in Fig. 3.6, where the mechanical setup was split into 16 smaller blocks, for which the thermal resistance and thermal capacitance were calculated.

In a real thermal conduction case and in the transient regime, the temperature of the body is continuously changing, which in turn modifies the thermo-physical properties of the material. In this way, the heat transfer coefficient and all other values considered constant (thermal diffusivity, density, specific heat, thermal conductivity, etc.) change [64]. Therefore, the analytical methods cannot be applied and a numeric computation is done in specific fluid dynamics simulators. However, for the current materials and temperatures attained in the present work, the analytical calculated thermal resistance and heat capacity that are related to the above mentioned thermo-physical material properties do not vary with more than 10%. For example, the thermal conductivity of copper varies with ~2% in the range of 0 - 100℃. The duralumin's thermal conductivity varies with ~10% for the same temperature range 0 -100℃. Although the maximum temperature attainted in the experiments is 85℃ for copper, the values recorded for duralumin are between 80℃ and 20℃ in the experiments. In this way, the material properties were considered constant in the temperature ranges that were investigated. If a higher temperature is necessary in practice, this approach will lead to erroneous results if the thermo-physical properties are considered constants. In this case, the thermal resistance and capacitance values must be temperature dependent.

The thermal resistance and heat capacity are computed using Eq. 3.3 and 3.4 [64].

$$R_{th} = \frac{1}{k \cdot \frac{A}{\delta}} \text{ [K/W]} \tag{3.3}$$

$$C_{th} = \rho \cdot c_p \cdot V \text{ [J/K]} \tag{3.4}$$

where ***k*** is the thermal conductivity, ***A*** is the area of the material and $\boldsymbol{\delta}$ its width, $\boldsymbol{\rho}$ is the material density, $\boldsymbol{c_p}$ represents the specific heat capacity and ***V*** represents the volume.

The values ***k***, ***ρ*** and $\boldsymbol{c_p}$ that characterize the material were taken from thermodynamic tables [63] and are presented in [Appendix D]. The thermodynamic tables also present the variations against temperature for all the materials used in designing the mechanical test rig.

The test rig's components from Fig. 3.6 have been separated into six main parts, representing the cooling part that is comprised of ***CB1*** (Cooling Block 1) and ***CB2***, the ***TEMs*** thermal part (***TEMs***), and the hot part consisting of ***HB1*** (Hot Block 1), ***HB2*** and ***HB3***.

The thermoelectrical SPICE model for the two TEMs and the mechanical setup proposed in Fig. 2.1 is presented in Fig. 3.7.

The simulation model for the test rig is updated with two additional elements $\boldsymbol{R_{isoH}}$ and $\boldsymbol{R_{isoC}}$ – the thermal resistances of the isolated chamber presented in Fig. 2.6. The values for the thermal resistances were computed based on the properties of the materials used and the dimensions involved. In order to test and validate the model, the test rig was inserted in the isolated chamber in order to ignore the convective heat transfer between the ambient and the mechanical system. Each part of the circuit from Fig. 3.7 is explained in Table 3.3. The six main parts depicted in Fig. 3.6 are also highlighted in the model below (Fig. 3.7).

The setup presented in Fig 3.6 is used in two experiments – in the first an external power source is connected to the TEMs, case in which they will operate like a heat pump and the second where the resistive heater is used to simulate a waste heat power source. For the first, a power source (lower right corner in Fig. 3.7) is connected to the TEMs for a determined period after which is disconnected. When the resistive heater is used, the $\boldsymbol{V_3}$ power source (Fig. 3.7) simulates the temperature values of the waste heat source and the TEMs will generate an output voltage, case in which the 8V power source (lower right corner in Fig. 3.7) is no longer needed. The simulation process and input values prescription will be further detailed in subchapters 3.3, 4.4 and 4.5. In the following, the first experimental process is further discussed.

Several simplifications had to be adopted. Because of the complex mechanical system, the ***E*** chamber had to be split into three blocks and for the inner block containing the cooling pipes an average value for the heat capacity was calculated. Here, however, error sources may appear because the block is simplified to a homogenous one while in reality it is not. The heat capacity of the ***J*** Selitherm board was not taken into account because of the isolation characteristics of the material. The heater element's complicated geometry led to the need of another simplified model where a mean heat capacity was calculated. All these simplifications will lead to some errors into the final results.

The simulation that reproduces the experiment ran for a total period of 2.4ms (equivalent to 2400s in reality as a scaling factor of 1000 was adopted), with an 8V power source connected to the TEMs (TEC connection) for a period of 1ms after which the power source was disconnected and the TEMs were acting like a TEG as in [37] and the result was compared to the experiment. In simulation, the time has been scaled down by a factor of 1000, changing seconds to milliseconds. The simulation was completed with the above described inputs only for the Melcor module. For the Everredtronics TEG, taking into account that the maximum output current the manufacturer claims (1A) and the fact that the device is optimized to work as a TEG, only 2.5V/module was fed to its input, for a period of 600s. This was done in order to prevent the device from damage.

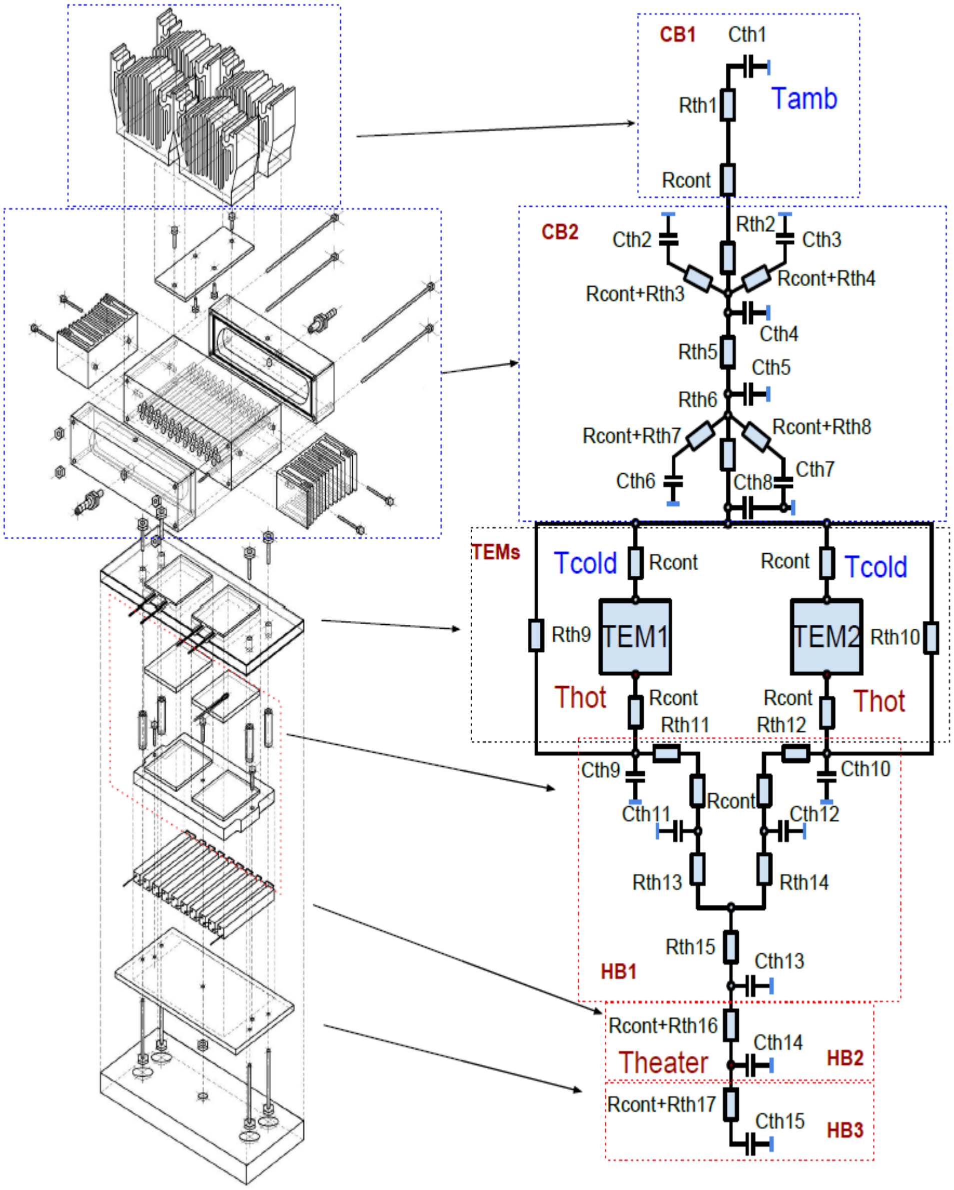

Figure 3.6 Mechanical blocks discretization using the thermal to electrical analogy. Source [original]

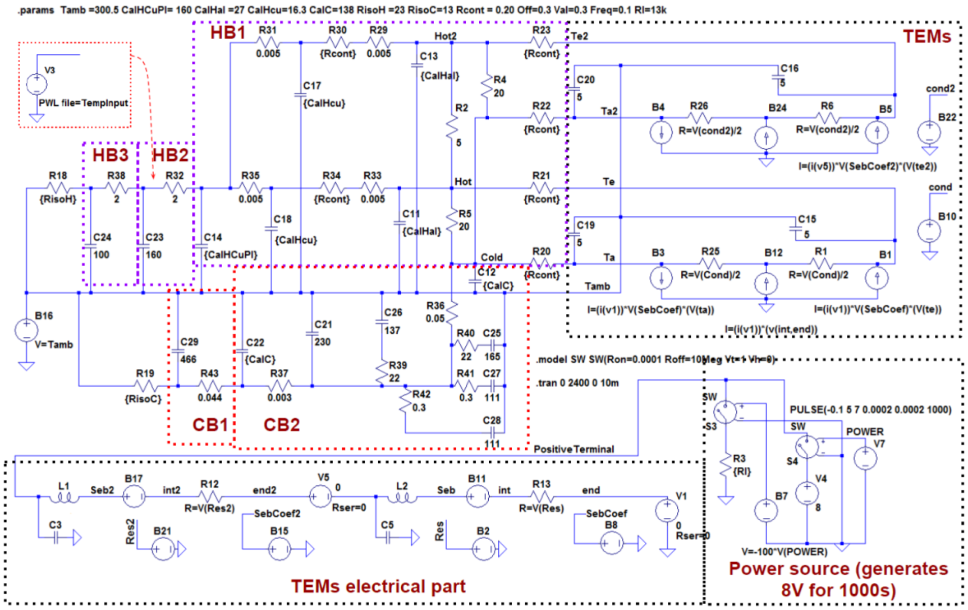

Figure 3.7 SPICE implementation of the test rig and TECs thermoelectrical model in closed chamber. Source [original]

Table 3.3 TEC's thermal part circuit components including the mechanical parts and their designation

Circuit component	**Designation**
R_{18}	Calculated thermal resistance of the isolated chamber for the hot side.
R_{19}	Calculated thermal resistance of the isolated chamber for the cold side.
R_{38}	Thermal resistance between the middle of the ***H*** resistive heater and the heater support. Current value is 2 K/W.
R_{32}	Thermal resistance between the middle of the ***H*** resistive heater and ***C*** copper plate. Current value is 2 K/W.
R_{31}, R_{35}	Internal thermal resistances of the ***C*** copper plate (seen as two parallel blocks that will each come in contact with the ***D*** blocks – Fig. 2.1). Current calculated value is 0.005 K/W.
R_{30}, R_{34}, R_{23}, R_{22}, R_{21}, R_{20}	Contact thermal resistance of the thermal grease applied between ***C*** and ***D*** blocks. Current calculated value is 0.2 K/W.
R_{29}, R_{33}	Internal thermal resistances of each ***D*** duralumin block. Current calculated value is 0.005 K/W.
R_{28}, R_{27}, R_{26}, R_{25}	Distributed thermal resistance of the TEM (two for each module). Current value is $\left(1/((-0.00067)\cdot(V_{(te)}-V_{(ta)})+0.35)\right)$.

R_2	Thermal resistance between the two TEMs, generated by the ***J*** Selitherm isolation board. Current value is 25 K/W.
R_4, R_5	Thermal resistances between the cold and hot sides of the TEM generated by the 2mm air gap which is considered stationary. Current value is 28 K/W.
R_{39}, R_{40}	Thermal resistances of the ***F*** sealing between the ***E*** block and ***G_1*** respectively ***G_2*** blocks. Current value is 22 K/W.
R_{41}, R_{42}	Thermal resistances between the ***E*** block and ***L_1*** respectively ***L_2*** heatsinks.
R_{36}	Thermal resistance representing 1/3 of the ***E*** block. This block was split in 3 serial blocks because of the inner cooling pipes. Current value is 0.05 K/W.
R_{37}	Thermal resistance representing 1/3 of the ***E*** block. This block was split in 3 serial blocks because of the inner cooling pipes. Current value is 0.003 K/W.
R_{43}	Thermal resistance between the ***E*** block and ***K*** cooling heatsink.
C_{24}	Heat capacity of the heater support. Current value is 100 J/K.
C_{23}	Heat capacity of the ***H*** resistive heater. Current value is 160 J/K.
C_{14}	Heat capacity of the C copper plate except the $2 \cdot 0.04 \cdot 0.04 \cdot 0.003$ m^3 volume. Current value is 160 J/K.
C_{17}, C_{18}	Heat capacities of the ***C*** copper plate $0.04 \cdot 0.04 \cdot 0.003$ m^3 equivalent volumes. Current value is 16.3 J/K for each.
C_{13}, C_{11}	Heat capacities of the ***D*** duralumin blocks. Current value is 27 J/K for each.
C_{20}, C_{16}, C_{19}, C_{15}	Distributed calculated heat capacities of the TEM modules. Current value is 10 J/K for each pair of two capacitances.
C_{12}	Heat capacitance representing 1/3 of the ***E*** duralumin cooling block. The discretization was made for this block by splitting it into three serial connected blocks. Current value is 138 J/K.
C_{25}	Heat capacitance for the ***G_2*** upper cover. Current value is 165 J/K.
C_{26}	Heat capacitance for the ***G_1*** lower cover. Current value is 137 J/K.
C_{28}, C_{27}	Heat capacitances for the lateral ***L_1***, ***L_2*** heatsinks. Current value is 111 J/K for each.
C_{21}	Heat capacitance representing 2/3 (the middle block) of the ***E*** cooling chamber. Current value is 230 J/K.
C_{22}	Heat capacitance representing the 3rd block of the ***E*** cooling chamber. Current value is 138 J/K.
C_{29}	Heat capacitance of the ***K*** heatsinks. Current value is 466 J/K.
B_8	Seebeck coefficient expressed using an ABVS source. Current value is $\left((0.0033) \cdot \ln(0.05 + V_{(te)} - V_{(ta)}) + 0.049\right)$
B_2	Internal resistance expressed using an ABVS source. Current value is $\left((0.021) \cdot (V_{(te)} - V_{(ta)}) + 3.1\right)$
L_1	Internal parasitic inductance. Current value is 1.11µH as experimentally determined.
C_3	Internal parasitic capacitance. Current value is 59nF as experimentally determined.

The results are presented in Chapter 4 and demonstrate a good agreement with the experiment, the simulation showing 2% errors for one case (Everredtronics) and 4% errors for the other (Melcor), at the maximum temperature values for which the experiments have been conducted.

3.3 Convective Heat Transfer SPICE Model

The model presented in paragraph 3.2 was considered without convective heat losses because the simulation and the experiment were conducted inside an isolated chamber.

In this paragraph, the author proposes a method for simulating the convective heat loss, in constant temperature natural ambient and with no additional air current flow. This implementation is desired when designing energy harvesting devices based on TEMs, where electrical engineers need to know the output power the TEM generates under normal conditions. Taking into account that the thermoelectric module operation is based on the temperature difference of its two sides and that in normal conditions it is placed in a natural environment, a SPICE model would ease the designer's work. A separate thermal simulation (that is usually done in a specialized software) of the heat transfer mechanism in the mechanical device where the TEM is placed would be of great importance, but the result needs to be integrated or correlated to the ones obtained in an electrical circuit simulator. Moreover, a detailed thermal simulation that predicts the heat flow in each part of the simulated system is not very helpful for an electrical engineer that needs only the temperature difference on the TEM's sides in order to obtain the output power the TEM device delivers.

In this chapter, an alternate solution is proposed, where both thermal and electric simulations are made in the same software simulator– SPICE.

The study of physical phenomena occurring at normal scale is often hindered by the dimensions or parameters of the original model [51]. As a solution, the similitude criteria can be used to determine the heat transfer coefficients. Numerous criteria exist and each is used in specific cases, but it is the user's assignment to select that one suitable for the specific case he is handling. In [Appendix E] the concept of similitude criteria is explained and also the means of how these criteria have been determined from the Fourier-Kirchhoff equation, the Navier-Stokes equations, the continuity equation and the Fourier equation.

For the natural heat convection process that is discussed in this topic, only three similitude criteria will be used, that correspond to the free convection category. The natural heat convection will be studied in stationary regime and for this the Prandtl, Nusselt and Grashof criteria will be used. Grashof criteria or number contains the temperature gradient which is the cause the fluid (air) is moving. Nusselt number contains the "***α***" convection coefficient that needs to be determined and Prandtl number takes into account the fluid characteristics.

$$\mathrm{Pr} = \frac{\nu}{a} = \frac{\rho \cdot c_p \cdot \nu}{k} \tag{3.13}$$

$$Nu = \frac{\alpha \cdot l}{k} \tag{3.14}$$

where l represents the length of the heat exchange surface [m].

$$Gr = \frac{g l^3 \beta \Delta T}{\nu^2} \tag{3.15}$$

The equation that has to be solved can be written as [64]:

$$Nu = C(Gr \cdot \Pr)^n \tag{3.16}$$

The C and n constants are determined with respect to the values of *Gr* and *Pr* numbers [51], [64] and depending on the dimensions and orientation of the object that resides in the fluid that cools it. The test rig's (Fig. 2.1) spatial displacement of the constituent parts was correlated to the available C and n constants for different configurations. The constants values have been chosen to correspond to the current test rig configuration and are presented in Table 3.4.

Table 3.4 Constant values for different configurations of the plate with respect to the cooling fluid. Source [selected from 64]

Situation (fluid flow is laminar)	**C constant**	**n constant**
Plane horizontal plate with the heated face up	0.71	0.25
Plane horizontal plate with the heated face down	0.35	0.25
Vertical plate	0.59	0.25

The constructive parts of the test rig presented in Fig. 2.1 and 2.2 were split into smaller, discrete blocks and for each (that have parts in contact with the cooling fluid - air), the heat transfer coefficient was calculated. A special attention was paid to determine the heat transfer coefficient of the lateral heat-sinks with vertical and horizontal fins. For the heat transfer process that takes place when the thermal flux passes through a wall employing fins a separate mathematical model must be used.
Referring to Fig. 3.8, that represents an approximation of the heatsink used in the current work, the thermal heat flux is divided into the heat flux transmitted by the plane wall (Φ_w), without fins and the heat flux transmitted by the fin (Φ_f).

An additional dimension is introduced in [52] – the fin's efficacy (ε_f) as the ratio between the heat flux transmitted through the fin's surface and the heat flux that would be transmitted through the same surface if this would be at a constant temperature. The distance between fins is usually chosen as:

$$L_f = (1 \ldots 1.5) \cdot \delta_{w\max} \tag{3.17}$$

where δ_w represents the width of the plane wall (Fig. 3.9).

In the current topic, the chosen heatsink employs an $L_f << \delta_w$ and $L_f << l$, and consequently the fins heat transfer coefficient α_f is decreasing reported to α_{f0}, that represents the heat transfer coefficient of one fin. The α_f/α_{f0} ratio function of fin's spacing is presented with thick line in Fig. 3.9, as described in [52].

In [52], the ratio is presented only up to **l/L_f** = 7. In the current topic, due to the geometry of the heatsink used, the ratio reaches 15 – 16. In order to acquire this value for **l/L_f**, the initial slope was approximated by an exponential function and extrapolated (thin line in Fig. 3.9), to obtain the **α_f/α_{f0}** ratio.

The fitting function used to extrapolate the original characteristic exhibits a good approximation of **R^2**=0.985 as pictured in Fig. 3.9, where **R^2** is the coefficient of regression.

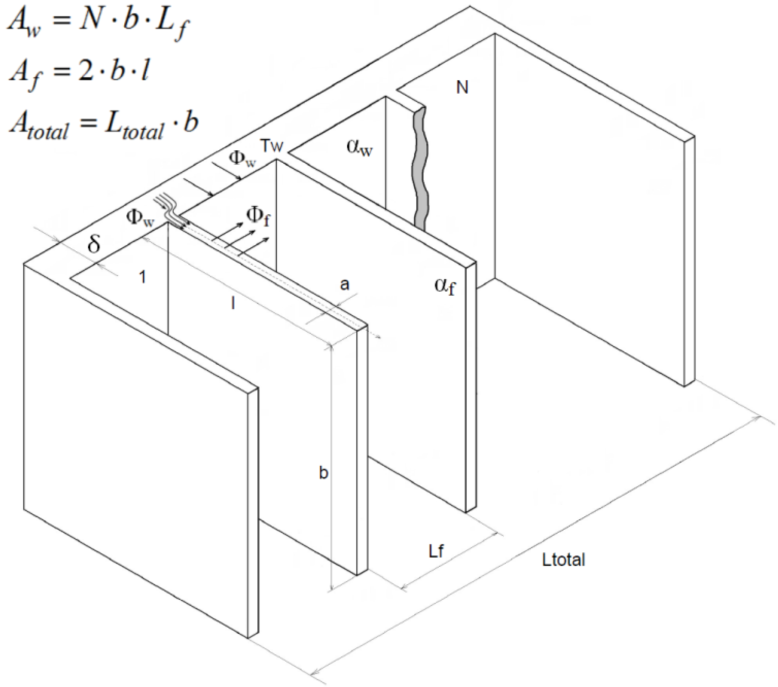

Figure 3.8 Simplified description of the test rig's vertical fins heatsink HTC. Source [original]

The rate of heat flow transmitted by the entire surface of the wall (**A_w**) not covered by fins is expressed as:

$$\Phi_W = \alpha_W \cdot A_W \cdot T_W \tag{3.18}$$

where **T_w** represents the wall temperature.

The heat flow transmitted by the fin is:

$$\Phi_f = \alpha_f \cdot A_f \cdot T_W \cdot \varepsilon_f \tag{3.19}$$

The mean heat transfer coefficient has the form [52]:

$$\alpha_{hseq} = \alpha_W \frac{A_W}{A_{total}} + \alpha_f \frac{A_f}{A_{total}} \tag{3.20}$$

The mean heat transfer coefficients for each heatsink are determined by using equations 3.20 and 3.16 and computing the HTC **α_f** and **α_w** individually.

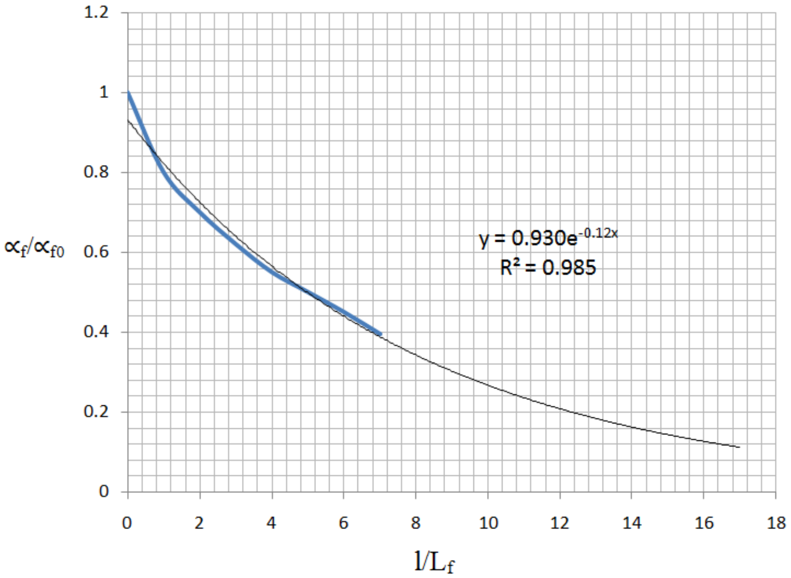

Figure 3.9 Extrapolation of α_f/α_{f0} ratio versus the spacing between fins. Source [original]

The mean heat transfer coefficient was computed for each part of the test rig (*K, L_1, L_2, G_1, G_2, J* in Fig. 2.1) that are in contact with the cooling fluid. A numerical computation of the heat transfer coefficients for a temperature difference ranging from 0 - 30℃ and a minimum step of $\Delta T = 0.5$℃ was implemented in a Matlab application [Appendix F]. This is necessary because the method presented above determines the average heat transfer coefficient only for a stationary temperature difference between the body that is cooling and the fluid that cools the body (air).

For each part, the specific heat transfer coefficient was expressed as a thermal resistance [K/W] that separates the mechanical part from the environment which resides at a certain temperature.

The obtained values were implemented with the help of lookup tables as variable resistances in the SPICE simulator, in order to create a dynamic simulation of the convective heat transfer process.

The complete equivalent SPICE model of the mechanical test rig together with the thermal part of the TEMs is depicted in Fig. 3.10.The model is presented with the additional **V_1** power source that implements the temperature of the resistive heater. In this experiment, the TEMs act like a voltage generator (TEG), case in which the Everredtronics modules were used.The 8V power source depicted in Fig. 3.7, where the Melcor TEC modules were used, is not needed any longer.

Table 3.5 describes in detail each additional circuit element of the model presented in Fig. 3.10 compared to the model from Fig. 3.7.

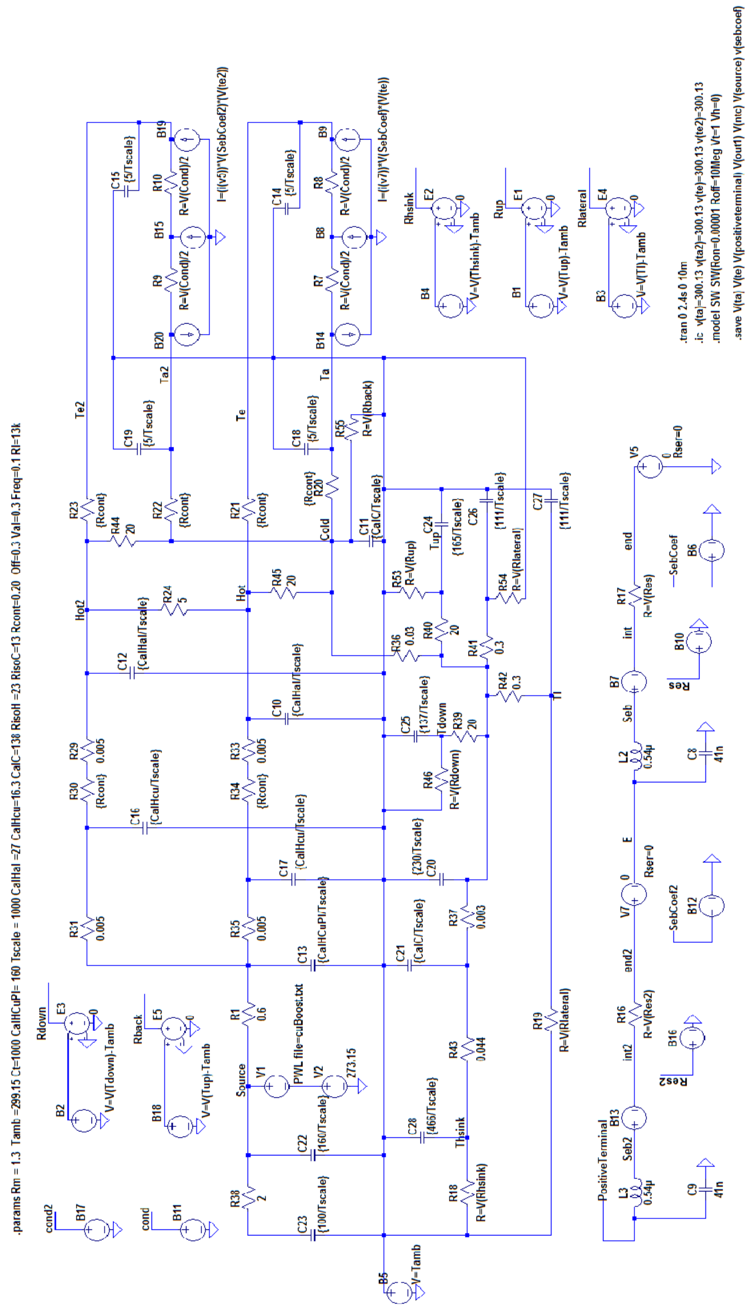

```
.params Rm = 1.3  Tamb =299.15 Ct=1000 CalHCuPl= 160 Tscale = 1000 CalHal =27 CalHcu=16.3 CalC=138 RisoH =23 RisoC=13 Rcont=0.20  Off=0.3 Val=0.3 Freq=0.1 Rl=13k
```

```
.tran 0 2.4s 0 10m
.ic  v(ta)=300.13 v(ta2)=300.13 v(te)=300.13 v(te2)=300.13
.model SW SW(Ron=0.00001 Roff=10Meg Vt=1 Vh=0)
.save V(ta) V(te) V(positiveterminal) V(out1) V(ntc) V(source) v(sebcoef)
```

Figure 3.10 SPICE thermal model describing the test rig in natural environment. Source [original]

Table 3.5 SPICE circuit components for the test rig under normal condition operation

Circuit element	**Designation**
R_1	Implementation of the thermal contact resistance between the ***H*** resistive heater and the ***C*** copper plate. Current value is 0.6 K/W.
R_{55}	Implementation of the heat transfer coefficient [W/m^{2}K] of the ***E*** chamber "hot" face oriented towards the ***J*** insulation board as a thermal resistance [K/W]. The heat transfer coefficient is expressed as a resistor between the plate and the fluid (air). Current value is given by the $\boldsymbol{V_{(Rback)}}$ of the $\boldsymbol{E_5}$ ABVS source. The $\boldsymbol{E_5}$ source implements as a lookup table the results from the numerical computation of the heat transfer coefficient function of temperature difference. The temperature difference is taken between $\boldsymbol{T_{cold}}$ (of the TEG) and the fluid's temperature – ambient temperature (300K).
R_{54}, R_{19}	Implementation of the heat transfer coefficients of the $\boldsymbol{L_1}$ and respectively $\boldsymbol{L_2}$ heatsinks. Current value is given by the $\boldsymbol{V_{(Rlateral)}}$ of the $\boldsymbol{E_4}$ ABVS source.
R_{53}	Implementation of the heat transfer coefficient of the $\boldsymbol{G_2}$ upper cover. Current value is given by the $\boldsymbol{V_{(Rup)}}$ of the $\boldsymbol{E_1}$ ABVS source.
R_{46}	Implementation of the heat transfer coefficient of the $\boldsymbol{G_1}$ lower cover. Current value is given by the $\boldsymbol{V_{(Rdown)}}$ of the $\boldsymbol{E_3}$ ABVS source.
R_{18}	Implementation of the heat transfer coefficient for the ***K*** heatsink. Current value is given by the $\boldsymbol{V_{(Rhsink)}}$ of the $\boldsymbol{E_2}$ ABVS source.
Cold, T_{up}, T_{down}, T_l, T_{hsink}	Connection label points for the cold side of the TEM temperature, $\boldsymbol{G_2}$ upper cover temperature, $\boldsymbol{G_1}$ lower cover temperature, $\boldsymbol{L_1}$ and $\boldsymbol{L_2}$ lateral heatsinks and ***K*** heatsink temperatures.
E_1	Implementation through a lookup table of the numerical computation results of the heat transfer coefficient for the $\boldsymbol{G_2}$ upper cover. Current value is (0.1 58,…35 13.7) representing (temperature difference [K], thermal resistance [K/W]) pairs.
E_2	Implementation through a lookup table of the numerical computation results of the heat transfer coefficient for the ***K*** heatsink. Current value is (0.1 22.2,… 35 5.2).
E_3	Implementation through a lookup table of the numerical computation results of the heat transfer coefficient for the $\boldsymbol{G_1}$ lower cover. Current value is (0.1 82.2,… 35 19).
E_4	Implementation through a lookup table of the numerical computation results of the heat transfer coefficient for the $\boldsymbol{L_1}$ and $\boldsymbol{L_2}$ lateral heatsinks. Current value is (0.1 129,… 35 29) for each.
E_5	Implementation through a lookup table of the numerical computation results of the heat transfer coefficient for the ***E*** chamber hot face. Current value is (0.1 152,… 35 35.8).
T_{scale}	Represents a time scaling factor for lowering the simulation time because the experiments are taking thousands of seconds. Current value is 1000 – 1second equals 1ms in simulation.
V_1	Implementation of the heater's temperature as {temperature value, time point} pairs, needed as input for the simulation. The values were saved in a *.txt file that is accepted by the LTspice simulator.

B_{12}	Seebeck voltage generator implemented through an ABVS source. Current value for the TEG module is $V=(-2.6820E-4)\cdot(((v(t)-38.68)/5.14)^{4})+$ $+(3.3495e-05)\cdot(((v(t)-38.68)/5.14)^{3})+$ $+(4.5904e-4)\cdot(((v(t)-38.68)/5.14)^{2})+$ $+(2.9812e-4)\cdot(((v(t)-38.68)/5.14))+0.0444$ where v(t) represents the mean temperature of the two sides.
B_{16}	Internal resistance value implemented through an ABVS source. Current value for the TEG module is $\left((0.0076)\cdot(V_{(te)}+V_{(ta)}-546.3)/2+1.09\right)$

The simulation results and comparison to the experiments are presented in Chapter 4. The simulation results are in good agreement with the experiments, showing maximum 12% errors (up to the temperatures where the experiments have been conducted).

3.4 Conclusions

Taking into account the adopted simplifications of the mechanical test rig, the result can be considered in good correspondence with the experiment. Special care had to be taken when the heat transfer coefficient of the ***K*** heatsink (Fig. 2.1) was calculated.

The methodology presented in paragraph 3.3 could be used to model the convective heat transfer because of the physical dimensions of the TEGs test rig and its construction. The method cannot be applied for a very complex mechanical design for which analytical similitude criteria do not exist. In either case, a computational fluid dynamics simulator is usually desired as it provides more relevant results and with fewer errors. In this case, the mechanical design must be modelled in CAD software.

The implementation of the current dependent sources in the SPICE thermal model of the TEM proved to solve convergence problems that appeared due to the voltage dependent sources.

By implementing the TEMs internal heat capacity as distributed parameters, the SPICE model was able to predict the real behavior of the device more accurate, from two points of view. First, their presence smoothened the temperature variation on the hot and cold side of the TEM when the input power was connected/disconnected. Without the internal heat capacity, unreal and sudden variations would appear in the temperature values. Second, if an AC signal is fed to the TEM’s input and the internal heat capacity is not implemented in the model, the hot and cold side temperature would “follow” the applied voltage, no matter the signal frequency. This behavior is unreal and was discussed at the end of subchapter 2.5. The simulation results are presented in subchapter 4.6.

3.5 Contributions

1. **An improved SPICE thermoelectrical TEM model** was implemented with dynamic S, R_t and R_e (Seebeck coefficient, thermal resistance and electrical resistance) variation against temperature. The variations were implemented through ABVS sources and 1st order or logarithm fitting functions that approximate the experimental measured values.
2. **The experimentally determined parasitic components L_{peq} and C_{peq} were implemented in the new SPICE model**.
3. **The thermal part that describes the TEM was improved by adding the computed heat capacitance of the module and using distributed parameters** when representing the thermal resistance and heat capacitance.
    - The TEM model employing distributed thermal resistance and three current dependent sources proved to help the simulations converge at points where the model with one voltage and one current dependent sources failed in computing the results.
4. **The mechanical parts of the test rig were split in 16 blocks** and for each the thermal capacitance and resistance was calculated. The thermal resistance of the air gaps and other elements (thermal contact grease, rubber sealing) was also calculated. Also, the equivalent thermal resistance of the isolated chamber was calculated
5. **The overall SPICE thermoelectrical model of the system that is tested in thermally isolated conditions was implemented**.
6. **A novel implementation involving the convective heat transfer process that appears under normal working conditions of the built test rig has been performed in SPICE**.
    - A thermodynamic study was required to determine the necessary similitude criteria that apply in the current topic.
    - For each mechanical part that is in contact with the cooling fluid (air), the HTC under laminar flow was calculated.
    - Due to the complicated geometry of the heatsink, an approximation had to be made to analytically calculate the mean heat transfer coefficient.
    - **A numerical computation** was performed in Matlab to generate the thermal resistances associated to the heat transfer coefficients versus temperature.
        - A temperature step of 0.5℃ was assumed satisfactory when computing the thermal resistance variation with temperature as it provided a very good resolution.
        - The computation was necessary because the HTC calculation using the similitude criteria is made for the stationary regime of temperatures and the results obtained are for a given temperature difference (ΔT) that enters in the Grashof number formulation.
7. **The equivalent SPICE model development** (implemented in Linear Technology LTspice).

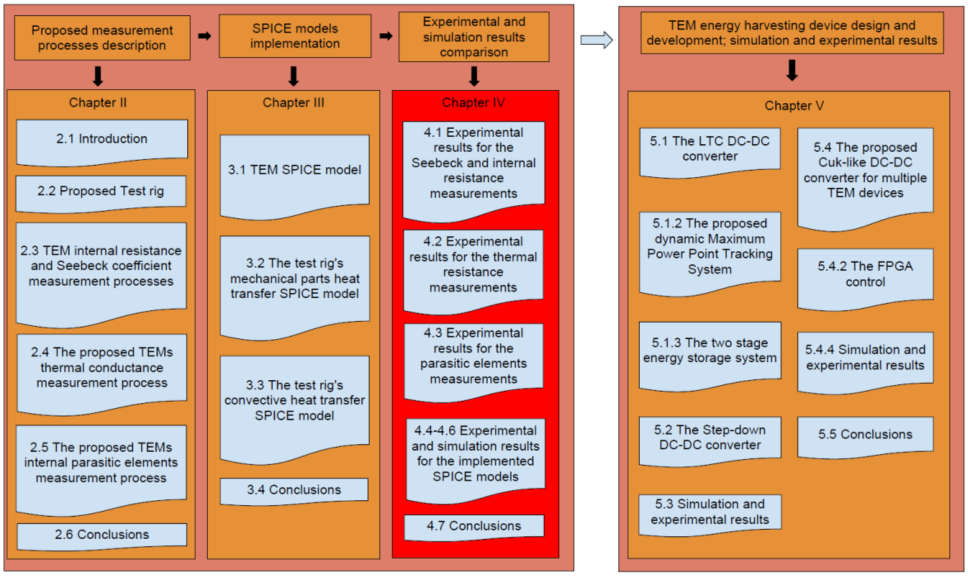

Chapter 4

Experimental and simulation results

In this chapter, the simulation and experimental results are presented for all the measurement processes described in Chapter 3. The internal resistance, Seebeck coefficient, thermal conductance and parasitic components existent in a TEM were experimentally determined and the results are compared to simulation models.

4.1 Results for the Seebeck and internal resistance measurements

The proposed test rig can operate in three cooling configurations:

1. Using only the ***K*** heatsinks, as presented in Fig. 2.1 and without the additional thermosyphon, as in Fig. 3.11.
2. Using both the ***K*** heatsinks and the thermosyphon.

3. Without the ***K*** heatsinks, in which case a heat pipe must be used instead.

In the following, the output voltage results depending on the achieved temperature difference (when cooling configurations 1 and 2 are used) are presented. In both cases, the same heat power source was used; therefore, the temperature difference reached is related to the system's cooling ability. The heatpipe was used in the configuration presented in Appendix H.

The experiment has been made by applying 29 successive voltages to the resistive heater and for each, a period of 3600 seconds was necessary to let the system reach the steady state regime. The 29 successive voltages correspond to a hot side temperature ranging from 0 - 85℃, with 2° increment, as detailed in paragraph 2.3.

It can be observed that the thermosyphon improves the cooling ability of the system, the TEGs output voltage being with 42% higher compared to the case when no thermosyphon was used (Fig 4.1). This proves that in a TEM based energy harvesting device, the thermosyphon cooling solution is an efficient passive method, if the physical placement of the energy harvesting system allows its installation.

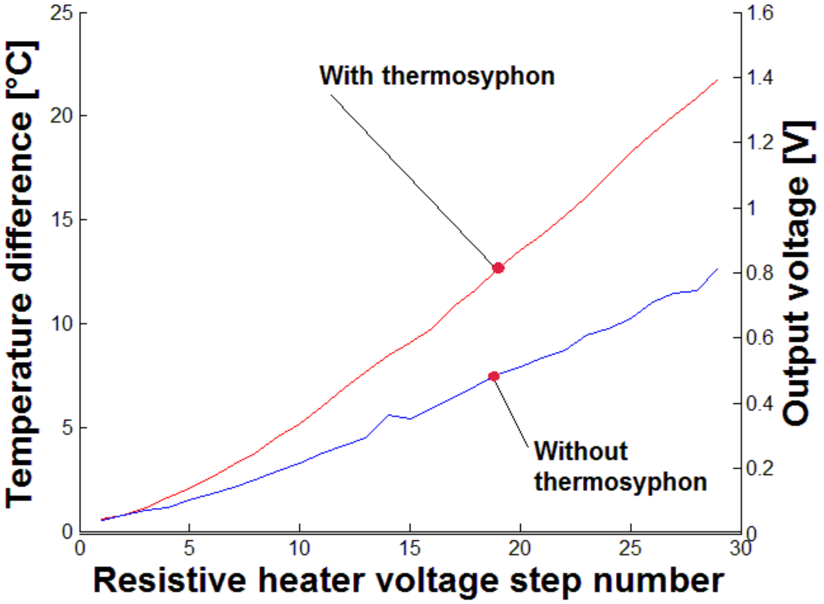

Figure 4.1 Comparison between the test rig working with and without a thermosyphon. Source [experimental data]

In Fig. 4.2, the internal resistance against temperature difference for the Everredtronics module is presented. The red line represents the fitting function.

The resistance measurement process was described in Chapter 2.3. The R^2 from Fig. 4.2 refers to the coefficient of determination and describes how well a regression line fits a set of data, where 1 represents 100% match.

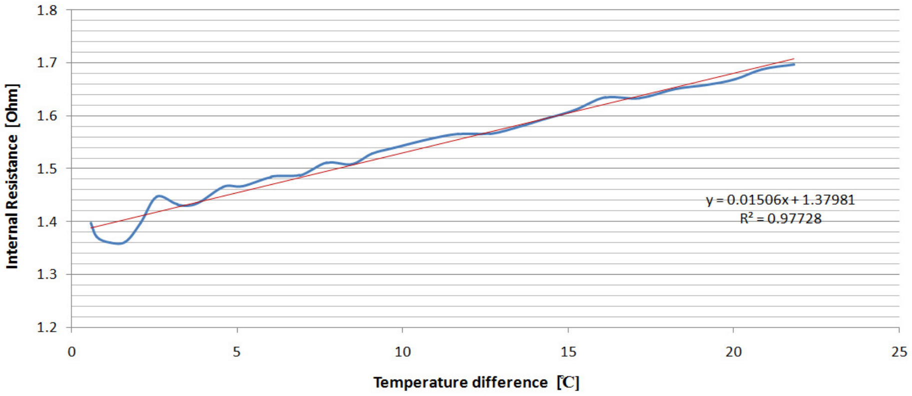

Figure 4.2 TEG's internal resistance variation versus temperature difference. Source [experimental data]

In Fig. 4.3, the Melcor module's internal resistance variation with temperature difference is presented. One can observe that in this case, the 1st order fitting offers a better approximation for the resistance variation. The experimental data show that the resistance of the TEG Everredtronics module has a higher variation with respect to the 1st order fitting function.

It can be observed that the resistance value differs on the two modules – 1.4 Ω at room temperature for the TEG module and 3.1 Ω for the TEC module.

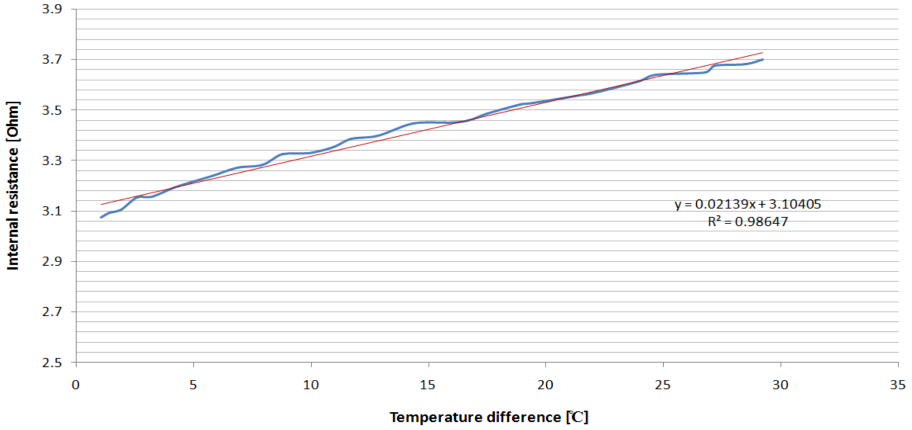

Figure 4.3 TEC's internal resistance variation function of temperature difference. Source [experimental data]

The Seebeck coefficient values for the TEG and TEC modules are presented in Fig. 4.4 respectively 4.5. The associated measurement processes were explained in detail in Chapter 2.4.

Analyzing these the two figures, the differences can be observed in terms that the variation of the Seebeck coefficient function temperature is smoother for the Melcor module than for the Everredtronics one.

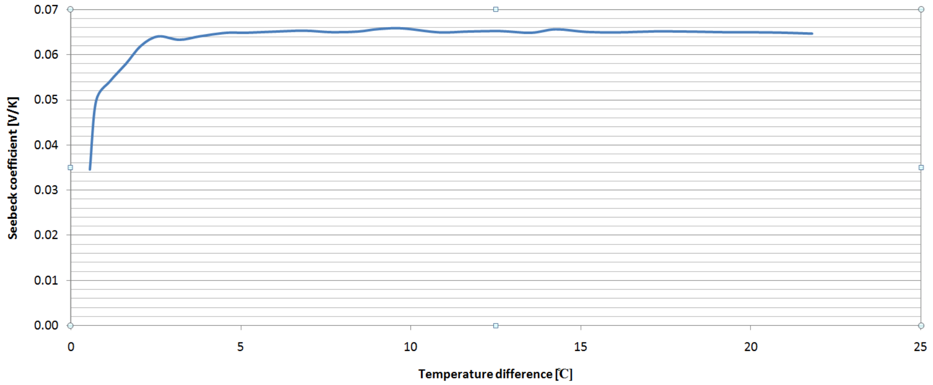

Figure 4.4 TEG's Seebeck coefficient variation function of temperature difference. Source [experimental data]

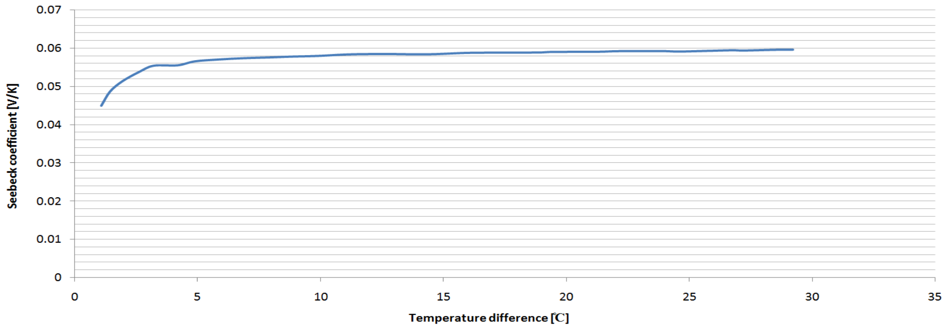

Figure 4.5 TEC's Seebeck coefficient variation function of temperature difference. Source [experimental data]

The experiments show that the variations of the TEG's internal parameters with respect to the room temperature values (27℃) are higher than for the TEC module, as presented in Table 4.1.

Table 4.1 Parameters variation for each module type with respect to room temperature values.

TEM	R_m	S
TEG	21.3%	87.3%
TEC	15.6%	31.4%

4.2 *Experimental results for the thermal conductance measurements*

In Fig. 4.6, the front VI of the thermal conductance measurement process is presented. It can be observed that first the heating of the hot side takes place after which the input power is lowered and the steady state process is obtained by controlling the water pump flow.

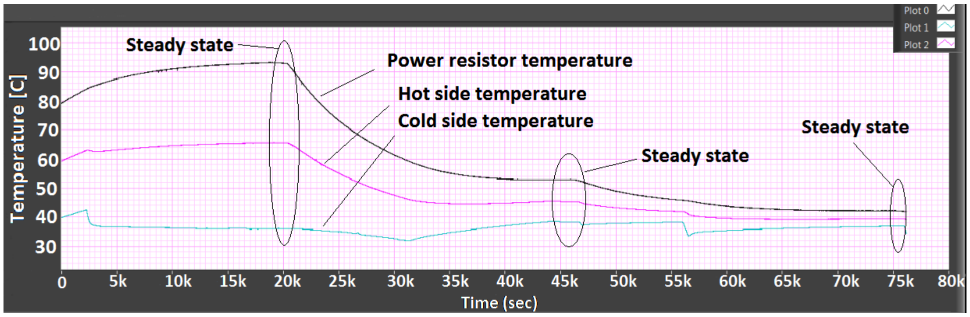

Figure 4.6 Thermal conductance LabVIEW VI front panel. Source [experimental data]

One can see that the measurement process is a time consuming one. For three measurements, 125 minutes were necessary.

Figure 4.7 presents the thermal conductance measurement result for the Everredtronics module and the corresponding fitting function. The maximum temperature difference achieved on the TEGs sides in this experiment was 15℃. This is because the module has a high thermal conductance and the heat reached the cold side easier, making it difficult for the water pump and the available cooling system to maintain a lower temperature on the cold side of the TEM. The fitting function in this case, if extrapolated, will show a decrease of the thermal conductance as temperature difference increases although this may not be the real behavior of the module. In [9], Rowe presents the curves for different doped thermo-elements and shows that the thermal conductance can have rising and falling slopes as temperature increases.

For the Melcor module, the experimental results, presented in Fig 4.8 were compared to the approximation function given by the datasheet. The results are presented in Fig. 4.9 and although an offset can be observed, the datasheet approximation shows a good correlation with the measured value. The decreasing slope of the thermal conductance can be observed for both modules. However, for the Melcor module, the datasheet value exhibits an increased slope starting from a temperature difference of 15℃, compared to the measured values where the slope is maintaining its decreasing. This can be explained through the fact that heat losses that were not taken into account when measuring the thermal conductance are leading to errors, as the temperature increases.

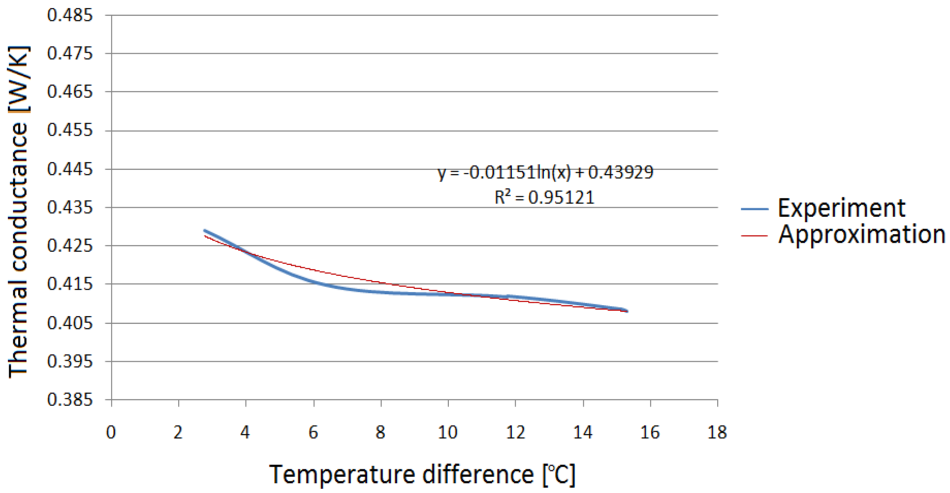

Figure 4.7 Thermal conductance results and fitting function for the Everredtronics module. Source [experimental data]

For the Melcor module, the results presented in Fig. 4.8 show a reduced thermal conductance, for this reason also the temperature difference achieved during measurements is higher, reaching 28℃. The linear fitting function shows a better approximation (*R^2=0.967*) for the measured data.

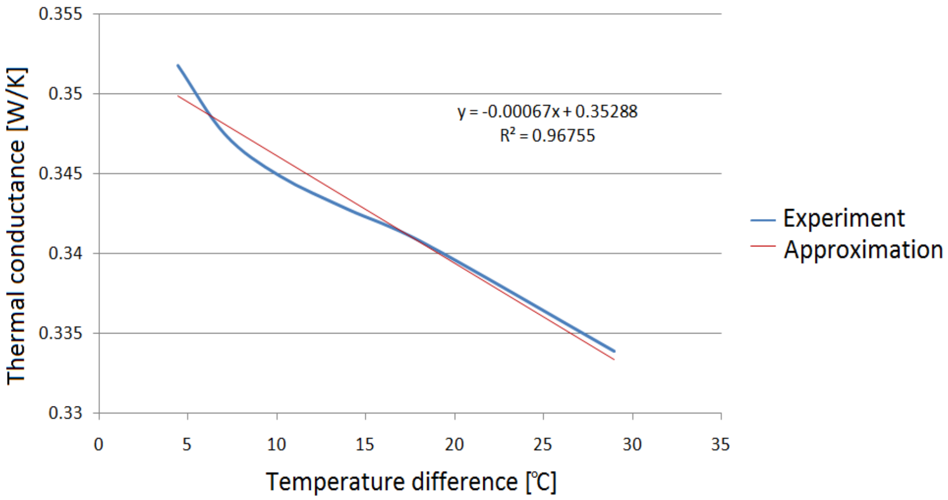

Figure 4.8 Thermal conductance results and fitting function for the Melcor module. Source [experimental data]

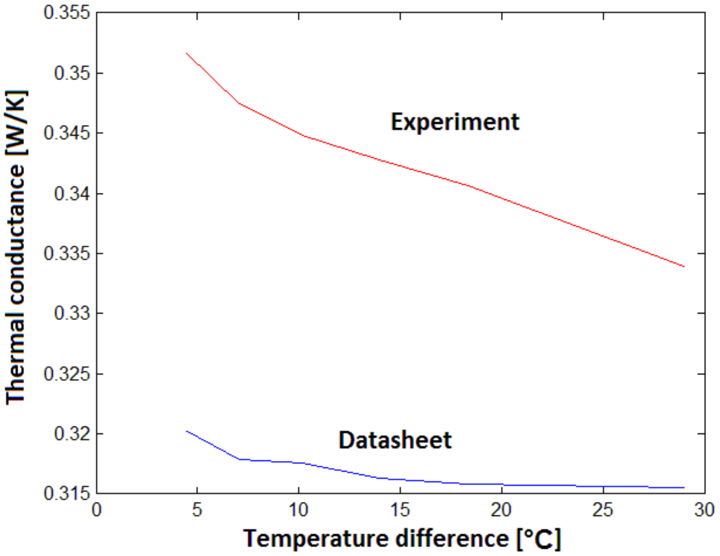

Figure 4.9 Thermal conductance results and datasheet approximation for the Melcor module. Source [experimental data]

The measured value, starting from the temperature difference of 5℃ and up to 28℃ is with 4.2% smaller than the initial one. Taking into account that six measurements have been made in this interval, the difference between two consecutive measured values was 0.7%. Adding the heat losses that were not taken into account, the error of the measurement device and that the experimentally determined values are in close correlation to the datasheet ones, the author concluded the measurement with the available instruments and setup achieved its limits and can be considered that have provided good results.

4.3 Results for the parasitic inductances and capacitances measurements

The measurements of the parasitic inductances and capacitances have been made for six TEG (Everredtronics) modules and two TEC (Melcor) modules. The acquisition mode of the oscilloscope was configured for averaging 128 acquisitions. This mode requires a longer time until the result is displayed and is used to reduce the random noise [54]. Taking into account that the signal is periodic and the delay required to output the results was not relevant, this acquisition mode was desired for the current measurements to improve the accuracy. Five measurements were made for each frequency and for each module, counting 20 measurements for one module. Afterwards, the average value and the standard deviation were computed.
Figure 4.10 shows the phase shift at 100 kHz input for one of the Everredtronics module. It can be observed the inductive behavior of the TEG.

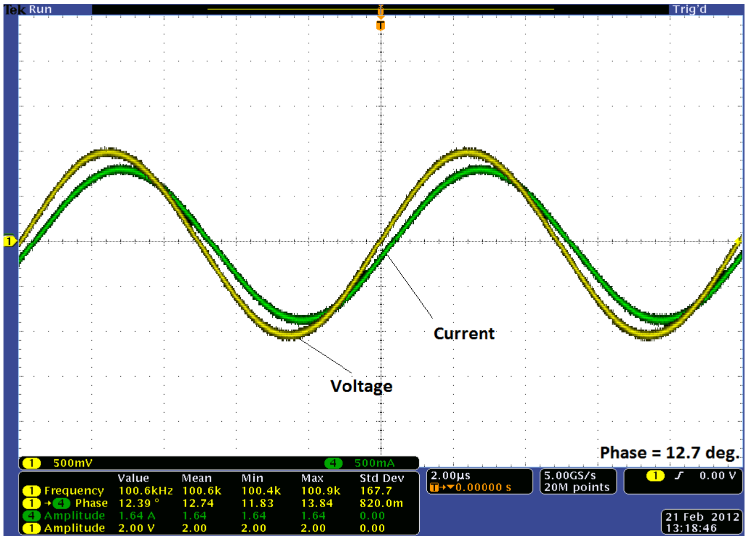

	Value	Mean	Min	Max	Std Dev
1 Frequency	100.6kHz	100.6k	100.4k	100.9k	167.7
1 → 4 Phase	12.39 °	12.74	11.83	13.84	820.0m
4 Amplitude	1.64 A	1.64	1.64	1.64	0.00
1 Amplitude	2.00 V	2.00	2.00	2.00	0.00

Figure 4.10 Everredtronics TEG phase shift measurement at 100 kHz. Source [experiment]

Figure 4.11 presents the phase shift at 200 kHz for the same TEG module.

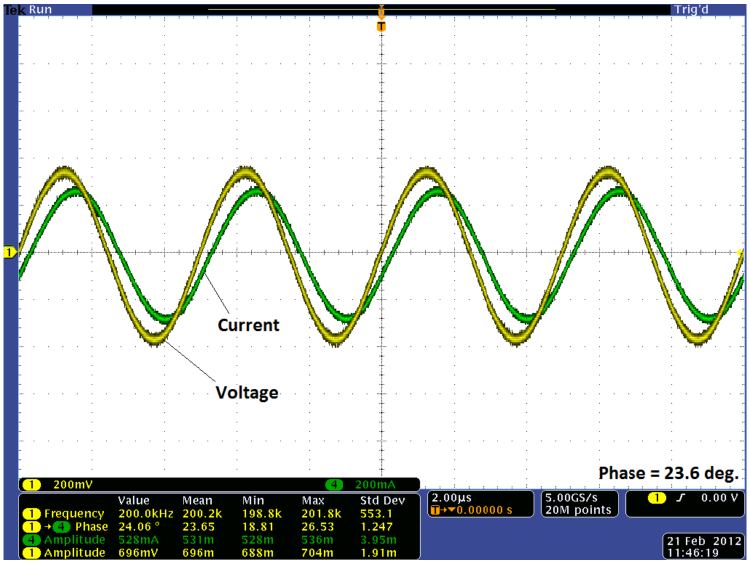

	Value	Mean	Min	Max	Std Dev
1 Frequency	200.0kHz	200.2k	198.8k	201.8k	553.1
1 → 4 Phase	24.06 °	23.65	18.81	26.53	1.247
4 Amplitude	528mA	531m	528m	536m	3.95m
1 Amplitude	696mV	696m	688m	704m	1.91m

Figure 4.11 Everredtronics TEG phase shift measurement at 200 kHz. Source [experiment]

In Fig. 4.12, the phase shift at 100 kHz for one of the TEC modules is presented. The module exhibits the same inductive behavior; however the phase shift has a lower value than for the TEG module.

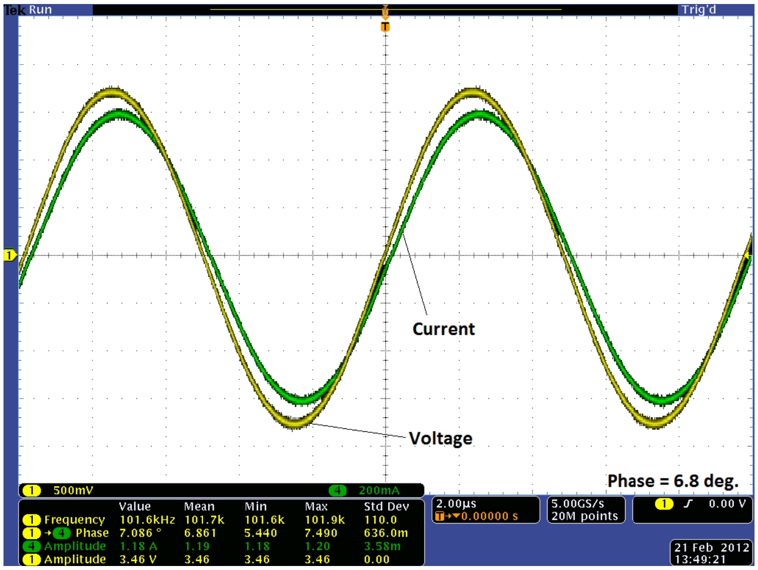

	Value	Mean	Min	Max	Std Dev
1 Frequency	101.6kHz	101.7k	101.6k	101.9k	110.0
1 → 4 Phase	7.086 °	6.861	5.440	7.490	636.0m
4 Amplitude	1.18 A	1.19	1.18	1.20	3.58m
1 Amplitude	3.46 V	3.46	3.46	3.46	0.00

Figure 4.12 Phase shift at 100 kHz for the TEC module. Source [experiment]

At 200 kHz (Fig 4.13), the phase shift is approximately half the value obtained for the TEG module.

The results are presented in Table 4.3 where for each module and for two chosen frequencies (100 and 200kHz) the average phase offset value was computed from five measurements.

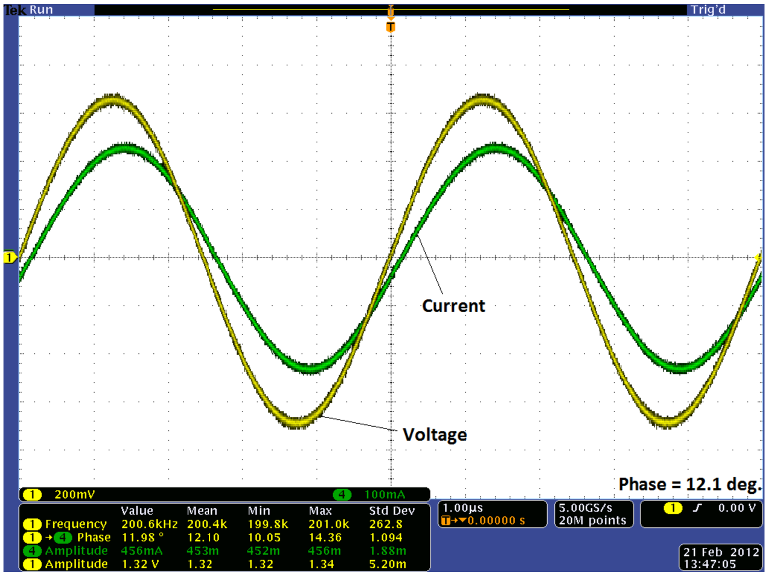

	Value	Mean	Min	Max	Std Dev
1 Frequency	200.6kHz	200.4k	199.8k	201.0k	262.8
1 → 4 Phase	11.98 °	12.10	10.05	14.36	1.094
4 Amplitude	456mA	453m	452m	456m	1.88m
1 Amplitude	1.32 V	1.32	1.32	1.34	5.20m

Figure 4.13 Phase shift at 200 kHz for the TEC module. Source [experiment]

In Table 4.3, also the standard deviation between the 5 measurements made at each frequency and for each of the eight modules is presented.

Table 4.2 Measurements standard deviation computed at each frequency and for each module

Module	Frequency	Standard deviation	Standard deviation in percent of average value	Phase shift value
TEG1	50 kHz	0.3°	4.3%	7.02
	100 kHz	0.29°	2.3%	12.46°
	150 kHz	0.29°	1.7%	17.4°
	200 kHz	0.38°	1.6%	23°
TEG2	50 kHz	0.42°	6.7%	6.28°
	100 kHz	0.63°	5.2%	12.1°
	150 kHz	0.09°	0.5%	16.5°
	200 kHz	0.68°	3.1%	21.5°
TEG3	50 kHz	0.51°	6.7%	7.6°
	100 kHz	0.53°	4%	13.19°
	150 kHz	0.4°	2.3%	17.4°
	200 kHz	0.64°	2.9%	22.3°
TEG4	50 kHz	0.4°	7%	5.7°
	100 kHz	0.79°	9.4%	8.43°
	150 kHz	0.79°	6.7%	11.8°
	200 kHz	0.38°	2.6%	14.77°
TEG5	50 kHz	0.15°	2.6%	5.8°
	100 kHz	0.15°	1.4%	10.5°
	150 kHz	0.56°	3.7%	15.1°
	200 kHz	0.66°	3.5%	18.83°
TEG6	50 kHz	0.17°	4%	4.4°
	100 kHz	0.33°	3.5%	9.64°
	150 kHz	0.56°	4.1%	13.5°
	200 kHz	0.44°	2.5%	17.59°
TEC1	50 kHz	0.36°	8%	4.5°
	100 kHz	0.27°	3.8%	7.04°
	150 kHz	0.24°	2.5%	9.7°
	200 kHz	0.7°	5.7%	11.71°
TEC2	50 kHz	0.29°	7.1%	4.1°
	100 kHz	0.16°	2.5%	7.04°
	150 kHz	0.37°	4%	9.1°
	200 kHz	0.26°	2.2%	11.7°

In 93% of the cases the standard deviation between measurements is lower than 7%. For the TEG modules, the scattering between the highest and lowest average measured phases (for the 200 kHz input signal) is around 8.2°, that falls outside the standard deviation (maximum 0.8°) between multiple measurements which were conducted in similar conditions of temperature, input voltage and input frequency. This demonstrates the existence of differences between the TEG modules parasitic components values. For the Melcor modules, a general conclusion cannot be taken because only two modules were available for testing.

Using the equivalent circuit from Fig. 2.17, that is expected to represent the internal structure of our TEMs, one can write Eq. 4.1 and 4.2 that represent the equivalent impedance of an inductor respectively capacitor:

$$x_L = j\omega L \tag{4.1}$$

$$x_C = \frac{1}{j\omega C} \tag{4.2}$$

The equivalent impedance of the circuit from Fig. 2.17 is:

$$Z_{ech} = \frac{(R_m + j\omega L_{peq})\cdot\dfrac{1}{j\omega C_{peq}}}{R_m + j\omega L_{peq} + \dfrac{1}{j\omega C_{peq}}} = \frac{R_m + j\omega L_{peq}}{1 - \omega^2 L_{peq} C_{peq} + j\omega R_m C_{peq}} =$$

$$= \frac{R_m - j\omega R_m{}^2 C_{peq} + j\omega L_{peq} - j\omega^3 L_{peq}{}^2 C_{peq}}{(1-\omega^2 L_{peq} C_{peq} + j\omega R_m C_{peq})\cdot(1-\omega^2 L_{peq} C_{peq} - j\omega R_m C_{peq})} \tag{4.3}$$

The value of φ (phase angle) is:

$$\varphi = arctg\frac{\mathrm{Im}(Z)}{\mathrm{Re}(Z)} \tag{4.4}$$

One can write:

$$tg(\varphi) = \frac{\omega L_{peq} - \omega^3 L_{peq}{}^2 C_{peq} - \omega R_m{}^2 C_{peq}}{R_m} \tag{4.5}$$

For each of our two modules there are two systems of equations that can be solved.

System of Equations:

Everredtronics

$$\begin{cases} \omega_1 L_{peq} - \omega_1{}^3 L_{peq}{}^2 C_{peq} - \omega_1 R_m C_{peq} = R_m \cdot tg(\varphi_1), \\ \varphi_1 = 23.6^\circ, f_1 = 200kHz \\ \omega_2 L_{peq} - \omega_2{}^3 L_{peq}{}^2 C_{peq} - \omega_2 R_m C_{peq} = R_m \cdot tg(\varphi_2), \\ \varphi_2 = 12.7^\circ, f_2 = 100kHz, R_m = 1.3\Omega \end{cases} \tag{4.6}$$

Melcor

$$\begin{cases} \omega_1 L_{peq} - \omega_1{}^3 L_{peq}{}^2 C_{peq} - \omega_1 R_m C_{peq} = R_m \cdot tg(\varphi_1), \\ \varphi_1 = 12.1^\circ, f_1 = 200kHz \\ \omega_2 L_{peq} - \omega_2{}^3 L_{peq}{}^2 C_{peq} - \omega_2 R_m C_{peq} = R_m \cdot tg(\varphi_2), \\ \varphi_2 = 6.8^\circ, f_2 = 100kHz, R_m = 3\Omega \end{cases} \tag{4.7}$$

Solving the two systems of equations, the results for all the tested modules are presented in Table 4.4.

Table 4.3 Computed parasitic inductances and capacitances for each TEM

Module	**Computed parasitic L_{peq} inductance**	**Computed parasitic C_{peq} capacitance**
TEG 1	0.49 µH	56 nF
TEG 2	0.53 µH	91 nF
TEG 3	0.63 µH	121 nF
TEG 4	0.44 µH	127 nF
TEG 5	0.49 µH	97 nF
TEG 6	0.48 µH	86 nF
TEC 1	1.16 µH	59 nF
TEC 2	1.08 µH	52 nF

For the Everredtronics TEG module, a maximum scattering of around 30% exist between the parasitic inductance of two modules. As for the capacitance, the values are sometimes even three times higher.

For the Melcor module, a general conclusion cannot be drawn because only two modules were available.

The TEMs intrinsic parasitic components are important when developing DC – DC converters and energy harvesting systems. These converters work with a switching frequency of 50 - 100 kHz (like the LTC3105 DC – DC converter) or even higher (≥1 MHz) if the external L and C components need to have low values and dimensions. At such frequencies, the inductive components become important and the topology of the converter must be taken into account. In such cases, converters that have an inductance in series with the input source are preferable to those that employ a switch. Also, decoupling capacitors must be employed. However, for the boost converter topology, where an inductor is placed in series with the input power source, the possibility of using the TEM's internal inductor in order to reduce the number of additional components must be investigated.

The TEM's SPICE model employing the parasitic components has been simulated for both TEM types. In order to validate the model, a sine wave signal was generated by an ideal power source with the same amplitude as in the real system. In order to validate the simulation, the test frequencies were selected to be different (50 kHz and 150 kHz) than the ones used for computing the component values (100 kHz and 200 kHz). The simulation results proved to be in good agreement to the experimental ones, as presented below.

Figure 4.14 presents the simulation results for one TEG (number 3 in Table 4.1 – 4.3). The phase shift value predicted by the simulation – 17.83° was verified with the experiment, where the measured average phase value was 17.41° (Fig. 4.15).

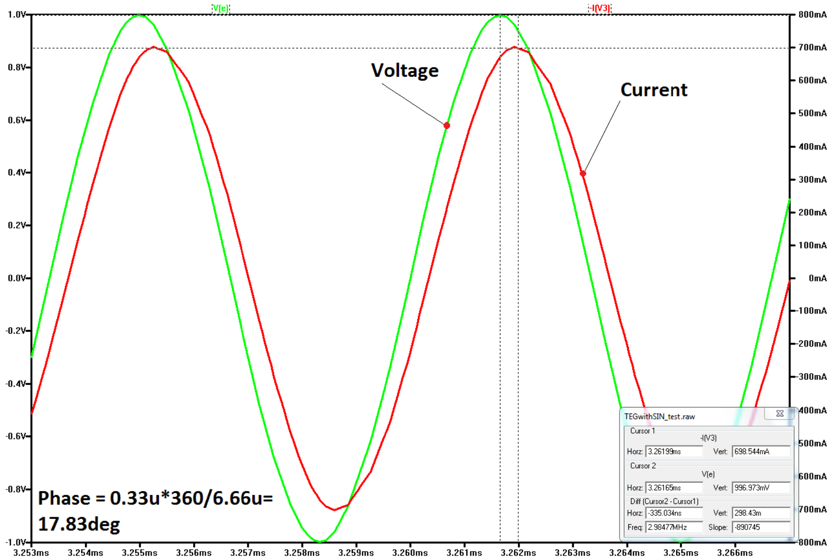

Phase = 0.33u*360/6.66u=
17.83deg

TEGwithSIN_test.raw

Cursor 1
-I(V3)
Horz: 3.26199ms Vert: 698.544mA

Cursor 2
V(e)
Horz: 3.26165ms Vert: 996.973mV

Diff (Cursor2 - Cursor1)
Horz: -335.034ns Vert: 298.43m
Freq: 2.98477MHz Slope: -890745

Figure 4.14 Phase shift simulation results for one TEG with $2V_{pp}$@150 kHz input signal. Source [original]

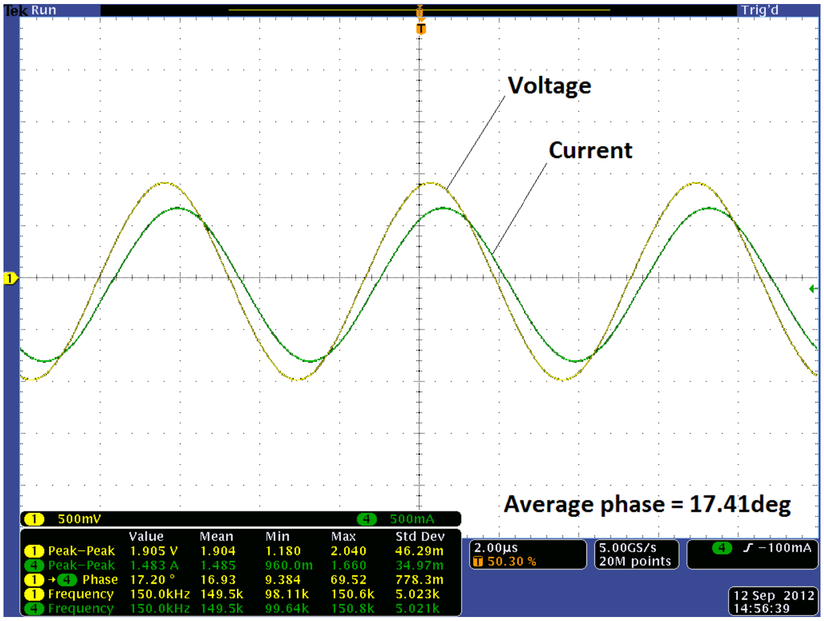

Average phase = 17.41deg

	Value	Mean	Min	Max	Std Dev
1 Peak−Peak	1.905 V	1.904	1.180	2.040	46.29m
4 Peak−Peak	1.483 A	1.485	960.0m	1.660	34.97m
1 → 4 Phase	17.20 °	16.93	9.384	69.52	778.3m
1 Frequency	150.0kHz	149.5k	98.11k	150.6k	5.023k
4 Frequency	150.0kHz	149.5k	99.64k	150.8k	5.021k

Figure 4.15 Phase shift for one TEG with $2V_{pp}$@150 kHz input. Source [experiment]

4.4 Experimental and simulation results in the isolated chamber

The results presented in Fig. 4.16 and 4.17 show the simulated temperature difference of the TEG sides for the Everredtronics module and the voltage on its terminals because this will be the normal scenario for this device and the correct output voltage prediction is of concern. The TEG was first connected to a 2.5V power source for 600s after which it was decoupled. The experimental testing process was explained at the end of Chapter 3.2.

The simulation results were compared to the experiment (Fig. 4.18) where the measured voltage value that corresponds to an arbitrary selected temperature difference (12℃) is 0.52V. It can be observed that the output voltage is better predicted by the varying parameters model (0.529V), the errors being in this case lower than 2%. For the constant parameters model, the error rises up to 12% (0.457V).

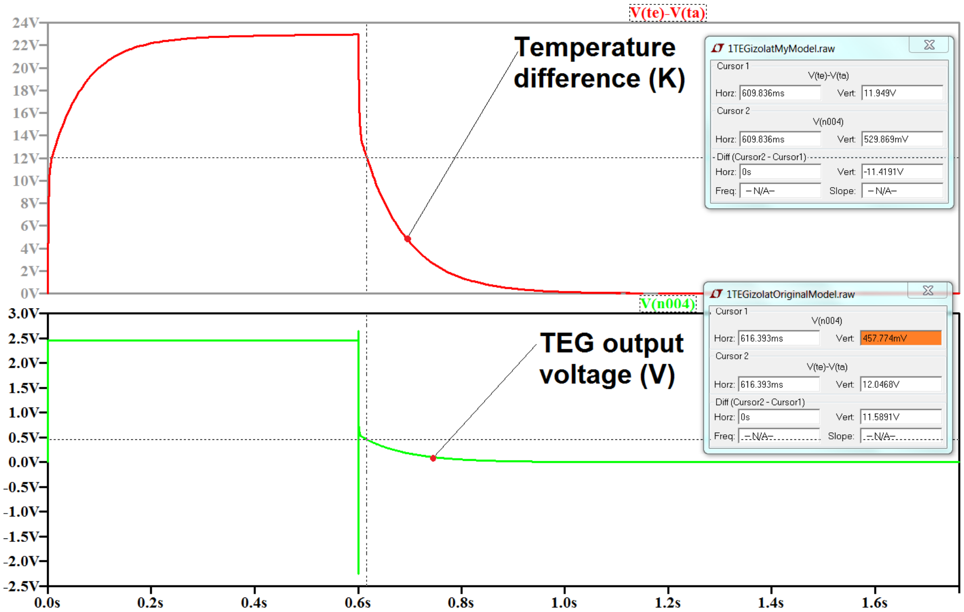

1TEGizolatMyModel.raw

Cursor 1 V(te)-V(ta) Horz: 609.836ms Vert: 11.949V

Cursor 2 V(n004) Horz: 609.836ms Vert: 529.869mV

Diff (Cursor2 - Cursor1) Horz: 0s Vert: -11.4191V

Freq: – N/A– Slope: – N/A–

1TEGizolatOriginalModel.raw

Cursor 1 V(n004) Horz: 616.393ms Vert: 457.774mV

Cursor 2 V(te)-V(ta) Horz: 616.393ms Vert: 12.0468V

Diff (Cursor2 - Cursor1) Horz: 0s Vert: 11.5891V

Freq: – N/A– Slope: – N/A–

Figure 4.16 Output voltage and temperature difference for the constant parameters TEG SPICE model. Source [original]

Figure 4.19 presents the same experiment conducted with the Melcor modules. In this case, an 8V power supply was fed to the TECs for a period of 1000s.

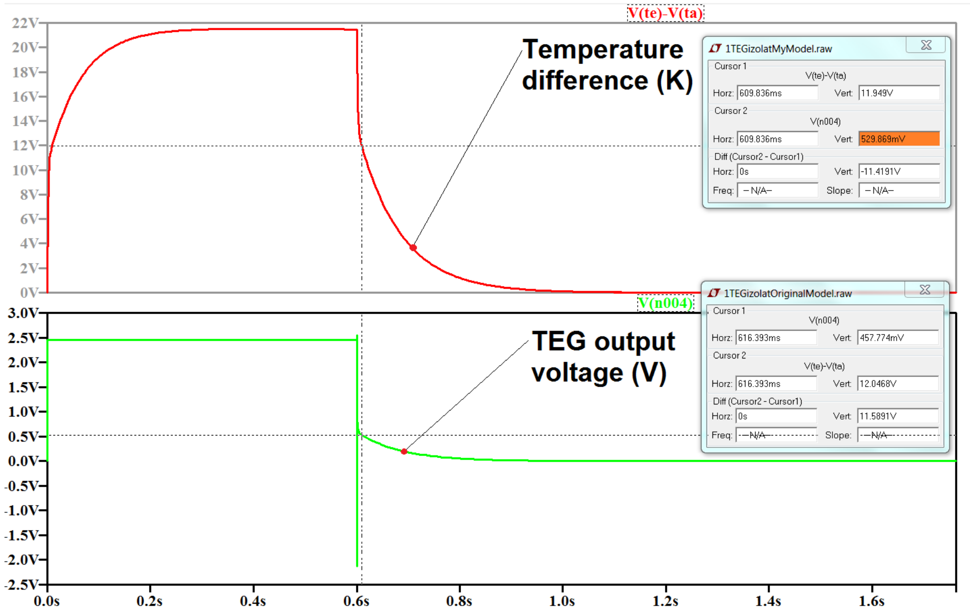

1TEGizolatMyModel.raw

Cursor 1
V(te)-V(ta)
Horz: 609.836ms Vert: 11.949V

Cursor 2
V(n004)
Horz: 609.836ms Vert: 529.869mV

Diff (Cursor2 - Cursor1)
Horz: 0s Vert: -11.4191V
Freq: – N/A– Slope: – N/A–

1TEGizolatOriginalModel.raw

Cursor 1
V(n004)
Horz: 616.393ms Vert: 457.774mV

Cursor 2
V(te)-V(ta)
Horz: 616.393ms Vert: 12.0468V

Diff (Cursor2 - Cursor1)
Horz: 0s Vert: 11.5891V
Freq: –N/A– Slope: –N/A–

Figure 4.17 Output voltage and temperature difference for the varying parameters TEG SPICE model. Source [original]

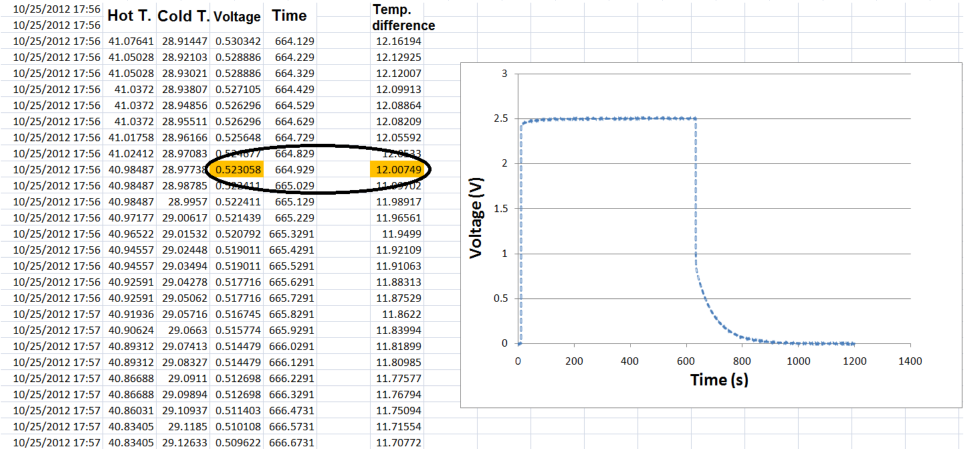

10/25/2012 17:56	Hot T.	Cold T.	Voltage	Time		Temp. difference
10/25/2012 17:56						
10/25/2012 17:56	41.07641	28.91447	0.530342	664.129		12.16194
10/25/2012 17:56	41.05028	28.92103	0.528886	664.229		12.12925
10/25/2012 17:56	41.05028	28.93021	0.528886	664.329		12.12007
10/25/2012 17:56	41.0372	28.93807	0.527105	664.429		12.09913
10/25/2012 17:56	41.0372	28.94856	0.526296	664.529		12.08864
10/25/2012 17:56	41.0372	28.95511	0.526296	664.629		12.08209
10/25/2012 17:56	41.01758	28.96166	0.525648	664.729		12.05592
10/25/2012 17:56	41.02412	28.97083	0.524677	664.829		12.0533
10/25/2012 17:56	40.98487	28.97738	0.523058	664.929		12.00749
10/25/2012 17:56	40.98487	28.98785	0.522411	665.029		11.99702
10/25/2012 17:56	40.98487	28.9957	0.522411	665.129		11.98917
10/25/2012 17:56	40.97177	29.00617	0.521439	665.229		11.96561
10/25/2012 17:56	40.96522	29.01532	0.520792	665.3291		11.9499
10/25/2012 17:56	40.94557	29.02448	0.519011	665.4291		11.92109
10/25/2012 17:56	40.94557	29.03494	0.519011	665.5291		11.91063
10/25/2012 17:56	40.92591	29.04278	0.517716	665.6291		11.88313
10/25/2012 17:56	40.92591	29.05062	0.517716	665.7291		11.87529
10/25/2012 17:57	40.91936	29.05716	0.516745	665.8291		11.8622
10/25/2012 17:57	40.90624	29.0663	0.515774	665.9291		11.83994
10/25/2012 17:57	40.89312	29.07413	0.514479	666.0291		11.81899
10/25/2012 17:57	40.89312	29.08327	0.514479	666.1291		11.80985
10/25/2012 17:57	40.86688	29.0911	0.512698	666.2291		11.77577
10/25/2012 17:57	40.86688	29.09894	0.512698	666.3291		11.76794
10/25/2012 17:57	40.86031	29.10937	0.511403	666.4731		11.75094
10/25/2012 17:57	40.83405	29.1185	0.510108	666.5731		11.71554
10/25/2012 17:57	40.83405	29.12633	0.509622	666.6731		11.70772

Figure 4.18 Experimentally determined output voltage and temperature difference. Source [original]

The difference between the two testing procedures of the two modules comes from the fact that the TEG device is supposed to generate voltage from a temperature gradient of maximum 250℃ (as the manufacturer specifies) but its maximum current is limited to 1A. Taking this into account, a lower voltage was fed to its input and for a shorter period of time, to prevent it from damage.

In the TECs case, the temperature values of the two sides were displayed because in the normal operation regime the device operates as a heat pump and what interests us is the temperature values.

The simulation results show in the case of varying parameters model a better approximation for the hot side temperature where the error is ~1% compared to 5% obtained when the constant parameters model was used. For the cold side temperature and on the heating period (t<1000s), the varying parameters model employs ~3% errors at its maximum, compared to the case of constant parameters model (~1.5%). However, in the region where the power source was decoupled (t>1000s) the varying parameters model offers a better prediction for the two temperature values (the error is with 50% lower) as it can be observed from Fig. 4.19. The error integral for the 2400s period is lower in the case of the varying parameters model.

The erroneous prediction of the cold side temperature can be explained by the thermal model of the mechanical test rig. The model presents some errors because approximations have been done to simplify its representation in one dimension. The errors are higher on the cold side of the test rig, where the mechanical parts are non homogenous.

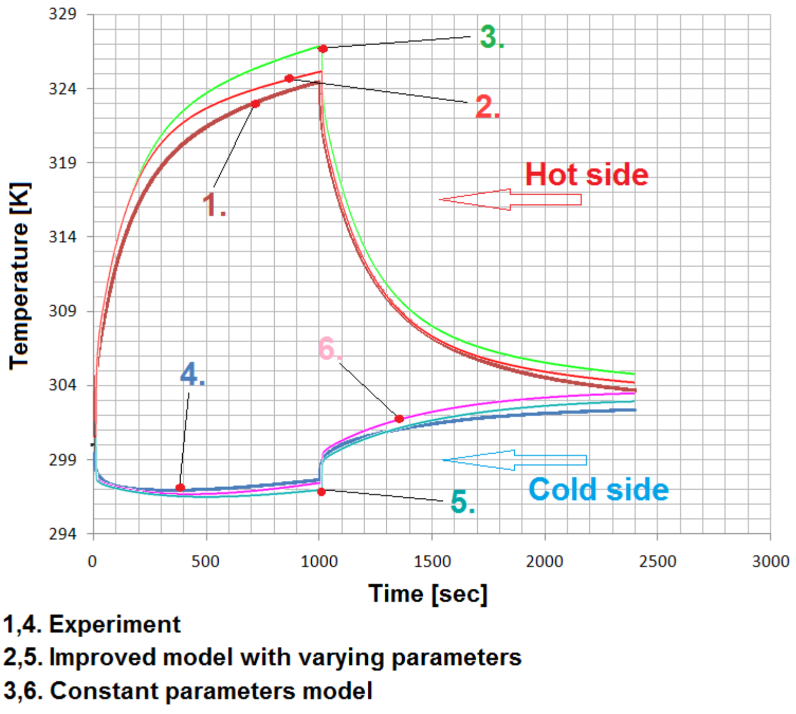

Figure 4.19 Experimental and simulation results conducted with the Melcor module in the isolated chamber. Source [original]

Figure 4.20 presents the temperature difference between the hot and cold sides of the TEC module versus time. The errors can also be observed in this case, the varying parameters model being able to better predict the temperature difference with errors of ~4% at t=1000s compared to the case when the constant parameters model is used (9% at t=1000s).It can be observed from Fig. 4.19 that as the average temperature rises, the hot side temperature prediction error increases if the constant parameters model is used. This behavior takes place because the variation of the internal parameters values with respect to the room temperature values is getting higher as the temperature rises.

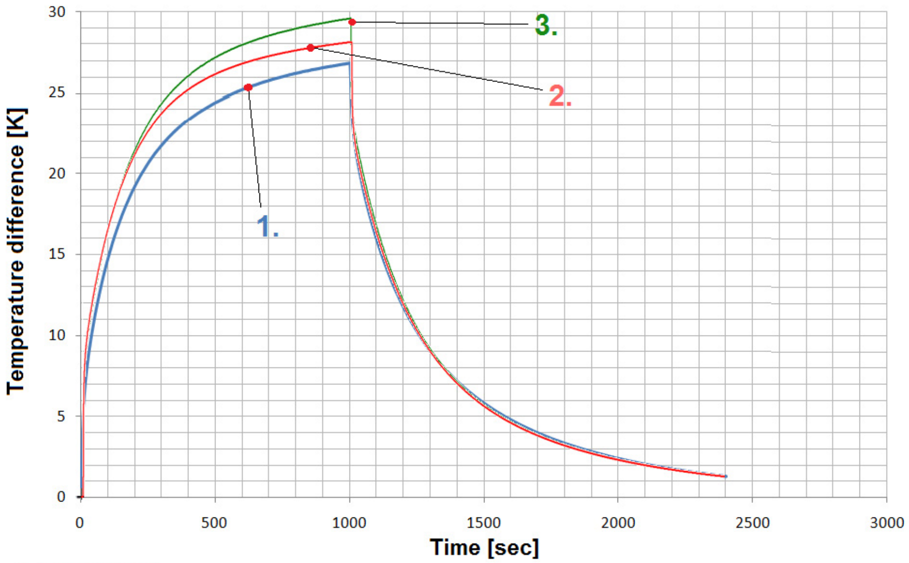

1. Experiment
2. Improved model with varying parameters
3. Constant parameters model

Figure 4.20 Experimental and simulation results of the temperature difference variation for the Melcor module. Source [original]

The two improved models are in conformity with the experimental results. The prediction for the Melcor model temperature difference value employs errors lower than 4%, which can be considered a good result.

4.5 Experimental and simulation results in natural environment

For the experiments conducted in natural environment, the test rig presented in Fig. 2.1 was placed in a controlled temperature room, with no additional air currents flow, where the temperature was set to 27℃. The Everredtronics TEG modules were selected for this experiment. The TEG’s output was floating, no load being connected to it.

The simulated SPICE model was presented in Fig. 3.10. The results are presented in Fig. 4.21.

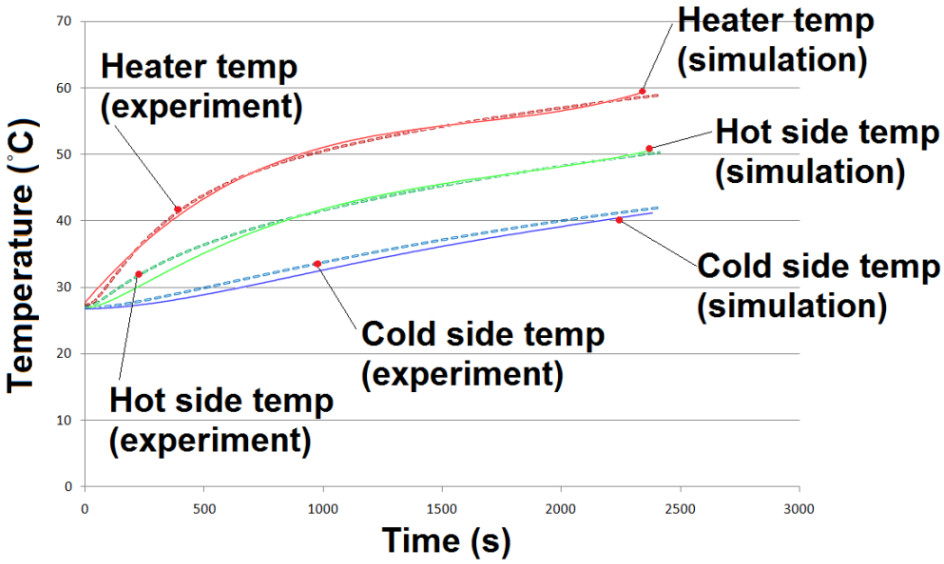

Figure 4.21 Experimental and simulation results presenting the temperature values inside the test rig when operating in natural environment. Source [original]

The experiment was conducted for 40 minutes and the heater, TEM’s hot and cold side temperatures values were recorded into a file. The resistive heater was connected to the P6100 voltage source programmed to output 40V, in order to rapidly heat the system. During the experiment, the test rig employed no thermosyphon, the cooling being assured only by the convective heat transfer between the system’s heatsinks and the environment.

The heater’s measured temperatures during the experiment were approximated with a 4th order fitting function. Afterwards, with the help of a custom built Javascript application, the fitting function was used to rescale the measured temperature values and generate a .txt file containing (temperature - time) pairs. The .txt file was used as an input for the V_1 source (explained in Table 3.5) from the SPICE model that implements the temperature values of the heater, at predefined time points.

The results presented in Fig. 4.21 show that the approximation function of the heater’s temperature is not precisely following the real values. However, the simulation results of the hot side’s temperature are in accordance with the experiment (1% errors), while ~4% errors are being observed at the cold side of the module at t=1000s. The SPICE model of the test rig’s cooling side that required a discretization employs reductions that are clearly visible in the simulation’s output results, as also shown in the previous simulations (Fig. 4.19).

The increased homogeneity of the test rig’s hot side makes the simulated hot side temperature accurately predict the real behavior of the system.

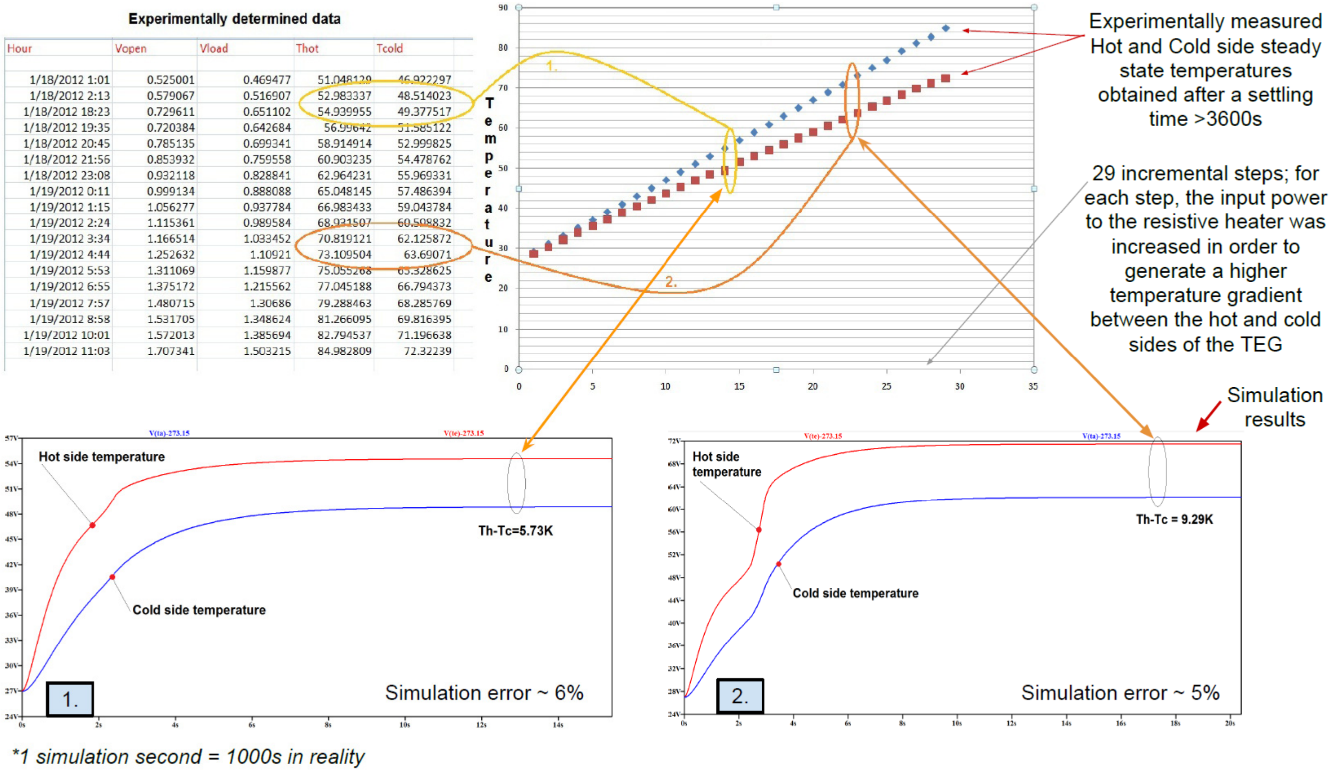

Experimentally determined data

Hour	Vopen	Vload	Thot	Tcold
1/18/2012 1:01	0.525001	0.469477	51.048129	46.922297
1/18/2012 2:13	0.579067	0.516907	52.983337	48.514023
1/18/2012 18:23	0.729611	0.651102	54.939955	49.377517
1/18/2012 19:35	0.720384	0.642684	56.99642	51.585122
1/18/2012 20:45	0.785135	0.699341	58.914914	52.999825
1/18/2012 21:56	0.853932	0.759558	60.903235	54.478762
1/18/2012 23:08	0.932118	0.828841	62.964231	55.969331
1/19/2012 0:11	0.999134	0.888088	65.048145	57.486394
1/19/2012 1:15	1.056277	0.937784	66.983433	59.043784
1/19/2012 2:24	1.115361	0.989584	68.931507	60.508832
1/19/2012 3:34	1.166514	1.033452	70.819121	62.125872
1/19/2012 4:44	1.252632	1.10921	73.109504	63.69071
1/19/2012 5:53	1.311069	1.159877	75.055268	65.328625
1/19/2012 6:55	1.375172	1.215562	77.045188	66.794373
1/19/2012 7:57	1.480715	1.30686	79.288463	68.285769
1/19/2012 8:58	1.531705	1.348624	81.266095	69.816395
1/19/2012 10:01	1.572013	1.385694	82.794537	71.196638
1/19/2012 11:03	1.707341	1.503215	84.982809	72.32239

Experimentally measured Hot and Cold side steady state temperatures obtained after a settling time >3600s

29 incremental steps; for each step, the input power to the resistive heater was increased in order to generate a higher temperature gradient between the hot and cold sides of the TEG

Simulation results

**1 simulation second = 1000s in reality*

Figure 4.22 Experimental and simulation results presenting the stabilized temperature values inside the test rig when functioning in natural environment. Source [original]

Figure 4.22 presents the situation when the system has reached thermal equilibrium. In this case, the hot and cold side temperatures have been recorded into a file. This experiment is necessary to test the correct implementation of the convective heat transfer model that is supposed to cool the system to a certain temperature. Two different scenarios are presented, the first when the hot side temperature of the TEG reached 54℃ and the second when it has been regulated to 71.9℃. It can be observed that the cold side temperature is in both cases in good correlation to the experiment, the errors being ~6%.

If the convective heat transfer wouldn't be implemented and the system would be simulated as being in an isolated closed chamber, the hot and cold side temperatures would eventually reach the same equilibrium value.

The results presented in Fig 4.21 and 4.22 demonstrate the good correspondence between the implemented model and the experiment.

For the case when the experiment with the resistive heater is performed in an isolated environment (the isolated chamber from Fig. 2.6), the error that appears in the thermal model of the test rig is depicted.

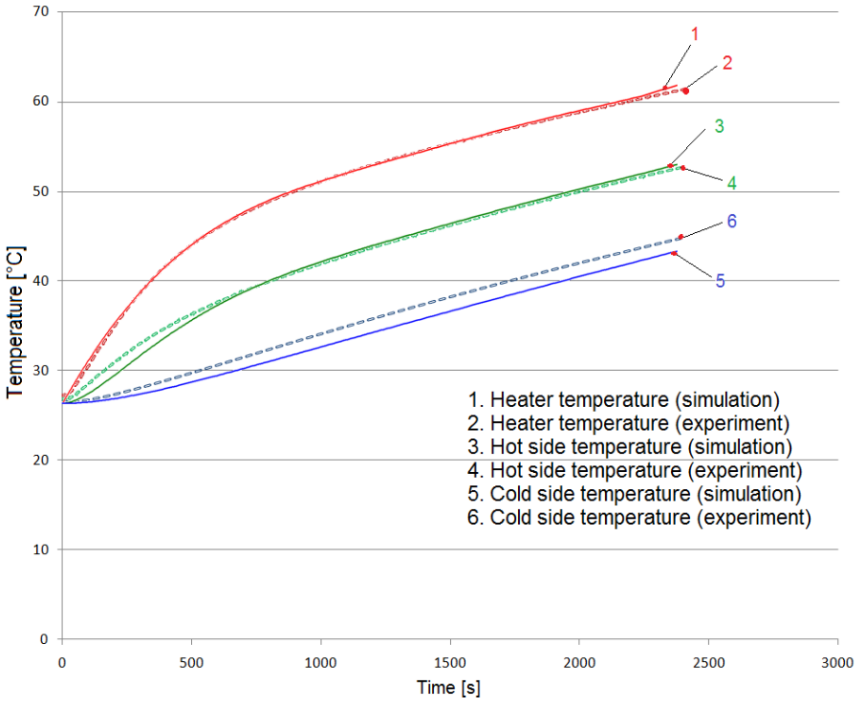

Figure 4.23 Experimental and simulation results presenting the temperature values inside the test rig when functioning in an isolated environment. Source [original]

It can be observed that the highest error appear on the cold side of the test rig (~6% at t=1000s), a similar behavior as in Fig. 4.21.

4.6 TEM behavior under AC input signal

The calculated heat capacity of the TEM modules and the behavior explained at the end of Chapter 2.5 are related. Because of the internal heat capacity of the module, the TEC's sides' temperatures cannot follow an AC applied voltage beyond a certain frequency (approximately 1 Hz in the current case). In order to reproduce this behavior, the TEC was placed between two polystyrene insulating boards and on each side an NTC thermistor was attached. High conductivity thermal grease was used at the contact point between the sensors and the TEC's sides for increased measurements accuracy. A 100 kHz sine wave of 2V peak-to-peak amplitude was fed using the custom built amplifier (Fig. 2.20) and a signal generator. The setup is presented in Fig. 4.24.

In the simulation model, the signal generator and power amplifier were replaced by an ideal AC power source. The internal resistance, Seebeck coefficient and thermal conductance of the TEC under test were considered constants as no temperature difference was created during the experiment. The internal heat capacity was implemented as presented in Fig. 3.3 and 3.4. The insulation boards were represented by two thermal resistances and their values were calculated taking into account the boards dimensions and material properties.

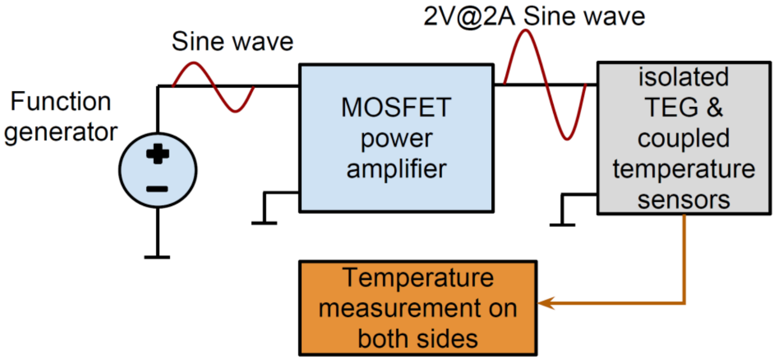

Figure 4.24 Experimental setup for determining the TEG's behavior under AC input signal. Source [original]

The simulation and experimental results are presented in Fig. 4.25.

The results are in conformity to the experimental ones and they prove that above a critical frequency, the TEM starts acting like a resistor, where the Joule effect is observed through the released heat. Below the critical frequency, the module's hot and cold side temperatures are able of "tracking" the applied AC voltage as it can be seen in Fig. 4.25.

Figure 4.26 shows how the temperatures on each side of the TEM have a sinusoidal variation. The simulation and experimental temperature values are in phase, the temperature mean values being also similar. However, the instantaneous temperature value in simulation is higher than in the experiment.

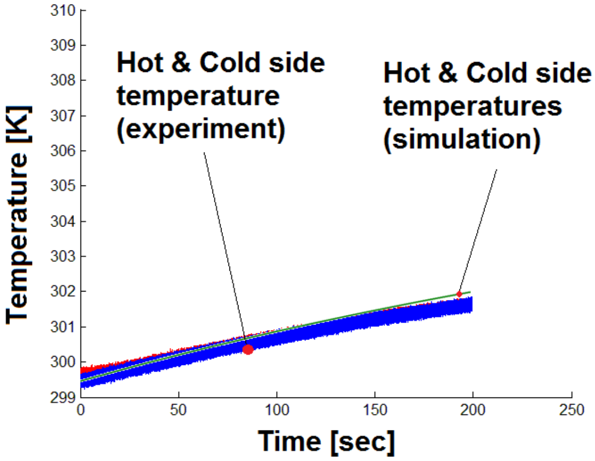

Figure 4.25 Temperature variations on TEC's sides with $2V_{pp}$@100kHz AC signal as input. Source [original]

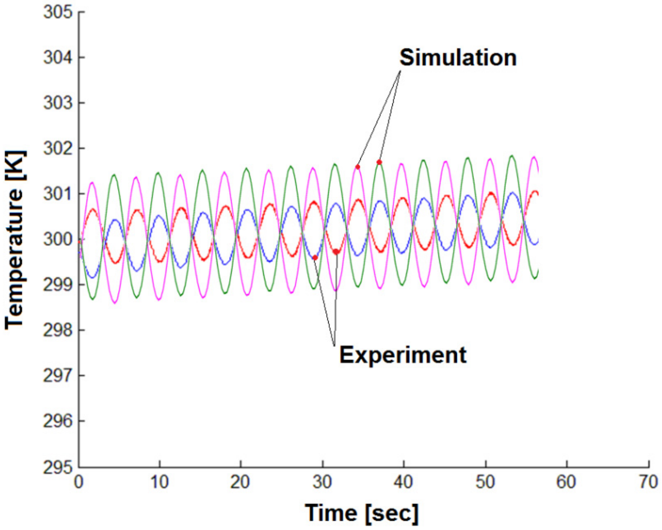

Figure 4.26 Experiment and simulation of the TEC's sides temperatures with $4V_{pp}$@0.2Hz input signal. Source [original]

In the simulations, the variation of the Seebeck coefficient and internal resistance with temperature were not taken into account and also, the Thomson coefficient was neglected. These simplifications lead to some errors than affect the simulation model temperature prediction.

4.7 Conclusions

In this chapter, a comparison was performed between the experimental results and the simulation models that were built to reproduce the TEM's behavior in a real system and in natural environment.

The proposed cooling solution, that uses a thermosyphon and distilled water as cooling agent, proved efficient and increased the temperature difference by 40%, which in turn resulted in an increased TEM output voltage. A TEM based energy harvesting device efficiency should be considered by taking into account both the TEM's efficiency and the cooling ability of the mechanical system. The Everredtronics TEG employs the maximum efficiency at the maximum rated temperature difference. This requires a special care in the design of the cooling system in order to improve its efficiency.

The experiments conducted for determining the Seebeck coefficient and internal resistance of the two TEM manufacturers revealed that the TEG's parameters have an increased variation with temperature in comparison to the TEC's parameters. This has a direct impact on the simulation models and on the differences between the constant parameters model and varying parameters one. As the parameters have a low variation with temperature, then they can be considered as constants. As shown in the experiments, the TEC's internal resistance varied with 15% (at the highest temperature attainted in the experiments) compared to the room temperature value. For the TEG module, the difference was of 21%.

The thermal conductance was experimentally measured for both module types and for the Melcor module, the results proved to be in agreement with the datasheet values. The thermal conductance variations with respect to the temperature difference showed a measured resolution between two consecutive values of 0.7%, which can be considered a very good result taking into account the measurement errors and the heat losses. The experimental results were validated by comparison with the datasheet values provided by the Melcor product.

A model was proposed for the internal parasitic inductances and capacitances of a TEM. The phase shift method was used to determine the parasitic components. First, the phase between voltage and current was measured and the results at two different frequencies (100 kHz and 200 kHz) were used to solve a system of equations in order to obtain the parasitic L_{peq} and C_{peq} values. The parasitic components were added to the SPICE model of the TEM and the simulation results were compared to the experiment. A frequency of 150 kHz was used for the comparison and the simulation results were in conformance with the experimental one within 2.5% error. The presence of the inductance and capacitance is of great importance when dealing with DC-DC converters and energy harvesting devices based on TEM's. As the frequency of operation of such converters is continuously increasing (>1MHz) in order to reduce the size and weight, the topology of the converter becomes important and must be taken into account if the input power source (in this case TEMs) employs an inductance. At high frequencies, a 0.6μH parasitic series inductance (the highest measured value for a TEG) becomes important and a DC-DC converter with a bypassing input capacitor and series inductance is desired. The Buck-Boost topology that employs a switch in series with the input power source should be used with care because transient input voltages will appear due to the parasitic TEM's internal inductance.

For both manufacturers modules (TEG and TEC), the experiments and simulations were first performed in the isolated chamber. The errors when the parameters were considered constant are higher for the TEC module (9%), compared to the case where the parameters variation was added to the simulation model (4%). The errors were considered at the maximum temperature difference that was measured in the experiments, but as it can be seen from Fig. 4.19 - 4.20 the error will increase as the temperature difference increases. For the Everredtronics TEG module, the parameters have a higher variation versus temperature difference, therefore the constant parameters model will generate higher errors (12%) compared to the varying parameters model (2%). For the TEG module, the output voltage was represented because it is the output value of interest (TEM working as voltage generator) while for the TEC module, the temperature values are important (TEM as heat pump).

The simulation results of the system in natural environment, where the convective heat transfer was implemented in the SPICE model, show that the model is in conformity to the experiment, the highest error (~4%) in this case being reported at the cold side of the TEG. The hot side temperature predicts the real behavior with 1% errors. Taking into account the experiments in the isolated chamber presented in Fig. 4.19, 4.21 and 4.23 it can be observed that the cold side temperature of the TEM is in all the cases approximated with higher errors than the hot side. This behavior can be explained by the non-homogeneity of the cold side mechanical structure. The discretization of the cold side mechanical parts supposed a series of reductions out of which the ***E*** chamber that employs the cooling pipes was approximated only by three discrete parts. Because of the internal empty spaces filled with air, this discretization proves not to be enough if a precise model is of concern. The steady state temperature simulation of the TEGs system that is operating in natural environment shows a maximum error of 6% that can be considered a good result.

The simulation of the temperature variation on the TEC's sides proved that the internal heat capacity of the module allows the TEM to follow an applied AC voltage and generate alternating temperatures on its two sides. Beyond the critical frequency, the module is not able of generating alternating temperatures; instead, it will only release heat due to the Joule effect and will act like a resistor.

4.8 Contributions

1. **Experimental measurements have been conducted in order to determine the internal parameters variation with temperature for two different TEM types (TEG & TEC), including the intrinsic parasitic inductance and capacitance values that were not taken into account so far.**
    - The simulation results obtained for the existent TEM model were compared to the experimental data and to the new TEM model in order to highlight the increased accuracy of the latter.

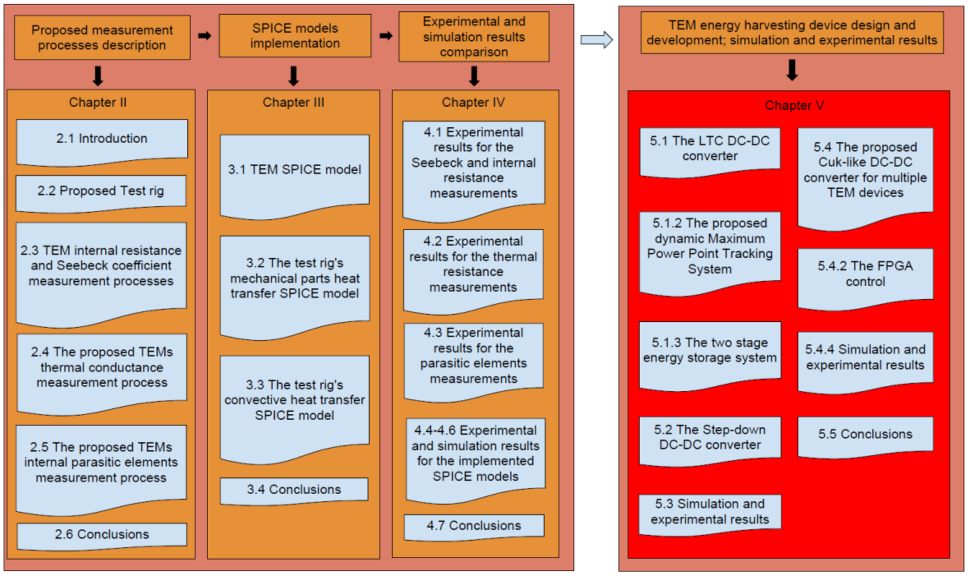

Chapter 5

The proposed energy harvesting system

This chapter presents the implementation of the proposed energy harvesting system. Two novel solutions for a dynamic maximum power point tracking system are simulated and implemented in practice. The energy harvesting system is simulated and the results are compared to the experimental data. An improved Cuk converter is simulated and built. The converter aims to harvest the energy from multiple serial coupled TEGs and store it into rechargeable batteries.

5.1 The LTC3105 DC-DC converter

In Chapter II, a modular test stand was proposed for TEM's parameters extraction, that can also be used in an energy harvesting system. In the following the proposed system will be described together with its SPICE model and the simulation results that takes advantage of the TEM improved SPICE model presented in Chapter 3.1.
The system purpose is to harvest unused heat, convert it to electrical energy and store it into rechargeable batteries. The energy stored is to be used in sensor measurements and long range data transmission.

The energy harvesting system is comprised of two major units. The main unit was presented in Fig. 2.1. The second unit contains the electronics necessary to convert the electrical power generated by the TEGs and store it into rechargeable batteries.
The electronics from the second unit is built around the LTC 3105 Step-Up DC-DC converter. This device allows a low start-up voltage of only 250mV with adjustable output voltage from 1.5 to 5.25 V. Its internal block diagram is presented in Fig. 5.1.

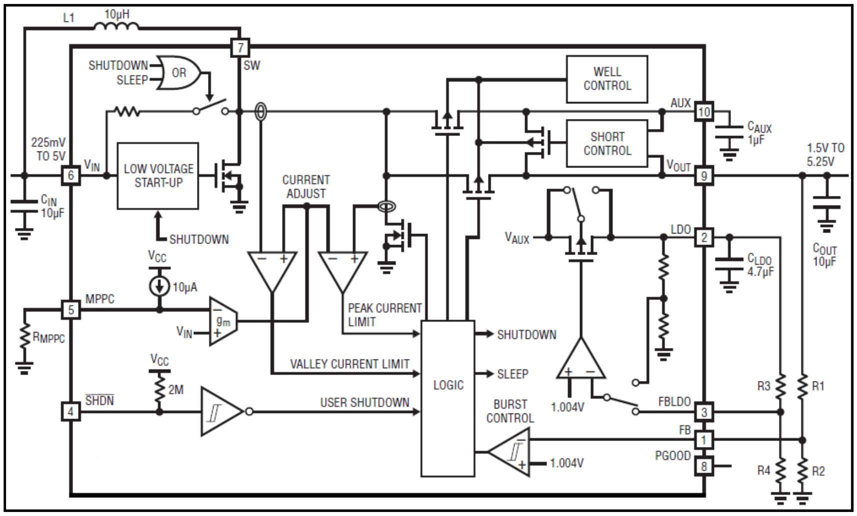

Figure 5.1 Internal block diagram of the LTC 3105 DC-DC converter. Source [44]

An important function of the LTC3105 is the built-in maximum power point tracking controller (MPPT) that enables the operation from low voltages and high impedance sources such as TEGs. This circuit allows the user to set the optimal input voltage operating point for a given power source [44], controlling the inductor current to maintain V_{in} at the voltage set on the MPPT pin. The converter features an auxiliary LDO regulator that can output 6mA@2.2V and can be used as energy source for a low power microcontroller. The datasheet states that the maximum attainable current on the LDO pin is limited to 12mA.The LTC3105 has been optimized for use with high impedance power sources like thermoelectric generators [44].

The energy harvesting system proposed in this work employs two serial connected TEGs (Fig. 2.1). Although the LTC3105 can be used with multiple stacked power sources, the number is limited by the output voltage of 5.25V and the current limit of 400mA. If more than two TEGs are used as input power source, the maximum attainable temperature is to be taken into account as the input voltage needs to have a lower value than the output setpoint for the normal operation of the LTC3105. The proposed setup consists of two serial connected TEGs that provide a maximum of 2.9V at ΔT=23℃, as presented in Fig. 4.1

Taking into account that the internal parameters of the TEM (internal resistance, Seebeck coefficient, thermal conductance) vary with temperature (Fig 4.3), an autonomous way to track the maximum power point must be developed. The LTC3105 datasheet presents a couple of standard connections that take advantage

of the internal current source of 10μA. The internal current source together with an externally connected resistor or diode generates a voltage on the MPPC pin that represents the minimum value the V_{in} pin is maintained in order to extract the maximum power from the energy source. The converter datasheet [44] presents a photovoltaic energy harvesting solution where the temperature tracking is made with the help of diodes that are thermally coupled to the photovoltaic panel (PV). In PV panels, the output voltage is inversely proportional to the temperature; moreover the output voltage of a TEG has a stronger variation with temperature than the PV does. This solution cannot be used on TEGs, or in the current proposed system where the output voltage varies from 0V to 3V.
In the present topic, two dynamic maximum power point tracking systems are described and implemented. The circuits are intended to be used together with the LTC3105 converter and TEG power sources. The devices purpose is to charge Ni-Mh or Li-Ion batteries although the generated output power can be used to charge a super-capacitor, like the LTC converter's datasheet specifies [44].

5.1.1 The original dynamic MPPT system that uses the existing microcontroller

The dynamic maximum power point tracking system takes advantage of the microcontroller existing on the equipment (Fig. 5.2). A thermistor that is thermally coupled with the TEGs is used to determine the actual hot side temperature.

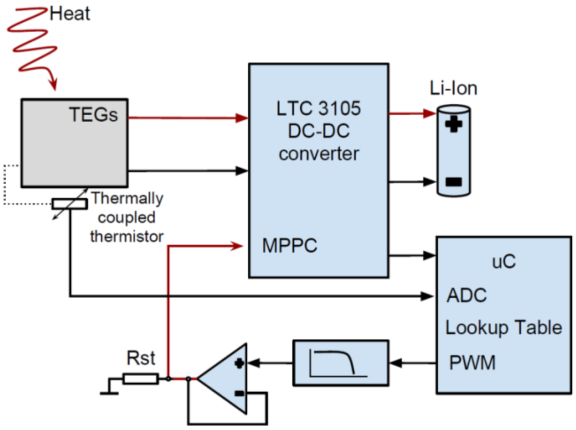

Figure 5.2 Proposed dynamic maximum power point tracking system that takes advantage of the microcontroller. Source [original]

A lookup table is implemented and stores the {output voltage, temperature value} pairs. The lookup table is used to compute the actual output voltage of the TEGs, based on the measured hot side temperature. Afterwards, the PWM output of the microcontroller together with an RC low pass filter is used as a DAC circuit to generate an output voltage. The operational amplifier (OA) connected in follower configuration is used to isolate the DAC output from the R_{st} resistor. This configuration is needed when the microcontroller is not powered by the LTC3105 LDO regulator. If the existent heat source that powers the TEGs is not providing enough energy, the microcontroller will have no supply voltage. If the wasted heat energy increases and the TEGs output exceeds 0.3V, the internal 10μA current source becomes active and the LTC converter will try entering the normal operation mode. However, at this point, the **V_{MPPC}** voltage is of great importance because if no resistance is connected at its output, the converter will not be able to enter the normal operation mode [44]. The output voltage at the V_{MPPC} pin is given by the 10μA internal current source and the resistor connected to the MPPC output ($V_{MPPC} = R_{st} \cdot 10\mu A$). This voltage represents the minimum value the input voltage is maintained in order to extract the maximum available power. As known, the maximum power extracted will occur when the load resistance equals the source resistance, or $V_{in} = \frac{V_{noLoad}}{2}$, where V_{in} is the LTC3105 input voltage and V_{noLoad} is the output voltage of the TEG when no load is connected to it. In this way, when no power is available on the LDO output, the R_{st} resistor will allow the converter to start operating from $V_{in} = 2 \cdot R_{st} \cdot 10\mu A$. After entering the normal operation mode when the microcontroller will be powered by the LDO output, the prescribed value for the V_{MPPC} pin will be provided by the microcontroller and the DAC circuit, based on the temperature measurement. The OA follower has a second purpose in this case, that of sinking the 10μA the MPPC pin is sourcing.

5.1.2 The second original analog dynamic MPPT system

In most cases, an analog solution, microcontroller free is desirable, due to several constraints that depend on the microcontroller's peripherals (e.g. only one PWM) or because specific designs employ no microcontroller. A completely autonomous analog solution for tracking the maximum power point is introduced in Fig. 5.3.

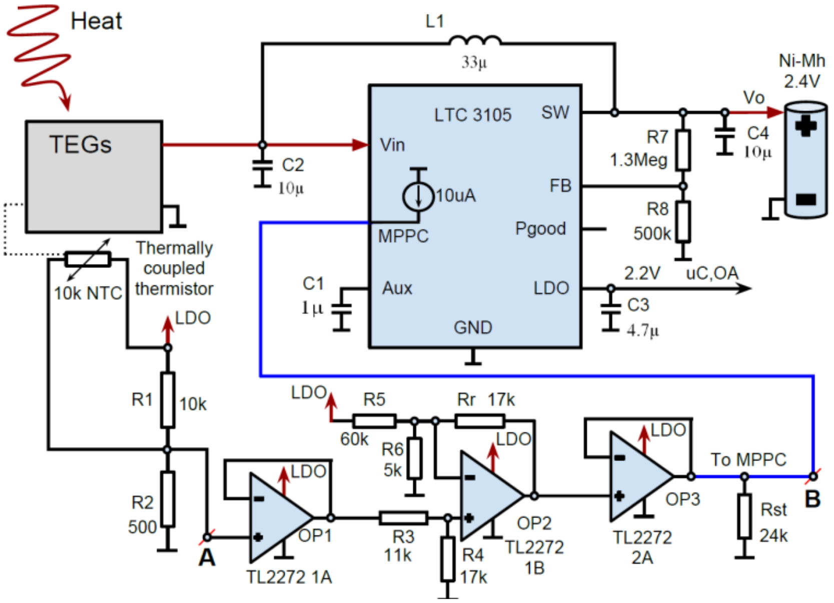

Figure 5.3 Dynamic Maximum Power Point Tracking system. Source [original]

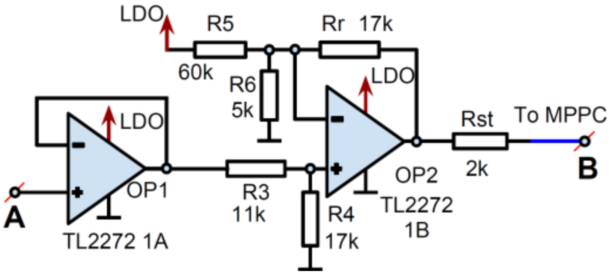

Figure 5.4 Alternative solution to dynamic MPPT system using a single OA IC (dual OA package). Source [original]

The novelty of the circuit is to use a NTC thermistor and linearize its variation with $\boldsymbol{R_1}$ and $\boldsymbol{R_2}$ resistors. The necessary output offset adjustment is performed by modifying the gain of $\boldsymbol{OP_2}$ operational amplifier (OA). OP_1 is connected as a follower and has the purpose to isolate the $\boldsymbol{R_3}$ and $\boldsymbol{R_4}$ resistors from $\boldsymbol{R_1}$, $\boldsymbol{R_2}$ and **thermistor**. $\boldsymbol{R_{st}}$ is a startup resistor that permits the LTC3105 to start functioning even if $\boldsymbol{OP_1}$, $\boldsymbol{OP_2}$ and $\boldsymbol{OP_3}$ are not powered. This is necessary if the battery is depleted and the LDO output voltage setpoint was not reached by the converter to power the operational amplifiers. In case no voltage is applied to $\boldsymbol{OP_1}$, $\boldsymbol{OP_2}$ and $\boldsymbol{OP_3}$, the voltage on the $\boldsymbol{V_{MPPC}}$ input is $R_{st} \cdot 10\mu A = 240mV$. $\boldsymbol{OP_3}$ is used as a second follower and has the purpose to isolate the rest of the resistor network from $\boldsymbol{R_{st}}$. It also ensures that the voltage on the MPPC pin is $R_{st} \cdot 10\mu A$ when no voltage is present on $\boldsymbol{V_o}$ output. After entering normal operation mode, when the output voltage reaches the setpoint value (2.2V in the actual case), $\boldsymbol{OP_1}$, $\boldsymbol{OP_2}$ and $\boldsymbol{OP_3}$ will be powered by the LDO output of the LTC converter. If the $\boldsymbol{V_o}$ output of the LTC converter wouldn't be used to power a battery, this output could be used as a supply voltage for $\boldsymbol{OP_1}$, $\boldsymbol{OP_2}$ and $\boldsymbol{OP_3}$. When a battery is charged by the LTC converter's output, the output voltage $\boldsymbol{V_o}$ will be influenced by the variable battery voltage (e.g. 2.1V when the battery is discharged and more than 2.4V when it is fully charged, as measured in the current experiments). This variation will cause an erroneous $\boldsymbol{V_{MPPC}}$ output, resulting in a lower efficiency in extracting the maximum available power.

In order to determine the correct slope for the output voltage of the $\boldsymbol{OP_2}$ amplifier versus temperature, to linearize the NTC variation and determine the $\boldsymbol{R_{st}}$ value, a NI LabView VI application (Fig. 5.5) was developed to dynamically select the components values. This solution was adopted because it was considered a fast method to obtain a visual feedback of the output in response to the modified values. The upper left corner graph from Fig. 5.5 presents the output voltage corresponding to the positive input pin of $\boldsymbol{OP_1}$ follower (Fig. 5.3). In the lower left corner the thermistors' characteristic function of temperature is presented. The graphic on the right side of Fig. 5.5 shows the output voltage of $\boldsymbol{OP_2}$ which is the prescribed voltage for the MPPC pin. The voltage output variation is represented as a function of TEGs hot side temperature. The offset and slope values can be adjusted from the $\boldsymbol{R_3}$, $\boldsymbol{R_4}$, $\boldsymbol{R_5}$, $\boldsymbol{R_r}$ resistors presented in Fig. 5.5. The resistors values are represented as sliders in the VI application from Fig. 5.5. The values are modified until the voltage - temperature variation corresponds to the experimentally determined characteristic.

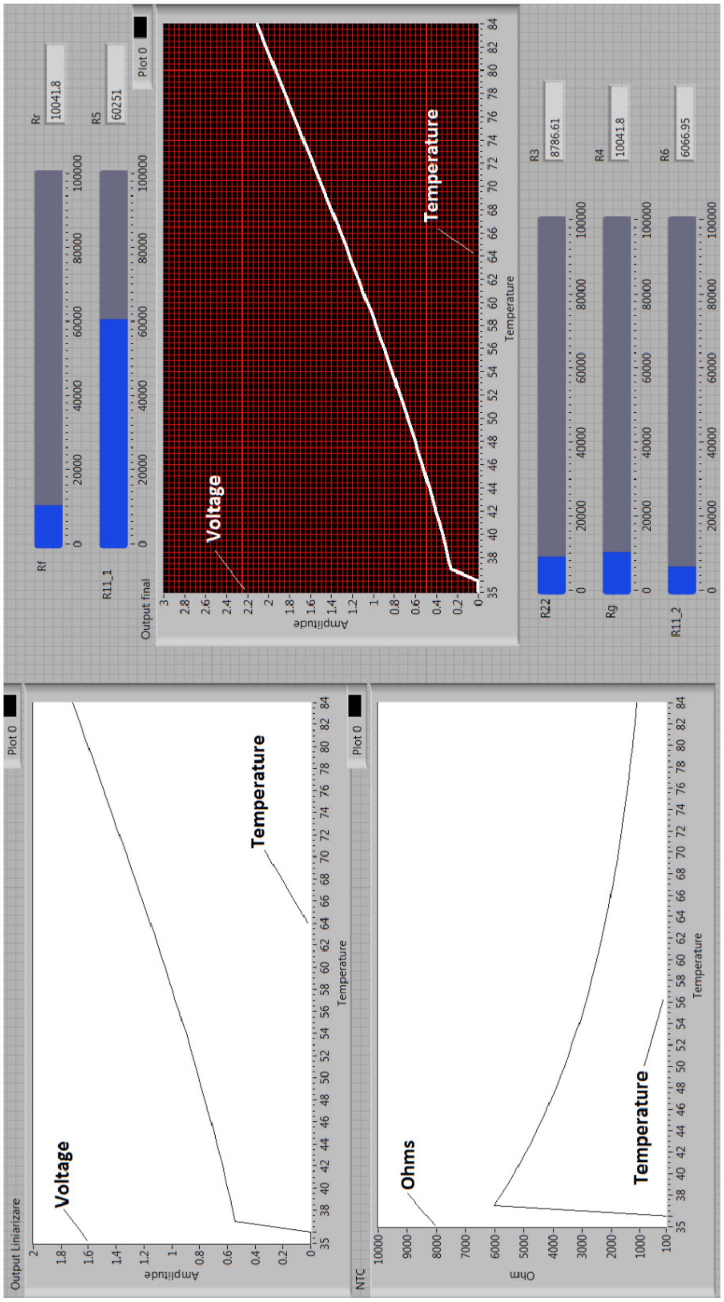

Rf 10041.8

R5 60251

R3 8786.61

R4 10041.8

R6 6066.95

Figure 5.5 LabView VI front panel describing the voltage-temperature characteristic at the output of *OP2* operational amplifier. Source [original]

Eventually, a simpler solution is possible (Fig. 5.4). Manipulating the values of the resistors, the same functionality can be achieved using only a single OA IC. The operation (when no voltage is present on the V_o output) is based on the equivalent resistance seen on the $\boldsymbol{V_{MPPC}}$ pin. The voltage on $\boldsymbol{V_{MPPC}}$ becomes:

$$\left(R_{st}+R_r+\left(R_5+\left(R_{thermistor}//R_1+R_2\right)\right)//R_6\right)\cdot 10\mu A \simeq 230mV$$

Both solutions offered the same functionality in the tests performed.

The circuits were first simulated in LTspice simulation software (Fig. 5.6).

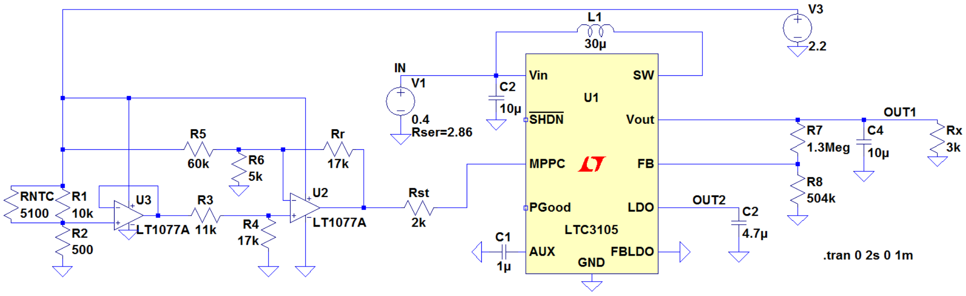

Figure 5.6 Simulation model of the proposed dynamic MPPT system and the LTC converter. Source [original]

The circuits were both implemented and the TEM operating under heat flux was emulated through a programmable power source and a potentiometer (Fig. 5.7). The control of the power source was implemented using LabVIEW and the measurements were made using the NI DAQ 6251.

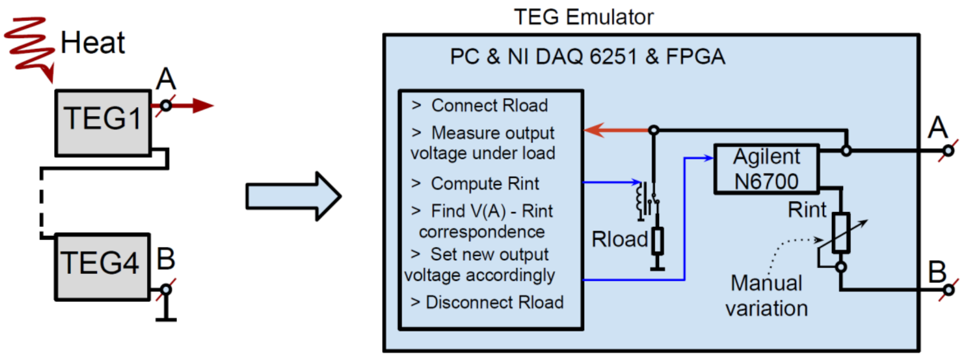

Figure 5.7 TEG emulator using a manual potentiometer and a programmable N6700B power supply. Source [original]

The implemented TEG emulator disconnects the A point (Fig. 5.7) from the rest of the circuit with the help of a relay. Afterwards, the R_{load} resistor is connected and the dropout voltage is measured, in this was computing the R_{int} resistor value. Using the lookup table, the corresponding output voltage is prescribed to the Agilent N6700 power source. The data from the lookup table was experimentally determined and presented in Fig. 4.1 - 4.5. By varying the internal resistance of the TEM, the behavior of the real device is emulated. According to the TEM's sides temperature difference, the output voltage and internal resistance changes.

For the steady-state behavior test, three voltages (0.4V, 1V, 2.2V) where fed to the LTC input and the output current was measured with a current probe on a variable resistive load. The maximum current was recorded up to the point where the output setpoint voltage remained at the prescribed value (3.6V). The output currents of 1.1mA, 10.5mA and 50mA respectively were accordingly to the simulation results with the same inputs and same output resistive loads. The simulation and experimental results for 1V input voltage are presented in Fig. 5.8 – 5.9.

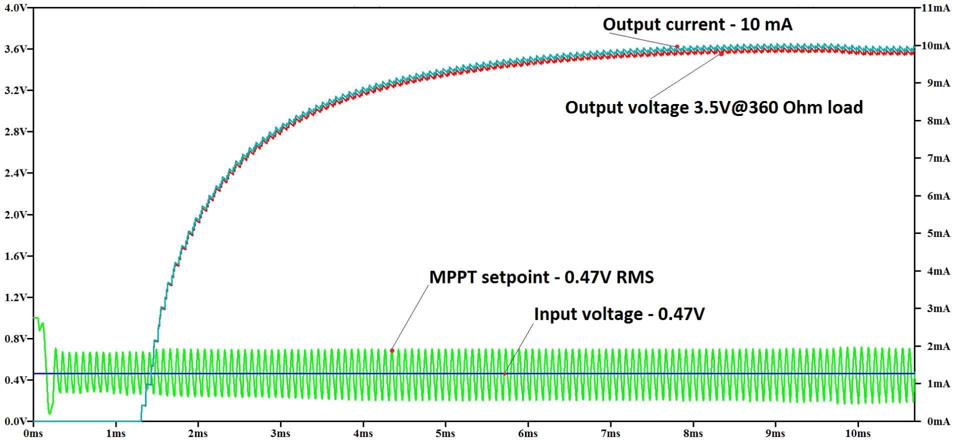

Figure 5.8 Simulation results for 1V input and 360Ω load. Source [original]

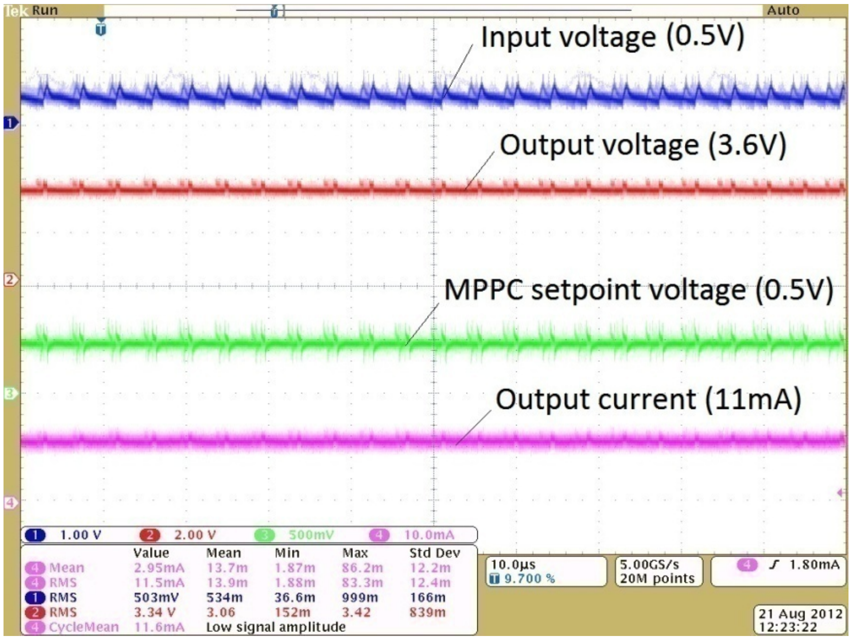

	Value	Mean	Min	Max	Std Dev
4 Mean	2.95mA	13.7m	1.87m	86.2m	12.2m
4 RMS	11.5mA	13.9m	1.88m	83.3m	12.4m
1 RMS	503mV	534m	36.6m	999m	166m
2 RMS	3.34 V	3.06	152m	3.42	839m
4 CycleMean	11.6mA	Low signal amplitude			

Figure 5.9 Practical implementation results for 1V input and 360Ω load. Source [original]

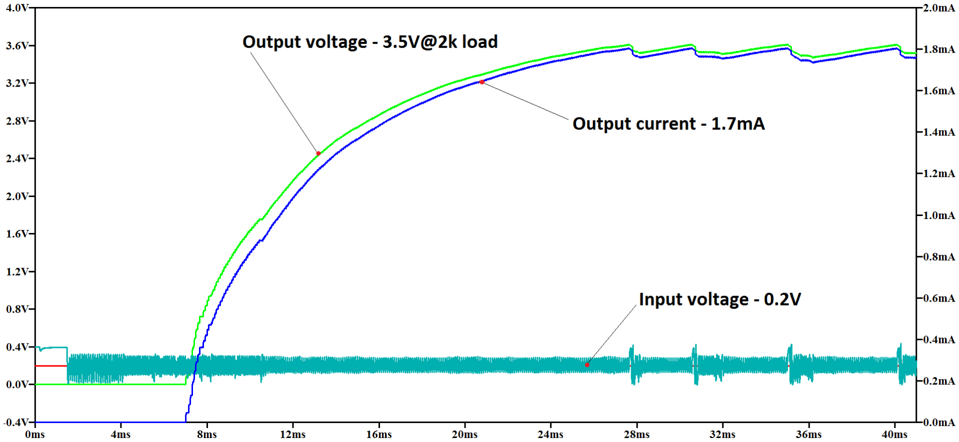

Figure 5.10 Simulation results for 0.4V input and 2kΩ load. Source [original]

The dynamic tracking was also verified with the real system, the circuits being first tested without the output battery that would have powered the operational amplifiers. The dynamic MPPT proved to operate as expected with both configurations presented in Fig. 5.3, 5.4 and was able to maintain the maximum output current.

5.1.3 The original energy harvesting system employing dynamic maximum power point tracking and a two stage energy storage system.

Figure 5.11 presents the proposed system which employs a two stage energy storage solution. The first stage uses two battery packs of 2.4V Ni-Mh. A series of MOS switches can connect the battery packs in series or parallel. The idea is to charge each battery separately from the prescribed 3.6V LTC output. After each pack gets fully charged, the two batteries are connected in series and a 4.8V equivalent battery is obtained.

The idea of this setup has several advantages that are explained in the following.
The efficiency of LTC3105 converter versus the input voltage is presented in the datasheet in the two cases – 3V and 5V prescribed output. The two diagrams are presented in Fig. 5.12. One can see that if the input voltage has low values (< 1.5V), a higher output voltage setpoint (5V) has a negative impact on the converter efficiency. Taking into account that the proposed energy harvesting device is designed to work with low temperature conditions (< 85℃) and that low temperatures are more probable than high ones, the output voltage of the TEGs in the proposed device will be centered around 1.5V. For this input voltage value, the efficiency is higher when a lower output voltage is prescribed to the LTC3105 converter output.

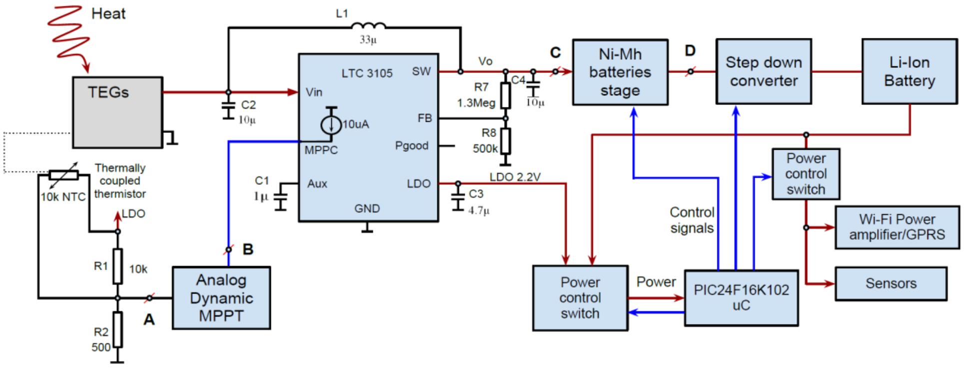

Figure 5.11 The proposed energy harvesting system general overview. Source [original]

This fact was the first that led to the adoption of the 3.6V as the prescribed output voltage level. Also, this voltage is necessary to override the Ni-Mh battery pack voltage, even when it approaches full charge (>2.8V). With a higher output voltage, also a higher voltage battery pack can be used. In this case, a 3.6V Ni-Mh battery would be the maximum allowable value (a 4.8V would require the LTC3105 to provide more than 5.25V). Having a 3.6V Ni-Mh battery would require a step up – step down converter (to charge the second stage battery) that needs more components (with increased costs) than the currently employed step down topology.

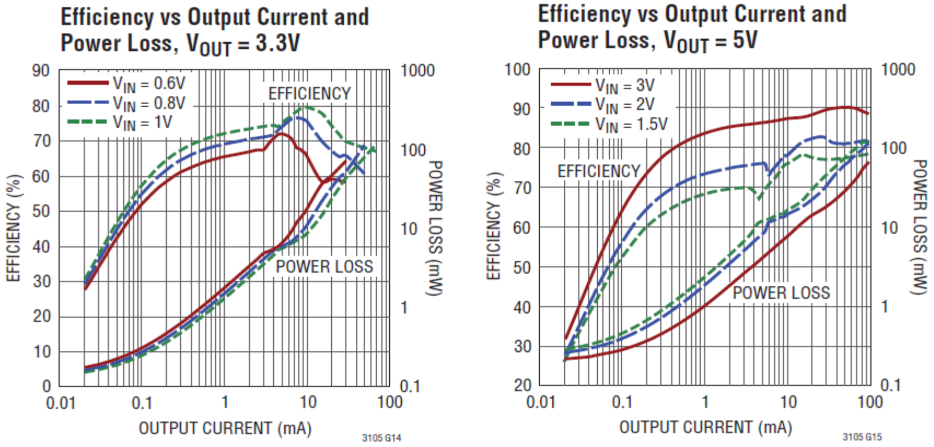
Efficiency vs Output Current and Power Loss, V_{OUT} = 3.3V

Efficiency vs Output Current and Power Loss, V_{OUT} = 5V

Figure 5.12 LTC3105 datasheet detail representing the efficiency curve function of output current at different input voltages. Source [44]

Another reason for adopting the 3.6V output voltage and the Ni-Mh technology for the first storage stage is that the Ni-Mh can be charged from a low current source [66] without damage. In this way, by charging the battery with low current, trickle charge mode and combining this procedure with the full discharge process, the battery health can be maintained over a longer period. Also, the adoption of the required charging regime for the Li-Ion battery will also lead to the preservation of the batteries health.

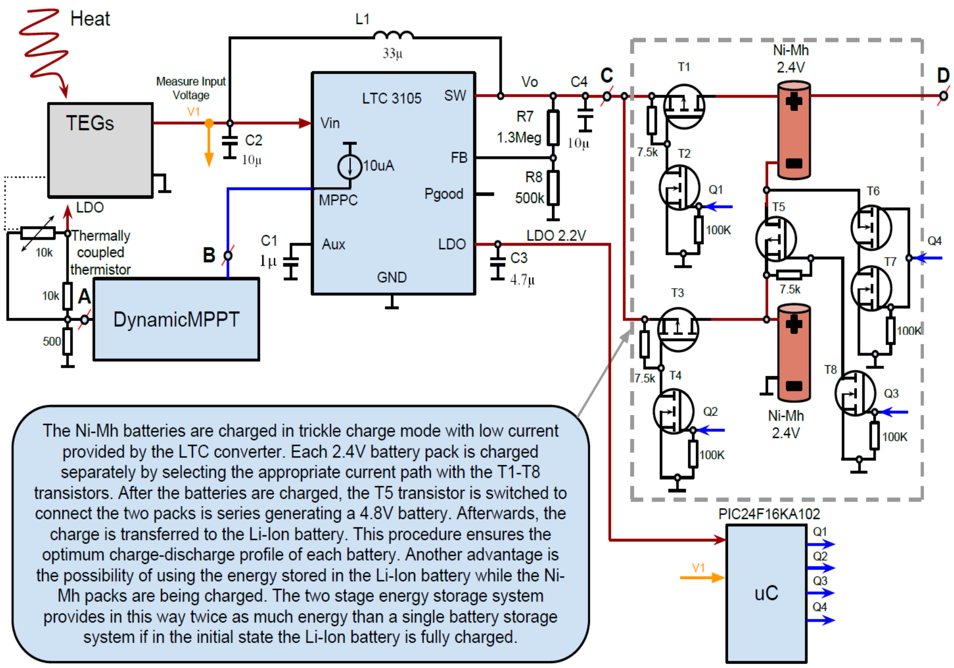

The Ni-Mh batteries are charged in trickle charge mode with low current provided by the LTC converter. Each 2.4V battery pack is charged separately by selecting the appropriate current path with the T1-T8 transistors. After the batteries are charged, the T5 transistor is switched to connect the two packs is series generating a 4.8V battery. Afterwards, the charge is transferred to the Li-Ion battery. This procedure ensures the optimum charge-discharge profile of each battery. Another advantage is the possibility of using the energy stored in the Li-Ion battery while the Ni-Mh packs are being charged. The two stage energy storage system provides in this way twice as much energy than a single battery storage system if in the initial state the Li-Ion battery is fully charged.

Figure 5.13 Detail of the Ni-Mh batteries stage design. Source [original]

Figure 5.13 presents the Ni-Mh batteries stage and the power paths controlled by the MOS switches. An N-Mos together with a P-Mos pair (e.g. T_1 and T_2 or T_3 and T_4) form a line switch. The diode present on the P-Mos drain to source terminals allows the battery to be decoupled from the LTC output when the switch is in the OFF state. T_5 and T_8 are used to put the batteries in series when they are completely charged and form a 4.8V battery.

Pull-down resistors were used to prevent the accidental turning on of the switches when no signal is available from the microcontroller. N-Mos power transistors (forward current >1A) with low r_{dson} resistance were used to minimize the losses generated when charging the Li-Ion battery with currents higher than 1A.

By measuring the input voltage value (V_1 in Fig. 5.13), knowing the converter efficiency and integrating over time, the energy provided to the battery pack can be computed in order to determine the full charge moment.

Figure 5.14 presents the step down converter and the power switches array that are used to route the energy stored into the Li-Ion battery to different devices as Wi-Fi, sensors and microcontroller. The switches array that is used to control the batteries charging or to route the power from the Li-Ion battery will be referred as the Power Control Switch (PCS).

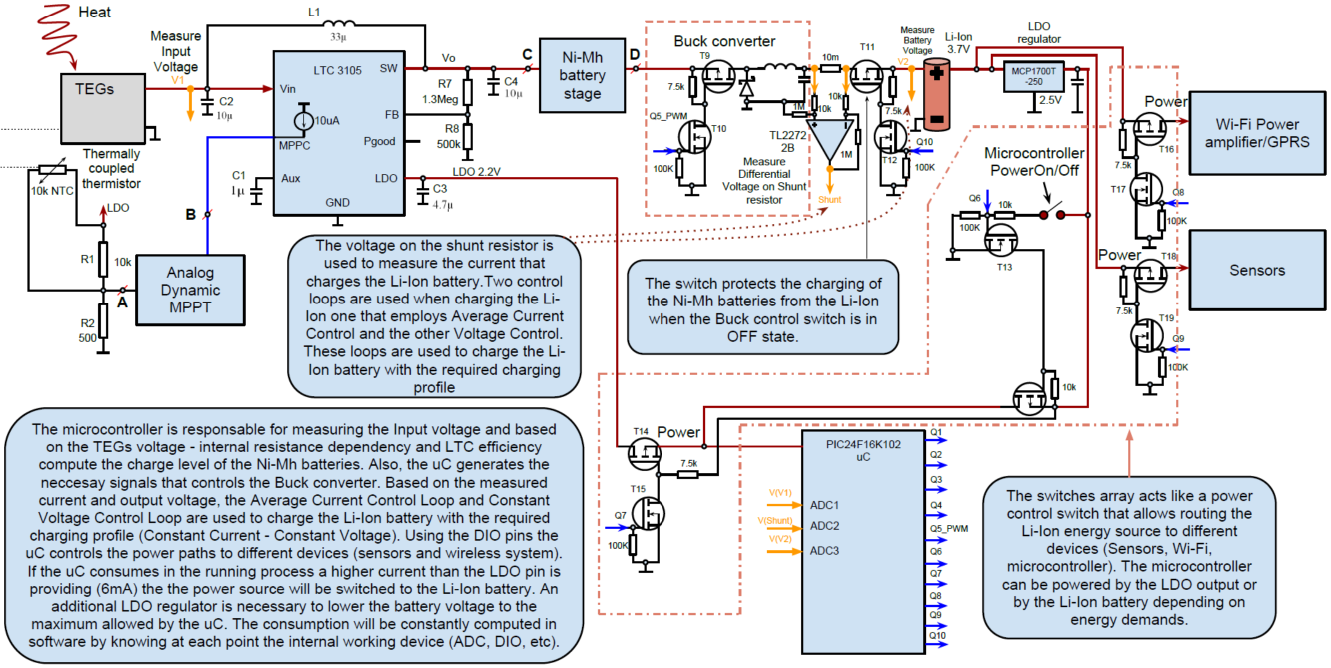

The voltage on the shunt resistor is used to measure the current that charges the Li-Ion battery.Two control loops are used when charging the Li-Ion one that employs Average Current Control and the other Voltage Control. These loops are used to charge the Li-Ion battery with the required charging profile

The switch protects the charging of the Ni-Mh batteries from the Li-Ion when the Buck control switch is in OFF state.

The microcontroller is responsable for measuring the Input voltage and based on the TEGs voltage - internal resistance dependency and LTC efficiency compute the charge level of the Ni-Mh batteries. Also, the uC generates the neccesay signals that controls the Buck converter. Based on the measured current and output voltage, the Average Current Control Loop and Constant Voltage Control Loop are used to charge the Li-Ion battery with the required charging profile (Constant Current - Constant Voltage). Using the DIO pins the uC controls the power paths to different devices (sensors and wireless system). If the uC consumes in the running process a higher current than the LDO pin is providing (6mA) the the power source will be switched to the Li-Ion battery. An additional LDO regulator is necessary to lower the battery voltage to the maximum allowed by the uC. The consumption will be constantly computed in software by knowing at each point the internal working device (ADC, DIO, etc).

The switches array acts like a power control switch that allows routing the Li-Ion energy source to different devices (Sensors, Wi-Fi, microcontroller). The microcontroller can be powered by the LDO output or by the Li-Ion battery depending on energy demands.

Figure 5.14 Detail of the Li-Ion battery stage, step down converter, additional devices and power control switch. Source [original]

5.2 The Buck converter

The values for the converter components are calculated to meet the electrical requirements. The current programmed mode controller is chosen and designed to meet the stability criterion then simulated using analog circuits. The discrete form of the control loop is derived using the bilinear transform and implemented using NI Labview and the NI DAQ 6251 board. As required by the Li-Ion charging profile a constant voltage control loop is also implemented.

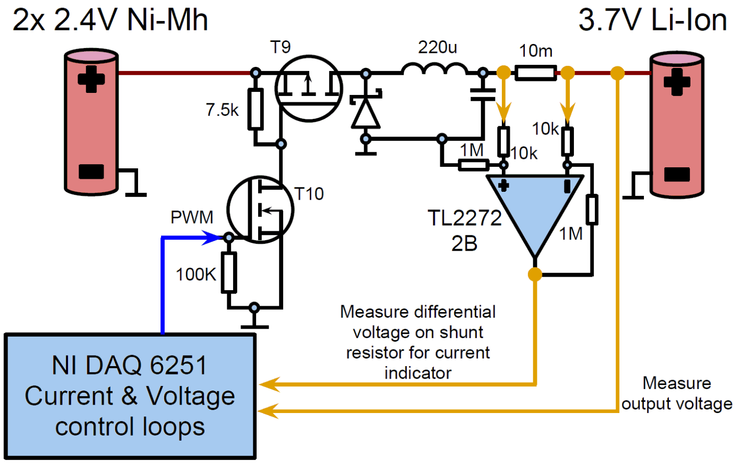

Figure 5.15 Detail of the Buck converter design and control system. Source [original]

The Li-Ion battery was conceived and developed in Japan and was accepted immediately because of its high-energy density, good performance, and no memory effect as compared to nickel–cadmium (Ni–Cd) or nickel-metal hydride (Ni–MH) batteries. Li-Ion batteries have been used mainly for portable electronics and recently the application area has been extended to power tools and hybrid electric vehicles [67].

Li-Ion batteries are also widely used for energy storage devices despite the drawback that they require a complicated charging procedure if the lifetime of the battery is of concern. As stated in [68], a strict charging regime is necessary to safely charge Li-Ion batteries. Also, a protective circuit is used to prevent overcharge and over discharge. Charging is limited to a maximum voltage of 4.3 V/cell while the discharge voltage is limited between 2.7 – 3 V/cell.

The battery requires a controlled charge regime composed of two stage charge cycles – constant current and constant voltage (CC/CV). The first stage charges the battery at a constant current until the voltage reaches 4.1 to 4.2 V. When this value is reached, a constant voltage charge is initiated until the charge current reduces to 3% of the rated current. The charging regime is represented in Fig. 5.16.
Another drawback of using Li-Ion batteries as energy storage devices is the need of a high charging current. This is hard to obtain in most cases, and sometimes the battery is replaced with a super capacitor or other batteries with different chemistry.

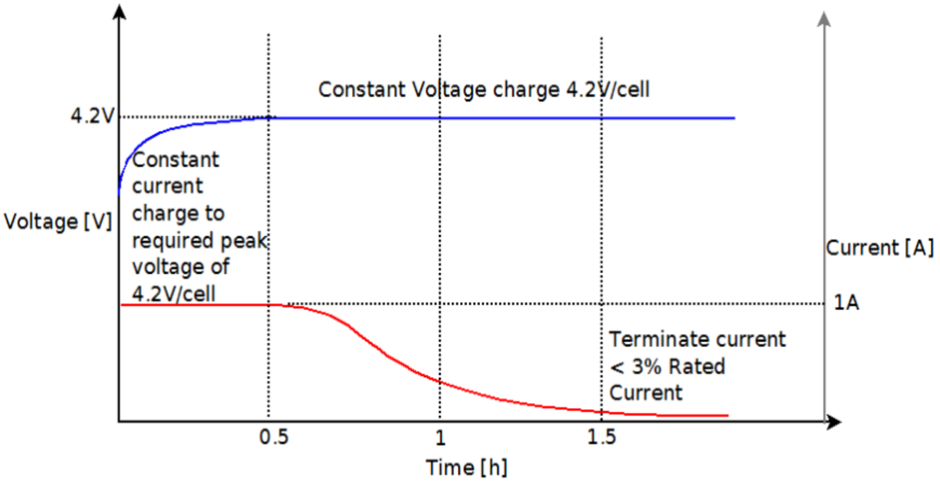

Figure 5.16 Charging profile of a Li-Ion battery. Source [reproduced]

The maximum current that must be delivered to the rechargeable Li-Ion battery must be $1 \cdot C$ of its capacity which leads to a value of 1A for a 1000mAh battery capacity. The values for the converter components - inductor and capacitor are calculated based on the following two formulas [69]:

$$L \geq \frac{4Dc(Vi - Vo)}{I \cdot f_s} = 4\frac{\frac{Vo}{Vi}(Vi - Vo)}{I \cdot f_s} \tag{5.1}$$

$$\frac{Dc \cdot (1 - Dc) \cdot Vi}{8 \cdot L \cdot C \cdot f_s^2} \leq \frac{1}{10} \cdot Vo \tag{5.2}$$

where *Vi* – input voltage, *Vo* – output voltage, f_s – sampling frequency, *I* – inductor current, *L* - inductor value, *C* – capacitor value, *Dc* – duty cycle. Eq. 5.1 imposes continuous conduction mode operation while in Eq. 5.2 the capacitor is chosen so that the ripple will not exceed 10% of the DC output voltage.

By solving Eq. 5.1 and 5.2 for f_s = *50kHz,* the values of *220μH* for the inductor and *100μF* for the capacitor are obtained.

5.2.1 Current programmed control

For the current application of Li-Ion battery charging, the average current control method (ACC) was chosen due to the fact that it has a large noise margin, no requirement for slope compensation, excellent voltage and current regulation and easy to obtain stability requirements. The goal is that the average value of the inductor current should follow a given reference value during a switching period. The principle of ACC is represented in Fig. 5.17 while the error amplifier is depicted in Fig. 5.18.

The open loop transfer function for the system represented in Fig 5.17 is:

$$T(s) = H_{AE}(s) \cdot H_{PWM}(s) \cdot H_{CONV}(s) \cdot H_{CRTTRAD}(s) \tag{5.3}$$

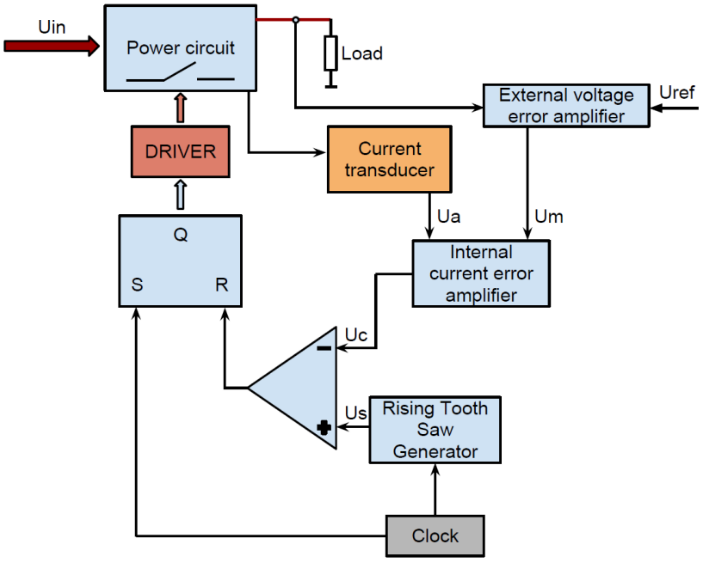

Figure 5.17 Average current control loop topology amplifier structure. Source [69]

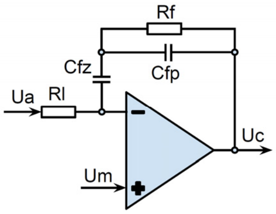

Figure 5.18 Error amplifier structure. Source [69]

It can be easily deduced that the transfer function of the error amplifier is:

$$H_{AE} = \frac{Uc}{Ua} = \frac{1 + sR_f(C_{fp} + C_{fz})}{sR_l C_{fz}(1 + sR_f C_{fp})} \tag{5.4}$$

Except for the pole in the origin, the error amplifier transfer function exhibits the following poles and zeros:

$$fp = \frac{1}{2\pi R_f C_{fp}} \tag{5.5}$$

$$fz = \frac{1}{2\pi R_f (C_{fp} + C_{fz})} \tag{5.6}$$

As shown in [69], at high frequency the open loop transfer function can be written as:

$$T(s) = \frac{1}{Vpp} \cdot R_s \cdot \frac{Vi}{sL} \frac{R_f}{R_l} \tag{5.7}$$

where: V_{pp} is the peak to peak amplitude of the sawtooth and R_s the trans-resistance value of the current transducer.

For designing the amplifier, the desired cutoff frequency must be chosen, according to [69].

$$f_C = \frac{1}{2\pi} \cdot \frac{R_f}{R_l} \cdot \frac{Vi}{Vpp} \cdot \frac{R_s}{L} \tag{5.8}$$

For optimum design [69], f_z is chosen to be sufficiently higher than f_p. For the cutting frequency the maximum value $f_{C\max} = \frac{f_S}{2\pi Dc}$ is chosen. The pole frequency must be equal to the sampling frequency (switching frequency) for best performance: $f_C = f_{C\max}, f_z = \frac{1}{10} f_p, f_p = f_s$.

Denoting by

$$m = \frac{Vpp}{Vo} \cdot \frac{L}{R_s} \cdot f_S \ . \tag{5.9}$$

the values of the capacitors can be expressed as:

$$C_{fz} = \frac{9}{2\pi \cdot m \cdot f_S \cdot R_l} \ . \tag{5.10}$$

$$C_{fp} = \frac{1}{2\pi \cdot m \cdot f_S \cdot R_l} \ . \tag{5.11}$$

Eq. (5.8) to (5.10) are next implemented in a Matlab custom application for determining the component values to be used in the simulation.

For implementing the current programmed control loop in a digital counterpart the transfer function must be converted to a discrete form. This approach is preferred because the converter can be driven by a microcontroller already existent on the energy storage device. Numerical implementations have already been made in [70], [71] and [72]. The bilinear transform or Tustin's method is required to transform the continuous-time system representation to discrete time and vice-versa:

$$s = \frac{2}{T} \cdot \frac{1 - z^{-1}}{1 + z^{-1}} \tag{5.12}$$

where: *1/T* is the sampling frequency.

The error amplifier transfer function can be rewritten as:

$$H_{AE}(s) = \frac{1}{s} \cdot k_1 + \frac{k_2}{s \cdot \sigma + 1} \ ;$$

where:

$$k_1 = \frac{1}{R_l \cdot C_{fz}}, k_2 = k_1 \left(\frac{1}{2\pi f_z} - \frac{1}{2\pi f_p} \right) \tag{5.13}$$

Appling the bilinear transform we obtain the digital controller time equations:

$$y_1[n] = k_1 x[n] + k_1 x[n-1] + y_1[n-1].$$

$$y_2[n] = \frac{x[n] + x[n-1] - (1-\sigma) y_2[n-1]}{(\sigma + 1) \cdot 2 \cdot f_s} \ ;$$

where:

$$\sigma = \frac{1}{2\pi \cdot f_p} \tag{5.14}$$

5.2.2 Simulation results

Fig. 5.19 describes the circuit simulation using Caspoc software [73]. First, the controller was simulated using analog blocks. A load of 4.2 Ohm is applied to the Buck output. The simulation result is presented in Fig. 5.20.

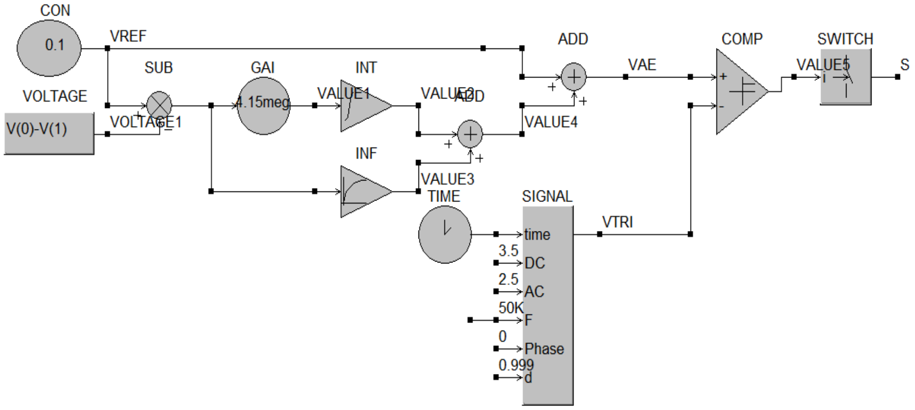

Figure 5.19 Analog Average Current Control mode simulation. Source [original]

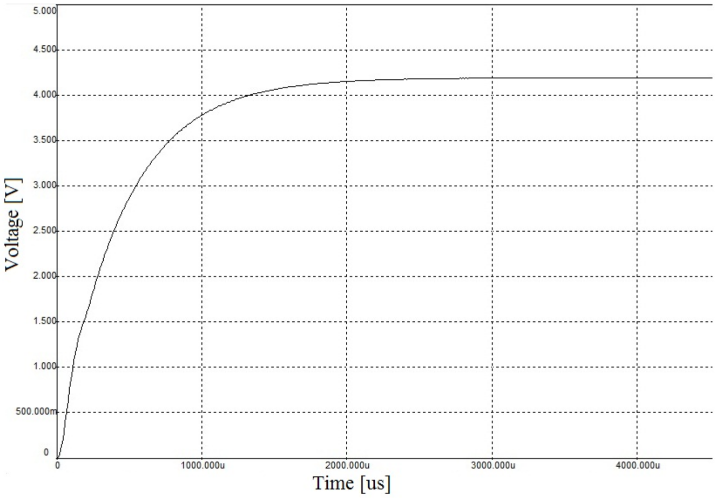

Figure 5.20 Simulation result of the analog ACC mode. Source [orignal]

The *Voltage* block from Fig. 5.19 measures the voltage across the shunt resistor determining in this way the inductor current. Blocks *GAI*, *INT*, *INF* and *ADD* simulate the error amplifier. The *GAI* block represents a gain and its value corresponds to the k_1 constant from Eq. 5.13. The *INT* block is an integrator and corresponds to the first term in the right hand side of Eq. 5.13. The second term in the right hand of this equation corresponds to the *INF* block. The *TIME* and *SIGNAL* blocks compose the sawtooth generator.

In the waveform represented in Fig. 5.20, one can see that the regulator maintains the prescribed current of 1 A (the voltage across the 4.2 Ohm load is 4.2V). Fig. 5.21 depicts the discrete solution simulation. Fig. 5.22 shows that the circuit behaves correctly. The analog blocks in the simulation diagram represented in Fig. 5.19 have been replaced with digital blocks. Shift registers are used to retain the old values as required by Eq. 5.14. The *GAI* block together with *ACCUMULATOR2* and *ADD* blocks represent $y_1[n]$ from Eq. 5.14. *LIM* is a limit block that converts the output to stay between 0.1 – 0.99 range of the switch duty cycle. The output switch block controls the S transistor of the Buck converter.

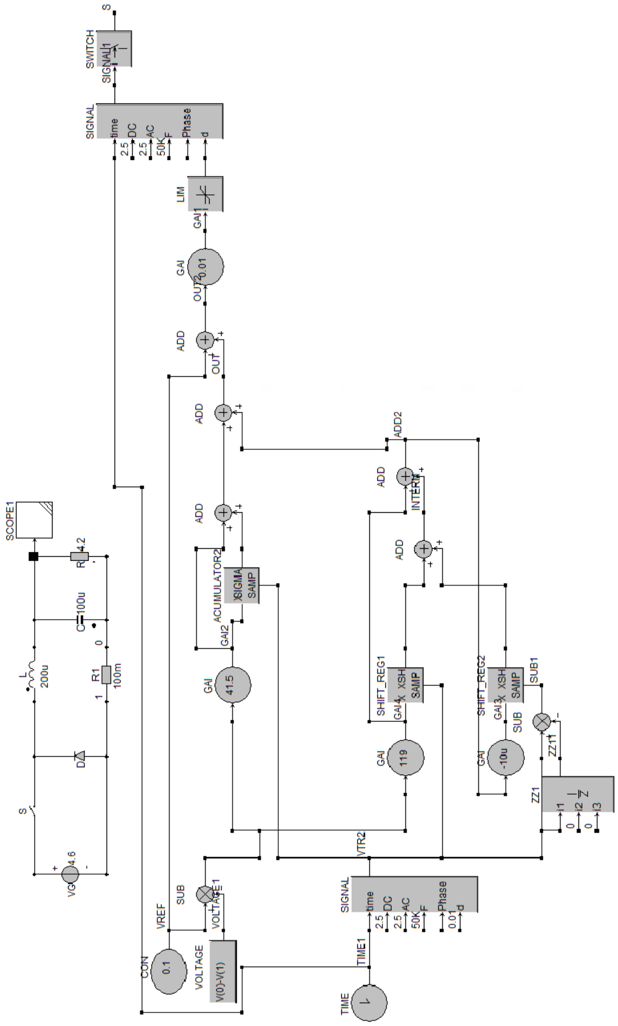

Figure 5.21 Digital Average Current Control mode simulation. Source [original]

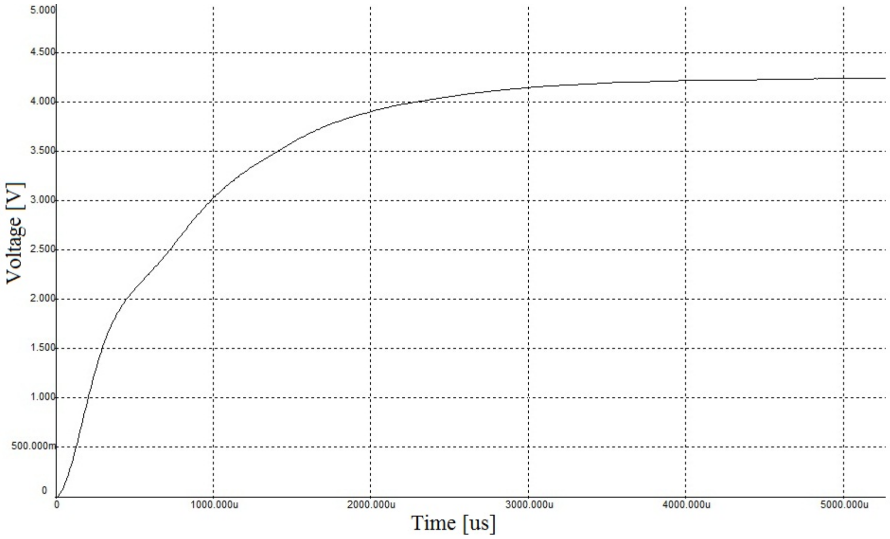

Figure 5.22 Simulation result of the digital ACC mode. Source [original]

5.2.3 *Implementation and experimental results*

The flowchart diagram of the LabView implementation is represented in Fig. 5.23. The ACC loop is implemented using shift registers and the constant voltage control loop using a built in PI regulator. The experimental setup can be seen in Fig. 5.24.

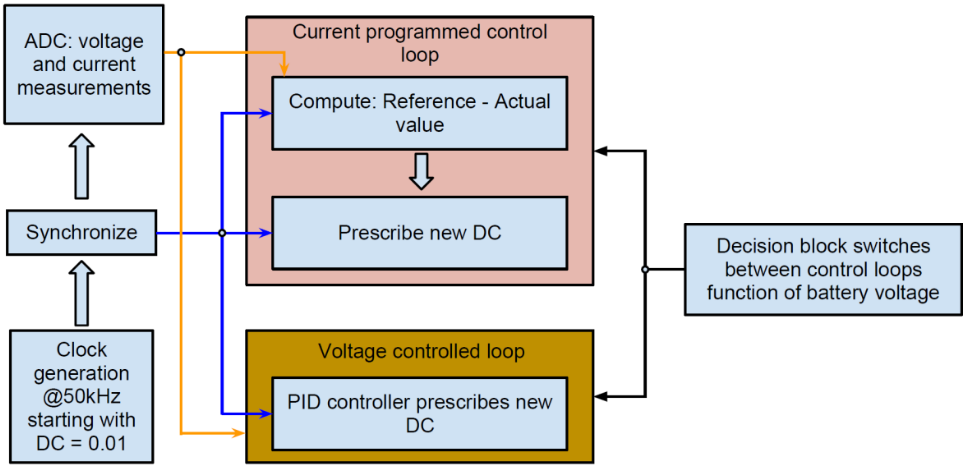

Figure 5.23 Logic diagram of the digital control implemented with the NI DAQ 6221. Source [original]

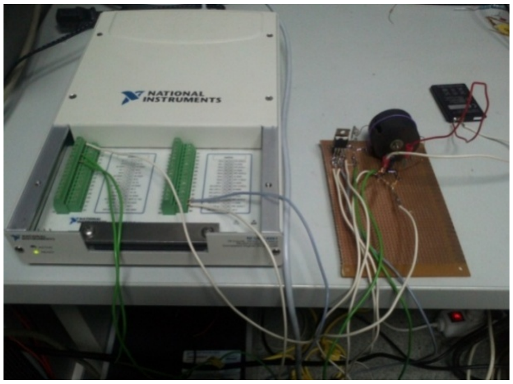

Figure 5.24 Buck converter practical implementation. Source [original]

Fig. 5.25 shows the response (actual current and voltage) of the running charging process. In Fig.5.25, on the *left* side, it can be seen that the charging current is regulated at a constant value of 1 Amp. The constant current cycle ends when the voltage across the battery equals 4.2V, and then the constant voltage control loop comes into action, keeping the voltage across the battery at a constant value of 4.2V until the charge current reduces to 3% of the rated current – *right* side of the figure. The spike in the figures represents the switching from one control loop to another. The results show that the behavior of the experimental converter follows the simulated one (in ACC mode). The experimental results showed that the converter is able of mainaining a constant charge current and voltage even under perturbations. The chosen control methods: average current control and PI regulation of the constant voltage provide very good results for the proposed application of battery charging. The numerical implementation of these controls can be easily implemented in a microcontroller.

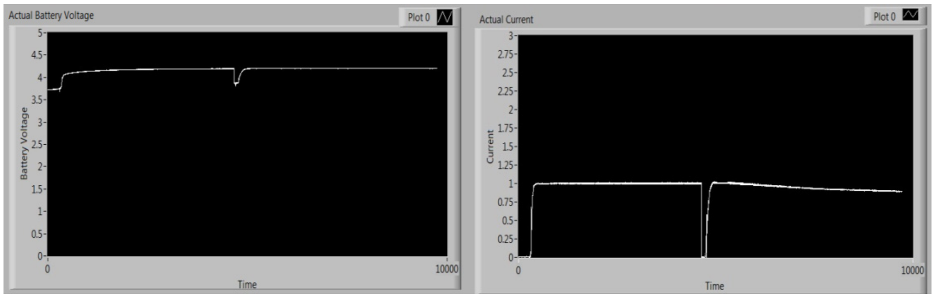

Figure 5.25 Front Panel of the running VI - The current loop is first active afterwards the voltage control loop is running. Source [experiment]

5.3 *Energy harvesting system simulation and experimental results*

The proposed energy harvesting system presented in Fig 5.13 was simulated in LTspice using the SPICE thermal model presented in Fig. 3.10, where the convective heat transfer was implemented. In this way, the natural environment conditions were also simulated. The same procedure as in subchapter 4.5 was adopted, where the resistive heater from Fig. 2.1 was connected to the P6100 power source and the real temperature values were recorded into a file. A fitting function was used to approximate the temperature variation of the heater and afterwards, a specific purpose Javascript application was used to generate the temperature values – time points file needed for the SPICE simulator. The specific purpose Javascript application was necessary in order to generate the temperature values and time point pairs giving the possibility to rescale the fitting function and generate the discrete points with the desired time step. The procedure is presented in Fig. 5.26.

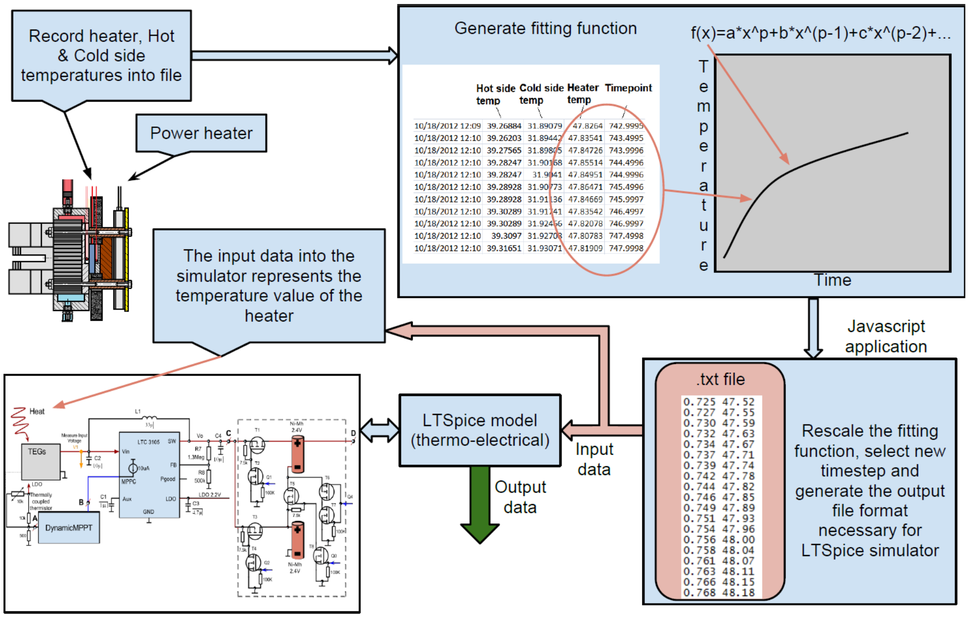

	Hot side temp	Cold side temp	Heater temp	Timepoint
10/18/2012 12:09	39.26884	31.89079	47.8264	742.9995
10/18/2012 12:10	39.26203	31.89442	47.83541	743.4995
10/18/2012 12:10	39.27565	31.89805	47.84726	743.9996
10/18/2012 12:10	39.28247	31.90168	47.85514	744.4996
10/18/2012 12:10	39.28247	31.9041	47.84951	744.9996
10/18/2012 12:10	39.28928	31.90773	47.86471	745.4996
10/18/2012 12:10	39.28928	31.91136	47.84669	745.9997
10/18/2012 12:10	39.30289	31.91741	47.83542	746.4997
10/18/2012 12:10	39.30289	31.92466	47.82078	746.9997
10/18/2012 12:10	39.3097	31.92708	47.80783	747.4998
10/18/2012 12:10	39.31651	31.93071	47.81909	747.9998

```
0.725 47.52
0.727 47.55
0.730 47.59
0.732 47.63
0.734 47.67
0.737 47.71
0.739 47.74
0.742 47.78
0.744 47.82
0.746 47.85
0.749 47.89
0.751 47.93
0.754 47.96
0.756 48.00
0.758 48.04
0.761 48.07
0.763 48.11
0.766 48.15
0.768 48.18
```

Figure 5.26 Logic representation of the procedure that generates the input data for the heater temperatures in the SPICE simulator. Source [original]

The comparisons between the experimental obtained values and the simulation ones are presented in the figures below. The experiments were conducted with the system operating in natural environment conditions.

In Fig. 5.27, no load was connected to the TEGs output. One can observe that the simulated values follow the experimentally obtained ones. The simulated hot side temperature is following better the real behavior, the error being less than 1%. The simulated cold side temperature presents a 3% error with respect to the experimentally determined data.

Figure 5.28 presents the temperature difference between the hot and cold sides of the TEGs under test, in both simulation and experiment. One can observe that the highest error is generated around the 1000s time step. The simulated process generates a temperature difference of ~ 1.2℃ higher than in reality, mainly due to the lower cold side temperature (Fig 5.28). This, in turn, will generate a higher output voltage by ~ 0.1V in the simulation that represents ~ 14% of the real experimentally determined value. This is presented in Fig. 5.29 where both simulation and experimental results are shown.

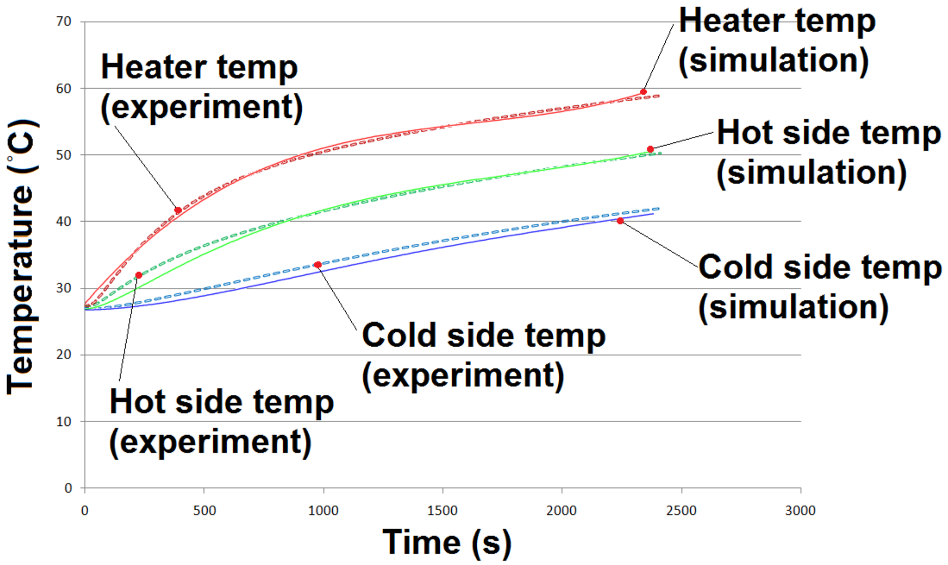

Figure 5.27 Experimental and simulation results from the TEGs system without load, in natural environment. Source [original]

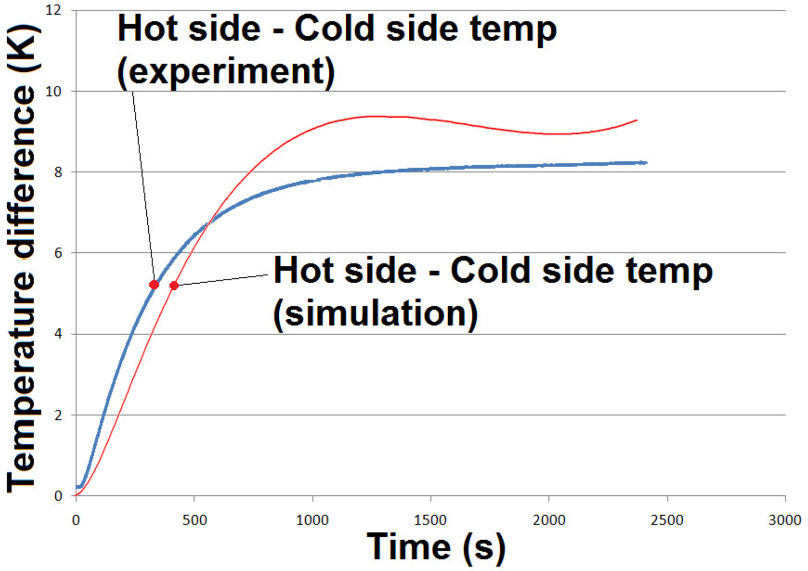

Figure 5.28 Experimental and simulation results of the temperature sides difference from the TEGs system. Source [original]

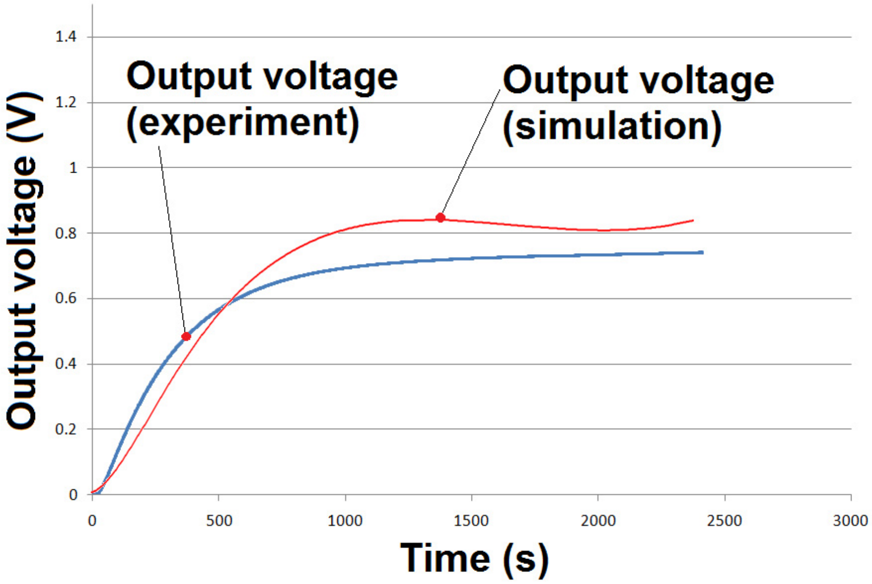

Figure 5.29 Experimental and simulation results from the TEGs output voltage. Source [original]

The wave like oscillation of the TEGs simulated output voltage comes from the temperature input values generated with the procedure explained in Fig. 5.26. The oscillating heater temperature value is also present in the results presented in Fig. 5.27, where it can be observed that the simulated temperature values are tracking the real behavior.

The simulation model when the load is connected to the TEGs output is presented in Fig. 5.30, where "TEG Positive Terminal" represents the output voltage from the TEGs model that is not displayed in the figure.

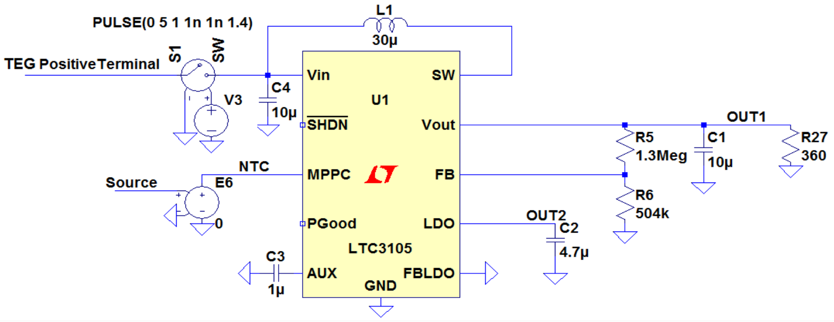

Figure 5.30 Simulation model representing the DC-DC converter and load that are connected to the TEGs system's output. Source [original]

Figure 5.31 presents the temperature values from the simulation and experimental data, when the load (LTC 3105 converter with 360 Ω resistive output load) was connected to the TEGs output after 1000s since the recording procedure started. The output voltage of the LTC converter was set to 3.6V and the dynamic maximum power point tracking system was employed in both simulation and experiment.The simulation error is below 3%, proving a strong correlation to the experiment.

When the load is connected, one can see that the hot side of the TEGs temperature is getting lower while the cold side temperature increases. From the physical point of view, this phenomenon can be explained due to the diffusion process, as when the electrons start flowing (through the load connected to the TEG's output) from the hotter region of the TEG to the colder one, the first one losses heat while the latter absorbs heat.

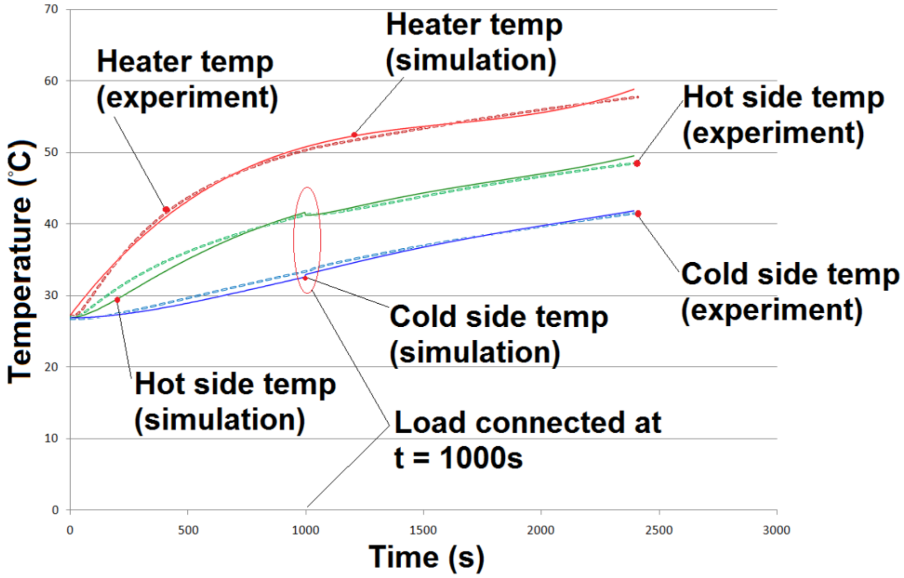

Figure 5.31 Experimental and simulation results from the TEGs system with the load connected after 1000s, in natural environment. Source [original]

Figure 5.32 presents the differences between the simulated model and the experimentally data, when the LTC converter along with the 360 Ω load is connected to the TEGs output. The output voltage of the LTC converter, the TEGs output voltage, the MPPT voltage and the load current were recorded using a digital oscilloscope for a period of 2000s and compared to the simulation results. It can be observed that the simulated output voltage of the LTC converter (at its maximum point) is higher by 14% compared to the experimentally determined one. The 14% error is present in the region of 1400s. However, starting from 1500s, the error is lower than 8%, reaching 4% in the region of 2000s, proving a strong correlation to the experiment.

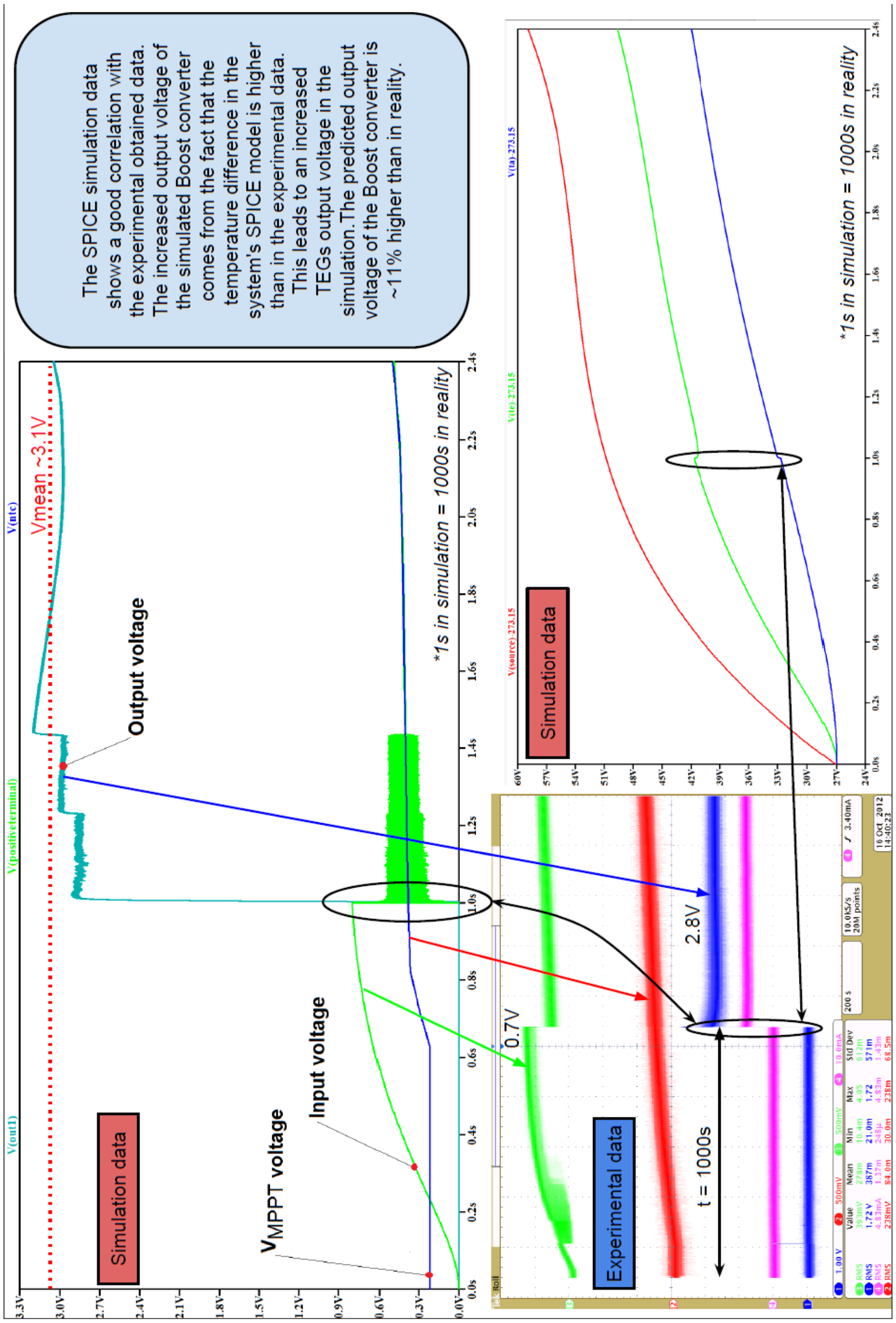

The SPICE simulation data shows a good correlation with the experimental obtained data. The increased output voltage of the simulated Boost converter comes from the fact that the temperature difference in the system's SPICE model is higher than in the experimental data. This leads to an increased TEGs output voltage in the simulation.The predicted output voltage of the Boost converter is ~11% higher than in reality.

Figure 5.32 Simulation and experiment correlation of the TEGs system that is operating in natural environment with load. Source [original]

If the TEG constant parameters model is used, the simulation errors are increased by 28%. Although the thermal conductance is in this case constant, the TEG's hot and cold sides' temperatures variations are with less than 3% different compared to the case when the varying parameters model was used. But when the constant parameters model is used, the output voltage of the TEGs is 0.66V at 1000s time step instead of being around 0.8V as would be in reality for the temperature difference at that point. This leads to an additional error of ~18% generated by the electrical component of the TEG model. In the current case, this error is destructively interfering with the thermal error generated by the mechanical model and the output voltage of the TEG (0.66V) is closer to the real one (0.7V). However, the total error generated by both thermal and electrical models is ~28%, in some cases being even higher.

Figure 5.33 presents the output voltage of the LTC3105 converter, along with the TEGs output voltage and MPPT voltage, when the TEG constant parameters model was used. The variations of the hot and cold sides temperatures were not displayed, the differences of <3% obtained in this low temperature case and mentioned before making the two situations look practically the same. The major differences between the two TEG models in this case come from the internal resistance variation with temperature and the Seebeck voltage coefficient. If higher temperatures are attained, the thermal conductance variations can become important.

Figures 5.34 - 5.37 present a series of experimental results with the TEGs system operating and charging the two Ni-Mh batteries. Figure 5.34 depicts the charging of the first Ni-Mh battery when the TEGs output voltage is 1V. The dynamic MPPT system keeps the input voltage to 0.5V in this case, maintaining the optimum power transfer to the output of the DC-DC converter.

In Fig. 5.35, the PCS was controlled to charge the second Ni-Mh battery. Figure 5.36 presents the scenario when the battery charging process is completed and the two batteries are connected in series to generate a 4.8V Ni-Mh battery.

In Fig. 5.37, the dynamic heating process of the TEGs system is presented. One can observe the increasing output voltage of the TEGs and in the same time the MPPT voltage. The DC-DC converter starts operating from ~ 0.3V but for this input voltage and with the Ni-Mh battery connected as load, the converter is not able to reach the output prescribed voltage of 3.6V. Only when the TEGs output voltage reaches ~ 0.5V, the LTC3105 output voltage attains 3.6V and the battery is starting to charge.

The proposed battery charging device operates as desired and the analog dynamic MPPT system improves the efficiency of the system by continuously adapting the voltage on the LTC3105 MPPT pin, in order to extract the maximum available power.

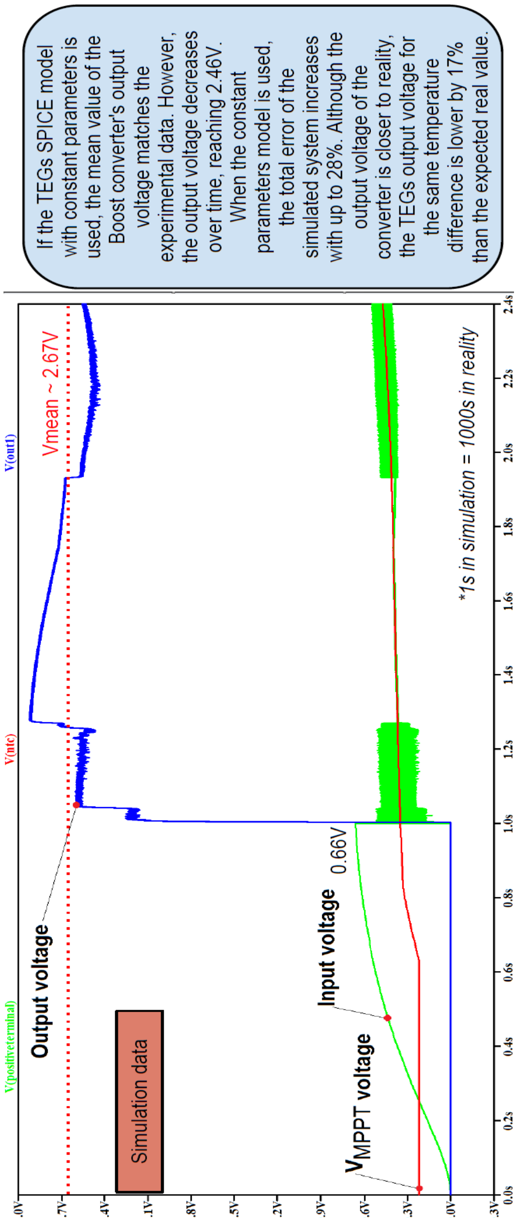

If the TEGs SPICE model with constant parameters is used, the mean value of the Boost converter's output voltage matches the experimental data. However, the output voltage decreases over time, reaching 2.46V. When the constant parameters model is used, the total error of the simulated system increases with up to 28%. Although the output voltage of the converter is closer to reality, the TEGs output voltage for the same temperature difference is lower by 17% than the expected real value.

Figure 5.33 Simulated TEGs output voltage, MPPT voltage and LTC output voltage when the constant parameters model was used. Source [original]

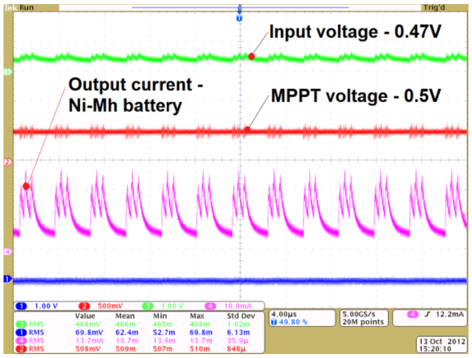

Figure 5.34 Experimental results with 1V generated by the TEGs system and first battery charging.

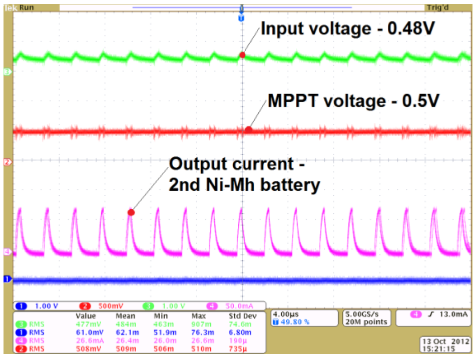

Figure 5.35Experimental results with 1V generated by the TEGs system and second battery charging.

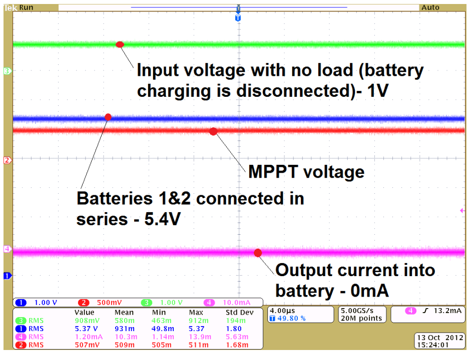

Figure 5.36 Experimental results with 1V generated by the TEGs system and batteries connected in series with the help of the Power Control Switch.

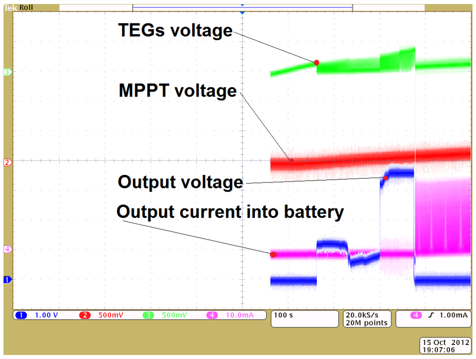

Figure 5.37 Experimental results with the dynamic heating of the TEGs system and the first battery connected for charging.

For the experiments conducted in this section, two NI DAQ boards were used – 6221 and 6251. The first, along with a specific built autonomous testing system controlled the P6100 power source that heated the power resistors and took care of recording the temperatures values and the input and output voltage values of the TEGs and the LTC converter. The second NI DAQ board was used to control the PCS system (Fig. 5.38).

In Fig. 5.38, the TEMs test rig can be observed on the left side of the picture, where the temperature and voltage values are monitored by one NI DAQ 6221 (not shown) while the electronics (dynamic MPPT, converter, batteries) are controlled by the second NI DAQ 6251 (lower right corner). The current and voltage values at the converter output are monitored by the oscilloscope (upper right corner).

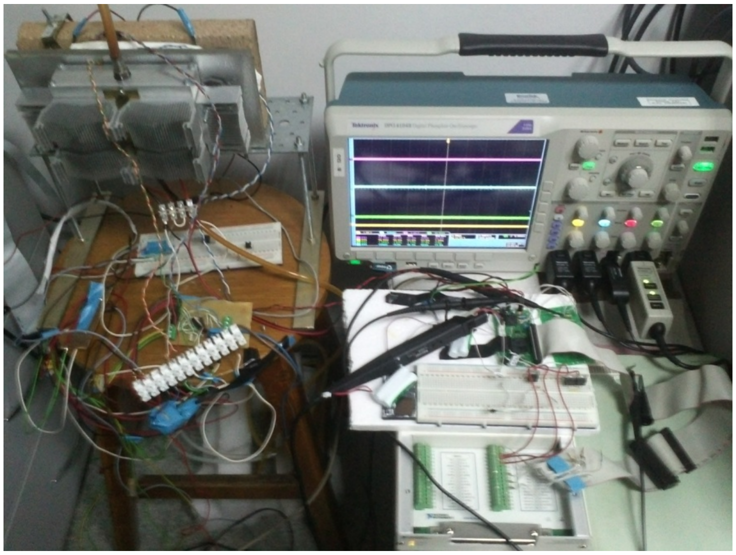

Figure 5.38 Complete TEGs system experimental setup.

5.4 The improved Ćuk converter for multiple TEGs

In order to extract the maximum available power from a TEG, efficient DC – DC converters are needed. Several devices of this kind already exist (e.g. LTC 3105, LTC 3108, MAXIM 17710, etc) but their usage is limited to one or two input energy sources – TEGs [44], [74]. The LTC3105 for example, like presented in subchapter 5.1 has the output current limited to 400mA and the output voltage scalable from 1.5 to 5.25V. However, if the energy source has physically large dimensions (e.g. heat engines), several serial connected TEGs would provide more power than a single module would. For this kind of applications, custom DC – DC converters must be developed. In this way, a Ćuk converter that is supposed to operate from four (or a higher number) serial connected TEGs is proposed. The converter purpose is to charge a pack of either Li-Ion or Ni-MH batteries with maximum efficiency while adapting its impedance with that of the equivalent power source (TEGs). In this way, at any moment, the converter will work by transferring the maximum available power to the battery. In order to control this behavior, an indirect current control loop was developed. The loop is based on the continuous measurement of the TEGs output voltage and an a priori built lookup table that stores the output voltage – internal resistance correspondence of the TEGs. The correspondence has been experimentally measured and is necessary because a TEG's internal resistance and Seebeck coefficient varies with temperature.

Figure 5.39 presents the proposed Ćuk design where, in order to increase efficiency, the original diode [75] has been replaced by an N-Mos switch. An isolation transformer is used to reverse the output voltage polarity and assure the operation of the second N-Mos. In standard configuration, a Ćuk converter generates an output voltage with reversed polarity compared to the input [76]. The control of the switches is performed by an 80 MHz Spartan 3E FPGA that is able to provide several nanosecond timing necessary when no cross conduction of the N-Mos switches is required. A small delay that depends on each of the transistor's rise and fall time needs to be implemented for dead time control. The need for such precise timing comes from the fact that the rise and fall time of any transistor differ, the falling time being usually higher than the rising one.

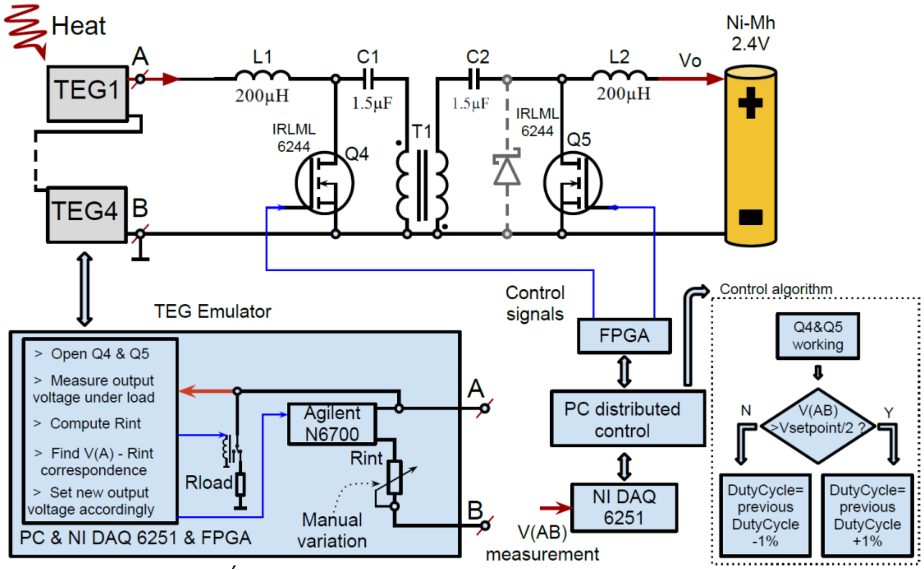

Figure 5.39 Proposed Ćuk converter employing TEG emulator and FPGA dead time control. Source [original]

In order to measure the voltage necessary to control the duty cycle of the switches, a NI DAQ 6251 measurement board was used.

5.4.1 The SPICE simulation model

The simulation model was implemented under Linear Technology LTspice software (Fig. 5.40). The component values and manufacturer were chosen from the simulator library and also represent the real components chosen in the real implementation. In the practical implementation, the transformer was specially designed and built for this specific application. Taking this into account, the transformer simulation model employed lossless inductor values and mutual coupling was considered first 1, afterwards being reduced to 0.99995 to reproduce the real behavior (leakage inductance responsable for spikes generation).

The simulated model employs both the Schottky diode and the N-Mos synchronous rectifier switch that replaces it. When the Schottky diode was used in simulation, the second's N-Mos switch control signal was connected to the $\boldsymbol{V_7}$ power source (Fig. 5.40) that outputs 0V signal. Two loads were alternatively used, the R_2 resistor and the V_2 battery.

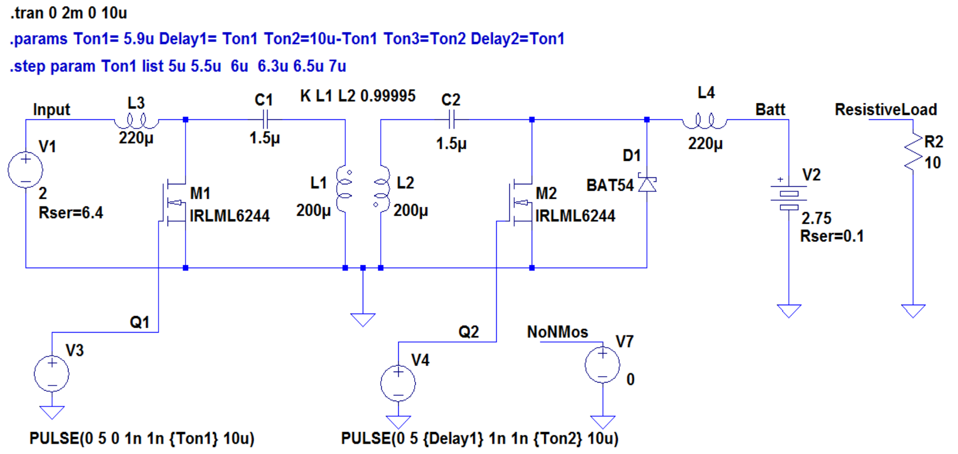

```
.tran 0 2m 0 10u
.params Ton1= 5.9u Delay1= Ton1 Ton2=10u-Ton1 Ton3=Ton2 Delay2=Ton1
.step param Ton1 list 5u 5.5u  6u  6.3u 6.5u 7u
```

Figure 5.40 Ćuk converter LTspice simulation model using real components values. Source [original]

By writing the current through L_3 and L_4 inductors and imposing for the current ripple not to exceed 25% of the correspondant DC value, one obtains:

$$\Delta I_{L_3} \leq \frac{1}{4} I_{L_3} \tag{5.15}$$

$$\Delta I_{L_4} \leq \frac{1}{4} I_{L_4} \tag{5.16}$$

$$\Delta I_{L_3} = \frac{Dc \cdot V_g}{L_3 \cdot f_s} \tag{5.17}$$

$$\Delta I_{L_4} = \frac{(1 - Dc) \cdot V_o}{L_4 \cdot f_s} \tag{5.18}$$

$$V_o = \frac{Dc}{1 - Dc} \cdot \frac{n_2}{n_1} \cdot V_g \tag{5.19}$$

$$I_{L_3} = \frac{{V_o}^2}{R \cdot V_g} = \frac{Dc^2 \cdot V_g}{(1 - Dc)^2 R} \tag{5.20}$$

$$L_3 \geq 4 \frac{R}{f_s} \cdot \frac{(1 - Dc)^2}{Dc} \tag{5.21}$$

Where $\boldsymbol{Dc}$ represents the duty cycle of the swithces driving signal, $\boldsymbol{V_g}$ is the input voltage, $\boldsymbol{V_o}$ the output voltage, $\boldsymbol{f_s}$ represents the switching frequency, $\boldsymbol{R}$ is the output resistance and $\boldsymbol{n_2/n_1}$ represents the transformer turns ratio. A switching frequency of 100 kHz was chosen to drive the N-Mos switches. The frequency was adopted in order to obtain low values for the components and based on the transistor's rise and fall time datasheet ratings.

By solving Eq. 5.15 - 5.21 the values for the L_3 and L_4 inductors are obtained. In the current case, the components values were chosen such as the converter to process a maximum 5V at 500mA input power. By imposing the $\boldsymbol{C_1}$ and $\boldsymbol{C_2}$ capacitor's voltage ripple to be less than 25% of the corespondent DC values, we obtain:

$$\Delta V_{C_1} \le \frac{1}{4}\cdot V_{C_1}; \Delta V_{C_1} = \frac{I_{L_3}\cdot(1-Dc)}{C_1\cdot f_s} \tag{5.22}$$

Using Eq. 5.22 we obtain the value for the ***C_1*** capacitor and similar, the value for ***C_2***. The simulation was first run with the converter in standard configuration, where a BAT54 Schottky low voltage drop diode was used together with a 10Ω resistor as load.

A parametric step simulation was adopted to determine the correct duty cycle value that corresponds to the maximum transferred power between input and output. The simulation results are presented in Fig. 5.41, for 3V input voltage and the duty cycle corresponding to the maximum power transfer.

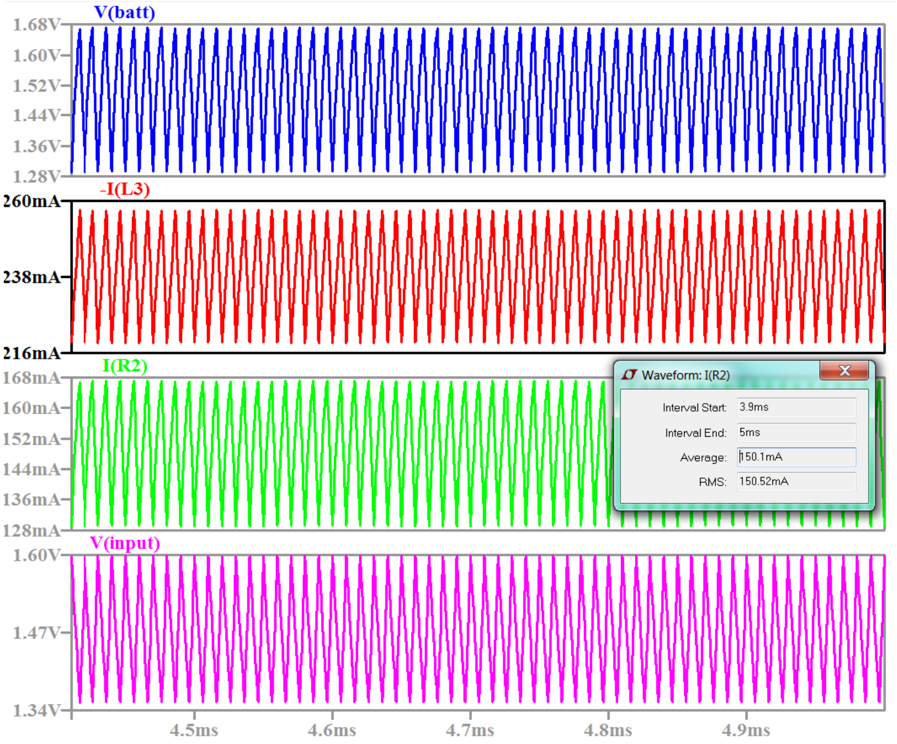

Interval Start: 3.9ms
Interval End: 5ms
Average: 150.1mA
RMS: 150.52mA

Figure 5.41 Output voltage and current for 3V input and BAT54 Schottky diode. Source [original]

Figure 5.42 presents the simulation where the second N-Mos switch replaced the Schottky diode in order to improve the efficiency.

It can be seen that for the same input voltage, when the converter impedance is adapted for maximum power transfer, the current into the resistive load is 15% higher compared to the case when the Schottky diode was used.

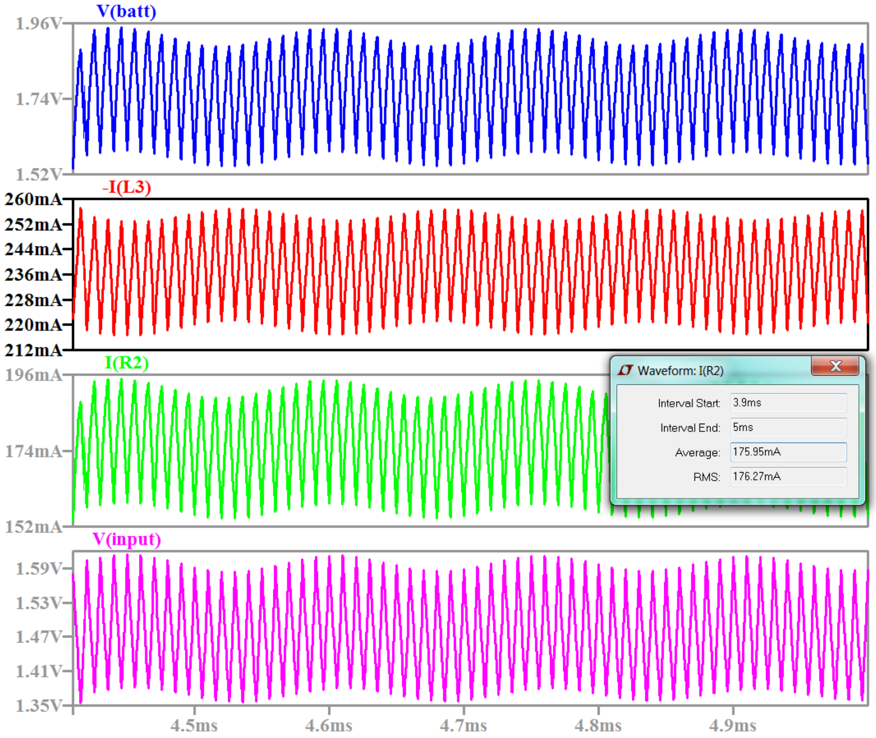

Interval Start: 3.9ms
Interval End: 5ms
Average: 175.95mA
RMS: 176.27mA

Figure 5.42 Output voltage and current for 3V input and N-Mos switch that replaces the Schottky diode. Source [original]

The simulations were repeated with a 2.4V battery pack as load. The battery was simulated by a 2.75V power source in series with an internal resistance. The selected supply voltage value was chosen as experimentally determined with a 2.4V Ni-Mh battery pack.

Figure 5.43 present the converter efficiency with three different loads – the Ni-Mh battery, a 50Ω resistor and a 100Ω resistor. The efficiency is computed over an input range starting from 1.5V and up to 5V, when the duty cycle of the N-Mos switches was chosen to provide maximum power transfer between input and output. One can see that the efficiency of the converter in the input range of 1.5-5V, when the Ni-Mh battery is used as load is around 90%.

The efficiency when the Schottky diode is used instead of the second N-Mos switch is also presented in Fig. 5.43. One can observe that in this case efficiency is up to 20% lower. While the input voltage increases, the decreasing slope of the efficiency is higher in the case of the Schottky diode. This is due to fact that as the input voltage is higher the duty cycle will get lower resulting in a longer conduction time for the diode ***(1-Dc)/f$_s$*** and consequently a lower efficiency.

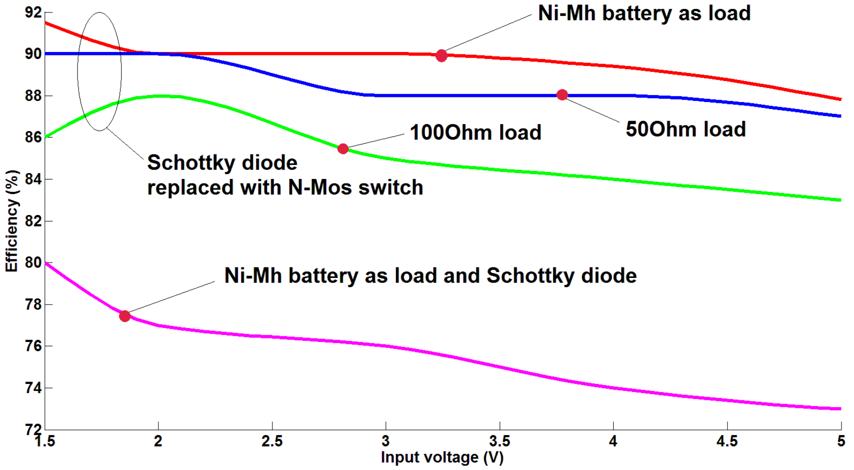

Figure 5.43 Efficiency vs. input voltage for three different loads – Ni-Mh battery, 50Ω load and 100Ω resistive load and when the Schottky diode is used. Source [original]

Simulation results prove that replacing the diode by the N-Mos switch leads to increased efficiency that reaches 90%. However, the simulation was performed considering ideal signal sources which in practical implementation will lead to a decrease in the efficiency.

Figure 5.44 displays the simulated efficiencies when the N-Mos switch replaced the diode and both switches were controlled by a 50kHz control signal. It can be observed that the efficiency for a 50Ω load is now lower, compared to the case presented in Fig. 5.43. This can be explained by the commutation losses of the switches, that in the case of the 100kHz control signal are higher than the conduction losses.

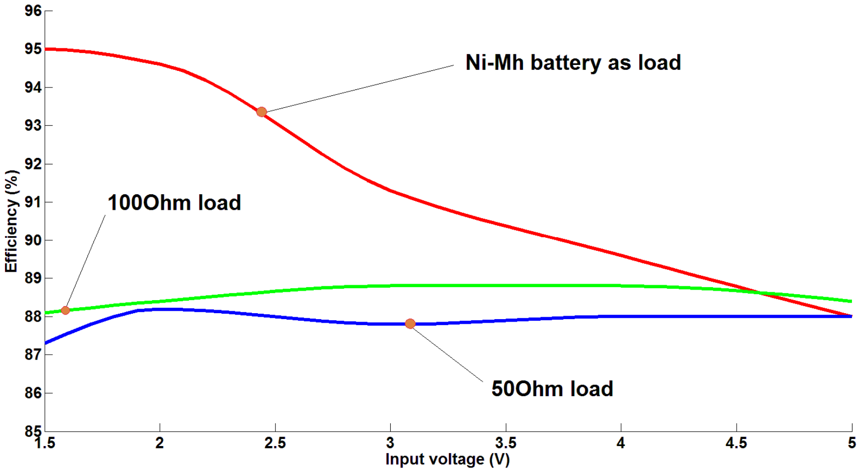

Figure 5.44 Simulated efficiencies when a 50KHz control signal was used. Source [original]

5.4.2 The FPGA control

When replacing the diode from the original Ćuk topology with an N-Mos switch, the simultaneous conduction of the two transistors must be taken into account. Simultaneous conduction will appear because of the different rise and fall times of the N-Mos switches. The datasheet of the IRLML6244 transistor states that the typical total rise time is 12.4 ns while the fall time is 31ns. The datasheet values are generic ones and can vary between manufacturers and between different product samples which may lead to larger differences between the practical rise and fall time.

In order to prevent simultaneous conduction of the N-Mos switches nano-second resolution dead time control must be implemented. In the current work this is achieved with the help of an intially 50MHz SPARTAN 3E FPGA, on which an 80MHz oscillator was added. The increased oscillator frequency allows the FPGA to provide output signals with 12.5 ns resolution.

Figure 5.45 presents a 62.5ns delayed control signals that drive the N-Mos switches.

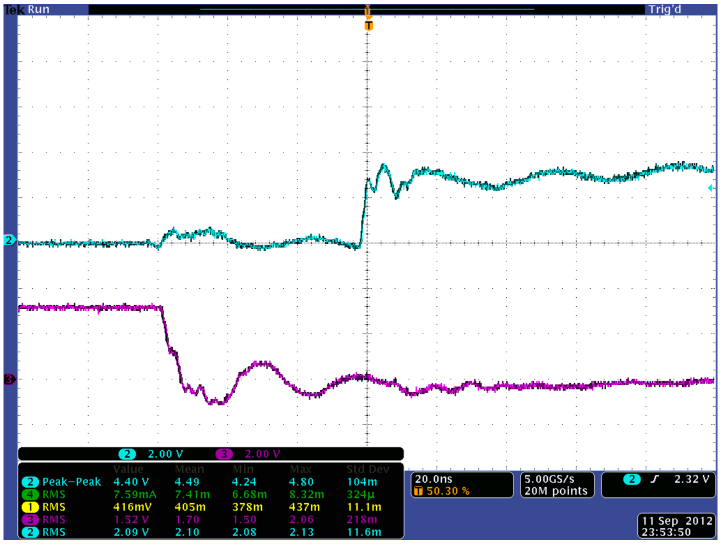

	Value	Mean	Min	Max	Std Dev
2 Peak−Peak	4.40 V	4.49	4.24	4.80	104m
4 RMS	7.59mA	7.41m	6.68m	8.32m	324µ
1 RMS	416mV	405m	378m	437m	11.1m
3 RMS	1.52 V	1.70	1.50	2.06	218m
2 RMS	2.09 V	2.10	2.08	2.13	11.6m

Figure 5.45 Oscilloscope view of the FPGA control signals output with 5 ticks delay (62.5ns). Source [experiment]

A LabVIEW FPGA VI (virtual instrument) was built to generate two control signals. For the N-Mos switch that replaces the diode, a user controlled delay that allows the adjustment of the control signal with an offset with respect to the first N-Mos switch, like in Fig. 5.44, was built.

5.4.3 The control algorithm and the experimental setup

In the experimental setup, the thermoelectrical generator input power source was emulated by a programmable Agilent N6700 power source in series with a variable resistor, the same as in the process explained in Fig. 5.7. An autonomous application has been built in LabVIEW that, at specified time intervals, decouples the converter with the help of a relay (Fig. 5.39), measures the output voltage of the emulated TEG (power source in series with the variable resistance) and modifies accordingly to the implemented lookup table the output voltage of the power source. In this way, a TEG that works under various temperature differences is emulated. Voltage measurements are performed with the help of NI DAQ 6251 board and LabVIEW. The NI DAQ is also responsible for driving the relay that connects or disconnects the load resistance in Fig. 5.39, which in turn enables the computation of the actual internal resistance of the TEGs. In normal operation mode, when the converter charges the battery, the relay in Fig. 5.39 is opened and the load resistance is disconnected. The NI DAQ board measures the input voltage of the converter that is the TEGs output voltage. The output voltage of the converter will also be measured by the NI DAQ board, which is helpful when observing the charging status of the battery.

A LabVIEW VI was built on the PC which accesses, through the NI driver, the SPARTAN 3E FPGA and also controls the NI DAQ 6251 board. The PC VI allows "on the fly" update of the FPGA control signals and allows the user to see the computed internal resistance R_{int} of the emulated TEG and the input and output voltages of the converter.

The control algorithm that allows the proposed Ćuk converter to operate in the maximum power transfer regime was implemented in the LabVIEW PC VI. The maximum power transfer will occur when the resistance of the load equals the resistance of the source or $V_{in} = \frac{V_{noLoad}}{2}$, where $\boldsymbol{V_{in}}$ is the Ćuk converter's input voltage and V_{noLoad} is the output voltage of the TEG when no load is connected to it. The control algorithm is implemented in such way that during normal operation, the measured input voltage of the converter is maintained to half the TEGs output voltage value, when no load is connected to it. The TEGs output voltage is measured at definite periods of time (10 seconds or more), when switch Q_1 is opened and the relay is connected, to check if the internal resistance has been modified.

The control algorithm increments or decrements with two ticks step the N-Mos switches duty cycle, until the desired setpoint has been reached. Taking into account that temperature variation is a slow process and no fast variations are expected, the proposed control algorithm proved effective in maintaining the prescribed setpoint, as will be presented in the following paragraph.

5.4.4 Experimental results

The converter has been implemented using the components specified in the LTspice simulation model. Using the emulated TEG device, different input voltages have been applied, as in the simulation. A 2.4V Ni-Mh battery has been used as load. The input and output voltages have been measured using the oscilloscope probes and the input and output currents by using a 1mA resolution Tektronix TCP0030 inductive current probe (Fig. 5.46).

First, the experiments have been conducted using the original Schottky diode instead of the N-Mos switch. The results showed a lower efficiency by 9.5%, compared to the case when the N-Mos switch was used.

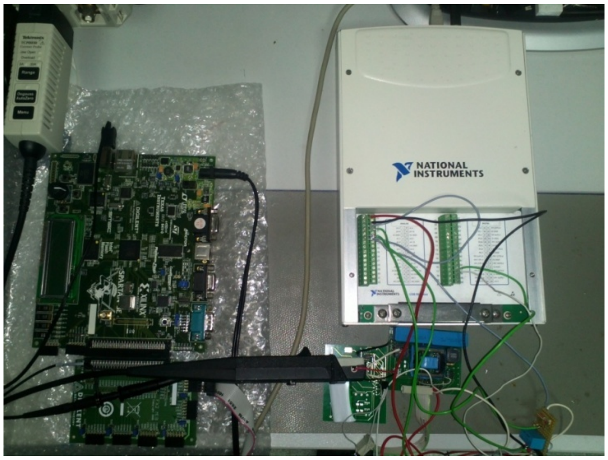

Figure 5.46 Experimental setup: Cuk converter, SPARTAN FPGA, NI DAQ board. Source [original]

Figure 5.47 presents the experimentally computed efficiency versus input voltage, in two cases, with the N-Mos switch and the Schottky diode and with two different loads, the 2.4V Ni-Mh battery and a 100Ω resistor.

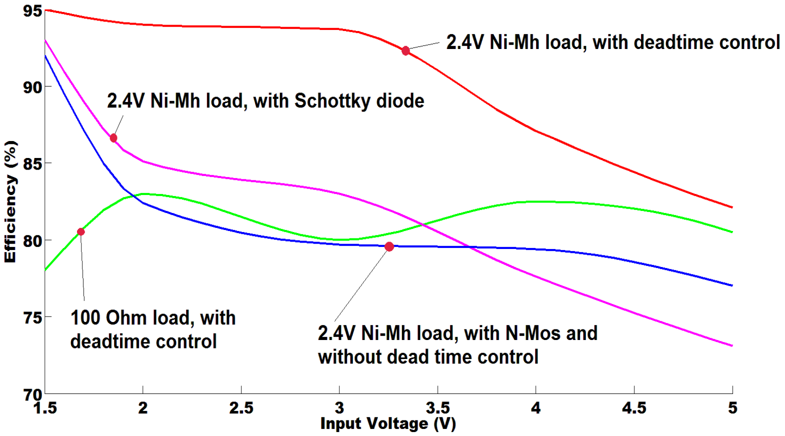

Figure 5.47 Experimentally determined efficiency function of input voltage of the proposed Ćuk converter. Source [original]

The experimentally determined efficiency is 7% lower than the simulated one (Fig. 5.43) when the Ni-Mh battery was used as load. As mentioned, the simulation was conducted using ideal control signal sources with zero output impedance and infinite current sourcing. Due to the fact that the digital logic output of the FPGA has nonzero output impedance and a finite output current, a push-pull stage should be employed to improve the efficiency by rapidly charging the input capacitors of the Q_4 and Q_5 N-Mos switches.

Figure 5.48 presents the drain to source voltage of the two N-Mos switches with a 2.4V Ni-Mh battery pack load, without dead time control. Figure 5.49 show how 100ns dead time control leads to no simultaneous conduction of the two switches.

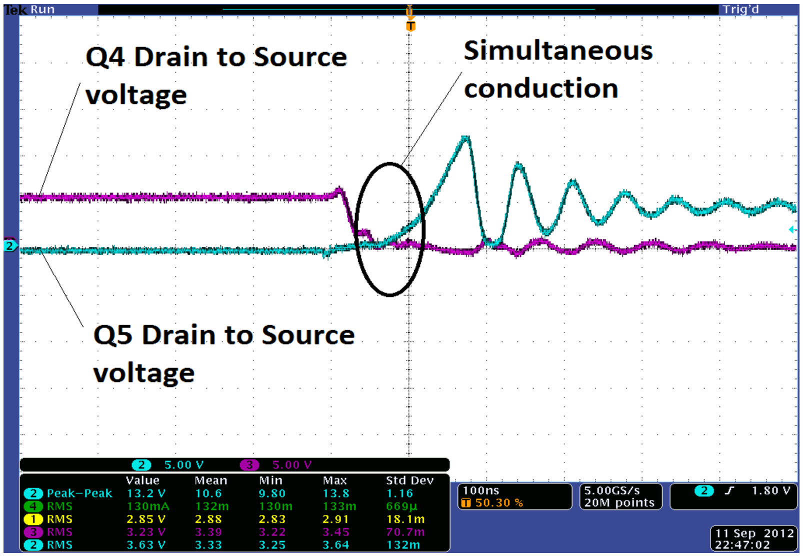

	Value	Mean	Min	Max	Std Dev
2 Peak−Peak	13.2 V	10.6	9.80	13.8	1.16
4 RMS	130mA	132m	130m	133m	669µ
1 RMS	2.85 V	2.88	2.83	2.91	18.1m
3 RMS	3.23 V	3.39	3.22	3.45	70.7m
2 RMS	3.63 V	3.33	3.25	3.64	132m

Figure 5.48 Q_4 and Q_5 Drain to Source voltages and the simultaneous conduction when no dead time is implemented. Source [experiment]

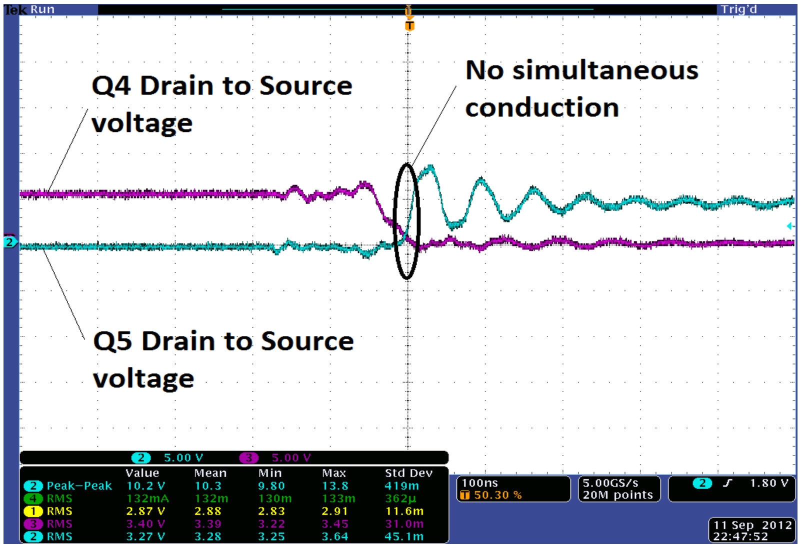

	Value	Mean	Min	Max	Std Dev
2 Peak−Peak	10.2 V	10.3	9.80	13.8	419m
4 RMS	132mA	132m	130m	133m	362µ
1 RMS	2.87 V	2.88	2.83	2.91	11.6m
3 RMS	3.40 V	3.39	3.22	3.45	31.0m
2 RMS	3.27 V	3.28	3.25	3.64	45.1m

Figure 5.49 Q_4 and Q_5 Drain to Source voltages showing no simultaneous conduction with 100ns dead time. Source [experiment]

Figure 5.50 and 5.51 presents the input voltage, output voltage and current through load for the two cases: with and without dead time control implementation.

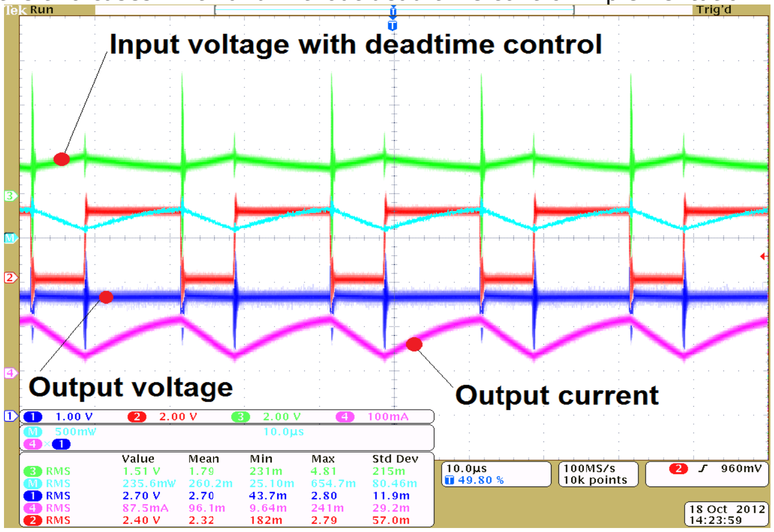

	Value	Mean	Min	Max	Std Dev
3 RMS	1.51 V	1.79	231m	4.81	215m
M RMS	235.6mW	260.2m	25.10m	654.7m	80.46m
1 RMS	2.70 V	2.70	43.7m	2.80	11.9m
4 RMS	87.5mA	96.1m	9.64m	241m	29.2m
2 RMS	2.40 V	2.32	182m	2.79	57.0m

Figure 5.50 Experimental results for 5V input and with dead time control implementation. Source [original]

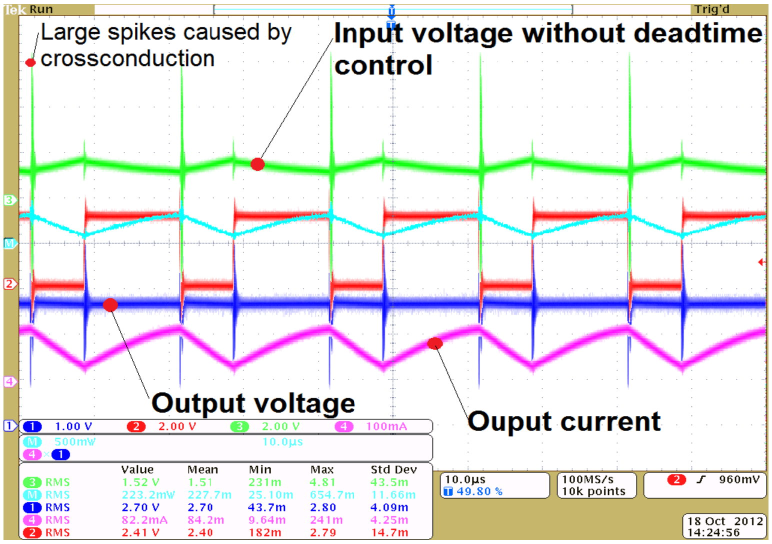

	Value	Mean	Min	Max	Std Dev
3 RMS	1.52 V	1.51	231m	4.81	43.5m
M RMS	223.2mW	227.7m	25.10m	654.7m	11.66m
1 RMS	2.70 V	2.70	43.7m	2.80	4.09m
4 RMS	82.2mA	84.2m	9.64m	241m	4.25m
2 RMS	2.41 V	2.40	182m	2.79	14.7m

Figure 5.51 Experimental results with 5V input voltage and without dead time control. Source [original]

One can observe that when dead time control is not implemented, large spikes appear in the input and output voltages. These are generated by the simultaneous conduction of the two N-Mos switches and are harmful to these switches as can exceed their rated drain to source voltage. Also, the output current is lower in the situation when dead time control is not implemented (82mA) with respect to the situation when 100ns delay was implemented (87mA).

5.4.5 Discussions

The experimental results show an increased efficiency with up to 12% when the dead time is present.
Simulation and experimental results show that when replacing the Schottky diode with an N-Mos switch with adequate dead time control, efficiency is increased with up to 9.5%. By employing a push-pull stage able to rapidly charge the input parasitic capacitors of the N-Mos switches, efficiency can be further increased.
The proposed autonomous control algorithm proved effective in maintaining the desired setpoint, while the TEG power source emulator was helpful in observing the dynamic behavior of the converter and in prescribing real values to the converter's input.

After the design phase, the precise dead time control can be implemented in an ASIC or advanced microcontroller device.

5.5 Conclusions

In the first paragraphs of the fifth chapter 5.1 – 5.4, the author presented the electronics of the proposed energy harvesting device. The design of the electronics part started from the LTC 3105 DC-DC converter which was presented in Chapter 5.1. The converter is designed to work with solar panels or TEGs and allows the adjustment of the output voltage value, offering high efficiency (~80%). The presence of an internal MPPT feature makes the LTC3105 converter an excellent device for harvesting low power energy source as it allows the maximum available power to be transferred to the output. The MPPT feature works by adjusting the equivalent impedance of the converter to match the one of the energy source. This is achieved by the MPPT voltage pin that prevents the input source from collapsing below the used programmable MPPT threshold. However, the datasheet application note of the device presents solutions that work only with solar panels. Taking into consideration that in the current application the TEGs internal resistance vary with temperature in an inverse way it does on solar panels (as the sunlight intensity increases the output voltage lowers), a specific circuitry must be designed. Two solutions, analog and digital were presented. The digital one takes advantage of the existing microcontroller that in the current application is existent on the system. However, in some cases a microcontroller is not available and an analog solution is preferred. The analog solution was first simulated in LTspice and it employs two or three OA devices depending on the user's choice. The solution is based on an NTC thermistor of which exponential temperature characteristic was linearized using two resistors. An ensemble of two OA realize the scaling and slope adjustment in such way that the output voltage of the proposed circuitry (input voltage to the MPPT pin) represents half the TEGs output voltage as it increases with temperature. In this way, a dynamic MPP system was developed. The powering of the OA was provided by the linear output voltage of the LTC converter. As this voltage output is only available when the input power source exceeds 0.25V, the dynamic MPP was designed such that when the circuit is not powered, the equivalent resistance seen by the MPPT pin to have the required value in order to enable the converter operation.

A dedicated LabVIEW application was implemented in order to help correlating the output voltage of the dynamic MPP to the experimentally determined characteristic of the TEGs voltage against temperature and find the necessary resistors values. The simulation results proved the correct functioning of the system. For the experimental circuit, very low powers OAs were chosen (~50μA I_{cc}/amplifier). In this way, the current consumption is below 0.5mA@2.2V. The circuit was implemented and proved to operate as in the simulation being able to maintain the maximum power transfer from TEGs to the LTC converter output. For the practical device testing, a TEG emulator device was designed and built. With the help of a programmable Agilent N6700 power source, a relay, a manual potentiometer and a dedicated LabVIEW application an autonomous TEG emulator was implemented. The correspondence between the TEGs output voltage, internal resistance and temperature were stored in a lookup table and depending on the potentiometer value the N6700 power source generates the appropriate voltage. The potentiometer was manually varied and this action corresponds to a higher or lower temperature value on the TEGs faces.

Section 5.1.3 presents the electronics for the entire energy harvesting device. A PCS (Power Control Switch) system was developed to route the output of the LTC converter to two different 2.4V Ni-Mh batteries that are sequentially charged. After their complete charge, the PCS decouples the input energy source and puts the two batteries in series generating a single 4.8V Ni-Mh battery. Also, the PCS is responsible for routing the energy from the second Li-Ion battery to different devices – GPRS/High power Wi-Fi, sensors, etc.

Paragraph 5.2 presents the step down converter that charges the second Li-Ion battery from the two 2.4V Ni-Mh batteries that are serially connected for this procedure. Two control algorithms were developed, one for constant current charge of the Li-Ion battery, the other for constant voltage. The constant current, constant voltage charge procedure represent the required charging regime of the Li-Ion battery in order to preserve its lifetime and capacity. For the current charge regime, the average current control mode (ACC) was employed. The control algorithm was first simulated using the standard analog devices after which the bilinear transform was used to implement the digital control in a microcontroller. The converter and the digital ACC mode were implemented in practice and the NI DAQ 6251 board was used to control the converter. The digital ACC mode was implemented in LabVIEW. The current was measured using a 10mΩ shunt resistor. For the constant voltage charge regime, a PI regulator was implemented in LabVIEW. The LabVIEW control algorithm also employed the charge mode switching (constant current to constant voltage) in an autonomous way. The practical results proved the correct operation of the device, the control algorithms being able to preserve the charging of the 3.7V Li-Ion battery even when perturbations are present. The efficiency of the Buck converter was not taken into account in this stage of the development. The efficiency can be improved if the Schottky diode is replaced by an N-Mos switch.

Further on, the TEGs system (mechanical parts and TEGs), the LTC converter, dynamic MPP system, PCS system, the batteries and power routes were tested in a real environment (with convective heat transfer). The PCS system was controlled in this stage by the NI DAQ 6251 board. The input and output voltage of the LTC3105 were measured by the NI DAQ 6221 board and also recorded with a TEKTRONIX DPO4104B oscilloscope along with the batteries charging current. The TEGs sides' temperatures were recorded and the values written into a file by the use of an autonomous testing system implemented in LabVIEW and with the NI DAQ 6221 as real world interface. The experimental obtained data were compared to the simulation. A tight correspondence was observed between the two results with errors that did not exceed 14% in the worst case. All the implemented systems (dynamic MPP, Ni-Mh battery sequentially charge, PCS system, power routes) acted as desired, proving the correct operation of the entire system.

A comparison was made between the two TEG models – the one employing varying parameters and the constant parameters one. The first proved to generate the lowest errors. By correlating the experimental measured data to the model of the TEG, the electrical behavior of the device was accurately reproduced in simulation.
The largest error was observed in the prediction of the cold side temperature of the TEGs. This region is associated with the mechanical part of the TEGs system that has the most complex design. This leads to the conclusion that the thermal model of the mechanical setup can be further improved and that it is the one responsible for the erroneous results. If the system would be modelled in a dedicated FEM application, the errors could be reduced at the expense of a detailed and complex model of the mechanical system.

The simulation results of the proposed system can be now used to design an intelligent and specific software power management system that takes into account the charging time of the batteries and how the energy should be used to increase the system efficiency. The detailed steps can further offer a design methodology to be followed when building similar systems.

In subchapter 5.4, an improved Ćuk converter is proposed. The converter aims to harvest the energy from multiple stacked TEGs and charge a battery by continuously adapting the converter impedance to match the one of the TEGs. This type of converter is needed when the waste heat energy spreads over a larger surface and/or the source wastes a high energy (has a high temperature). In this case, the dedicated low power devices are no longer of use as their output power is limited. For the proposed converter, the efficiency was of concern so several solutions were adopted in order to increase it. The Ćuk topology was chosen in order to obtain a step up – step down converter that is necessary when the input power source develops a high voltage and a specific voltage level is needed on the converter output. In order to improve efficiency, the diode existent in the original Ćuk topology was replaced by an N-Mos transistor. The transistors used for building the converter in practice were chosen to have very low r_{dson} resistance (20mΩ), low voltage threshold (0.8V) and dead time control was implemented using a 80MHz FPGA to prevent the simultaneous cross conduction of the switches. The converter was first simulated and then implemented. The experimental results showed a average efficiency of 90% with a 2.4V Ni-Mh battery as load and input voltages from 1.5-5V. The dead time control necessity was analyzed and the experimental results were used to demonstrate the differences between the Schottky diode implementation and the N-Mos switch synchronous rectifier.

The converter impedance was matched to the TEGs internal resistance by imposing the voltage on the converter input to equal half the TEGs output voltage when no load was connected to it. In this way, no current sensor is needed to determine the maximum power transfer to the load.

Although the control was implemented in the design phase using a FPGA, it can be performed in an advanced microcontroller or ASIC after the required dead time delay between the control signals is correctly determined.

5.6 Contributions:

1. **Design, test and implementation of an analog dynamic maximum power point tracking system to be used with the LTC3105 converter.**
    - Design of a LabVIEW application to generate the resistances values.
    - Simulation of the circuit in LTspice using real components values.
    - Implementation using very low power OA.
2. **Design, test and implementation of a two stage energy storage system – the first uses Ni-Mh batteries and the second a 3.7V Li-Ion battery.**
    - The device was implemented, a PCB was designed and low power SMD N and P-Mos switches were used.
3. **Design, test and implementation of a Power Control Switch (PCS) system that routes the output voltage of the LTC converter to two different batteries that are sequentially charged. The two batteries can be connected in series to generate a 4.8V Ni-Mh battery.** The PCS also routes the output energy from the Li-Ion battery to different devices – GPRS/Wi-Fi, sensors, etc.
4. **Design, test and implementation of a step down converter that aims to charge the Li-Ion battery from the 2xNi-Mh batteries using the two charging regimes necessary for the Li-Ion technology (constant current - constant voltage).**
    - Simulation of the analog average current control method (ACC).
    - Implementation and simulation of the digital average current control method.
    - Implementation of the digital ACC in LabVIEW using the NI DAQ 6251 board for the switch control.
    - Implementation of the constant voltage mode control using a PI regulator in LabVIEW and using NI DAQ 6251.
5. **An autonomous testing system was developed in LabVIEW to automatically heat the power resistors and record the temperature and voltage values into an .xls file using the NI DAQ 6251 board.**
6. **A TEG emulator was developed using a potentiometer, a relay, an Agilent N6700 programmable power supply, NI DAQ 6251 board and LabVIEW and used to test the system at specific temperature values.**
7. **An improved Ćuk converter was designed, tested and implemented.**
    - The efficiency of the original topology was increased by replacing the Schottky diode with a N-Mos switch.
    - Enhanced HEXFET low power components were used to improve efficiency.

- Dead time control was implemented using a FPGA to prevent the cross conduction of the two switches that affects the performance of the converter.
- The converter was simulated in LTspice and implemented in practice on a PCB using SMD components and taking into consideration the necessary routing techniques to eliminate losses.

Chapter 6

Conclusions and contributions

6.1 Thesis overview and conclusions

In this work, the internal parameters of a TEM were investigated and based on the experimental results an improved SPICE model was developed. The model is based on the classical governing thermodynamic equations where the parameters dependency of temperature and also the parasitic intrinsic elements were taken into account. Furthermore, an original TEG based energy harvesting system was simulated and implemented.

Chapter 1 reviews over the advances accomplished in the research and industry area of thermoelectric devices. In the last years (2009-2012) attention has been granted to TEGs based energy harvesting systems. Their usage is preferred among other reasons because of no moving parts involved and the robustness of the devices.

The existent SPICE TEM models are also analyzed and the errors that appear when considering the internal parameters constant are highlighted.

An original waste heat energy harvesting system is proposed. The system aims to provide a solution for a self sustainable Wi-Fi condition monitoring system. The system can be used to monitor various parameters (vibrations, temperature, pressures, gases, etc) from heat dissipation machines (turbines, electrical generators, etc).

In **Chapter 2**, the author presents the design of a modular test rig that will be further used in extracting the internal parameters of the TEM and also in the proposed energy harvesting system. The design represents a second version of a setup (Appendix B) used as a guide for developing the current setup. In the current version, care was taken to design the system in such way to prevent the heat reaching from the hot side of the TEG to the cold side through other paths than the TEG itself. This was realized by using low thermal conductivity materials and also by employing 3mm air spacing between the low thermal conductivity Selitherm board and the liquid cooling block of the test rig (Fig. 2.1 – 2.2). Two cooling solutions were adopted, a heat pipe and a thermosyphon. The thermosyphon was built and optimized for the current system while the heat pipe was recovered from a Technics electronic audio power amplifier where it was used for cooling.

A thermally isolated chamber was built in order to measure the thermal conductance of TEMs. The chamber was designed in such way to permit the TEMs test rig fit inside like in Fig. 2.6. The Selitherm board above mentioned has also the purpose of blocking the heat flow reaching the cold side of the chamber through other paths than the TEM itself, when the thermal conductance measurement is in progress. The board also separates the two sides (hot and cold) of the isolated chamber. The chamber was analyzed using a FLIR thermal camera with the TEMs test rig inside, while 10, 40 and 90W power were sequentially fed to the resistive heater, each for a period of approximately 30-40min. The thermal camera inspection validated the thermal isolation ability of the chamber for the temperature ranges the system was tested (lower than 90℃).

Conclusions:
The author found necessary to implement automated measurement processes because of the long settling times for the temperatures and the necessity of logging all the desired data. Also, because some measurement processes as the thermal conductance required a complex control algorithm (feedback control for a water pump, power source control, software signal filtering, etc.), an autonomous process is usually desired. The control algorithms and all the measurement processes were implemented in LabVIEW. For interfacing with the real world (temperature measurements, relay and pump control), two NI DAQ measurement boards - 6251 & 6221 were used. Additional electronic devices were implemented as active second order low pass filtering, H bridge DC motor control, inductive and resistive current measurement devices.

The author implemented a method for measuring the parasitic elements inside a TEM. The phase shift method was used, where a high power, high frequency sine wave was fed to the TEM and the voltage-current phase shift was measured using a digital oscilloscope. Two power amplifiers were implemented but their usage was limited by their frequency characteristics. In order to achieve low distortions at frequencies up to 200 kHz and high output current (~2A), a professional EV Q44 650W amplifier was used. The sine wave was generated by an Agilent signal generator 33250A, that provides mHz resolution. A measurement system was designed in this way, where the intrinsic parasitic components for all the eight tested TEM devices (Everredtronics and Melcor type) could be investigated in the same conditions.

In **Chapter 3**, the author presents a method for the implementation of the new TEM SPICE model. The LTspice simulator was used and all the internal parameters variations with temperature from a TEM were implemented using Arbitrary Behavioral Voltage Sources, where the temperature dependent parameter was expressed as an n^{th} order fitting function. A methodology for creating a thermal model for a complex mechanical test rig using the thermal to electrical analogy is also implemented. The test rig was split into 16 smaller blocks and for each the thermal resistance and capacitance were calculated based on the material properties. Furthermore, the author proposes a method to model the convective heat transfer by the help of the thermodynamic similitude criteria. This method cannot be applied for complex mechanical structures for which analytical similitude criteria do not exist. In either case, a computational fluid dynamics simulator is usually desired as it provides more relevant results and with lower errors. In this case, the mechanical design must be modelled in specialized CAD software.

Conclusions:
By replacing the voltage dependent source from the thermal model of the TEM with current dependent sources, different convergence simulation problems could be

solved. Based on the TEM's material properties, its thermal capacitance (or heat capacity) was calculated. By implementing the thermal capacitance as two distributed parameters, one for each side of the TEM, the SPICE model was able to predict the real behavior of the device more accurate, from two points of view. First, their presence smoothened the temperature variation on the hot and cold side of the TEM when the input power was connected/disconnected. Without the internal heat capacity, unreal and sudden variations would appear in the temperature values. Second, if an AC signal is fed to the TEM's input and the internal heat capacity is not implemented in the model, the hot and cold side temperature would "follow" the applied voltage, no matter the signal frequency. This behavior is unreal and was discussed in detail at the end of paragraph 2.5.

A thermodynamic study was required to determine the necessary similitude criteria that apply when modelling the convective heat transfer process.A numerical computation was performed in Matlab, to generate the thermal resistances associated to the heat transfer coefficients versus temperature. The computation was necessary because the heat transfer coefficient calculation using the similitude criteria is made for the stationary regime of temperatures and the results obtained are for a given temperature difference (ΔT) that enters in the Grashof number formulation.

In **Chapter 4**, the experimental results made to determine the TEM parameters and its behavior under various circumstances are presented. A comparison is made to the simulation results that proved to be in good correlation to the experiments. The constant parameters TEM model is also compared to the new model that predicts the real behavior with an increased accuracy. However, some errors are observed in the temperature prediction of the TEM's sides. The author concluded that these are due to the simplifications adopted when implementing the thermal model of the test rig. The model adopted for representing the intrinsic parasitic components inside a TEM was validated through experiment, the errors being less than 3%.

Conclusions:

The modelling of the convective heat transfer phenomena was in accordance with the real behavior observed through experiment, the errors being below 6%.

The simulated output voltage of a TEG was predicted with 2% error when the varying parameters model was used, in comparison to the constant parameters model that exhibited 12% error.

The simulation results of the TEM's behavior when two signals of 0.2 Hz and 100 kHz are applied to its input were compared to the experiment, showing a good correlation, with a maximum error of 10%.

The simulation results obtained for the existent TEM model were compared to the experimental data and to the new TEM model in order to highlight the increased accuracy of the latter.

In **Chapter 5**, a detailed description of the electronic schematic of the proposed energy harvesting system is made. The author also implemented a novel analog dynamic MPPT system that is able of tracking the TEMs temperature and continuously adjusts the LTC3105 impedance in order to extract the maximum available power from the thermoelectrical generator. The circuit takes advantage of the internal MPPT from the LTC3105 converter. The implemented circuit extends the converter datasheet applications and can also be used in any other device that supports the same (MPPT) functionality.

The motivation for choosing a two stage energy storage system (first is using 2x2.4V Ni-Mh batteries while the second 1x3.7V Li-Ion) is explained through the increased efficiency of the battery charging procedure together with the increased battery lifetime and secondly by the available energy in a topology where one power source is used while the other is regenerating.

The methodology to implement a step down DC-DC converter with a digital average current control method is also presented. The converter is necessary in charging the second battery stage of the harvesting system while obeying the charging regimes of a Li-Ion battery (constant current/constant voltage). The experimental results validate the efficacy of the converter in transferring the charge from the first energy storage stage to the second, in this way also extending the lifetime of both batteries through complete charging/discharging cycles. The efficiency of the step down converter can be increased by replacing the diode from the original topology with an N-Mos transistor, at the expense of increased control logic. A power control switch is also implemented by the author. The PCS is able of independently charging the two 2.4V batteries, afterwards it connects them in series, thus generating a 4.8V equivalent battery.

Conclusions:
The entire system (TEM test rig, DC-DC converter, dynamic MPPT, PCS, batteries) was simulated and implemented, the results showing a good correlation between experimental data and simulation model with ~10% errors. Very low power OAs were used in the implementation of the dynamic MPPT system to achieve as low as possible current consumption (<0.5mA) for the maximum power point tracking system. Simulations also show that an incorrect voltage on the V_{MPPC} pin affects the harvested energy resulting in a lower output current. The same simulated system (without using the varying parameters model) shows an output current value lowered with 40%. If the accurate prediction of the harvested energy is of interest, the error generated by considering the TEMs internal parameters constant will lead lo large errors as presented in the results. These errors can moreover be amplified by other two factors. One is the thermal model of the test rig or system that generates the heat and deals with the cooling of the TEM device. The second error comes from the behavior of the DC-DC converter. For the LTC3105 converter, the efficiency is lowered by 5% if for the same output current, the input voltage drops from 1.5 to 1V. In this way, if the predicted output voltage of the TEG is erroneous, the error of the energy prediction on the converter output is amplified. This demonstrates the usefulness of the varying parameters TEM model and that considering the parameters constant leads to large errors.

In **the final paragraph**, an improved efficiency Ćuk converter is implemented where the diode from the original topology is replaced by an N-Mos. The converter can be used to charge a battery from a waste heat energy source that has physically large dimensions typically when a number of TEMs can be serially connected. The necessary control logic for the converter is implemented in an FPGA along with 100ns dead time control.

Conclusions:
The experimental results show that when charging a 2.4V Ni-Mh battery, the efficiency of the proposed converter is increased to a average value of 90%, for the input voltage range of 1.5-5V. In the standard topology, with a Schottky diode, the efficiency is ~83% as determined in the experiments.

6.2 Contributions

In the following, a review is made over the twelve major contributions.

1. **A complete self-sustainable wireless device for waste heat recovery is proposed.**
   The device aims to recover the waste heat produced by industrial machinery to power a conditional monitoring system that communicates with a base system via a high power Wi-Fi transceiver. The proposed device is completely autonomous and employs a two stage energy storage system. Based on the improved TEM SPICE model later proposed, the waste heat recovery device output power can be accurately predicted and various algorithms can be optimized for optimum power consumption.
2. **Design and development of a modular test rig used for parameters extraction and also for the energy harvesting system (thermal to electrical conversion and cooling).**
   The author also proposed and implemented two cooling solutions, one using a thermosyphon and the other a heat pipe. The thermosyphon was specifically designed and manufactured for the current setup.
3. **Designing and development of automatic measurement applications for measuring the thermal conductance, internal resistance and Seebeck coefficient of a TEM.**
   A two layer thermally isolated chamber was designed and manufactured to be used in the thermal conductance measurement process. A thermo vision analysis of the isolated chamber was performed to determine the heat leakage. This analysis was necessary for validation of the enclosure isolation ability. PI controllers were used for water pump flow control and temperature setpoint regulation and the tuning parameters have been experimentally determined. An H bridge motor controller was implemented to control the water pump used in the thermal conductance measurement process. Second order active filters were implemented for filtering the measurement signal noise together with additional software moving average filters. A measurement application was implemented in LabVIEW and the real world interfacing was performed with an NI DAQ 6221 board.
4. **TEM parasitic inductance and capacitance analysis and measurement using the phase shift method.**
5. **Proposal of an equivalent SPICE electrical model employing the internal parasitic elements of a TEM.**

The integration of the thermodynamic governing equations was made in order to highlight the TEM resistor-like behavior, when high frequency AC signals (50-200 kHz) are fed to its input.

The experimentally determined parasitic components L and C were implemented in the new SPICE model.

6. **An improved SPICE thermoelectrical TEM model was implemented with dynamic S, R_t and R_e (Seebeck coefficient, thermal resistance and electrical resistance) variation against temperature**.

   The variations were implemented through ABVS sources and 1st (or higher) order or logarithm fitting functions that approximate the experimental measured values.

   The thermal part that describes the TEM was improved by adding the computed thermal capacitance of the module and using distributed parameters when representing the thermal resistance and thermal capacitance.

   The TEM model employing distributed thermal resistance and three current dependent sources proved to help the simulations converge at points where the model with one voltage and one current dependent sources failed in computing the results.

   The mechanical parts of the test rig were split into smaller blocks and for each the thermal capacitance and resistance was calculated. The thermal resistance of the air gaps and other elements (thermal contact grease, rubber sealing, isolated chamber resistance) was also calculated.

   The overall SPICE thermoelectrical model of the system that is tested in thermally isolated conditions was implemented.

7. **A novel SPICE implementation of the convective heat transfer process that appears under normal operating conditions of the test rig.**

   For each mechanical part that is in contact with the cooling fluid (air), the heat transfer coefficient under laminar flow was calculated. Due to the complicated geometry of the heatsink, an approximation had to be made to analytically calculate the average heat transfer coefficient.

8. **Experimental measurements to determine the internal parameters variation with temperature for two different TEM types (TEG & TEC) including the intrinsic parasitic inductance and capacitance values that have not been taken into account so far.**

9. **Design, test and implementation of an analog dynamic maximum power point tracking system to be used with the LTC3105 converter.**

   A LabVIEW application was implemented to generate the resistances values. The model of the circuit was built and simulated in LTspice using real components values.

10. **Design, test and implementation of a two stage energy storage system – the first uses Ni-Mh batteries and the second a 3.7V Li-Ion battery.**

The device was implemented, a PCB was designed and low power SMD N and P-Mos switches were used.

11. **Designing, testing and implementation of a step down converter that aims to charge the Li-Ion battery from the 2xNi-Mh batteries using the two charging regimes necessary for the Li-Ion technology (constant current - constant voltage).**

    The analog average current control method (ACC) was simulated and based on it the digital average current control method was derived and simulated. The digital ACC method was implemented in LabVIEW using the NI DAQ 6251 board for the switch control, current and voltage measurements. A constant voltage mode control method was implemented in LabVIEW using a PI regulator.

    A **TEG emulator** was developed using a potentiometer, a relay, an Agilent N6700 programmable power supply, a NI DAQ 6251 board and LabVIEW and used to test the system at specific temperature values.

12. **An improved Ćuk converter was designed, tested and implemented.**

    The efficiency of the original topology was increased by replacing the Schottky diode with a N-Mos switch. Enhanced HEXFET low power components were used to improve the efficiency. Dead time control was implemented using a FPGA to prevent the cross conduction of the two switches that affects the performance of the converter.

    The converter was simulated in LTspice and implemented in practice on a PCB using SMD components and taking into consideration the necessary routing techniques to eliminate losses.

References

[1] Minnich, A., “Modeling the Thermoelectric Properties of Bulk and Nanocomposite Thermoelectric Materials”, MSc dissertation, MIT, USA, 2008.

[2] ‘REN21’, Renewables 2011 Global Status Report, www.ren21.net, last visited 1st November 2012.

[3] ‘REN21’, Renewables 2012 Global Status Report, www.ren21.net, last visited 1st November 2012.

[4] ‘BP’, Statistical Review of World Energy, June 2012, www.bp.com/statisticalreview, last visited 1st November 2012.

[5] Yu Zhou, “Energy Harvesting Using a Thermoelectric Generator and Generic Rule-Based Energy Management”, MSc dissertation, Case Western Reserve University, Cleveland, USA, 2008.

[6] Summary Report, Science of Sustainability 2006 - A view from Japan, 2006, www.sos2006.jp, last visited 1st November 2012.

[7] Bitschi, A., “Modelling of thermoelectric devices for electric power generation”, Ph.D. dissertation, Swiss Federal Institute of Technology Zurich, ETH Zurich, 2009.

[8] Yu, J., Zhao, H.,”A numerical model for thermoelectric generator with the parallel-plate heat exchanger”, Science Direct, Journal of Power Sources 172 (2007), 2007.

[9] Rowe, D.M., “Thermoelectrics Handbook, Macro to Nano”, Taylor & Francis Group, 2006.

[10] Ciobanu G, Constantinescu, C., “Solid state physics”-in Romanian, Technical Publishing, Bucharest, 1982.

[11] Tutovan, V., “Electricity and Magnetism” – in Romanian, Technical Publishing, Bucharest, 1984.

[12] Zorbas, K.T., Hatzikraniotis, E., and Paraskevopoulos, K.M., „Power and Efficiency Calculation in Commercial TEG and Application in Wasted Heat Recovery in Automobile”, 5th European Conference on Thermoelectrics, Odessa, Ukraine, Volume: i, Issue: 3, 2007, pp. 292-298.

[13] Ziolkowski, P., Poinas, P., et al. ”Estimation of Thermoelectric Generator Performance by Finite Element Modeling”, Journal of Electronic Materials, Vol. 39, No 9, 2010.

[14] McCoy, J., „Thermoelectric Technology: Materials, Processes, Devices and Systems”, ASM San Diego Chapter, January 2012, www.hi-z.com, last visited 1st November 2012.

[15] Schock, H., Case, E., et al, „Thermoelectric Conversion of Waste Heat to Electricity in an IC Engine Powered Vehicle”, US Department of Energy, U.S. Department Energy Efficiency & Renewable Energy (EERE), January 2011, www1.eere.energy.gov, accessed November 2012.

[16] Crane D.T., „Thermoelectric Waste Heat Recovery Program for Passanger Vehicles”, U.S. Department Energy Efficiency & Renewable Energy (EERE), May 2012, www1.eere.energy.gov, accessed November 2012.

[17] Mazar, B., „State of the Art Prototype Vehicle with a Thermoelectric Generator”, TE Application Workshop, Baltimore, March, 2012, www1.eere.energy.gov, accessed November 2012.

[18] Eder, A., Linde M., „Efficient and Dynamic – The BMW Group Roadmap for the Application of Thermoelectric Generators", 2nd Thermoelectrics Applications Workshop, San Diego, January 2011, www1.eere.energy.gov, accessed November 2012.

[19] 'Automotive Waste Heat Recovery', www.gentherm.com, 2012, last visited 1st November 2012.

[20] Jovanovic, V., Ghamaty, S. and Bass, J., "Design, Fabrication and Testing of a Novel Energy Harvesting Thermoelectric Power Supply for Wireless Sensors", Proceedings of PWR2006 ASME Power, Atlanta, GA, USA May 2-4, 2006.

[21] Mateu, L.,Codrea, C., Lucas, N., Pollak, M. and Spies,P., 'Energy Harvesting for Wireless Communication Systems Using Thermogenerators', Proceeding of the XXI Conference on Design of Circuits and Integrated Systems (DCIS), Barcelona, Spain 2006.

[22] Miller, L., Chen, A., Zhu, Y., Madan, D., et al, "Energy Harvesting: MEMS Piezoelectric Vibration Harvesting and Thermoelectric Harvesting", University of California, Berkeley, 2011.

[23] Snyder, J., "Small Thermoelectric Generators", California Institute of Technology, USA, 2008.

[24] Russel, K., "A Hybrid Thermoelectric Cooler Thermal Management System for Electronic Packaging", MSc dissertation, McMaster University, Canada, 2011.

[25] Meisner, G.P., "Advanced Thermoelectric Materials and Generator Technology for Automotive Waste Heat at GM", 2011 Thermoelectrics Applications Workshop, San Diego, 2011.

[26] Taranovich, S., "The Rover's Energy", EDN magazine topic, Mission to Mars: NASA Engineering and the Red Planet, August 9, 2012.

[27] Zhang, X., Chau, K.T. and Chan, C.C., "Design and Implementation of a Thermoelectric-Photovoltaic Hybrid Energy Source for Hybrid Electric Vehicles", World Electric Vehicle Journal Vol. 3 - ISSN 2032-6653, 2009, AVERE, 2009.

[28] Kraemer, D., Hu, L., Muto, A., Chen, X., Chen G., et al, "Photovoltaic-thermoelectric hybrid systems: A general optimization methodology", Appl. Phys. Lett. 92, 243503 (2008), 2008.

[29] Vorobiev, Y., Gonzalez-Hernandez, J., Vorobiev, P., Bulat, L., "Thermal-photovoltaic solar hybrid system for efficient solar energy conversion", Science Direct, Solar Energy 80 (2006), 2006.

[30] Rosendahl, L.A., Rezania, A., "Considering Thermoelectric Power Generation Device Efficiency Using Microchannel Heat Sink", V European Conference on Computational Fluid Dynamics ECCOMAS CFD 2010, Lisbon, Portugal, 14–17 June 2010.

[31] Chen, W.H., Liao, C.Y., Hung, C.I., "A numerical study on the performance of miniature thermoelectric cooler affected by Thomson effect", Elsevier, Applied Energy 89 (2012) 464–473, 2012.

[32] Meng, F., Chen, L., Sun, F., "A numerical model and comparative investigation of a thermoelectric generator with multi-irreversibilities", Elsevier, Energy 36 (2011), 2011.

[33] Du, C.Y., Wen, C.D., "Experimental investigation and numerical analysis for one-stage thermoelectric cooler considering Thomson effect", International Journal of Heat and Mass Transfer 54 (2011) 4875–4884, Elsevier, 2011.

[34] Apertet, Y., Ouerdane, H., Glavatskaya, O., Goupil, C. and Lecoeur, P., "Optimal working conditions for thermoelectric generators with realistic thermal coupling", EPL, 97 (2012), 2012.

[35] Apblett, C.A., Whalen, S.A., Moorman, M.W., Aselage, T.L., Siegal, M.P. and Frederick, S.K., "A Miniaturized mW Thermoelectric Generator for NW Objectives: Continuous, Autonomous, Reliable Power for Decades", SANDIA REPORT SAND 2006-6956, 2006.

[36] Lossec, M., Multon, B., Ben Ahmed, H., Goupil, C., "Thermoelectric generator placed on the human body: system modeling and energy conversion improvements", The European Physical Journal Applied Physics 52, 1 (2010), 2010.

[37] Lineykin, S., and Yaakov, S.B., "Modeling and Analysis of Thermoelectric Modules", IEEE Transactions on Industry Applications, 2007.

[38] Yang, M., Xu W. and Tang, W., "Thermal analysis of laser diode module by an equivalent electrical network method", Optoelectronics Letters Vol.2 No.4, 15 Jul. 2006.

[39] Alaoui, C., "Peltier Thermoelectric Modules Modeling and Evaluation", International Journal of Engineering (IJE), Volume (5), Issue (1), 2011.

[40] Mirocha, A., Dziurdzia, P., „Improved Electrothermal Model of the Thermoelectric Generator implemented in SPICE", International Conference on Signals And Electronic Systems, ICSES, Krakow, Poland, September 2008.

[41] Chen, M., Student Member, IEEE, Rosendahl, L.A., Condra, T.J. and Pedersen, J.K., Senior Member, IEEE, "Numerical Modeling of Thermoelectric Generators With Varing Material Properties in a Circuit Simulator", IEEE Transactions on Energy Conversion, Vol. 24, No. 1, March 2009.

[42] Chen, M., Rosendahl, L.A., Bach, I., Condra, T., Pedersen, J.K., "Transient Behavior Study of Thermoelectric Generators through an Electro-thermal Model Using SPICE", IEEE, 2006 International Conference on Thermoelectrics, 2006.

[43] LabVIEW, NI Application Software, www.ni.com, 2012, last accessed November 2012.

[44] ‚LTC 3105 Step-Up DC/DC Converter', *Linear Technologies Datasheet*, http://www.linear.com/product/LTC3105, 2011, last accessed November 2012.

[45] Feynman, R., "Lectures on Physics Mainly Mechanics, Radiation and Heat", Addison-Wesley Publishing, 1977.

[46] 'Selitherm', Info Sheet, www.selit.com, last accessed November 2012.

[47] 'Everredtronics LTD. Technical Info', http://www.everredtronics.com, accessed August 2012.

[48] Melcor, 'Application Notes for Thermoelectric Devices', former www.melcor.com, acquired by Laird Technologies, www.lairdtech.com, last visited October 2012.

[49] 'Seintek P6100 Power supply', Info Sheet, www.seintek.com, last accessed November 2012.

[50] 'FLIR ThermaCAM E2', Datasheet, www.flirthermography.com/E2data, last accessed August 2011.

[51] Leonachescu, N., "Thermotechnics" – in Romanian, Didactica and Pedagogica Publishing, 1981.

[52] Bazil, P., "The thermotechnician engineer handbook" – in Romanian, *Technical Publishing*, 1986.

[53] 'BK Precision 889B Bench LCR/ESR Meter User Manual', www.bkprecision.com, last accessed November 2012.

[54] 'Tektronik DPO4104B User Manual', www.tek.com, last accessed November 2012.

[55] '303 Circuits', Elektor Electronics, England, 1988.

[56] 'Electro-Voice Q44 Stereo Power Amplifier product specifications', www.electrovoice.com, last accessed November 2012.

[57] Linear Technology SPICE Simulator, www.linear.com, last accessed November 2012.

[58] Wang, T.Y., Chen, C.C., "SPICE-Compatible Thermal Simulation with Lumped Circuit Modeling for Thermal Reliability Analysis based on Modeling Order Reduction", 5th International Symposium on Quality Electronic Design, IEEE Proceedings, 2004.

[59] Laprade, A., Pearson, S., Benczkowski, S., Dolny, G., Wheatley, F., "A New PSPICE Electro-Thermal Subcircuit For Power MOSFETs", *Fairchild Semiconductor Application Note 7534*, July 2004.

[60] Gorbachuk, N.P, Bolgar, A.S., Sidorko, V.R. and Goncharuk, L.V., "Heat Capacity and Enthalpy of Bi_2Si_3 and Bi_2Te_3 in the Temperature Range 58-1012K", Powder Metallurgy and Metal Ceramics, Vol.43, 2004.

[61] 'Elements, Chemical and Chemistry', *Molar Mass of Bismuth telluride*, www.chemicalaid.com, last acceseed November 2012.

[62] Nenitescu, C.D., "General Chemistry" – in Romanian, Didactic and Pedagogical Publishing, Bucharest, 1972.

[63] Raznjevic, K., "Thermodynamic tables and diagrams" – in Romanian, Technical Publishing, 1978.

[64] Bica, M., Nagi, M., Cernaianu, C.D., Bara, N., "Heat transfer" – in Romanian, Universitaria Publishing, Craiova, Romania, 2009.

[65] Hensen, J.L., Nakhi, A.E., "Fourier and Biot Numbers and the Accuracy of Conduction Modelling", Proceedings of Bep 94 Conference "Facing the Future", pp. 247-256, 1994.

[66] 'Energizer Charger Handbook', Energizer Battery Manufacturing Inc, USA, version Chg 1.4, 2008.

[67] Yoshio, M., Lithium-Ion Batteries Science and Technologies, Springer, pp. XVII-XXV, 2009.

[68] 'Harding Battery handbook for Quest Rechargeable Cell and Battery Packs', Lithium Ion, Section 5, 2004.

[69] Popescu, V., Lascu, D., „Power sources used in telecommunications" – in Romanian, West publishing, Timisoara, pp.66-76, 2002.

[70] Purton, K.D., „Average current mode control in power electronics converters – Analog versus Digital", Electrical and Computer System Engineering, Monash University, Australia, 2002.

[71] Chattopadhyay, S., „A Digital Current-Mode Control Technique for DC–DC Converters", IEEE Transactions on Power electronics, vol. 21, no. 6, November 2006.

[72] Shin, J.W., „Digital Average Current Mode Control of Boost Converter Using Diode Current Sensing Technique", Proceeding of Power Electronics, Volume: 599, pp. 151–744, 2009.

[73] Caspoc 2005 simulator, www.simulation-research.com, last visited November 2012.

[74] 'MAXIM 17710', Application Note 5259, www.maximintegrated.com, last accessed March 2012.

[75] Erickson, R.W., „Fundamentals of Power Electronics Second Edition", Second Printing, pp. 440-482, 2001.

[76] Rashid, M.H., "Power Electronics Handbook (Second Edition)", Academic Press, 2007.

Published papers:

[1] **Mihail Cernaianu**, Adrian Cernaianu, Cosmin Cirstea, Aurel Gontean, "Thermo Electrical Generator Improved Model", ICPES 2012, published in Lecture Notes in Information Technology, Vol. 13, Power and Energy Systems, Hong Kong, 2012.
[2] **Mihail Cernaianu**, Cosmin Cirstea, Dan Lascu, Aurel Gontean, "Battery Charger System Employing Average Current Control", ICPES 2012, Hong Kong.
[3] **Mihail Cernaianu**, Aurel Gontean, "Parasitic Elements Modelling in Thermoelectric Modules", under IET review.
[4] **Mihail Cernaianu**, Aurel Gontean, "High Accuracy TEM model for Energy Harvesting Systems", provisionally accepted by IET – CDS journal.
[5] **Mihail Cernaianu**, Paul Harfas, "Balancing an Inverter Pendulum – a LabView FPGA & BLDC Motor Implementation", National Instruments Case Study Booklet Eastern Europe, 2011.
[6] **Mihail Cernaianu**, Paul Harfas, Aurel Gontean, "Code parallelization for wind speed model generator", ISSE, Warsaw, 2010.
[7] **Mihail Cernaianu**, Aurel Gontean, "Thermoelectric Modules Thermal Conductance Measurement System", ISETC2012, Timisoara, Romania, 2012.
[8] **Mihail Cernaianu**, Cosmin Cirstea, Aurel Gontean, "Thermoelectrical Energy Harvesting System: Modelling, Simulation and Implementation", ISETC2012, Timisoara, Romania, 2012.
[9] **Mihail Cernaianu**, Aurel Gontean, "Cuk Converter Employing Indirect Current Control Loop for TEG Energy Harvesting Devices", SIITME2012, Alba Iulia, Romania, 2012.
[10] **Mihail Cernaianu**, Aurel Gontean, "Dynamic Maximum Power Point Tracking System for TEGs", submitted for publishing to EDN electronics magazine.
[11] C. Cirstea, **M. Cernaianu**, A. Gontean, "Packet Loss Analysis in Wireless Sensor Networks Routing Protocols", 35th International Conference on Telecommunications and Signal Processing (TSP 2012), Prague, Czech Republic, ISBN 978-1-4673-1116-8, 3-4 July 2012, pp. 37-41.
[12] C. Cirstea, **M. Cernaianu**, A. Gontean, "A Cluster Head Election Method with Adaptive Separation Distance and Load Distribution for Wireless Sensor Networks", to be published at The Fourth International Conference on Emerging Network Intelligence, EMERGING 2012, September 23-28, Barcelona, Spain.
[13] C. Cirstea, **M. Cernaianu**, A. Gontean, "An Inductive System for Measuring Microampere Currents", SIITME2012, Alba Iulia, Romania, 2012.

APPENDIX A

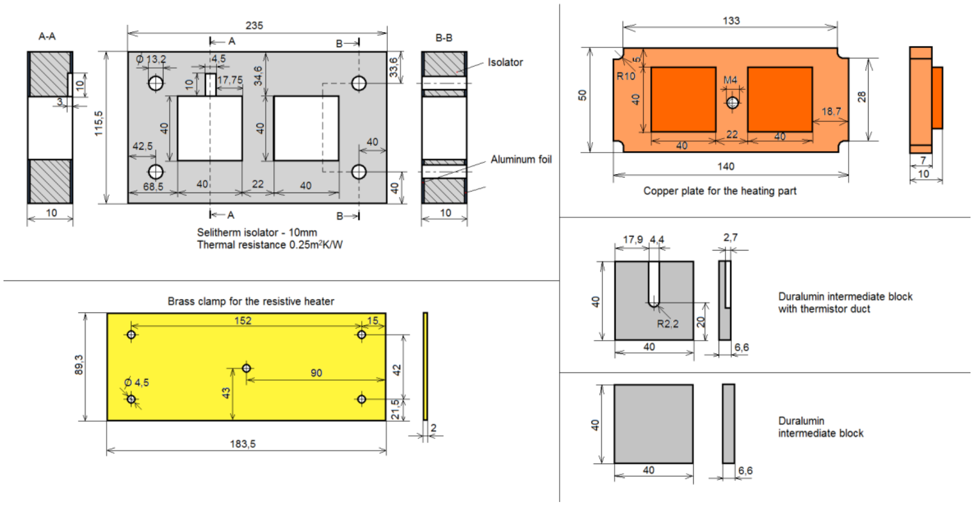

Figure A.1 Mechanical details for the TEM test rig. Source [original]

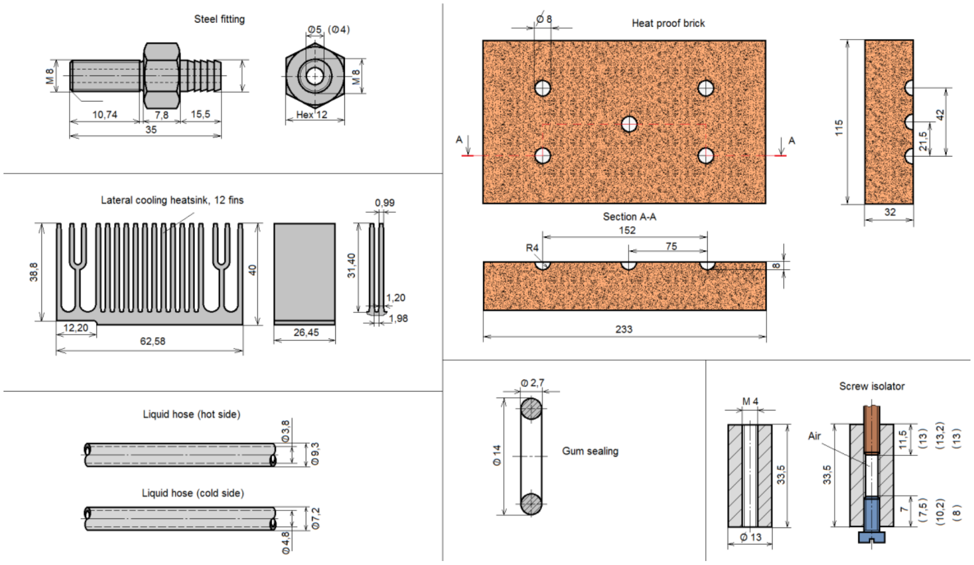

Figure A.2 Mechanical details for the TEM test rig (2). Source [original]

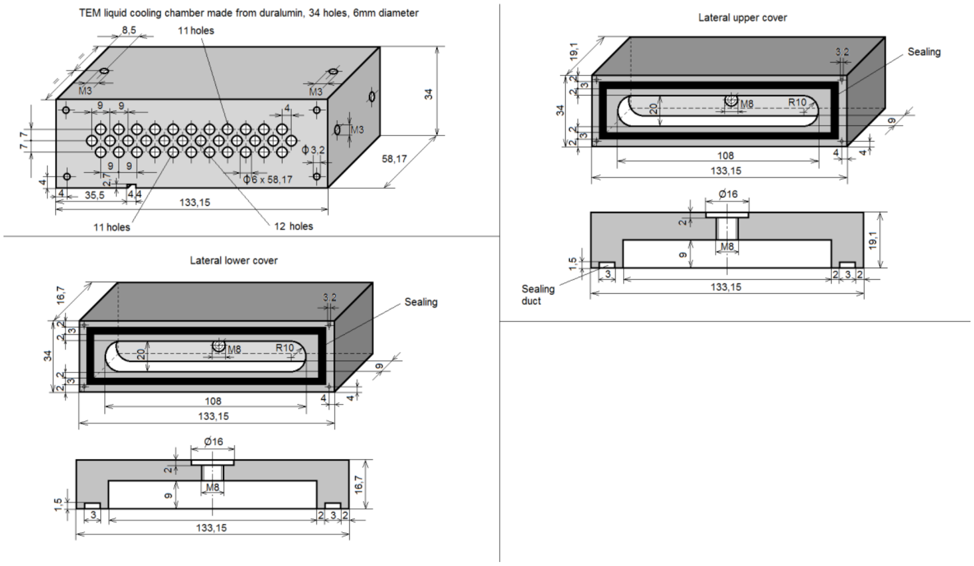

Figure A.3 Mechanical details for the TEM test rig (3). Source [original]

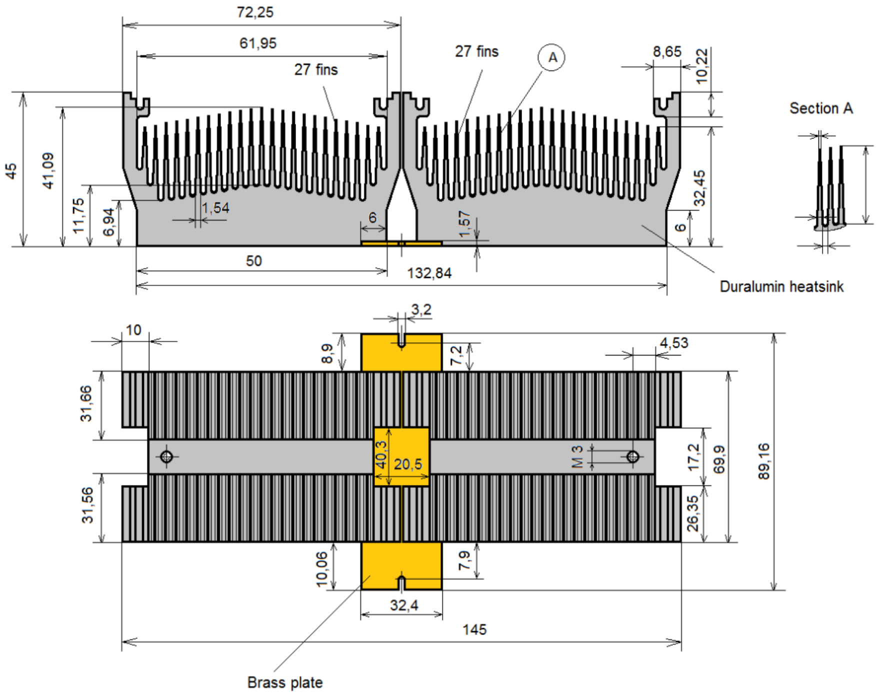

Figure A.4 Mechanical details for the TEM test rig (4). Source [original]

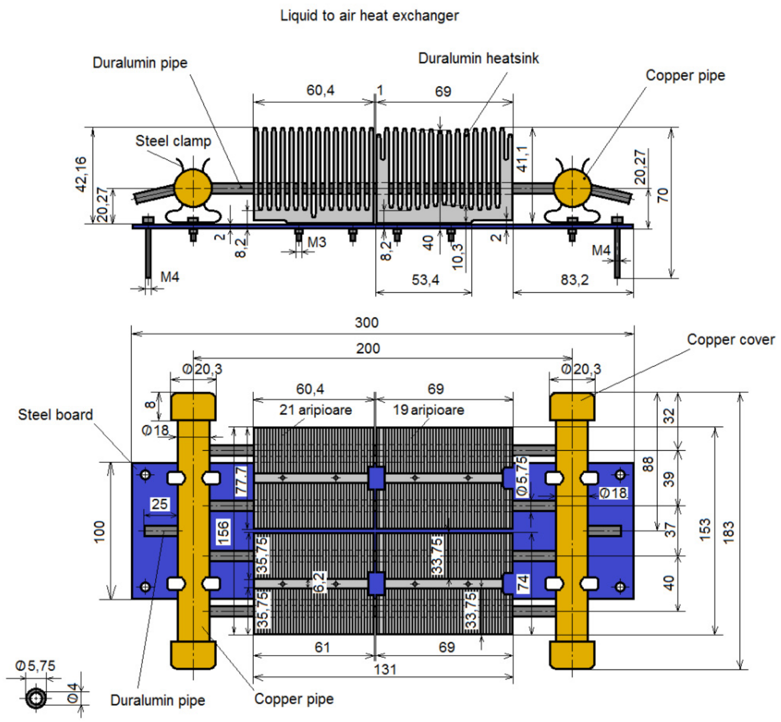

Figure A.5 Mechanical details representing the heat exchanger. Source [original]

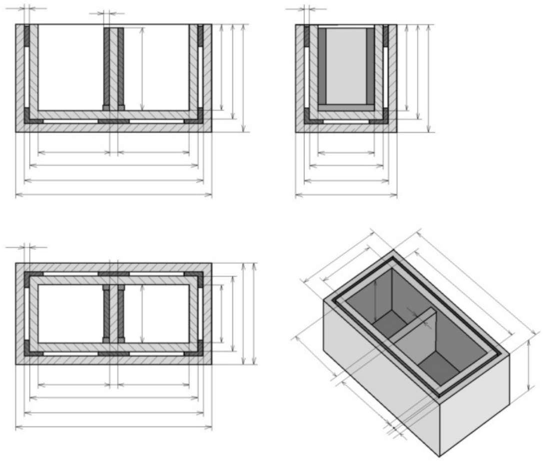

Figure A.6 Details representing the thermally isolated chamber. Source [original]

APPENDIX B

This section presents the original setup that was first built to house the TEMs. The test rig was useful in designing an improved setup, with no heat loss, better cooling ability and increased mechanical stability.

Figure B.1 Upper view of the original setup. Source [original]

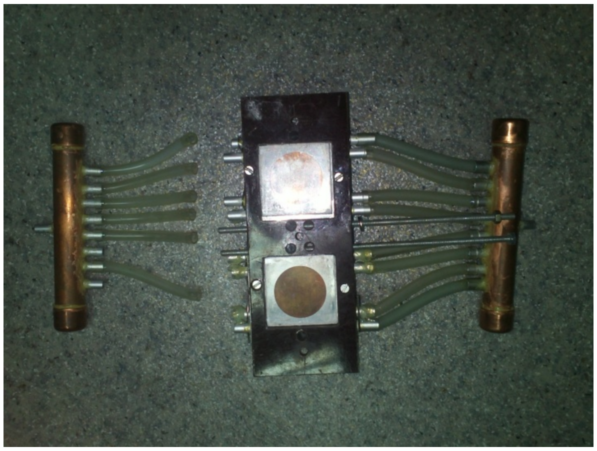

Figure B.2 Lower view of the original TEM test rig depicting the TEMs housing. Source [original]

APPENDIX C

Table C.1 Physical and measurement units analogy

Physical unit	Symbol	Measurement unit	Physical unit	Symbol	Measurement unit
Temperature	T	K	Electric potential	E	V
Heat flow	Φ	W	Electrical intensity	I	A
Thermal flux density	q	W/m^2	Electric current density	j	A/m^2
Thermal conductivity	k	W/m·K	Electrical conductivity	ρ_e	1/Ω·m
Thermal resistivity	r_t	m·K/W	Electrical resistivity	$r_e=1/\rho_e$	Ω·m
Thermal resistance	R_t	K/W	Electrical resistance	R_e	Ω
Heat capacity	C_t	J/K	Electrical capacity	C_e	F
Heat transfer coefficient	α	W/m^{2}K	Electrical specific conductibility	$1/R_e \cdot A_e$	1/ Ω·m^2

Table C.2 Equations analogy

Name	Expression	Name	Expression
Fourier law	$q = -k \cdot gradT$	Ohm's general law	$j = -\rho_e \cdot gradV$
Thermal flux transmitted through a non homogenous wall in stationary regime	$\Phi = \dfrac{\Delta T}{\sum_{i=1}^{n} R_{t_i}}$	Kirchhoff law for serial resistance	$I = \dfrac{V}{\sum_{i=1}^{n} R_{e_i}}$
Thermal flux transmitted under non-stationary regime	$\Phi = C_t \dfrac{\Delta(\Delta T)}{\Delta \tau_t}$	Electrical intensity with time varying voltage	$I = C_e \dfrac{\Delta V}{\Delta \tau_e}$
Newton's law	$\Phi = \alpha \cdot A_t \cdot \Delta T$	Ohm's law	$I = \dfrac{V}{R_e}$

APPENDIX D

Table D.1 Physical properties for the materials used in the test rig's construction

Material	Thermal conductivity (20℃)	Specific heat capacity	Density
Copper	395 W/m·K	381 J/kg·K	8900 kg/m^3
Duralumin	165 W/m·K	913 J/kg·K	2800 kg/m^3
Brass	100 W/m·K	381 J/kg·K	8600 kg/m^3
Porcelain	0.8-1.8 W/m·K	795 J/kg·K	2400 kg/m^3
Rubber	0.160 W/m·K	1424 J/kg·K	1200 kg/m^3
Polystyrene	0.03-0.157 W/m·K	1300 J/kg·K	1050 kg/m^3

APPENDIX E

It is known that for some differential equations that reflect a series of physical phenomena the mathematic analysis don't offer adequate solutions. The similitude in physics deals with the similarity between phenomena and offers the possibility to treat the original by the help of a model. The concept represents an extension to the similarity notion from geometry but instead using geometric elements, much more complex similitude criteria built from macroscopic parameters are applied.

The similitude in physics is built on three postulates and three laws. The laws are in close conjunction with the concept of similitude criteria that represent a dimensionless group of physical quantities bound by the multiplication operator and which characterize the similar phenomena.

The first similitude law states that physical phenomena are similar if the corresponding similitude criteria have identical values [51]. The second law states that any physical phenomena can be expressed by a criteria relationship. In this way the relationship between the macroscopic parameters:

$$f(k,\rho,c_p,T,\nu...)=0 \tag{E.1}$$

can be substituted with an equivalent criteria relationship with the form:

$$F(\Pi_1,\Pi_2,...\Pi_n)=0 \tag{E.2}$$

where Π_i represent a similitude criteria.

It is important to decide the similitude criteria between the scale model and the proposed test rig from this work in order to create a model for the convective heat transfer. The convective heat transfer respects the thermodynamic principles and implies substance transfer in the fluid [51]. One can distinguish two main categories of convective phenomena: free convection characterized by low movement speeds due to the Archimedes' forces and forced convection characterized by high movement speeds due to large pressure differences. The elements that influence the convection of heat and determine its complex character are the nature of the fluid involved together with its speed and acceleration fields, the temperature field within the fluid and the solid near the separation surface, the fluid's thermo physical quantities (density, viscosity, specific heat capacity, etc), pressure distribution, etc.

Newton's law stands on the basis of heat convection and predicts the thermal flux density on the surface of a solid body that resides at T temperature and which transfers that temperature to a moving fluid with T_{fluid} temperature.

$$\vec{q} = \alpha(T - T_{fluid})\ [\mathrm{W/m^2}] \tag{E.3}$$

where ***a*** is the convection coefficient or heat transfer coefficient.

The similitude criteria are determined by using the affine transform on the Fourier – Kirchhoff equation, the continuity equation, the Navier-Stokes equation and the Fourier equation.

The Fourier-Kirchhoff equation is valid for fluids in motion:

$$\frac{\partial T}{\partial t} + \vec{w} \cdot \nabla T = a\nabla^2 T + \frac{M}{\rho \cdot c_p} \tag{E.4}$$

where ***w*** is the fluid speed [m/s] , ***a*** represents the thermal diffusion coefficient [m^2/s], $\boldsymbol{\nabla^2 T}$ represents the Laplace operator applied to the temperature fields, $\boldsymbol{\rho}$ is the density of fluid [kg/m^3] and $\boldsymbol{c_p}$ is the specific heat capacity [J/kgK].

$$a = \frac{k}{\rho \cdot c_p}\ [\mathrm{m^2/s}] \tag{E.5}$$

The conservation of the fluid's mass it is given by the continuity equation:

$$\frac{\partial \rho}{\partial t} + \nabla(\rho \vec{w}) = 0 \tag{E.6}$$

Writing the second law of mechanics for a compressible and viscous moving fluid that exerts pressure, gravitation, inertia and friction forces the Navier - Stokes equation can be written as [51]:

$$\frac{\partial \vec{w}}{\partial t} + \vec{w}\nabla\vec{w} = \vec{g} - \frac{1}{\rho}\nabla p + \nu\nabla^2\vec{w} - \vec{g}\beta\Delta T + \frac{\nu}{3}\nabla \cdot div\vec{w} \tag{E.7}$$

where ***g*** is the free fall acceleration, $\boldsymbol{\nu}$ the kinematic viscosity coefficient, ***p*** refers to the pressure and $\boldsymbol{\beta}$ is the volumetric thermal expansion coefficient.

The Fourier equation is written as:

$$-k \cdot \nabla T = \alpha(T - T_{fluid}) \tag{E.8}$$

from which the convection coefficient must be determined.

The equations described above represent the mathematical model of the heat convection process. Due to the impossibility to solve the mathematical model through mathematical analysis methods, the similitude criteria represent the solution used in practice.

The similitude criteria are obtained by applying the mathematical model described above to the affine transform (e.g. $T=C_T \cdot T'$, where T' is associated with the model's temperature, ***T*** refers to the original temperature and $\boldsymbol{C_T}$ represents a constant).

APPENDIX F

This section presents the Matlab sequence used to generate the heat coefficients function of temperature.

```
lambda = 0.0271; % thermal conductivity
cp = 1000; % j/kgK
rho = 1.12; % air density
niu = 17*10^-6;
g=10;

tp = 25:0.5:60;
tp(1) = 25.1;
ta = 25;
tap = ta+tp;
Tm = 1./((tap./2)+273);
dT = tp-ta;
Beta = Tm; % Tm is the mean temperature between the plate temperature
and fluid temperature
An=2*(0.06*0.03);
Ap=29*(0.0015*0.06);
Apn=(0.06*0.05);

AnLatHs = 2*0.031*0.026;
ApLatHs = 16*0.002*0.026;
ApnLatHs = 0.062*0.026;

C1 = 0.59; %vertical plate
C2 = 0.71; %horizontal plate
C3 = 0.35; %horizontal plate face down


l=[0.03, 0.06, 0.13, 0.034, 0.031, 0.026]; % characteristic lengths

Pr = (rho*cp*niu)/lambda; %Prandtl number

%HeatSink front
Gr = (Beta*g.*dT*l(1)^3)/niu^2;
%Nu = alpha*l/lambda;

alphaN0 = (lambda*C1.*((Pr*Gr).^(0.25)))/l(1);
alphaN = 1.4*alphaN0;

Gr = (Beta*g.*dT*l(2)^3)/niu^2;
alphaP = (lambda*C1.*((Gr*Pr).^(0.25)))/l(2);
```

```
alphaEq = alphaP*Ap/Apn+alphaN*An/Apn;
ReqHeatsink = 1./(alphaEq*0.13*0.07);

%Horizontal Plate superior & inferior
Gr = (Beta*g.*dT*l(3)^3)/niu^2;
%Nu = alpha*l/lambda;

alphaHSup = (lambda*C2.*((Pr*Gr).^(0.25)))/l(3);
alphaHInf = (lambda*C3.*((Gr*Pr).^(0.25)))/l(3);

%Vertical Plate superior and Inferior
Gr = (Beta*g.*dT*l(3)^3)/niu^2;
%Nu = alpha*l/lambda;

alphaVSup = (lambda*C1.*((Pr*Gr).^(0.25)))/l(3);
alphaVInf = (lambda*C1.*((Gr*Pr).^(0.25)))/l(3);

%Vertical Lateral Plate superior and Inferior
Gr = (Beta*g.*dT*l(4)^3)/niu^2;
%Nu = alpha*l/lambda;

alphaVLateralSup = (lambda*C1.*((Pr*Gr).^(0.25)))/l(4);
alphaVLateralInf = (lambda*C1.*((Gr*Pr).^(0.25)))/l(4);

%Lateral HeatSink
Gr = (Beta*g.*dT*l(5)^3)/niu^2;
%Nu = alpha*l/lambda;

alphaN0LateralHsink = (lambda*C1.*((Pr*Gr).^(0.25)))/l(5);
alphaNLateralHsink = 1.6*alphaN0LateralHsink;

Gr = (Beta*g.*dT*l(6)^3)/niu^2;
alphaPLateralHsink = (lambda*C1.*((Gr*Pr).^(0.25)))/l(6);

alphaEqLateralHsink =
alphaPLateralHsink*ApLatHs/ApnLatHs+alphaNLateralHsink*AnLatHs/ApnLa
tHs;

%Interior resistance
Atotback=0.13*0.06-2*0.04*0.04;

%Equivalent resistances
ReqUpHplate = 1./(alphaHSup*0.13*0.034);
ReqDownHplate = 1./(alphaHInf*0.13*0.034);
ReqUpVplate = 1./(alphaVSup*0.019*0.13);
ReqDownVplate =1./(alphaVInf*0.0167*0.13);
```

```
ReqUpVLateralplate = 1./(alphaVLateralSup*0.019*0.034);
ReqDownVLateralplate =1./(alphaVLateralInf*0.0167*0.034);
ReqLateralHeatsink = 1./(alphaEqLateralHsink*0.06*0.03);

RupEq= 1./(1./ReqUpHplate+2./ReqUpVplate+2./ReqUpVLateralplate);
RdownEq
=1./(1./ReqDownHplate+2./ReqDownVplate+2./ReqDownVLateralplate);
RtotBackEq = 1./(alphaVSup*Atotback);

RupEq = RupEq';
RdownEq = RdownEq';
dT=dT';
RupEq = roundn(RupEq,-1);
RdownEq = roundn(RdownEq,-1);
fileID = fopen('RupEq.txt','r+');
fprintf(fileID,'%2.1f', RupEq);

fileID = fopen('dT.txt','r+');
fprintf(fileID,'%2.1f', dT);

fileID = fopen('RdownEq.txt','r+');
fprintf(fileID,'%2.1f', RdownEq);

fileID = fopen('ReqHeatsink.txt','r+');
fprintf(fileID,'%2.1f', ReqHeatsink);

fileID = fopen('ReqLateralHeatsink.txt','r+');
fprintf(fileID,'%2.1f', ReqLateralHeatsink);

fileID = fopen('BackChamber.txt','r+');
fprintf(fileID,'%2.1f', RtotBackEq);
```

APPENDIX G

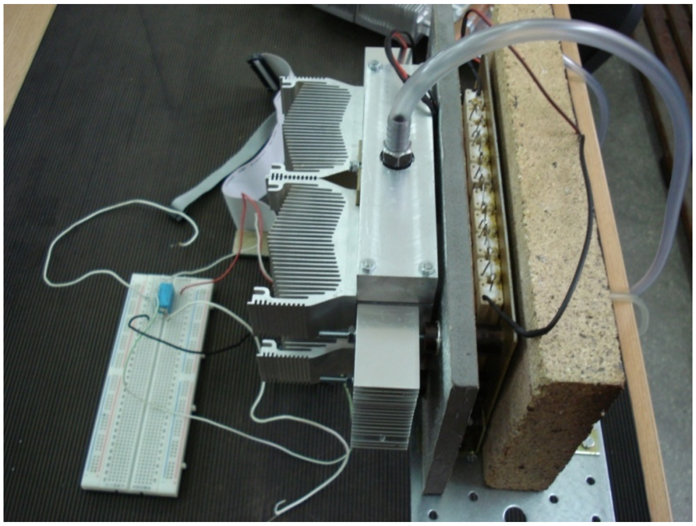

Figure G.1 TEM setup. Source [original]

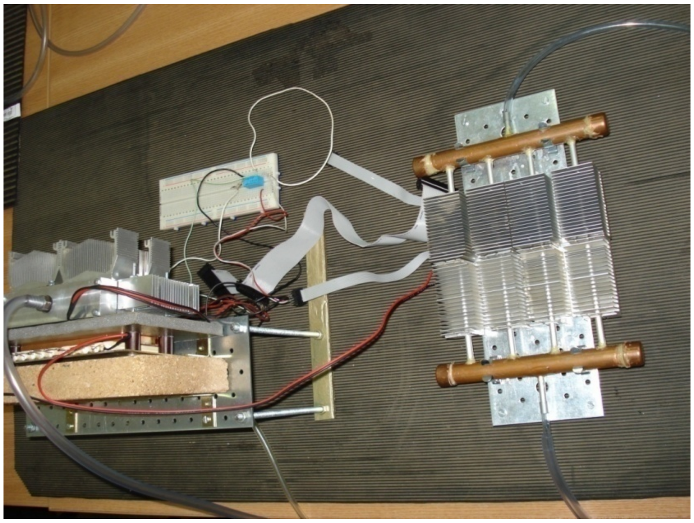

Figure G.2 TEM test rig with liquid to air heat exchanger. Source [original]

Figure G.3 TEM test rig placed in the thermally isolated chamber. Source [original]

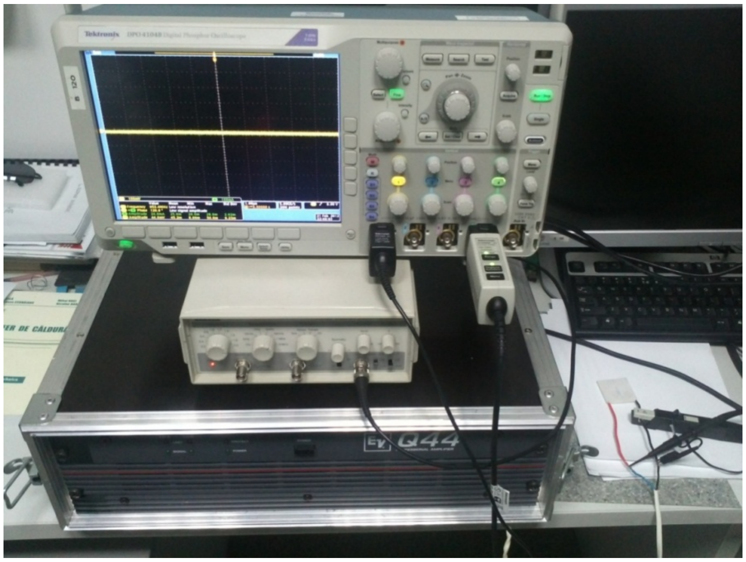

Figure G.4 Experimental setup used to determine the TEM intrinsic parasitic components. Source [original]

APPENDIX H (Vacuumed TEG)

The system was implemented to improve the efficiency of a TEG. The air inside the TEM and between the pellets was removed using a high power vacuum pump and the mechanical system presented below. A vacuum of $5 \cdot 10^{-5}$ bar was achieved. For testing, a resistive heater was placed on one side of the system while on the other a heat pipe was attached. The experimental results show that the efficiency has been increased by up to 4%. The vacuumed TEG was able of providing a higher output voltage for the same temperature of the heat source. The system also protects the TEG from moisture while also generating a compact device.

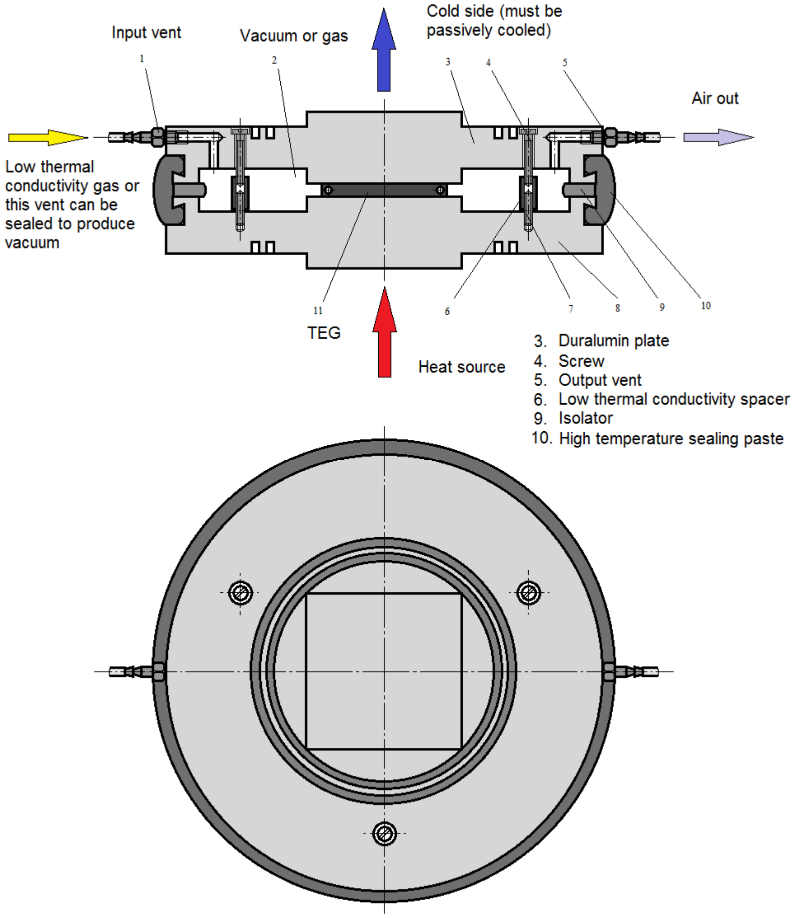

Figure H.1 Vacuumed TEG system cross sections. Source [original]

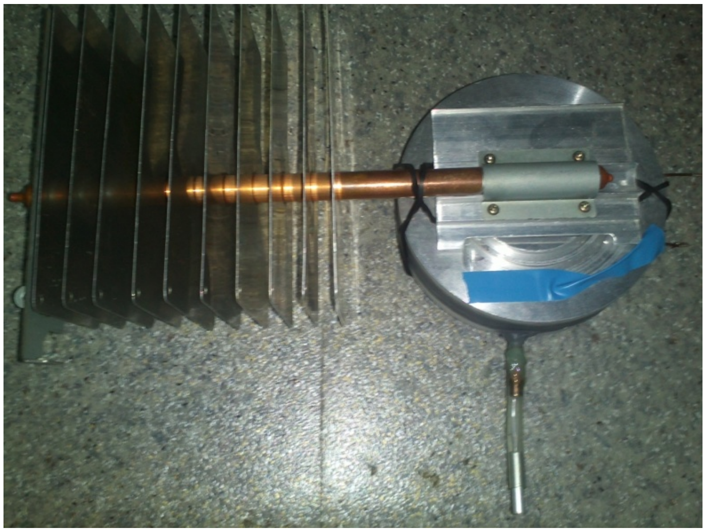

Figure H.2 Vacuumed TEG. Source [original]

APPENDIX I

Water pump control – representation of a block diagram part.

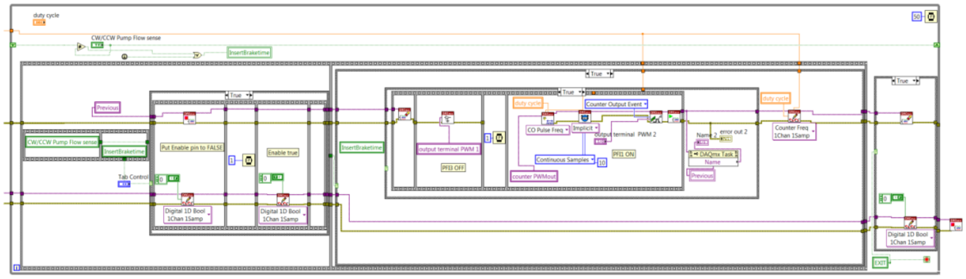

Figure I.1 LabVIEW VI of the pump control block diagram. Source [original]

Thermal conductance measurement front VI

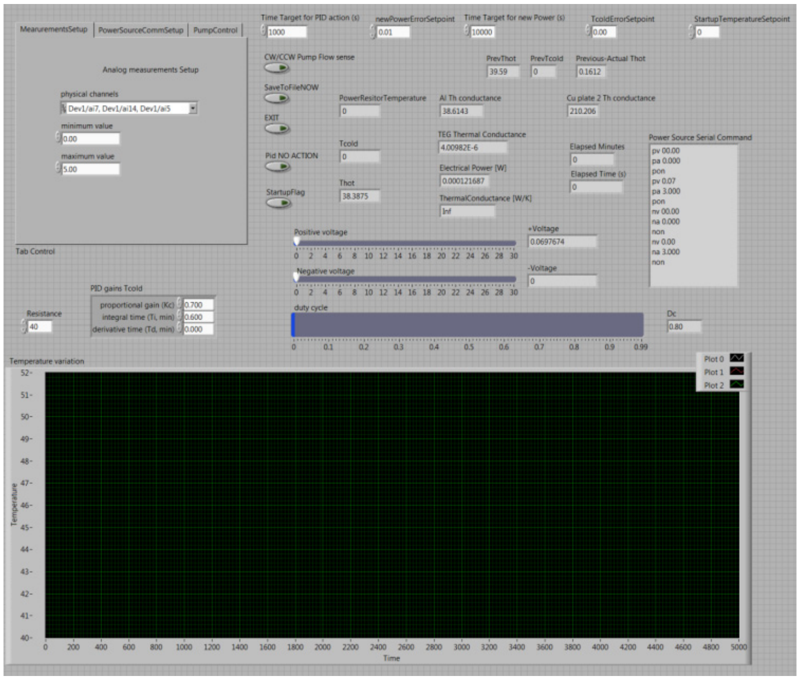

MeasurementsSetup | PowerSourceCommSetup | PumpControl

Analog measurements Setup

physical channels: Dev1/ai7, Dev1/ai14, Dev1/ai5

minimum value: 0.00

maximum value: 5.00

Tab Control

Time Target for PID action (s): 1000

newPowerErrorSetpoint: 0.01

Time Target for new Power (s): 10000

TcoldErrorSetpoint: 0.00

StartupTemperatureSetpoint: 0

PrevThot: 39.59

PrevTcold: 0

Previous-Actual Thot: 0.1612

PowerResitorTemperature: 0

Al Th conductance: 38.6143

Cu plate 2 Th conductance: 210.206

TEG Thermal Conductance: 4.00982E-6

Tcold: 0

Electrical Power [W]: 0.000121687

Thot: 38.3875

ThermalConductance [W/K]: Inf

Elapsed Minutes: 0

Elapsed Time (s): 0

Power Source Serial Command:

```
pv 00.00
pa 0.000
pon
pv 0.07
pa 3.000
pon
nv 00.00
na 0.000
non
nv 0.00
na 3.000
non
```

+Voltage: 0.0697674

-Voltage: 0

Dc: 0.80

Resistance: 40

PID gains Tcold

proportional gain (Kc): 0.700

integral time (Ti, min): 0.600

derivative time (Td, min): 0.000

Figure I.2 LabVIEW VI front panel for the thermal conductance measurement process. Source [original]

Block diagram for the battery charging control system (Buck converter control)

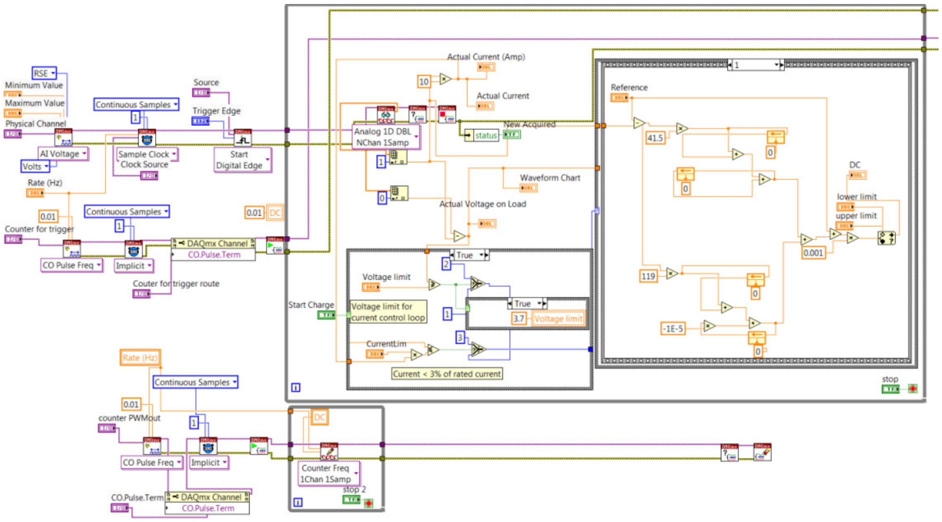

Figure I.3 LabVIEW VI control block diagram for the Buck converter